An Experimental and Theoretical Study of an Omnidirectional Pendulum Energy Harvester

PhD Thesis

Department of Mechanical and Aerospace Engineering
University of Strathclyde, Glasgow

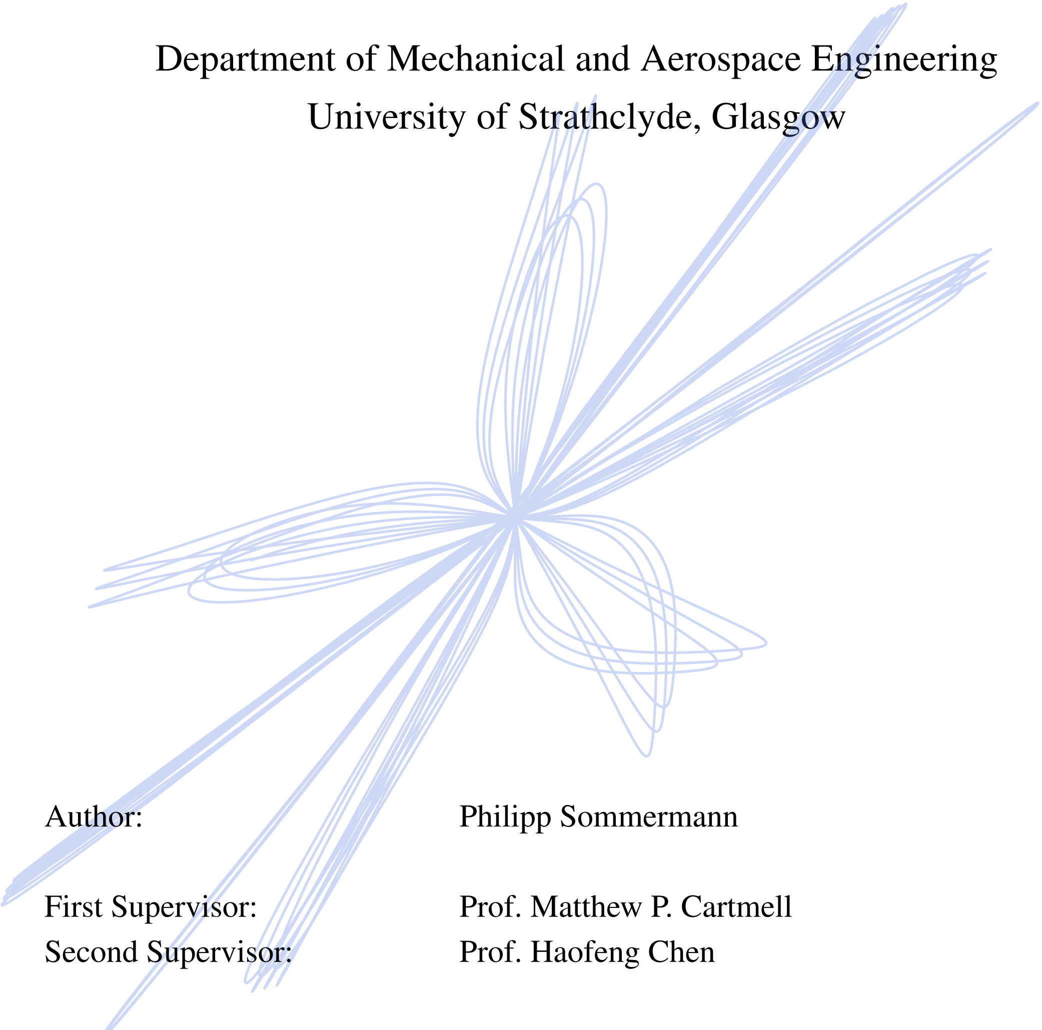

Author:	Philipp Sommermann
First Supervisor:	Prof. Matthew P. Cartmell
Second Supervisor:	Prof. Haofeng Chen
Location, Date of Delivery:	Glasgow, 28th January 2023

Declaration of Authenticity and Author's Rights

This thesis is the result of the author's original research. It has been composed by the author and has not been previously submitted for examination which has led to the award of a degree.

Signed: Philipp Sommermann

Date: 28th January 2023

Acknowledgements

I am profoundly grateful to my supervisor Professor Dr. Matthew Phillip Cartmell for all his support and invaluable advice. His constant support throughout the troublesome periods of the PhD especially during the pandemic he was very helpful and helped me to keep myself motivated. He is without question the best mentor I have had in my life. I would like to thank Professor Dr. Haofeng Chen for acting as the second supervisor for the project.

Additionally, I would like to thank my fellow PhD colleagues Alessia Abbati, Alessio Boaro, Georgie Crewdson, Dr. Guillermo Idarraga Alarcon, James Nash, Jonathan Marin Perez, Kieran Pugh, Michail Dellepiane, Miguel Ubago Torres, Sarah Davidson, and Dr. Sheen Mclean (alphabetically sorted by the first name, with the current title at the time of publication) for their help and support over the years. New friendships have formed over time and I hope that our paths will cross again in the future. Up to that point, I wish you the best and achievement in whatever you may choose to seek after.

I would like to thank my partner Nadine Heckel for the constant support and good advice.

A special thank you goes out to the technical staff who always helped me with manufacturing the experimental rig. Additionally, I would like to thank Professor Dr. Enrico Tubaldi and his team for providing the experimental equipment and the vibration shaker table. For various online discussions regarding *Mathematica*® related questions, I would like to thank Professor Dr. Christopher Klausmeier.

Scientific Contributions

Journal Article

[1] SOMMERMANN, P. & CARTMELL, M. P. The dynamics of an omnidirectional pendulum harvester. In: (May 2021), pp. 1–12. DOI: `10.1007/s11071-021-06479-z`. URL: `https://doi.org/10.1007/s11071-021-06479-z`

Journal Article Under Review

[2] SOMMERMANN, P. & CARTMELL, M. P. A comparison of the numerically and experimentally determined dynamics of an omnidirectional pendulum energy harvester. In: (2022), pp. -. DOI: `-`. URL: `-`

Abstract

The spherical pendulum is mathematically well described and different scholars contributed to the topic in the past. Nevertheless, in the field of pendulum-based energy harvesting the interoperation of a simple pendulum is prevailing over the spherical pendulum. The energy harvester's application areas, and probably its overall capacity, may be limited as a result of this reduction in degrees of freedom. To that end, this work presents the omnidirectional energy harvester that operates independently of the direction of excitation. The numerical evaluation of the energy harvester observes quasiperiodicity and chaotic dynamics for different forcing conditions but with an increase in the power take-off the dynamics of the energy harvester become generally more periodic. The dynamics of the system are highly dependent on the excitation frequency, excitation amplitude, damping ratio, and power take-off torque. In the experimental analysis two power take-off modes of different levels are compared. In the frequency responses the softening characteristics of the spherical pendulum are observed. Additionally, excitation frequency up- and down-sweeps are included to observe the broadening of the operational range of the energy harvester. Interestingly the excitation frequency up-sweep shows a large increase in the operational region meaning the spherical pendulum shows hardening characteristics. An optimal operational point is defined close to the maximum deflection in the upper nonlinear jump region. For the comparison of the numerical and experimental results the numerical results undergo a simple trigonometric transformation. With an adaption of the excitation amplitude the numerical results show the main characteristics of the experimental results including the hardening effect during the excitation frequency up-sweep of the experiments.

Table of Contents

List of Figures

List of Tables

Keywords

Bifurcation

Broadening

Chaos

Coupled excitations

Energy harvesting

Hardening

Mechanical oscillator

Method of multiple scales

Nonlinear dynamics

Nonlinear jump region

Numerical modelling

Numerical simulations

Parametric excitation

Parametric resonance

Pendulum energy harvesting

Power take-off

Softening

Spherical pendulum

Vibrational energy harvesting

List of Symbols

Symbols	**Definition**	**Unit**
l	Length	m
m	Mass	kg
g	Gravitational acceleration constant	$\frac{\mathrm{m}}{\mathrm{s}^2}$
t	Time	s
θ	Generalised pendulum coordinate	rad or deg
$\theta(t)$	Angular displacement of θ	rad or deg
$\dot{\theta}(t)$	Angular velocity of θ	$\frac{\mathrm{rad}}{\mathrm{s}}$ or $\frac{\mathrm{deg}}{\mathrm{s}}$
$\ddot{\theta}(t)$	Angular acceleration of θ	$\frac{\mathrm{rad}}{\mathrm{s}^2}$ or $\frac{\mathrm{deg}}{\mathrm{s}^2}$
ϕ	Generalised pendulum coordinate	rad or deg
$\phi(t)$	Angular displacement of ϕ	rad or deg
$\dot{\phi}(t)$	Angular velocity of ϕ	$\frac{\mathrm{rad}}{\mathrm{s}}$ or $\frac{\mathrm{deg}}{\mathrm{s}}$
$\ddot{\phi}(t)$	Angular acceleration of ϕ	$\frac{\mathrm{rad}}{\mathrm{s}^2}$ or $\frac{\mathrm{deg}}{\mathrm{s}^2}$
ξ_θ	Damping ratio in direction of θ	–
ξ_ϕ	Damping ratio in direction of ϕ	–
U_0	Excitation amplitude	m
V_0	Excitation amplitude	m
W_0	Excitation amplitude	m
Ω_u	Excitation frequency	$\frac{1}{\mathrm{s}}$ or Hz
Ω_v	Excitation frequency	$\frac{1}{\mathrm{s}}$ or Hz

Ω_w	Excitation frequency	$\frac{1}{\mathrm{s}}$ or Hz
ω_n	Natural frequency	$\frac{\mathrm{rad}}{\mathrm{s}}$
U	Potential energy	J
T	Kinetic energy	J
T_θ	Power take-off torque in direction of θ	Nm
T_ϕ	Power take-off torque in direction of ϕ	Nm

Dimensionless symbols

τ	Dimensionless time	–
ω_0	Dimensionless natural frequency	–
α_θ	Dimensionless damping in direction of θ	–
α_ϕ	Dimensionless damping in direction of ϕ	–
a_u	Dimensionless excitation amplitude	–
a_v	Dimensionless excitation amplitude	–
a_w	Dimensionless excitation amplitude	–
β_u	Dimensionless excitation frequency	–
β_v	Dimensionless excitation frequency	–
β_w	Dimensionless excitation frequency	–
P_θ	Dimensionless power take-off in direction of θ	–
P_ϕ	Dimensionless power take-off in direction of ϕ	–
ε_r	Radiusing parameter of the power take-off	–

Method of multiple scales

ε	Small parameter	–
$\bar{\alpha}_\theta$	Dimensionless damping in direction of θ	–
$\bar{\alpha}_\phi$	Dimensionless damping in direction of ϕ	–
$\bar{a}_u$	Dimensionless excitation amplitude	–

$\bar{a}_v$	Dimensionless excitation amplitude	–
$\bar{a}_w$	Dimensionless excitation amplitude	–
$\bar{P}_\theta$	Dimensionless power take-off in direction of θ	–
T_0	Time	–
T_1	Slower time scale	–
T_2	Slower time scale	–
A	Complex amplitude of the complementary function	–
$\bar{A}$	Complex amplitude of the complementary function	–
B	Complex amplitude of the complementary function	–
$\bar{B}$	Complex amplitude of the complementary function	–
a_p	Amplitude of secular terms	–
b_p	Amplitude of secular terms	–
α_p	Phase of secular terms	–
β_p	Phase of secular terms	–
σ_p	Detuning parameter	–
ψ	Transformed phase angle	–

Experimental Symbols

α_{offset}	Static angular Offset	deg
A	Excitation amplitude	mm
Ω	Excitation frequency	Hz
θ_{14}	Angular displacement of shaft 14	deg
θ_{23}	Angular displacement of shaft 23	deg
$avg.\ V_{14}$	Arithmetic mean rectified voltage output of shaft 14	V
$avg.\ V_{23}$	Arithmetic mean rectified voltage output of shaft 23	V
R_S	Series resistor (load resistor)	Ω
R_P	Parallel resistor (load resistor)	Ω

R_{low}	Sum of resistance in the low power take-off mode	Ω
R_{high}	Sum of resistance in the high power take-off mode	Ω
ξ_{14}	Damping ratio of shaft 14	–
ξ_{23}	Damping ratio of shaft 23	–
$avg.\ P_{14}$	Arithmetic mean rectified power output of shaft 14	W
$avg.\ P_{23}$	Arithmetic mean rectified power output of shaft 23	W
I_4	Current output of generator 4	A
I_3	Current output of generator 3	A
I_{14}	Current output of shaft 14	A
I_{23}	Current output of shaft 23	A
a_x	Acceleration in the x-direction	$\frac{\mathrm{m}}{\mathrm{s}^2}$
a_y	Acceleration in the y-direction	$\frac{\mathrm{m}}{\mathrm{s}^2}$
a_z	Acceleration in the z-direction	$\frac{\mathrm{m}}{\mathrm{s}^2}$
a_{abs}	Absolute acceleration	$\frac{\mathrm{m}}{\mathrm{s}^2}$

Comparison of experiments and numerical results

θ_{n14}	Angular displacement of shaft 14 numerical	rad or deg
θ_{n23}	Angular displacement of shaft 23 numerical	rad or deg

Duffing equation (in the introduction in Section 2.2.2)

y	Generalised coordinate	-
ζ	Damping ratio	-
α	Nonlinearity parameter	-
γ	Excitation amplitude	-
Ω	Excitation frequency	-

Alternative mathematical models of the spherical pendulum (in the introduction in Section 2.3.4)

γ	Generalised coordinate	rad or deg
ψ	Generalised coordinate	rad or deg
θ_x	Generalised coordinate	rad or deg
θ_y	Generalised coordinate	rad or deg

List of Abbreviations

1-DOF	One degree of freedom
2-DOF	Two degrees of freedom
emVEH	Electromagnetic vibration energy harvester
EOM	Equation of motion
eVEH	Electrostatic vibration energy harvester
FET	Field-effect transistor
ICs	Initial conditions
LCEs	Lyapunov characteristic exponents
ODE	Ordinary differential equation
PTO	Power take-off
pVEH	Piezoelectric vibration energy harvester
PWM	Pulse-width modulation
RMS	Root mean square
VEH	Vibration energy harvester

Chapter 1

Introduction

Energy harvesting is used to supply small devices with energy. Traditionally these small devices are powered with batteries, however they have one major downside which is that they are a finite energy source. This generally is not a problem as long as they are easily accessible products that can be charged every day. However, it gets more complicated if the battery is used in a remote area or is even inaccessible. A replacement or recharging of the battery in this area is either highly difficult or even impossible. And these are the areas where an energy harvesting device has major advantages over the battery as a power source.

Another downside of the battery is its dependency on rare materials. Materials like lithium, cobalt, and gold are rare, expensive, and limited, and on top of all things the ethical standards in the mining camps are heavily criticised by human rights watch organisations. It is therefore of crucial importance to reduce the usage of batteries and keep battery waste as little as possible.

The omnidirectional pendulum energy harvester in this work has an approximate volume of one cubic meter with this size an application in the area of wave energy harvesting is possible. But the system can be downscaled easily and it can be used to power for example a hearing aid or a pacemaker. Since the last one is inaccessible after fitting it has a great advantage that the energy harvester produces a supply voltage that powers the pacemaker. With this the energy storage device within the pacemaker can be reduced in mass which in return saves material and has the potential to increase the lifespan of the device. The in this work introduced omnidirectional energy harvester is a pre-prototype that is used to observe the general dynamics. These valuable results can then be further applied to the next development stage of the prototype.

In the literature a great number of simple pendulum energy harvesters are examined. But with a further increase in the degree of freedom the number of energy harvesters observed decreases drastically. This work is providing further numerical and experimental research to contribute to the common knowledge in the field of three-dimensional vibrational energy harvesting with a pendulum based system. The advantage of an additional degree of freedom is the increased potential of the energy harvester to operate under different forcing conditions independent of the direction of excitation. This is the main advantage that a spherical pendulum energy harvester as described in this thesis has over a simple pendulum energy harvester.

1.1 Research Aims & Objectives

From the previously described advantages of a two degree of freedom system over a one degree of freedom system four major research actions can be stated.

- Development of a mathematical model of the energy harvester with an active power take-off and investigate the mathematical model numerically.
- Conceptualise, develop, and build a pre-prototype of the omnidirectional pendulum energy harvester. Evaluate, analyse, and verify its capabilities experimentally.
- Investigate a possible broadening of the operational range of the omnidirectional energy harvester and define an optimal operational point.
- Compare the numerical and experimental results and investigate possible improvements of the numerical analysis.

1.2 Structure of the Thesis

Chapter 1 gives the reader an introduction in the thesis and an overview over the general structure.

Chapter 2 gives an overview ot the theoretical background. This includes four main fields of interest. These are energy harvesting, nonlinear dynamics, spherical pendulum, and the control of the electric power take-off.

Chapter 3 the methodology of the thesis is observed. This includes remarks on the numerical analysis, experimental design, post-processing of the experimental data, determination of the damping ratios, observation of internal vibrations in the experimental rig, and the introduction of the equations to compare experimental and numerical results.

Chapter 4 introduces the mathematical model for a forced spherical pendulum. Additionally, an active power take-off term is introduced, this transforms the mathematical model of the spherical pendulum into an omnidirectional pendulum energy harvester.

Chapter 5 gives a numerical analysis of the dynamics of the omnidirectional pendulum harvester. The dynamics are compared under different forcing conditions with and without an active power take-off.

Chapter 6 investigates the experimental results of the omnidirectional pendulum energy harvester. The results of the energy harvester are compared for an operation in a low and a high power take-off mode. Additionally, the broadening of the operational range of the energy harvester is observed by inclusion of excitation frequency sweeps. Videos have been uploaded to see the experimental rig in action [3].

Chapter 7 compares the numerical and experimental results in the low and high power take-off modes.

Chapter 8 introduces different areas of application of the omnidirectional pendulum energy harvester and proposes and investigates theoretically a controlled power take-off.

Chapter 9 shows the conclusions of this thesis.

Chapter 10 proposes different subjects for future scholars to investigate.

Chapter 2

Theoretical Background

2.1 Energy Harvesting

Energy harvesting is a large field of research and its popularity is constantly increasing over the past years. Nowadays the term energy harvesting covers a wide variety of different energy harvesting methods. This work therefore only considers the conversion of kinetic energy to usable energy which is mostly electric energy. Already in the antiques these ambient conditions were used by the Greeks with their water-powered mills in 280-220 BC [4] and the Roman used wind-powered machines in the first century AD [5] with which they mechanically grounded grains. The difference to today's energy harvesters is, apart from the massive technical improvements, for the most part the final product, electrical energy. These days ambient energy is harvested by a broad range of energy harvesters for example to utilize wind energy with large on- and offshore wind parks or to convert the energy of waves or tides. The last-mentioned harvester group is often located in the subgroup of the so-called vibration energy harvesters. This group of harvesters converts vibrational energy into electric energy. These come in different sizes, bigger wave energy harvesters [6], but also micro- or nanoscale machines are of interest for researchers [7–10]. These small devices can be used in remote or inaccessible areas, where they are self-sustained with applications in various fields for example as structural health monitoring devices [11] and medical devices [12].

2.1.1 Potential of Vibrational Energy Harvesting

The definition of vibration energy harvesters (VEH) is the conversion of kinetic energy (mechanical motion energy) into electrical energy [13]. Since there is a broad variety of mechanical motion sources available, the field of vibrational energy harvesting itself is a large field that is constantly growing [14]. Table 2.1 shows the potential of different vibration sources by displaying their acceleration and frequency. It can be seen that there are hardly any limitations to the range of applications, ranging from small electrical appliances e.g. blenders and microwaves over human motion [15] up to different parts of vehicles [16].

Table 2.1: Frequency and acceleration of different vibration sources [16]

Vibration Source	Acceleration $\left[\frac{\mathrm{m}}{\mathrm{s}^2}\right]$	Frequency [Hz]
Car engine compartment	12	200
Base of 3-axis machine tool	10	70
Blender casing	6.4	121
Clothes dryer	3.5	121
Person nervously tapping their heel	3	1
Car instrument panel	3	13
Door frame just after the door closes	3	125
Small microwave oven	2.5	121
HVAC vents in the office building	0.2 - 1.5	60
Windows next to a busy road	0.7	100
CD on notebook computer	0.6	75
Second storey floor of a busy office	0.2	100

To utilise the vibrational energy some kind of mechanical resonator that gets excited by the vibration source is needed. The standard concepts include energy harvesters with a single mass oscillator [17, 18], cantilever beam [19, 20], or a simple pendulum [21, 22]. The resonator can be adapted to its excitation source, by variation of the parameters of the resonator. This can be achieved by adapting e.g. the pendulum length, the mass, the damping ratio, and the stiffness of the system. This tuning means that there are virtually no limits to the operational range of the application. Only alternating differences in frequencies of the vibration source are hard to cope with.

2.1.2 Electromechanical Conversion

After the resonator has been set in motion, the kinetic energy must be converted to electrical energy. This is where the electromechanical conversion comes into the picture. The three main concepts for electromechanical conversion are electromagnetic induction, piezoelectric transduction, and electrostatic transduction [14, 23]. Examples of the energy harvesters with the different concepts are shown in Figure 2.1.

Electromagnetic vibration energy harvesters (emVEH) use electromagnetic transduction to convert the kinetic energy into electric energy [14]. The same principle of operation is used

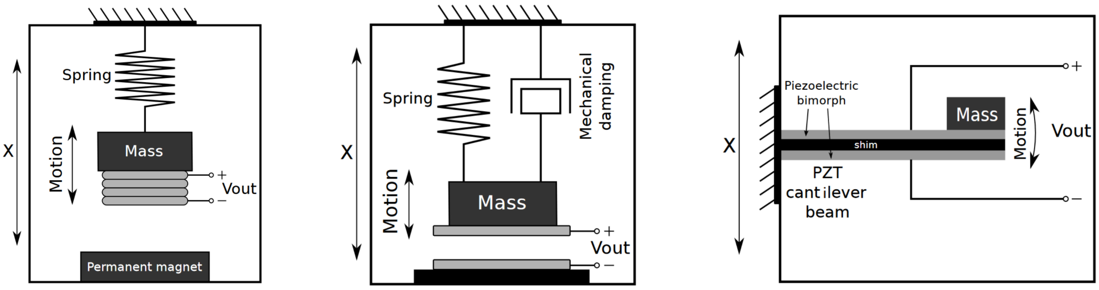

(a) Electromagnetic (b) Electrostatic (c) Piezoelectric

Figure 2.1: Commonly used electromechanical energy converters (adapted from [24])

for example in a DC motor. Figure 2.1a shows a simple design for emVEH, with the single mass oscillator as a mechanical resonator, it consists of a permanent magnet that is attached to the ground and a coil that moves vertically with a spring that applies a restoring force. When the coil and the magnet approach each other, Faraday's law predicts the electromotive force that is induced. Since the movement of the coil is an oscillation, an AC voltage is generated in the coil. This electric energy is drawn and utilized. Various different design of emVEH have been studied over the past, examples are [25–28].

Electrostatic vibration energy harvester (eVEH) "use a variable capacitor structure to generate charges from a relative motion between two plates" [28]. It is mandatory for the principle of operation that the two plates are charged and therefore have a potential to one another. Figure 2.1b shows a design for an eVEH. The design is similar to the single mass oscillator for the electromagnetic conversion. Over the past years various designs for eVEH have been introduced, examples are [29–31].

Piezoelectric vibration energy harvesters (pVEH) utilise the piezoelectric effect to convert mechanical energy into electric energy [14]. A large portion of the pVEH presented use a so-called cantilever beam, see Figure 2.1c. The cantilever beam is a beam with a mass at the end. The beam has a layer of piezoelectric material on the top and bottom which is deformed periodically by the movement of the mass. This deformation causes an electric charge which itself is utilised. Different energy harvesters with a piezoelectric electromechanical conversion were introduced, examples are [32–34].

In Table 2.2 the advantages and disadvantages of the different electromechanical conversions are shown. Pendulum energy harvesters usually rely on electromagnetic conversion with the help of a DC motor or some kind of other construction that utilises the principle of electromagnetic conversion. The pre-prototype examined in this work uses DC motors. These have the advantage that they do not require a supply voltage and are very robust, reliable and cost-effective. However, they have a disproportionately low output voltage and are rather difficult to scale down. In comparison, the disadvantages of electromagnetic conversion are not present in an electrostatic system. Since the electrostatic conversion has a high voltage output and is

Table 2.2: Advantages and disadvantages of different electromechanical conversions [14]

Transducer	Advantages	Disadvantages
Electromagnetic	No voltage source needed	Low output voltage
	Robust	Difficult to microscale
Electrostatic	High output voltage	Voltage source needed
	Suited to microscaling	Complex control electronics
Piezoelectric	No voltage source needed	Requires voltage rectification
	High output voltage and power	Fatigue of piezoelectric beams

well suited for downscaling. However, this must be considered in relation to an external supply voltage source that is needed and complex control electronics. In comparison, the piezoelectric conversion does not need a voltage supply and has a high voltage output. However, the output voltage needs to be rectified and the piezoelectric beams are fragile.

Even though Table 2.2 gives a good initial overview of the advantages and disadvantages of different types of energy harvesters some caveats need to be mentioned. The electromagnetic transducer has two additional disadvantages, firstly, the necessity for a permanent magnet and secondly voltage rectification is required in some cases as well. For the electrostatic transducer, the main disadvantage that is mentioned is that a voltage source is needed, which can be avoided by the use of an electret device. Additionally, the table would benefit greatly by mentioning different price points for the systems and adding the triboelectric energy conversion.

2.1.3 Nonlinearities of Vibration Energy Harvesters

Generally known are systems that are assumed to be linear such as the single-mass oscillator with a nonlinear spring or linearised systems such as a simple pendulum with a small angle assumption, but in reality these systems are not linear. Nonlinearity can occur because of different reasons and examples of this are material, geometric, and contact properties (e.g. friction). This means that vibrational energy harvesters show nonlinear properties which can make an at first glance simple looking system rather complex[1]. But, the dynamics of nonlinear systems have been studied extensively, and tools to analyse nonlinear dynamics are at our disposal. These tools and a general overview of nonlinear dynamics is located in Section 2.2. A prominent software tool to analyse nonlinear dynamics is AUTO [35] and the tool COCO can be used to benchmarking numerical optimization algorithms [36]. Besides the nonlinearities that appear because of mechanical properties there are also nonlinear effects observed in electrical com-

---

[1] This is exclusively referring to a first visual impression.

ponents, these are not discussed in this work since this would exceed the topic of the thesis. Literature recommendations for this topic are [37, 38].

The complex dynamics of a nonlinear system at first glance suggest that it cannot be advantageous to intentionally design a VEH with nonlinear behaviour. But here the first impression is deceptive because there are applications in which nonlinear behaviour is deliberately incorporated by design to the resonator. An example of this is the so-called broadening effect. The theoretical background for this was published in 1918 by the engineer Georg Duffing [39]. He investigated the so- called hardening and softening effects of the equations introduced by himself, the Duffing oscillator. The equation is discussed in Section 2.2.2. In Figure 2.2 these hardening and softening effects are shown with the help of a frequency response. The figure shows the amplitude response for different excitation frequencies. The response of a linear oscillator is shown in black, it shows the typical characteristics with an eigenfrequency at the coordinate origin. To convert energy effectively, the resulting amplitudes should be as physically large as possible[2], for a linear oscillator this is given in a narrow range at the natural frequency. This means that a linear energy harvest can only work effectively in a small working range of excitation frequencies. When looking at the amplitude resonance curve of the nonlinear oscillators, it can be seen that one leans to the left and the other one to the right. This is the previously mentioned softening and hardening effects. In addition, it can be seen that there are areas in the frequency response for the nonlinear oscillators, where there are two stable and one unstable solution (dashed green and blue line) present, this is the so-called multi-modality. Additionally, the hysteresis of the system is displayed with the help of the dashed grey lines. It can be seen that depending on the starting excitation frequency and the direction of the frequency sweep, different amplitudes are obtained [14]. The advantage of the nonlinear resonator, how-

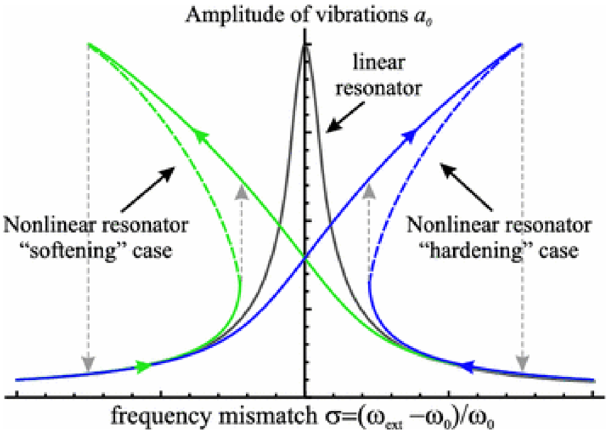

Figure 2.2: Broadening of a nonlinear oscillator. Originally produced by Blokhina et al. [14]

---

[2] This only applies to the purely mechanical system where the electrical effects i.e. parasitic damping are not considered. These interactions between the mechanical and electrical elements are not considered here for reasons of simplicity.

ever, is that the frequency range with predominant high amplitudes has widened and thus the range of application in which the system can operate is consequently larger. This broadening of the bandwidth for vibrational energy harvesters with help of softening and hardening effects is being studied by many researchers e.g. [40–43], and is also observed in the experimental and numerical section of this thesis.

2.1.4 Pendulum Based Energy Harvesters

The field of energy harvesting is very large and therefore it is not surprising that a great variety of energy harvesters has been presented that incorporate some kind of a pendulum. This section is concerned with the different concepts of pendulum energy harvesters, an examination of the dynamics and the mathematical models of spherical pendulums can be found in Sections 2.3.1 and 2.3.2.

The majority of the research is concerned with simple pendulums with one generalised coordinate. These have the advantage that the mathematical description has one generalised coordinate in comparison to the two generalised coordinates needed for the description of the spherical pendulum. Therefore the experimental design of the simple pendulum energy harvester is simpler compared to a pendulum with a higher number of degrees of freedom. Nevertheless, important information is gained from these systems which can also be applied to the spherical pendulum. Therefore, some interesting concepts of simple pendulum energy harvesters are presented in the following.

Dai [44] introduced a pendulum energy harvester which is excited in one vertical direction. In Figure 2.3a the concept is shown. The mass is in the shape of a triangle and magnets are attached to it in a semicircle, these move past a coil that is attached to the shaft. This induces a voltage which then can be utilised. This is the principle of electromagnetic induction. The au-

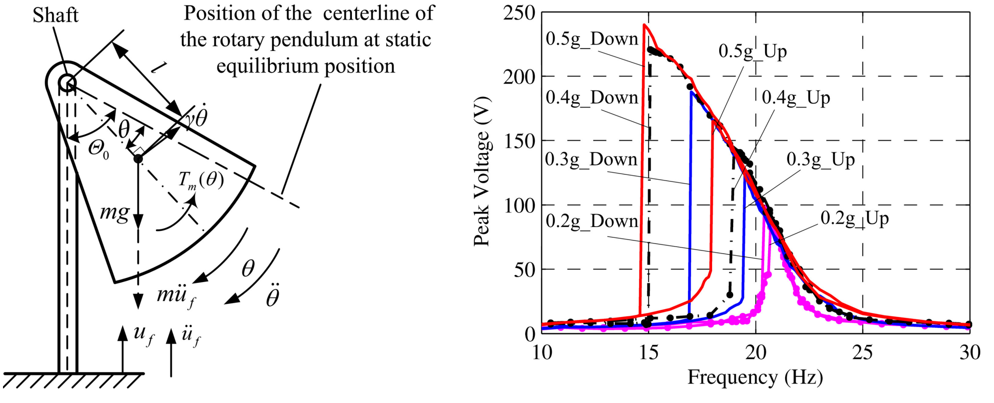

(a) Diagram of the pendulum energy harvester [44]

(b) Softening properties of the measured frequency response of the peak voltage [44]

Figure 2.3: Diagram and frequency response of the voltage output of a simple pendulum energy harvester. Originally produced by Dai [44].

thor compares theoretical and experimental results, which agree well. The results in Figure 2.3b show the nonlinearities of the simple pendulum energy harvester, the softening character and the resulting broadening of the operational range. Similar to the softening effect that is observed in Figure 2.2. Additionally, the author shows that the power output increases with an increase of the acceleration. A frequency doubling is observed as well which increases the power output of the pendulum harvester for low frequencies [44]. More on the effect of period doubling and the resulting route to chaos will be covered in Section 2.2.3. Other interesting concepts for simple pendulum energy harvesters are [21, 22, 45–47].

Based on the variations of the simple pendulum several interesting concepts for energy harvesters were introduced. Exemplary cases are spring pendulums [48, 49], coupled pendulums [50–52], a counterweight pendulum [53], a cantilever beam with a implemented simple pendulum [54], and an autoparametric inverted pendulums [55]. Another interesting concept for a simple pendulum is the adaptive oscillator that modifies the pendulum rod length and therefore can maintain larger deflections over a wider excitation frequency area [56]. These are just a few examples, regarding simple pendulum harvesters, but the diversity is clearly visible. The spherical pendulum energy harvester, on the other hand, is considered less frequent in the literature. This thesis aims to fill in some of the lacks in the literature.

In the PhD thesis by McRobb [57], different types of energy harvesters are presented. Interesting in the context for this work are the presented simple and spherical pendulum energy harvesters.

Another energy harvester that uses a slight modification of the spherical pendulum was presented by Anurakpandit, Townsend, and Wilson [6]. The authors show the numerical and experimental validation of a gimballed pendulum. Figure 2.4 shows the experimental setup of the gimballed pendulum harvester. The system has two degrees of freedom (2-DOF) which allows the system not to be restricted in the direction of the excitation. In their work, the authors examine the effect when one of the 2-DOF is blocked and compare the power output

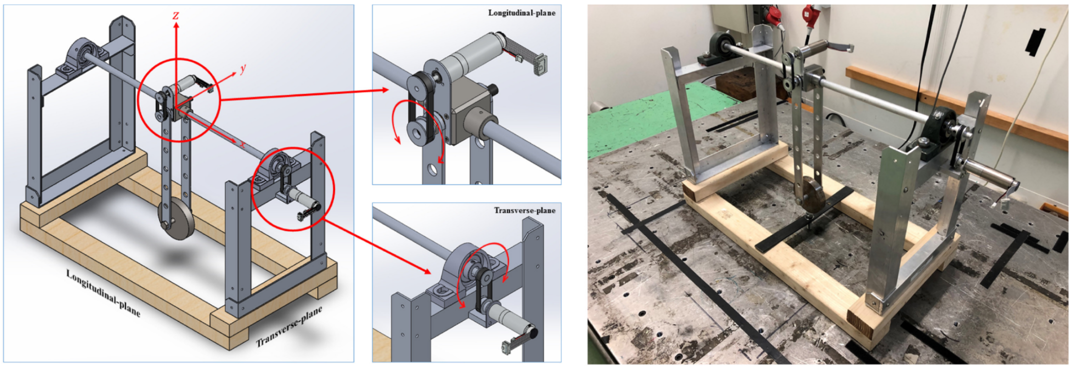

(a) Graphical design [6]

(b) Test rig [6]

Figure 2.4: Design of the gimballed pendulum harvester. Originally produced by Anurakpandit, Townsend, and Wilson [6].

to the free moving two degree of freedom system. Contrary to expectations, the excitation in which the system operates results in a higher power output for the 1-DOF system compared to the 2-DOF system [6]. As the 2-DOF system has two moving shafts and the 1-DOF system has one moving shaft it is reasonable to assume that the lower power output is because of the additional energy losses induced by the higher overall damping ration. However, this slightly lower power output is in contrast to the wider range of possible applications only a minor disadvantage. It is important to keep in mind that this work is only considering cases under ideal laboratory conditions. If a 1-DOF system is excited slightly off plane a defined amount of excitation energy, depending on the angle, can not be converted into kinetic movement energy of the energy harvester and therefore the overall energy efficiency of the energy harvesting system decreases.

Noteworthy is the work of Jahangiri and Sun that investigates the implementation of a spherical pendulum energy harvester in the tower of an offshore wind turbine which utilises the vertical movement of the wind turbine tower [58]. Also, Wang et al. introduce a pendulum based wave energy harvester that can rotate around two axes and is therefore not restricted by the direction of excitation [59].

2.2 Nonlinear Dynamics

Nonlinear behaviour is ubiquitous and can be found in many systems across different disciplines. However, the impression often conveyed is that nonlinear behaviour is disadvantageous and only increases the complexity of a system. And so it happens that in the engineering discipline systems are simplified and/or partial areas are considered in which the dynamics are assumed to be linear. A common example for this is the well known small angle assumption for the simple pendulum. However, this neglects positive effects that arise from nonlinear dynamics as well, as already briefly introduced in Section 2.1.3.

For the omnidirectional pendulum energy harvester that is presented in this work these simplifications to a linear system would affect the dynamics of the system strongly and it would simply defeat the purpose to assume linear behaviour[3]. Therefore, it is crucial to discuss nonlinear effects and nonlinear dynamics. However, nonlinear dynamics is a massive field of research and therefore this section is focused on the most important points with regard to the work.

2.2.1 Origin of Nonlinearities

Nonlinearities occur because of various reasons that are considered in the following. The simplest form of nonlinearity occurs because of geometrical properties of the system [60]. The geometrical nonlinearity can be shown with help of the well-known ordinary differential

---

[3] The work is mainly concerned with large deflections of the energy harvester.

equation of a simple pendulum (2.1). For this simplified example the damping term and forcing terms are not observed.

$$\ddot{\theta} + \frac{g}{l}\sin(\theta) = 0. \tag{2.1}$$

For small oscillations around the resting point ($\approx \pm 20^\circ$) the value of $\sin(\theta)$ can be linearised to $\approx \theta$. This small angle assumption is well-known and widely used. However, if the oscillations exceed an angle of $\pm 20^\circ$ the dynamics of the system are no longer linear but instead become highly nonlinear. This is the same effect that influences the dynamics of the omnidirectional pendulum energy harvester in this work. More on the softening characteristics of the pendulum is considered in greater detail in Section 2.2.2.

Another reason for nonlinearity are the physical properties of the material when it is deformed. Figure 2.5 shows the qualitative behaviour of stress with a variation of strain for the material glass, stainless steel and a plastic material. It can be seen that the material have areas in which the relations between stress and strain are linear and there are areas in which the relations are nonlinear. These material properties are then adapted in the dynamical system, for example by using a spring or a cantilever beam. This allows for a targeted incorporation of nonlinear properties in a resonator which then results in hardening or softening dynamics.

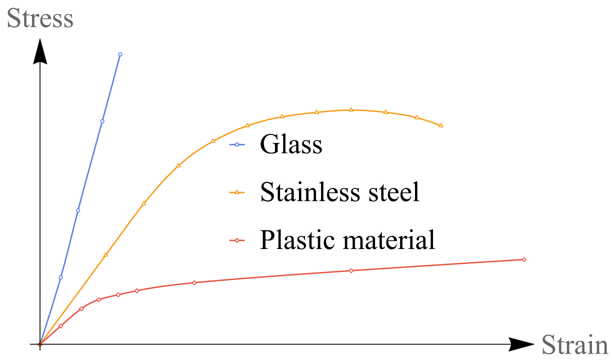

Figure 2.5: Qualitative stress strain curve for different materials

Nonlinearities can be caused by friction, because friction is not directly proportional to velocity in most cases [61]. Friction is normally described with the so-called friction coefficient μ, event though it is assumed to be a constant in most calculations it is in fact not a constant. Additionally, the friction coefficient is categorised in the slipping coefficient and the separating coefficient. Slipping can be assumed as soon as the applied force overcomes the sticking and the separated materials have an absolute velocity [60].

The last reason for nonlinear behaviour is that it is designed into the system intentionally [62, 63]. This can be achieved by adding an additional spring when a definable oscillation amplitude is exceeded or another option would be to constrain the movement with a limit stop. This allows a precise adjustment of the resonator to the operational region.

2.2.2 Hardening and Softening Effects

This section is to be seen as an extension of Section 2.1.3 and therefore goes more into depth on the theoretical aspects of hardening and softening effects and the resulting broadening of the frequency response. The concepts of hardening and softening are associated with Georg Duffing, and with his damped and forced Duffing oscillator [39]. The Duffing Equation (2.2) examined in the work of Brennan et al. [64] is shown below. Where y is the generalised coordinate which is depended on the dimensionless time τ. The different terms are the inertia term $\ddot{y}$, the damping term $2\zeta\dot{y}$, the restoring force term y, and α controls the nonlinearity of the restoring force. The term on the right-hand side of the equation is called the excitation or forcing term with γ defining the excitation amplitude and Ω defining the excitation frequency.

$$\ddot{y}+2\zeta\dot{y}+y+\alpha y^3=\gamma\cos(\Omega\tau). \tag{2.2}$$

The Duffing oscillator can show different nonlinear characteristics depending on the values that are chosen for the variables. Figure 2.6 shows a typical frequency response of the Duffing oscillator. When the control parameter α is positive the amplitude frequency curve leans to the right this is known as hardening effect and when the control parameter is negative the frequency response leans to the left and the system shows softening dynamics. Furthermore, it can be seen that the softening properties increase further when the magnitude of the control parameter for the nonlinear restoring force α is further increased. The dashed lines are shown in Figure 2.6 indicate unstable branches. These unstable branches are marked by a x and a circle ($\circ$) symbol. The x symbol indicates the limit frequency after which the amplitude jumps-up and the circle symbol denotes the maximum value for the amplitude and at the same time the jump down point [64].

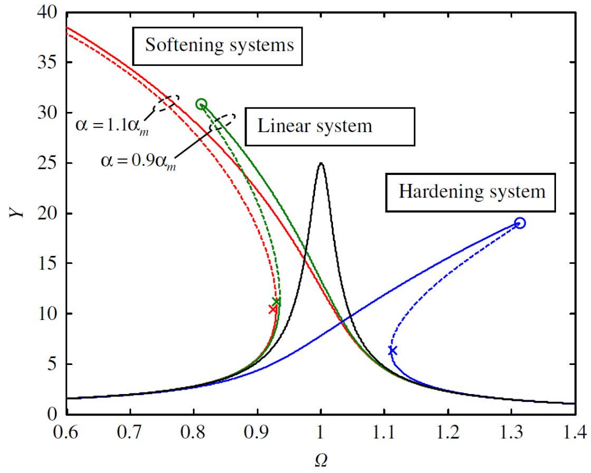

Figure 2.6: Frequency response curve for the Duffing oscillator adapted from [64].

From Figure 2.6 it can be concluded that only the control parameter α has an effect on the nonlinearities of the system. This means that only the part $+\alpha y^3$ of Equation (2.2) determines the intensity of the nonlinearity. Additionally, the sign of the nonlinear part of the restoring force defines whether the systems dynamics are show hardening or softening characteristics. But when recalling the previously mentioned Equation (2.1) of the simple pendulum the softening characteristics cannot be seen directly. However, if the $\sin(\theta)$ term is expanded with a Maclaurin expansion, it can be noticed that the sine term is split into a linear part of the restoring force term followed by a cubed part of the restoring force term. The second one shows similarities to the term in the Duffing equation that controls the level of nonlinearity see Equation (2.3). Moreover, it can be seen that the term has a negative sign and thus the softening behaviour of the simple pendulum can be seen.

$$\ddot{\theta} + \frac{g}{l}\sin(\theta) = \ddot{\theta} + \frac{g}{l}\left(\theta - \frac{\theta^3}{6} + ...\right) = 0. \tag{2.3}$$

The same softening characteristics apply to the spherical pendulum in this work, more on this in Section 2.3.2.

2.2.3 Representation of Nonlinear Dynamics and the Route to Chaos

As the complexity of the system increases, so do the findings consequently too. Therefore, in most cases it makes no sense to use the time wave form but instead special tools to analyse the dynamics of a nonlinear system are needed. These will be introduced in this section by observing the route to chaos.

2.2.3.1 Phase Space

The French mathematician Henri Poincaré introduced the concept of phase space or state space in the 1800s [65]. In the 1900s the physicist J. Willard Gibbs made the concept prominent and it was used in statistical mechanics since then [66]. The phase space plot is an indispensable representation of nonlinear dynamics. They show the general dynamics of a system with the advantage that they can show fixed points and limited cycles of nonlinear systems.

The phase space can be illustrated with a so-called phase portrait. These figures shows the generalised coordinate over the derivative of said coordinate. This is shown qualitatively in Figure 2.7 for a damped unforced spherical pendulum oscillator. For the computation of the qualitative Figures 2.7, 2.8, and 2.9 the Equations (4.36) and (4.37) were used. The parameters that were used for the analysis are shown in the caption of each figure, they were selected with a focus on showing the desired dynamics not on physical sensibility. Figure 2.7a shows the oscillation decay process in the classical time wave form of a damped system that is initially deflected and the amplitude decreases with each swing until its movement is completely decayed. The same dynamics are shown in Figure 2.7b in a phase portrait where on the x-axis

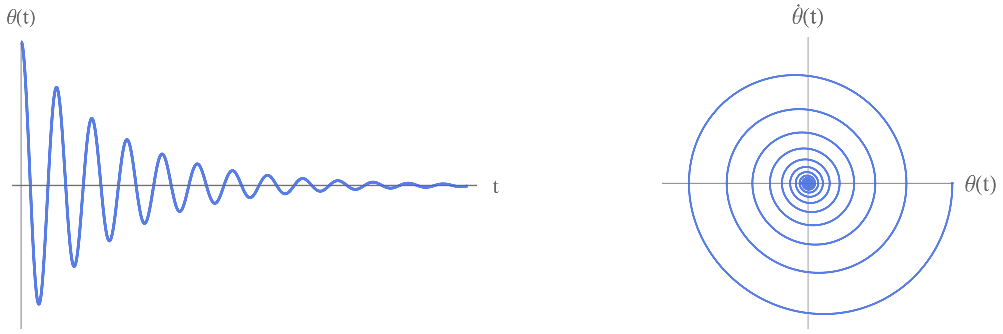

(a) $\theta(t)$ over time

(b) Phase portrait

Figure 2.7: Qualitative diagrams for the decay process for displacement over time and phase portrait from a damped unforced spherical pendulum. The parameters are set to: $l = 0.5$ kg, $m = 1.0$ kg, $g = 9.81\ \frac{\mathrm{m}}{\mathrm{s}^2}$, $\alpha_\theta = \alpha_\phi = 0.12$, $a_u = a_v = a_w = 0$, $\beta_u = \beta_v = 0.5\beta_w = 0$, and $P_\theta = P_\phi = 0$.

the deflection of θ is shown and on the y-axis the velocity of the coordinate θ is shown. Here the trajectory is spiralling towards a node (stable fixed point) in the middle of the coordinate system. The node or sink is a point that attracts trajectories in its vicinity. An example of this would be the resting point of the spherical pendulum. Other fixed points include repellers (unstable fixed points) which repel close trajectories when they are slightly deflected from the fixed point. An example of this is a balanced inverted pendulum where a slight deflection out of the equilibrium causes an acceleration of the pendulum bob because of the gravitational force acting on the pendulum bob. The last fixed points are the saddle points that repel trajectories in one direction and attract them in the other direction [65]. An example of this is a ball that is located on a hyperbolic paraboloid[4]. The mentioned fixed points apply to the spherical pendulum as well. In nonlinear dynamics, the discussion of fixed points plays a very important role, but with regard to this work they have a subordinate role and are therefore not considered further in greater detail.

Figure 2.8 shows the displacement over time and the phase portrait for an unforced and undamped spherical pendulum with periodic dynamics. The oscillator in the time domain shows classical periodic dynamics. These periodic dynamics are represented in the phase space by a circular shape which can be distorted depending on the scaling of the axes or when the dynamics do not follow a cosine/sine function as shown as in these figures.

Figure 2.9 shows non-periodic dynamics for a spherical pendulum. Each deflection of the coordinate θ shows a different value. The clear delineated circle in Figure 2.8b of the periodic dynamics becomes a squeezed circle that consist of many different trajectories for non periodic dynamics see Figure 2.9b. In this case, it cannot clearly be seen which dynamics are present in the system, however, the phase portraits can be used to determine so-called limit cycles. These are areas where the systems dynamic are periodic for some time in an area that otherwise shows

---

[4] In non-scientific terms this shape can be described as a Pringles® crisp.

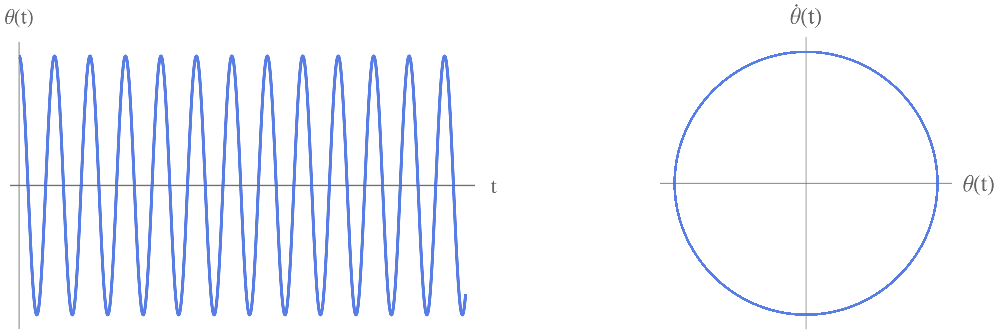

(a) $\theta(t)$ over time

(b) Phase portrait

Figure 2.8: Qualitative diagrams for displacement over time and phase portrait from an undamped and unforced spherical pendulum with periodic dynamics. The parameters are set to: $l = 0.5$ kg, $m = 1.0$ kg, $g = 9.81\ \frac{\mathrm{m}}{\mathrm{s}^2}$, $\alpha_\theta = \alpha_\phi = 0.0$, $a_u = a_v = a_w = 0$, $\beta_u = \beta_v = 0.5\beta_w = 0$, and $P_\theta = P_\phi = 0$.

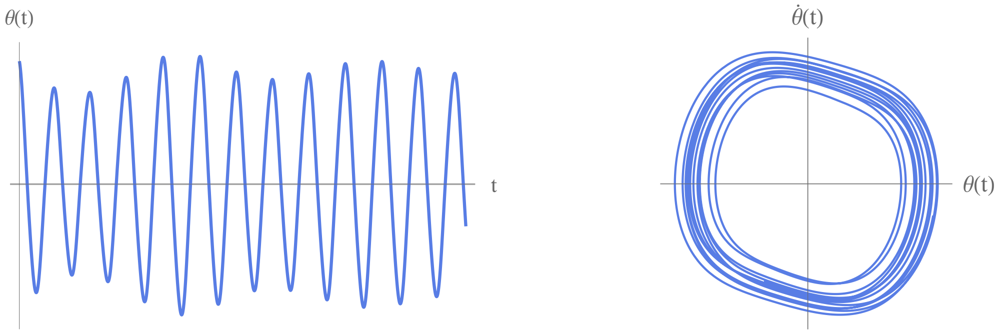

(a) $\theta(t)$ over time

(b) Phase portrait

Figure 2.9: Qualitative diagrams for displacement over time and phase portrait from a damped forced spherical pendulum with non-periodic dynamics. The parameters are set to: $l = 0.5$ kg, $m = 1.0$ kg, $g = 9.81\ \frac{\mathrm{m}}{\mathrm{s}^2}$, $\alpha_\theta = \alpha_\phi = 0.05$, $a_u = a_v = a_w = 0.16$, $\beta_u = \beta_v = 0.5\beta_w = 1.1$, and $P_\theta = P_\phi = 0$.

quasi-periodic or chaotic dynamics. Note that the phase portrait cannot determine whether the dynamics of a system are chaotic or quasi-periodic it can only give a general first impression. For this tools like Poincaré Sections, Bifurcation Diagrams and the Lyapunov exponent are needed. These are discussed in the following.

A nonlinear dynamical system can get into a state of chaotic dynamics when one or more control parameters are varied e.g. excitation amplitude or excitation frequency. During this progress the nonlinear system undergoes different dynamics this is referred to as route to chaos. And there are different routes that lead to chaotic dynamics in a system, e.g. Landau scenario, Ruelle-Takens scenario, route to chaos via intermittency and period-doubling which is attributed to Feigenbaum [67]. But for this work the transition from quasi-periodicity to chaos can be observed and is therefore solely introduced.

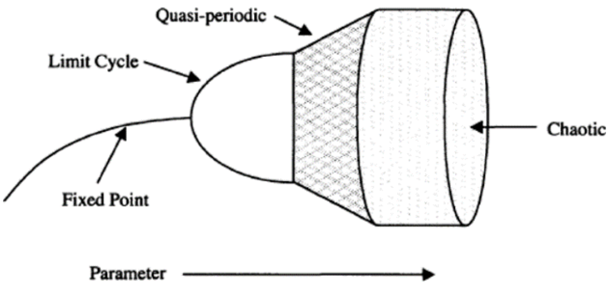

Figure 2.10: Schematic representation of quasi-periodic route to chaos of a forced system [65]

Figure 2.10 shows a schematic diagram of the route to chaos over the preliminary step of quasi-periodicity. For a small control parameter the system shows a fixed point. A fixed point shows the same deflection value for each excitational cycle and is therefore the same as periodic dynamics. Then when the control parameter is further increased the fixed point Hopf bifurcates in two so-called limit cycles. These limit cycles are to be understood as an oscillation that usually alternates between two or more different deflection values. This is followed by an area of quasi-periodic dynamics. When an oscillator shows quasiperiodicity it can show dynamics that appear to follow a repetitive pattern. However, "Quasiperiodic motion can certainly look very complicated and seemingly irregular, but it cannot be truly chaotic in the sense of exponential sensitivity to initial conditions" [68]. The last area of the bifurcation diagram shows chaotic dynamics, this area does not show any repetitive pattern in the time domain. The difference between the quasi-periodicity and chaotic dynamics is that close initial conditions can show high differences for the end result and this does not apply for the quasiperiodicity [68].

2.2.3.2 Poincaré Section

Whether the dynamics of a system are periodic, quasi-periodic or chaotic can be portrayed well in a so-called Poincaré section named after the scholar Henri Poincaré. In a Poincaré section the x-axis shows the deflection of the generalised coordinate and the y-axis shows the velocity of the same generalised coordinate. Figure 2.11b shows a Poincaré section that suggests chaotic dynamics. In comparison, a quasi-periodic system see Figure 2.11a is characterised by the fact that all the single points of the Poincaré section line up and from a shape often appears in a circular form [67]. A fixed point in a Poincaré section is indicated by a single point. The transition from fixed points to quasi-periodicity to chaos for a spherical pendulum is extensively studied more on these topics can be found in Section 2.3.3. The Poincaré section can be produced by storing the values when the oscillator passes by a defined threshold. But for the pendulum energy harvester the approach of storing the values with respect to the excitation frequency is used [69]. For this every full excitational circle the position and velocity of the pendulum bob is stored. This is realised over a pre-defined time period and then the stored coordinates are portrayed which gives a Poincaré section.

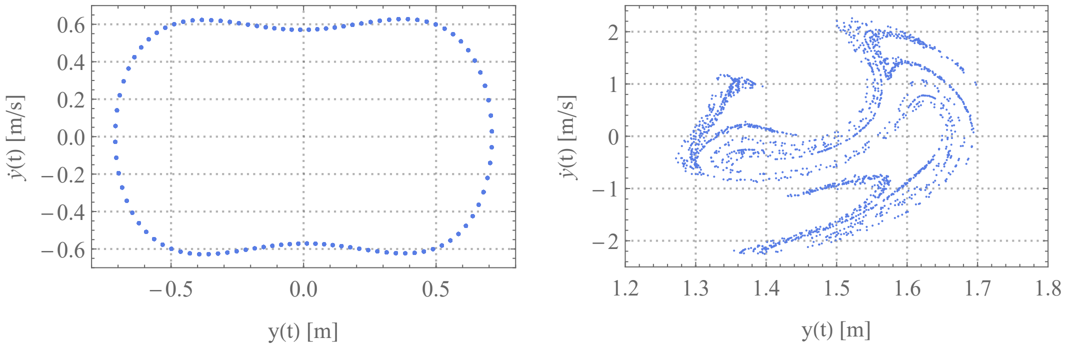

(a) $\gamma = 1$ and $\Omega = 1.11$ (b) $\gamma = 8.2$ and $\Omega = 0.5$

Figure 2.11: Poincaré sections for the Duffing oscillator in Equation (2.2) with the parameters set to arbitrary values of $\zeta = 0.015$ and $\alpha = 5$

2.2.3.3 Bifurcation Diagram

Another useful tool to get a broader overview of a dynamical system and a general idea of the dynamics is the bifurcation diagram. This shows the maximum values of the dependent variable over a variation of the control parameter, usually external control parameters are used which are the excitation amplitude or excitation frequency. This shows that the previously observed Figure 2.10 is technically a bifurcation diagram as well. In a bifurcation diagram fixed points, periodic orbits, and chaotic attractors can be observed. Figure 2.12 shows a bifurcation diagram for a simple pendulum with the excitation amplitude as control parameter. The qualitative bifurcation diagram is computed with the differential Equation (2.4) of a forced damped simple pendulum.

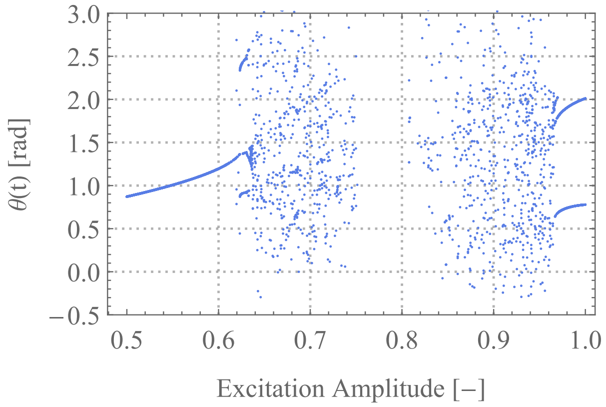

Figure 2.12: Qualitative bifurcation diagram for a forced simple pendulum. With the parameters set to $l = 0.5$ kg, $m = 1.0$ kg, $g = 9.81\ \frac{\mathrm{m}}{\mathrm{s}^2}$, $\zeta = 0.028$, and $\Omega = 0.6$Hz.

$$\ddot{\theta}(t) + 2\zeta\omega_n\dot{\theta}(t) + \sin(\theta(t)) = a\cos(\Omega t) \tag{2.4}$$

The lines that can be seen in the bifurcation diagram in Figure 2.12 actually consist of a large number of individual points that lie close to each other and therefore form a fixed point for a value of the excitation amplitude from 0.5 to 0.6. Additionally, a limit cycle can be seen at the end of the excitation amplitude range in the bifurcation diagram. The areas from an excitation amplitude of 0.65 to 0.75 and 0.85 to 0.95 show dynamics that suggest quasi-periodic or chaotic dynamics.

2.2.3.4 Lyapunov Exponent

The Lyapunov exponent is attributed to the mathematician Aleksandr Mikhailovich Lyapunov. It gives a way to quantify the chaos and it is therefore called the Lyapunov exponent. The Lyapunov exponent determines in which ratio close initial conditions converge or diverge in the state space. This is achieved with a numerical analysis over a long period with an averaging process [70–72]. Normally only the highest Lyapunov exponent is observed in a system since when at least one Lyapunov exponent in the system is positive the dynamics of the system are chaotic [72]. In the context for this work, the Lyapunov exponent does not play a role and will therefore not be explained in greater detail; recommended literature are the textbooks that are cited in this sub-section.

2.3 Spherical Pendulum

The first research for the pendulum was carried out by Galileo, Huygens, Newton, and Hook. With the help of the pendulum, the first findings on gravitational acceleration and the conservation laws [73] were made. Another mile stone was the Foucault pendulum in 1851, providing proof for the rotation of the earth. And even in our day and age journal articles are still published that observe the Foucault pendulum [74–81].

Nowadays it is common practice that every engineering student studies the simple pendulum, mostly a small angle assumption is used to remove the nonlinear part from the restoring force term. Thus, the undamped (conservative) simple pendulum has one force that acts on the pendulum bob which is the restoring force that comes from the gravitational acceleration. If the small-angle assumption is not used, the simple pendulum is one of the simplest nonlinear systems. However, this system can be further adapted to model real conditions and thus becomes more complex. Firstly, a damping coefficient (friction at the pivot point or aerodynamic dissipation at the pendulum bob) should be introduced this can happen with linear damping or nonlinear damping ratios [82, 83]. The damping ratio can be controlled with a magnetorheological damper and together with a nonlinear spring the dynamics of a pendulum can be changed [84, 85]. To model natural effects it is important to excite the entire system in different directions. Furthermore, chaos can be demonstrated if another degree of freedom is added to the pendulum. One method for this is the double pendulum [86–90]. The spherical pendulum, which has two degrees of freedom as well, can show chaotic dynamics which was discussed by various authors [91–93]. On the dynamics of the spherical pendulum is further elaborated on in Section 2.3.3.

2.3.1 Development of the Research on the Spherical Pendulum over the Near Past

The spherical pendulum is a planar pendulum that has been extended by a generalised coordinate, which describes the rotation of the planar pendulum, see Figure 2.13 in Section 2.3.2. The first noteworthy studies of the stability of a forced spherical pendulum were carried out by John W. Miles in 1962 [94]. Throughout his working life he published two more articles on the subject [95, 96] and thus laid the foundation for much of the research that followed, most of which is based, to some extent, on the equations he presented. Henceforth these equations are referred to as the Miles equations[5]. In 1978 M. G. Olsson published an article [97] in which he used the Lindstedt-Poincaré perturbation method to describe the planar movement of the spherical pendulum with small oscillations from the plane. Three years later the author published another article [98] that shows a simplified presentation of the problem to address the target group of undergraduate students, which he succeeded in doing. Tritton shows in 1986 [99] experimentally how a spherical pendulum movement behaves from complex to chaotic motions. Science has always been concerned with debunking pseudoscience and this is the case with the spherical pendulum with F. E. Irons's article [100] describing the movements of a dowsing pendulum and calculating that a small change of the movement of the operator's hand changes the dynamics of the system drastically. And therefore the author gives a mathematical explanation that the change in movement characteristics are most probably not connected to water streams in the ground but instead attributed to the changes in the movement of the operator's hand. In 1990 Bryant and Miles published 3 consecutive articles. Even though they deal with the simple pendulum, they are still indispensable for this PhD thesis, dealing with the different excitations of a pendulum. The simple pendulum is excitation by an applied torque [101], a horizontal force [102], and a vertical force [103]. De Jong investigates the chaotic dynamics of the simple pendulum [104]. Bryant published another article on the chaotic motion of a spherical pendulum in 1993 [105] and was the first to add Lyapunov exponents to quantify the chaotic behaviour. A similar article was published two years later by Kana and Fox [91] the main goal of the article was the investigation of the transition from periodic or quasi-periodic dynamics to chaotic dynamics. In 1999, two interesting articles were published, firstly, Tritton and Groves published an article dealing with the Lyapunov exponents of the Miles pendulum [106]. Secondly, Aston investigated the bifurcations and the Lyapunov exponents on a spherical pendulum. The interesting part about that article is that he introduces a new mathematical model

---

[5] The term 'Miles equations' is a commonly used term in the literature by authors that are concerned with the dynamics of the spherical pendulum.

that does not have a singularity at the resting point of the pendulum [69]. In the same year Markeyev published an article where he researched a spherical pendulum with a vibrating suspension [107]. The next interesting paper was published in 2006 by Leung and Kuang [108] and deals with chaotic dynamics of the spherical pendulum which is excited in the vertical direction and both horizontal directions. Similarly, Shvets is concerned with this, but his spherical pendulum is instead vertically excited [109]. Another experimental investigation was conducted by Cartwright and Tritton in 2010 [93]. They compared their experimental results with the Miles equations. In 2013 Náprstek and Fischer published an article on the quasi-periodic dynamics of the spherical pendulum [110] and one year later these two authors and Pospíšil published an 'Experimental analysis of the influence of damping on the resonance behaviour of a spherical pendulum' [111]. At the end of 2020 Litak et al. published the dynamic response of a spherical pendulum when horizontally forced with a Lissajous curve [112]. Anurakpandit et al. published an experimental and numerical examination of a gimballed pendulum that is used as an energy harvester [6]. Another two degree of freedom pendulum based energy harvester was introduced by Wang, Lou, and Zhu [59]. The design of their biaxial-pendulum incorporated two shafts and is therefore unrestricted in its movement. The energy conversion is done with coils and magnets that are fitted to the hemispherically shaped pendulum. To prove the capabilities of the energy harvester the system was excited with a six degree of freedom platform. Even with and arbitrary excitation direction and frequency the energy harvester was able to produce an energy output [59, 113].

2.3.2 Mathematical Model of the Spherical Pendulum

The basic model of the spherical pendulum consists of a massless rod with a length l that has a point mass m connected to it at its end. For the introduced system aerodynamic dissipation and mechanical friction at the pivot are ignored. But the mechanical friction will be added later for the numerical analysis see Chapter 4. There is one force of action on the system, the gravitational force, which acts on the point mass. As generalised coordinates the angles θ and ϕ are selected. As it describes the actual pendulum motion and therefore the characteristic of the system, the coordinate θ is clearly more important. The coordinate ϕ is a cyclic coordinate that describes the rotation of the planar pendulum around the z-axis, shown in Figure 2.13. The mathematical description of the spherical pendulum is well-known in the literature and it is derived with help of the following resources e.g. [57, 94, 98, 111, 112, 114]. The in the introduction section shown mathematical model of the spherical pendulum is a simplified version the complete mathematical model with an active power take-off term that is used for the numerical analysis is derived in Chapter 4. The calculation of the ordinary differential equations of the spherical pendulum was carried out by symbolic code written in *Wolfram Mathematica*®
language.

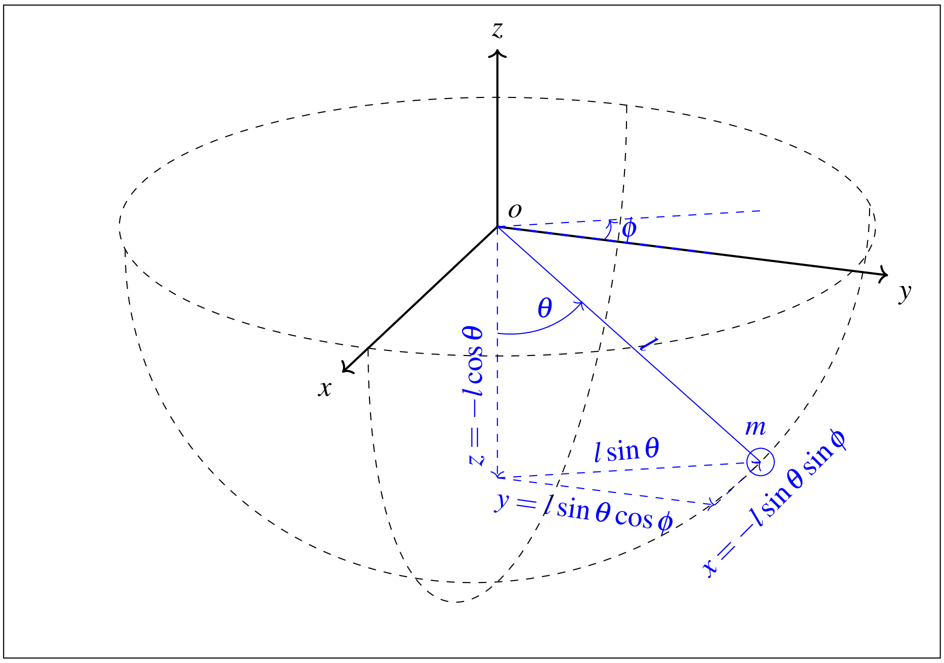

Figure 2.13: Diagram of a spherical pendulum with kinematics (adapted from previous publication related to this work [1])

Figure 2.13 gives the kinematic relations of the spherical pendulum depending on the generalised coordinates θ and ϕ, see Equations (2.5) to (2.7).

$$x = -l \sin\theta \sin\phi. \tag{2.5}$$

$$y = l \sin\theta \cos\phi. \tag{2.6}$$

$$z = -l \cos\theta. \tag{2.7}$$

Differentiating the kinematic relations from Equations (2.5), (2.6), and (2.7) with respect to time gives Equations (2.8), (2.9), and (2.10).

$$\dot{x} = -l\dot{\phi}\sin(\theta)\cos(\phi) - l\dot{\theta}\cos(\theta)\sin(\phi). \tag{2.8}$$

$$\dot{y} = l\dot{\theta}\cos(\theta)\cos(\phi) - l\dot{\phi}\sin(\theta)\sin(\phi). \tag{2.9}$$

$$\dot{z} = l\dot{\theta}\sin(\theta). \tag{2.10}$$

The Equations (2.5) to (2.10) are now introduced in the equations for the potential energy (2.11) and kinetic energy (2.12).

$$U = mgz(t) = -mgl\cos\theta(t). \tag{2.11}$$

$$
\begin{aligned}
T &= \frac{1}{2}mv(t)^2 = \frac{1}{2}m(\dot{x}(t)^2+\dot{y}(t)^2+\dot{z}(t)^2) \\
&= \frac{1}{2}m\Big(l^2\dot{\theta}(t)^2\sin^2(\theta(t)) \\
&+\Big(-l\dot{\theta}(t)\cos(\theta(t))\sin(\phi(t))-l\dot{\phi}(t)\sin(\theta(t))\cos(\phi(t))\Big)^2 \\
&+\Big(l\dot{\theta}(t)\cos(\theta(t))\cos(\phi(t))-l\dot{\phi}(t)\sin(\theta(t))\sin(\phi(t))\Big)^2\Big) \\
&= \frac{1}{2}ml^2(\dot{\phi}(t)^2\sin^2(\theta(t))+\dot{\theta}(t)^2).
\end{aligned}
\tag{2.12}
$$

In the following the Lagrange Equation of the second kind (2.13) is shown. The first part of the equation is the derivative with respect to time of the generalised momentum. This is followed by the derivative of the kinetic and potential energy with respect to the position. On the right-hand side of the equation a generalised force term is shown.

$$
\frac{d}{dt}\left(\frac{\partial T}{\partial \dot{q}}\right)-\frac{\partial T}{\partial q}+\frac{\partial U}{\partial q}=Q_q. \tag{2.13}
$$

The potential and kinetic energy are now introduced in the Lagrange Equation (2.13) and differentiated with respect to the coordinate $\dot{\theta}(t)$.

$$
\begin{aligned}
\frac{\partial T}{\partial \dot{\theta}(t)} &= \frac{1}{2}m\Big(2l^2\dot{\theta}(t)\sin^2(\theta(t))-2l\cos(\theta(t))\sin(\phi(t))\Big(-l\dot{\theta}(t)\cos(\theta(t))\sin(\phi(t)) \\
&-l\dot{\phi}(t)\sin(\theta(t))\cos(\phi(t))\Big)+2l\cos(\theta(t))\cos(\phi(t)) \\
&\Big(l\dot{\theta}(t)\cos(\theta(t))\cos(\phi(t))-l\dot{\phi}(t)\sin(\theta(t))\sin(\phi(t))\Big)\Big) \\
&= ml^2\dot{\theta}(t).
\end{aligned}
\tag{2.14}
$$

Differentiating Equation (2.14) with respect to time gives:

$$
\frac{d}{dt}\left(\frac{\partial T}{\partial \dot{\theta}(t)}\right) = ml^2\ddot{\theta}(t). \tag{2.15}
$$

Then differentiating the kinetic energy (2.12) with respect to the coordinate $\theta(t)$.

$$\begin{aligned}\frac{\partial T}{\partial \theta(t)} = \frac{1}{2}m\Big(&2l^2\dot{\theta}(t)^2\sin(\theta(t))\cos(\theta(t)) + 2\Big(l\dot{\theta}(t)\sin(\theta(t))\sin(\phi(t))\\ &- l\dot{\phi}(t)\cos(\theta(t))\cos(\phi(t))\Big)\Big(-l\dot{\theta}(t)\cos(\theta(t))\sin(\phi(t))\\ &- l\dot{\phi}(t)\sin(\theta(t))\cos(\phi(t))\Big)\\ &+ 2\Big(-l\dot{\theta}(t)\sin(\theta(t))\cos(\phi(t)) - l\dot{\phi}(t)\cos(\theta(t))\sin(\phi(t))\Big)\\ &\Big(l\dot{\theta}(t)\cos(\theta(t))\cos(\phi(t)) - l\dot{\phi}(t)\sin(\theta(t))\sin(\phi(t))\Big)\Big)\\ &= ml^2\dot{\phi}(t)^2\sin(\theta(t))\cos(\theta(t)).\end{aligned} \tag{2.16}$$

Now the potential energy (2.11) is differentiated with respect to the coordinate $\theta(t)$.

$$\frac{\partial U}{\partial \theta(t)} = mgl\sin(\theta(t)). \tag{2.17}$$

Introducing Equations (2.15), (2.16), and (2.17) in Equation (2.13) gives the equation of motion with respect to the coordinate θ without damping and forcing terms.

$$\ddot{\theta}(t) - \cos(\theta(t))\sin(\theta(t))\dot{\phi}(t)^2 + \frac{g}{l}\sin(\theta(t)) = 0. \tag{2.18}$$

The Lagrange calculations are repeated with respect to the coordinate ϕ. Therefore the kinetic energy is partially differentiated with respect to $\dot{\phi}(t)$.

$$\begin{aligned}\frac{\partial T}{\partial \dot{\phi}(t)} = \frac{1}{2}m\Big(&-2l\sin(\theta(t))\cos(\phi(t))\\ &\times\Big(-l\dot{\theta}(t)\cos(\theta(t))\sin(\phi(t)) - l\dot{\phi}(t)\sin(\theta(t))\cos(\phi(t))\Big)\\ &-2l\sin(\theta(t))\sin(\phi(t))\Big(l\dot{\theta}(t)\cos(\theta(t))\cos(\phi(t)) - l\dot{\phi}(t)\sin(\theta(t))\sin(\phi(t))\Big)\Big)\\ &= l^2m\dot{\phi}(t)\sin^2(\theta(t)).\end{aligned} \tag{2.19}$$

Differentiating Equation (2.19) with respect to time gives:

$$\frac{d}{dt}\left(\frac{\partial T}{\partial \dot{\phi}}\right) = l^2m\sin(\theta(t))\Big(\sin(\theta(t))\ddot{\phi}(t) + 2\dot{\theta}(t)\dot{\phi}(t)\cos(\theta(t))\Big). \tag{2.20}$$

Then differentiating Equation (2.12) with respect to the coordinate $\phi(t)$.

$$\begin{aligned}\frac{\partial T}{\partial \phi(t)} &= \frac{1}{2}m\Big(2\Big(-l\dot{\theta}(t)\cos(\theta(t))\sin(\phi(t)) - l\dot{\phi}(t)\sin(\theta(t))\cos(\phi(t))\Big)\\ &\times\Big(l\dot{\theta}(t)\cos(\theta(t))\cos(\phi(t)) - l\dot{\phi}(t)\sin(\theta(t))\sin(\phi(t))\Big)\\ &+2\Big(-l\dot{\theta}(t)\cos(\theta(t))\sin(\phi(t)) - l\dot{\phi}(t)\sin(\theta(t))\cos(\phi(t))\Big)\\ &\times\Big(l\dot{\phi}(t)\sin(\theta(t))\sin(\phi(t)) - l\dot{\theta}(t)\cos(\theta(t))\cos(\phi(t))\Big)\Big)\\ &= 0.\end{aligned} \tag{2.21}$$

Now the potential energy (2.11) is differentiated with respect to the coordinate $\phi(t)$.

$$\frac{\partial U}{\partial \phi(t)} = 0. \tag{2.22}$$

Introducing Equations (2.20), (2.21), and (2.22) in Equation (2.13) gives the equation of motion with respect to the coordinate ϕ without damping and forcing terms.

$$\begin{aligned}&l^2 m\sin(\theta(t))\Big(\sin(\theta(t))\ddot{\phi}(t) + 2\cos(\theta(t))\dot{\theta}(t)\dot{\phi}(t)\Big)\\ &= \sin(\theta(t))\ddot{\phi}(t) + 2\cos(\theta(t))\dot{\theta}(t)\dot{\phi}(t) = 0.\end{aligned} \tag{2.23}$$

As can be seen from Equations (2.18) and (2.23), the coordinate ϕ is not present as a restoring force term in the ordinary differential equations (ODEs), therefore ϕ is a so-called cyclic variable. To put it another way, ϕ can only be found in the ODEs (2.18) and (2.23) in the form of its first or higher derivative. The mathematical model can show different dynamics. A special case of the spherical pendulum is the so-called conical pendulum, this refers to a pendulum where it is assumed that $\dot{\theta} = 0$ and $\dot{\phi} =$ constant and thus the trajectory of the pendulum is a rotation in a circular pattern around the z-axis.

2.3.3 Research on the Chaotic Dynamics of the Spherical Pendulum

Although a simplified version of the spherical pendulum is shown in Section 2.3.2, the differential equations can be extended by damping, excitation in different directions and power take-off as needed. These are all included in this thesis and are considered in great detail see Chapter 4. In this section, the historical development listed in Section 2.3.1 will be examined in more detail with respect to the dynamics of the pendulum and finally under which conditions chaotic dynamics occur.

Many articles deal with the dynamics of the spherical pendulum and under which conditions a transition to chaotic dynamic occurs. Miles studies the stability [94] of a spherical pendulum is one of the first articles concerned with this topic. He gives three major results regarding the stability of the pendulum: “planar harmonic motion is unstable over a major proportion of the resonant peak, [...] non-planar harmonic motion is stable in a spectral neighbourhood above resonance [...] [and] non-stable, harmonic motions are possible in a finite neighbourhood of the natural frequency” [94]. Over the course of his working life he always came back to this topic and studied the resonant motion of a spherical pendulum by looking at the loci of the equilibrium points and bifurcations for a weakly nonlinear damped pendulum [95]. Additionally, Miles published an article on the "internal resonance of a detuned spherical pendulum" [115].

Most scholars who work on the topic of spherical pendulums refer to this article, which shows the importance of this fundamental research by Miles. Olsson [97] cites Miles in his research article where he observes how a small change in the excitation amplitude changes the dynamics of the system. That a forced spherical pendulum can develop complex and chaotic dynamics is already known but an experimental validation has not been carried out up to this point. The first one to do this was Tritton in 1985 [99]. He proposes an experimental validation in which he investigates how the dynamics of the pendulum change with different excitations and how periodic dynamics transits to a chaotic motion. A further investigation of the chaotic dynamics of a lightly damped and horizontal forced spherical pendulum was achieved by Bryant [105]. With changing of the excitation frequency the “typical sequence begins with stable, symmetric, nonplanar oscillations, followed by bifurcation to a stable, periodic modulation of the oscillations, then weakly chaotic modulation merging into fully chaotic modulation of the oscillations” [105]. Bryant uses Lyapunov exponents to determine the general dynamics of the system. Kana and Fox study the route to chaos for the spherical pendulum [91] theoretically and experimentally. They show that the “transition from quasi-periodic to chaotic motion can be carefully quantified in systems with very light damping” [91]. Up to this point, the spherical pendulum has mainly been investigated with an excitation close to the free damped natural frequency. But Markeyev investigates the stability of a vertically high-frequency excited spherical pendulum with small amplitudes. The author concludes that the pendulum forms trajectories that are close to a conical motion. He observes two cases, the first case is that the mass of the pendulum rotates below the pivot point and the second case is where the mass rotates above the pivot point. Regarding the stability of the cases Markeyev states the first case is stable and the second case is only stable when the mass rotation is well above the pivot point. An interesting study of the spherical pendulum was presented by Aston, who deviates from the mathematical representation of the spherical pendulum of his predecessors and creates a mathematical model which does not have its singularity at the resting point of the pendulum, see Section 2.3.4. As usual the author examines Poincaré sections, bifurcation diagrams and determines the stability of the chaotic solution with help of the normal Lyapunov exponent [69]. A broad study of the stability of the spherical pendulum equations derived by Miles was conducted by Tritton and Groves [106]. They conclude that both the likelihood of finding chaotic motion and the typical Lyapunov exponent is highly dependent on the damping of the system. Furthermore, they prove the "co-existence of alternative types of attractor in regions both inside and outside the range with non-stable fixed points and the occurrence of metastable chaos" [106]. A further validation of the equations of motion derived by Miles was carried out by Cartwright and Tritton, these authors find a correlation between the previous theoretical results and their experiments with regard to the chaotic dynamics of the spherical pendulum [93]. The authors Náprstek and Fischer are concerned with the quasi-periodic response of a two degree of freedom (2-DOF) autoparametric system. Their choice fell on the spherical pendulum, in which they determine the quasi-periodic dynamics of the system with the help of frequency sweeps [110]. In a follow-up article Pospíšil, Fischer and Náprstek compare experimentally and numerically the influence of damping on the resonance [111]. The excitation of the spherical pendulum with a Lissajous curve is introduced by Litak, Margielewicz, and Gąska. The authors show a wide variety of trajectories for different excitation parameters. Furthermore, they show bifurcation diagrams for the two generalised coordinates [112].

2.3.4 Alternative Mathematical Approaches for the Spherical Pendulum

As mentioned previously different approaches for the spherical pendulum were introduced as well, which have different advantages and disadvantages. Two of them are shown in the following.

2.3.4.1 Model of a Spherical Pendulum Introduced by Aston

In his work "Bifurcations of the horizontally forced spherical pendulum" [69], Aston presents a novel model of a spherical pendulum. The model can be seen in Figure 2.14, here excited in all directions and not just one horizontal direction as the original work. To obtain the original

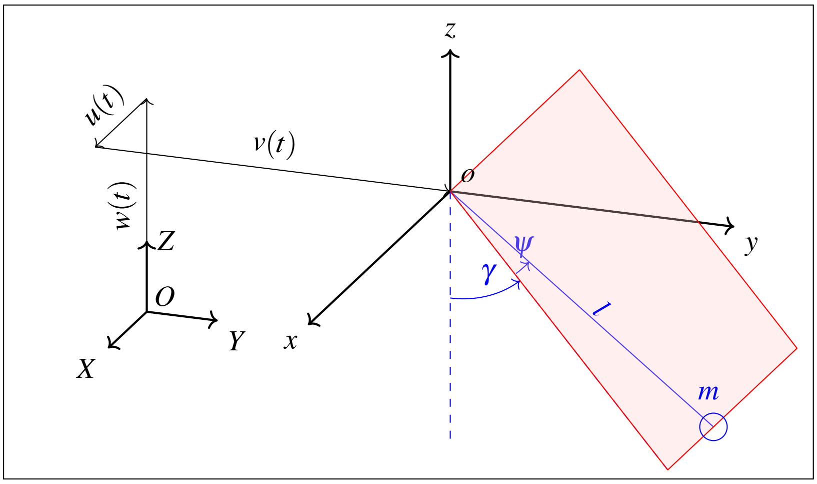

Figure 2.14: Diagram of a spherical pendulum with additional forcing terms and renamed generalised coordinates adapted from [69]

model from the article, the excitation $u(t)$ and $w(t)$ must be set to zero. Furthermore, the author uses the generalised coordinates α and β instead of ψ and γ. The coordinates used by the author are not used in the theory section to avoid a duplicate use with the methods of multiple scales. Aston recognises that most of the previous considered spherical pendulums have a singularity at $x = y = 0$, $z = \pm 1$. The singularity in the z-direction is obviously dependent on the length of the pendulum. Since the article is mainly considering th planar movement of the pendulum and small perturbations from this plane the author choose a coordinate system that has singularities at $y = z = 0$ and $x = \pm 1$.

The kinematics of Figure 2.14 are as follows.

$$\begin{aligned} x =& -l\sin(\psi). \\ y =& l\cos(\psi)\sin(\gamma). \\ z =& -l\cos(\psi)\cos(\gamma). \end{aligned} \tag{2.24}$$

After constructing the kinetic and potential energy with the added excitation terms of the system and introducing them into Lagrange's equation of the second kind two ordinary differential equations are obtained where the damping terms are also introduced.

$$\begin{aligned} &0.5\ddot{\gamma}(t) + 0.5\ddot{\gamma}(t)\cos(2\psi(t)) + 2\xi_\theta\omega_n\dot{\gamma}(t) - \dot{\gamma}(t)\dot{\psi}(t)\sin(2\psi(t)) \\ &\quad + \frac{g\sin(\gamma(t))\cos(\psi(t))}{l} - \frac{V_0\Omega_v^2\cos(\gamma(t))\cos(\psi(t))\cos(\Omega_v t)}{l} \\ &\quad - \frac{W_0\Omega_w^2\sin(\gamma(t))\cos(\psi(t))\cos(\Omega_w t)}{l}. \end{aligned} \tag{2.25}$$

$$\begin{aligned} &\ddot{\psi}(t) + 2\omega_n\xi_\psi\dot{\psi}(t) + 0.5\dot{\gamma}(t)^2\sin(2\psi(t)) + \frac{g\cos(\gamma(t))\sin(\psi(t))}{l} \\ &\quad + \frac{U_0\Omega_u^2\cos(\psi(t))\cos(\Omega_u t)}{l} + \frac{V_0\Omega_v^2\sin(\gamma(t))\sin(\psi(t))\cos(\Omega_v t)}{l} \\ &\quad - \frac{W_0\Omega_w^2\cos(\gamma(t))\sin(\psi(t))\cos(\Omega_w t)}{l}. \end{aligned} \tag{2.26}$$

After introducing the dimensionless parameters from Equations (4.33) the dimensionless differential equations are obtained. The subscripts have been adapted to the generalised coordinates of the system for this purpose.

$$\begin{aligned} &0.5\ddot{\gamma}(\tau) + 0.5\ddot{\gamma}(\tau)\cos(2\psi(\tau)) + \alpha_\gamma\dot{\gamma}(\tau) - \dot{\gamma}(\tau)\dot{\psi}(\tau)\sin(2\psi(\tau)) \\ &\quad + \sin(\gamma(\tau))\cos(\psi(\tau)) - a_v\beta_v^2\cos(\gamma(\tau))\cos(\psi(\tau))\cos(\beta_v\tau) \\ &\quad - a_w\beta_w^2\sin(\gamma(\tau))\cos(\psi(\tau))\cos(\beta_w\tau). \end{aligned} \tag{2.27}$$

$$\begin{aligned}\ddot{\psi}(\tau) &+ \alpha_\psi \dot{\psi}(\tau) + 0.5\dot{\gamma}(\tau)^2 \sin(2\psi(\tau)) + \cos(\gamma(\tau))\sin(\psi(\tau)) \\ &+ a_u\beta_u^2 \cos(\psi(\tau))\cos(\beta_u\tau) + a_v\beta_v^2 \sin(\gamma(\tau))\sin(\psi(\tau))\cos(\beta_v\tau) \\ &- a_w\beta_w^2 \cos(\gamma(\tau))\sin(\psi(\tau))\cos(\beta_w\tau)\,.\end{aligned} \tag{2.28}$$

2.3.4.2 Model of a Spherical Pendulum used by Ikeda, Harata, and Takeeda

In their work “Nonlinear responses of spherical pendulum vibration absorbers in towerlike 2DOF structures” [114] Ikeda, Harata, and Takeeda use a different approach for the spherical pendulum. Figure 2.15 shows how they describe the generalised coordinates θ and ϕ with θ_x and θ_y.

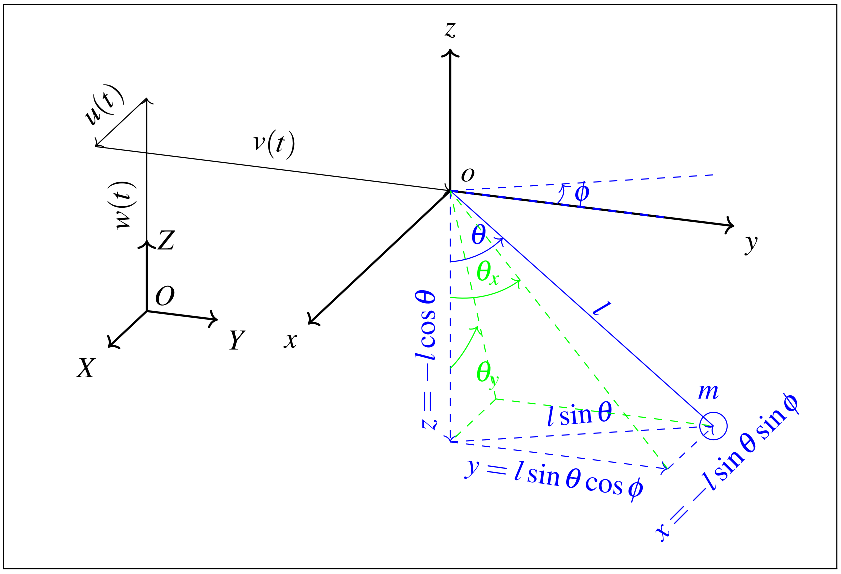

Figure 2.15: Diagram of a spherical pendulum with additional forcing terms adapted from [114]

This gives the following relations (2.29) and (2.30). These relations provide the basis for the conversion of the numerical coordinates to the experimental coordinates, see Chapter 7.

$$\theta_x = \theta\cos(\phi). \tag{2.29}$$

$$\theta_y = \theta\sin(\phi). \tag{2.30}$$

2.4 Application Based Background on the Electrical Power Take-Off

To develop an application based energy harvester the theoretical background needs to be introduced. When observing the field of wave energy harvesting it is evident that the excitation frequency range changes with time and season [116]. This is represented qualitatively in Fig-

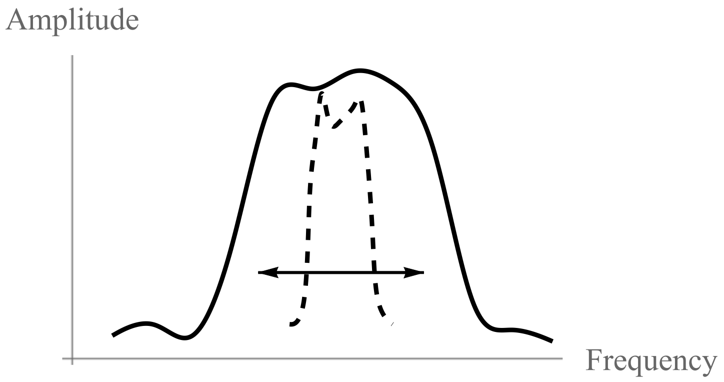

Figure 2.16: Representation of the wave spectrum (solid black line) compared to the frequency response of the omnidirectional energy harvester (dashed black line) (adapted from [116])

ure 2.16. The dotted line shows the narrow frequency response of the omnidirectional pendulum energy harvester and the solid line indicates the wave spectrum.

An optimal energy harvester has a high efficiency over the whole frequency spectrum which in return increases the cost-efficiency. Of course, bounds to the laws of physics restrict this. It can, however, be tried to adapt the energy harvester to different forcing conditions to see an increase in efficiency. This can be accomplished by moving the frequency response of the energy harvester along the axis of the excitation frequency. There are two main options to accomplish this. The first possibility is a design that changes the length of the pendulum arm. This change in length is equivalent to a change in the natural frequency of the energy harvester and therefore the operational range of the energy harvester is shifted to another position [56]. The second solution is a controlled power take-off. In the field of energy harvesting and in the subgroup of wave energy harvesting various examinations of different control, optimisation, and prediction strategies for wave energy harvesters are shown. Têtu summarises the most important control strategies which are a passive loading control, latching control, and reactive loading control [116].The latching control is described in greater detail in Section 2.4.1.

Ozkop and Atlas review different control methods for wave energy harvesters [117]. Zhou et al. simulate different control methods for a variable speed generator for a wave energy harvester with a permanent magnet generator [118]. Different power electronics for wave energy harvesters are compared by Kazmierkowski and Jasiński [119]. The development of the electrical power output of an oscillating cater column energy harvester was investigated by O'Sullivan et al. [120]. Kovaltchouk et al. note correctly that the energy harvesting applications are often discussed without observing the physical limitations of the electrical power take-off [121]. Therefore, the authors propose a model predictive control for a wave energy harvester. Dicken et al. examines power extraction circuits for piezoelectric energy harvester [122]. Additionally, two review articles were published that are concerned with the optimised control of different wave energy harvesters. Hong et al. classifies different wave energy harvesters according to their mechanical structure and compares their control strategies [123]. Another review of different control strategies of wave energy harvesters was carried out by Maria-Arenas et al. [124].

2.4.1 Latching Control

"The purpose of [a] latching control strategy is to force the velocity into phase with the excitation force. An on/off PTO force is applied by means of a latching system, to avoid a phase difference between the velocity and the incoming wave excitation force" [125]. This has the potential to increase the efficiency of the energy harvester drastically. Figure 2.17 shows the latching control used by Giorgi and Ringwood [125]. The authors state that the latching control is best suited for excitation frequencies that are bigger than the natural frequency of the oscillating element. Additionally, these authors provide a flow chart to explain a latching algorithm.

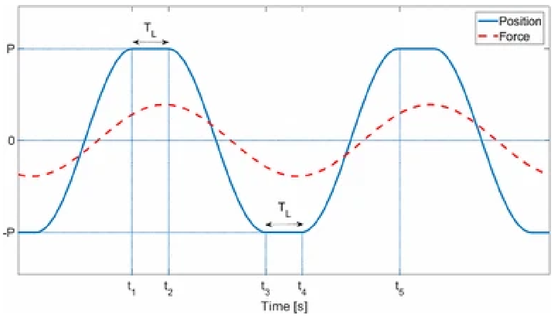

Figure 2.17: Latching calculations to put position and force in phase [125]

In an earlier article Ringwood and Butler examine the optimisation of the power take-off with latching control of a simple idealised wave energy harvester [126]. The power take-off is simulated with a damping ratio that can be controlled. They conclude that for an optimised power take-off various requirements are needed. It is necessary that the natural frequency of the oscillator is similar to the one of the excitation frequency. Then the power take-off can be optimised with a latching control to bring the phase of the oscillations of the oscillator in phase with the oscillations of the excitations in this case waves.

2.4.2 Power Electronics for the Omnidirectional Pendulum Energy Harvester

To explain the power electronics behind the electrical power take-off it is advantageous to discuss a related field. With the current ongoing electrification of individual transportation the term regenerative braking has become more visible for the general public. This term describes the electrical power take-off that is used to slow down a vehicle and convert the kinetic energy into an energy form that can be used later e.g. for the positive acceleration of the vehicle. The regenerative brakes are controlled and depending on the needed braking force more kinetic energy is converted which translates to a different braking force. The difference is that the regenerative braking sees a velocity that is applied in one direction and in the energy harvester the direction of velocity constantly changes direction. Nevertheless, the control of regenerative braking is similar to the one that is needed for the power take-off of the energy harvester. The terms are therefore used as synonyms in regards to this work. In the book "Electrical Engineering 101" [127] the operating and control principles of regenerative braking are explained. In Figure 2.18 a simplified motor control diagram is shown. The DC motor is connected to a battery and is controlled with a pulse-width modulation (PWM). Additionally two field-effect transistors (FET) are shown in the circuit. The primary FET is defined as the one that controls the PWM, in Figure 2.18 this FET at the bottom. The other FET shown in the figure is called a freewheel FET. Once one of the FETs is switched on the other one goes off and vice versa. In this discussion of the regenerative braking the different driving strategies for FETs are not discussed as they exceed the topic of this thesis. The principle of regenerative braking works as follows. Assuming that the initial state of the circuit in Figure 2.18 is as follows the DC motor was accelerated with the primary FET on and a defined PWM duty cycle of 80 %. Therefore, the DC motor is in motion and now a braking force needs to be applied. The first step to do this is to switch off the primary FET which in return switches on the freewheel FET. This results in the output voltage generated by the DC motor being shorted into the input of the DC motor. And this in return applies a braking force, and a current flows in the opposite direction according to Faraday's law of induction. This supplies current back into the battery and recharges it [127]. The strength of the regenerative braking can be controlled with the PWM applied to the freewheel FET.

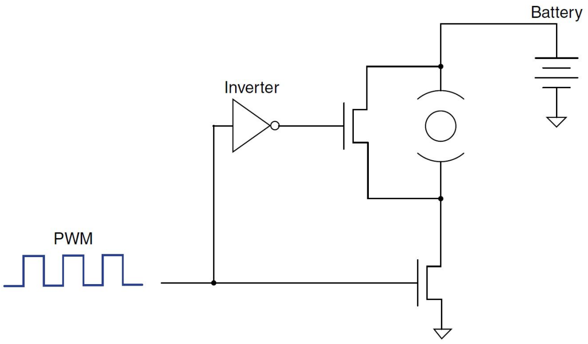

Figure 2.18: Simplified regenerative PWM motor control with a FET [127]

With the shown circuit in Figure 2.18 energy can only be regenerated in one rotational direction and the DC motor can only be driven in the opposite rotational direction. For the omnidirectional energy harvester used in this work it is a requirement that energy can be regenerated regardless of the direction of rotation. One way to do this is to use the H bridge. In Figure 2.19 a H bridge used as power electronics for a DC motor is shown. The operating principle or the regenerative braking is similar to the one described in Figure 2.18 but the difference

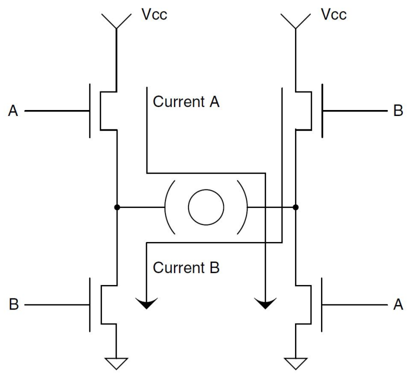

Figure 2.19: H-bridge motor control [127]

is the more complicated design of the H bridge. Simultaneous switching of the opposing high and low legs (arrows of current A and current B) creates a regenerative energy and therefore a braking force is applied on the DC motor. The differential amplifiers used for this need to be capable of operating under large voltage switches [127]. Different control strategies of the regenerative braking were investigated by various scholars [128–130]. In the field of energy harvesting the power electronics can be used for example to tune an electromagnetic energy harvester [131].

Chapter 3

Methodology

3.1 Numerical Analysis

The analysis of the numerical results is performed by symbolic code written in *Wolfram Mathematica*® language. As a numerical solver the code uses the 'NDSolve' function to "find numerical solutions to ordinary differential equations" [132]. For this the mathematical solver uses a suitable methodology for numerical integration e.g. the Runge Kutta method. But this approach can be subject to changes during the computation. The documentation of the software gives overviews of the different solving methods of numerical integration for ordinary differential equations [133, 134]. Within the function of 'NDSolve' the method of numerical integration can be changed if needed, however, for this work the default selected approaches to numerical integration are sufficient. Nevertheless, there are some fine-tuning parameters to increase the accuracy of the results. The most important ones are the 'AccuracyGoal' which defines the digits of the decimal places that are used during the computation, 'PrecisionGoal' gives the "digits of precision sought" [132] and 'WorkingPrecision' defines "precision to use in internal computations" [132]. According to Wolfram Research Inc. the results of the numerical analysis are accurate even with the fine-tuning parameters set to automatic, however they offer a tutorial on the verification and improvement of numerical results [135]. In Figure 3.1 the logarithm residual to the base of ten for the coordinate θ is shown for a numerical analysi with arbitrary selected values that indicate a computation with high and low accuracy. The residual is the difference between the left-hand side and the right-hand side of the ordinary differential equation. This value should be as small as possible since the difference between the right and left side of the ordinary differential equation should be equal to zero. With the introduction of higher accuracies, with the parameters 'WorkingPrecision' set to 30 and the 'AccuracyGoal' set to 10 the accuracy of the residual of calculated parameter θ decreases by the factor 10^{-2} which is an overall increase of the accuracy of the numerical analysis.

However, it must always be taken into account that a variation of a parameter can massively increase the computing time and this can lead to restrictions of the computer hardware. There-

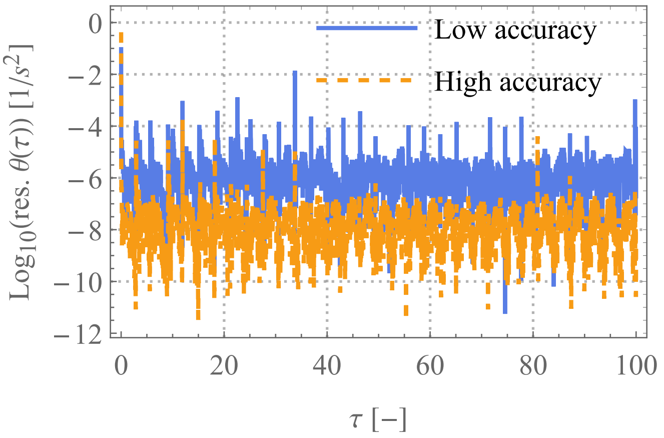

Figure 3.1: Difference of the residual between a low and high accurate numerical calculation of the spherical pendulum with the parameters set to: $l = 0.5$ m, $m = 1.32$ kg, $g = 9.81\ \frac{\mathrm{m}}{\mathrm{s}^2}$, $\alpha_\theta = \alpha_\phi = 0.0648$, $a_u = a_v = a_v = 0.064$, $\beta_u = \beta_v = 0.5\beta_w = 1$, and $P_\theta = P_\phi = 0$. For the low accuracy the numerical analysis the settings were set to the default and for the high accuracy the ’WorkingPrecision’ is set to 30 and the ’AccuracyGoal’ is set to 10.

fore, a balance between the most accurate results, time limitations, and computing hardware limitations must be observed for each case.

Additionally, two interesting numerical solving methods that can be considered for solving the differential equations are shown in the following. The Harmonic Balance Method (HBM) is a frequency domain method to calculate steady-state responses of nonlinear differential equations [136]. And the orthogonal collocations method is a finite elements method that is used where the solution has steep gradients [137].

The mathematical analysis for the different selected numerical analysis is uploaded to GitHub [138]. In the branch ’Numerical-Calculation’ the calculation of the ordinary differential equations with Lagrange, bifurcation diagrams, Poincaré sections, and time plots of different parameters are stored.

The damping ratios used for the numerical analysis is the mean value of the experimentally determined values for the two shafts, see Table 3.2.

3.2 Experimental Design

In this section the design and measurement equipment of the omnidirectional pendulum energy harvester is shown.

3.2.1 Design of Energy Harvester

The design of the omnidirectional pendulum energy harvester was implemented in SOLIDWORKS ®. The general dimensions of the cage of the pendulum energy harvester are 745 mm ×

745 mm × 1120 mm. It can accommodate pendulum lengths with a range from l =0.1 m to 0.75 m, see Figures 3.2 and 3.3. Since the examined energy harvester is a pre-prototype care has been taken to ensure that the design can easily be modified that a wide range of experiments can be realised. Most importantly, the entire power take-off sub-system can be adjusted by an offset angle to investigate different directions of excitation. For the construction mild steel was used for the non-rotating parts and an aluminium alloy was chosen for the moving parts to keep the mass moments of inertia as low as possible. With the exception of the pendulum rod which is made from a standard M8 steel threaded rod which is cut into length according to the requirements. The mass of the pendulum bob can be replaced. But for the experiments shown the pendulum bob mass slightly exceeds 1 kg, at a nominal mass of 1.32 kg, to ensure that sufficient restoring torque is available, even in areas where the velocities are low. Figure 3.2 shows the assembly diagrams of the pendulum energy harvester. The power take-off sub-system in Figure 3.2a consists of four individual generators/motors with coaxial gearboxes an integrated shaft encoders. There is one symmetrically configured pair of generators per axis, and the electric load presented by the generators acts back on the harvester as a mechanical load. Each shaft is connected to a 12 V DC motor/generator with a coaxial gearbox and encoder with a spring coupling. Two motors/generators are used to archive a uniform movement of the shaft. The direction of deflection of the shafts is defined with the coordinates θ_{14} and θ_{23}. The built in encoders emit 700 pulses per revolution of the shaft which results in the resolution after the gearbox of 0.51 deg/pulse. The power take-off sub-system is mounted to a supporting structure cage, see Figure 3.2b. This cage is then mounted onto the shaker table with M8 screws where the rough alignment of the table is in 45 ° steps. For the fine adjustment of the angle the power take-off sub-system can be rotated step-less to archive the desired offset angle. The mounting

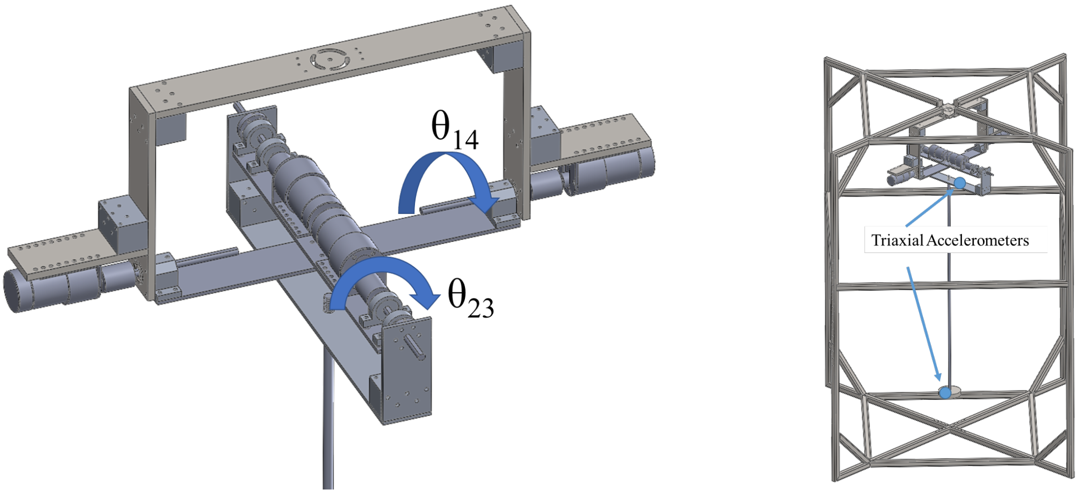

(a) Power take-off sub-system with coordinates θ_{14} and θ_{23}

(b) Complete assembly

Figure 3.2: CAD diagram of the experimental design of the energy harvester

points for the triaxial accelerometers are shown in Figure 3.2b. Because of the dimensions of the sensor and to ensure free movement of the shafts the accelerometers can unfortunately not be fixed onto an extension of the centre line of the pendulum rod. But instead a slight horizontal offset is needed as described in the following. The first accelerometer is attached to the top side of the pendulum bob. With the coordinate system that is defined in the following in Figure 3.4 the horizontal displacement of the sensor dependent on the centre of the coordinate system can be defined. The accelerometer on the pendulum bob has no displacement in the y-direction and a displacement of 3.9 cm in the x-direction, see Figure 3.4. The accelerometer at the lower flat bar of the power take-off sub-system is mounted on top of the flat bar. There is no displacement in the x-direction but in the y-direction the accelerometer has a negative displacement of -7.2 cm see Figure 3.4. The accelerometers were disassembled for most of the experiments and were attached only when needed. This is done to keep the mass moment of inertia as low as possible. The sensor specifications are discussed in the following Section 3.2.3.

3.2.2 Shaker Table

The energy harvester is mounted on a shaker table built by *Centrotecnica* SRL. With the shaker table a maximum excitation amplitude of 14.3 cm for a frequency range from static to 100 Hz is possible, which is more than adequate for the experiments. The maximum excitation amplitude decreases with an increase in excitation frequency. Because of the high dimensions of the experimental rig the maximum excitation amplitude is therefore restricted to a value of 5.0 cm. This is still sufficient to run the energy harvester properly, and to generate results of considerable interest. The shaker table only allows an excitation in one direction, therefore, a coupled excitation was unfortunately not achievable for the experiments. Since the forcing in the experimental section occurs in only one direction the symbol for the excitation amplitude is A and the symbol for the excitation frequency is Ω. Figure 3.3 shows the shaker table with the experimental rig mounted on top. The shaker table is connected to the computer with a CAN to USB cable of the type "Kvaser Leaf Light HS v2". This allows for a digital data transfer of the in- and output signal. In this case the transferred file is a text file.

In Figure 3.4 a top view diagram of the shaker table and the experimental rig is shown. The diagram shows the power take-off sub-system with the two generators. For clarity purposes it does not show the supporting structure and electrical equipment. It shows an important variable for the experiments the static angular offset α_{offset}, this angle defines the static rotation of the experimental rig to the shaker table. This is particular of interest since it defines the angle of the excitation direction. For an offset angle $\alpha_{offset} = 0^\circ$ this means that the complete oscillation is performed with shaft 23 and for an offset angle of $\alpha_{offset} = 90^\circ$ the only oscillations are observed only in shaft 14. However, with an offset angle of $\alpha_{offset} = 45^\circ$ a participation of both shafts is ensured and the energy harvester is behaving truly omnidirectionally. The motors/generators M1 and M4 are aligned and therefore they are considered as shaft 14 and motors M2

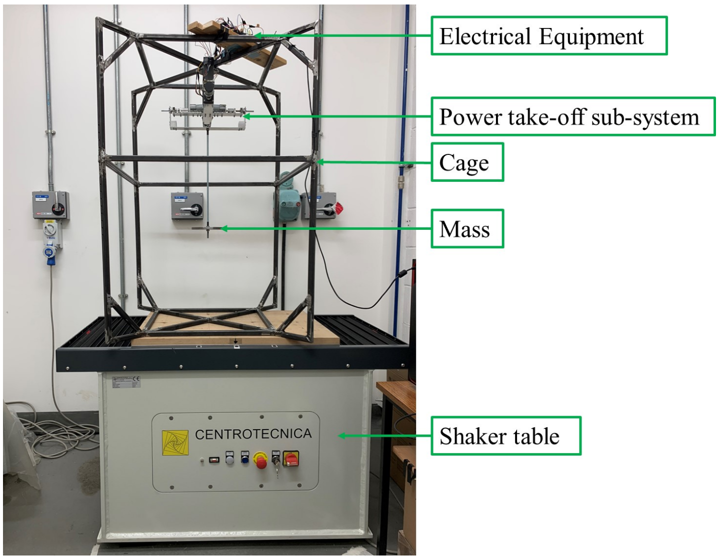

Figure 3.3: Shaker table with energy harvester mounted to the top

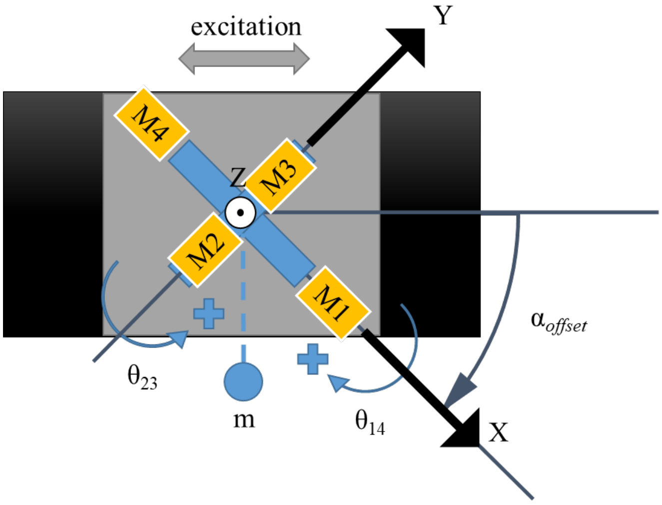

Figure 3.4: Top view of energy harvester to define the angular offset and the different rotation angles of the shafts with a deflected pendulum bob

and M3 are defined as shaft 23. Shaft 14 is defined by the rotation coordinate θ_{14} and shaft 23 is defined by θ_{23}, as already shown in Figure 3.2a. The direction of the rotation angles is defined from the perspective of motor 1 and motor 2. Thus, assuming that the point of reference is on either of these motors and the line of sight faces towards the spring coupling, from there a clockwise direction is defined as positive. To put it in other words when the pendulum bob is deflected as shown in Figure 3.4 both coordinates show positive values. Because of a limited budget the experimental design of the energy harvester was accomplished with the focus on economy and mechanical simplicity. Therefore the experimental coordinates are definitionally different from those used in the numerical analysis. An experimental coordinate system is introduced to allow a transformation between the coordinates, see Section 3.6. In the coordinate system, the *x*- and *y*-axes are parallel to the shafts and the *z*-axis points in the positive direction out of the page. When the offset angle is changed, the coordinate system will rotate as well. To put it in other words the *x*- and *y*-axis of the coordinate system are always aligned with shaft 14 and shaft 23.

3.2.3 Measurement Equipment and Power Take-Off

The choice of measurement equipment was made with the aim of using a solution that is fast and inexpensive but at the same time as accurate as possible. Therefore, the generators were procured with a built-in encoder and they were together with voltage dividers and current sensors connected to an Arduino MEGA 2560. Figure 3.5 shows the electrical schematic for the measurement equipment. To increase the clarity a larger version of the figure is located in the Appendix B. The current sensors that are used are the ACS712-5A and the voltage output is measured with a resistive voltage divider. These outputs are connected to the analogue pins (A3, A4, A5, A6, A8, and A9) of the microcontroller. The outputs from the DC-motors are from left to right the motor voltage output (+), motor ground (-), encoder ground (GND), supply voltage for the encoder (V_{cc}), encoder signal output A, and encoder signal output B. The output signals of the encoder are connected to the digital pins (2, 3, 5, 7, 9, 18, 19, and

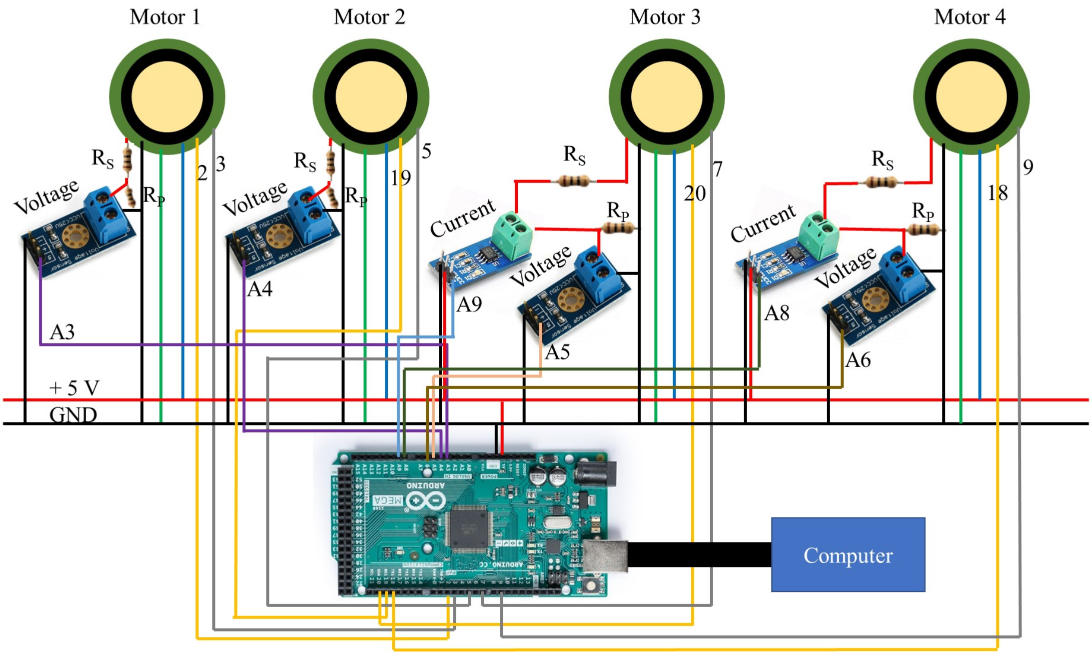

Figure 3.5: Electrical schematic for the measurement equipment with an Arduino MEGA 2560 (a larger version is located in Appendix B)

20) of the microcontroller, it is important that pin A is connected to a so-called interrupt pin (2, 18, 19, and 20) since otherwise the interrupt routine and therefore the measurement of the angular position would not be possible. The need for four interrupt pins was the reason why an Arduino MEGA was chosen over one of the smaller models in the Arduino series. The microcontroller stores the summed-up pulse trains from the encoder and the voltage and current output values at a rate of repetition, and 12 ms was chose for practical reasons. The rate of repetition is limited by the baud rate of the microcontroller. There is a series resistor (R_S) and a parallel resistor (R_P) built into the circuit, and their values can be changed as needed. The parallel resistor can be disconnected if necessary. This is indicated in the following way $R_P =$ NC this means that there is no physical connection between the in- and output before the voltage bridge. The first measurements are carried out with a value of $R_S = 10$ kΩ and $R_P =$ NC which ensures that the power take-off is as small as possible. Followed by measurements where the parallel resistor is included to increase the current output and therefore the power take-off. The values are set to $R_S = 0$ Ω and $R_P = 10$ Ω for these experiments. The lower the value for the parallel resistor the higher the power output. These two sets of resistor values are referred to in the following as low power take-off mode and high power take-off mode respectively. They are therefore just extremes of a continuum. Note that the term 'mode' as used here does not imply a flexural mode of vibration and instead refers to a basis of operation. The previously described power take-off modes are shown in greater detail in the circuit for one generator, see Figure 3.6. With the two switches (S1 and S2) opened the resistors of the voltage divider (blue double dotted frame) and the series resistor (R_S) are in connected in line. Note that the switches are only used as an aid for the explanation of the circuit, in the experimental set up the resistors are removed or added manually as already mentioned in Figure 3.5. The total resistance value

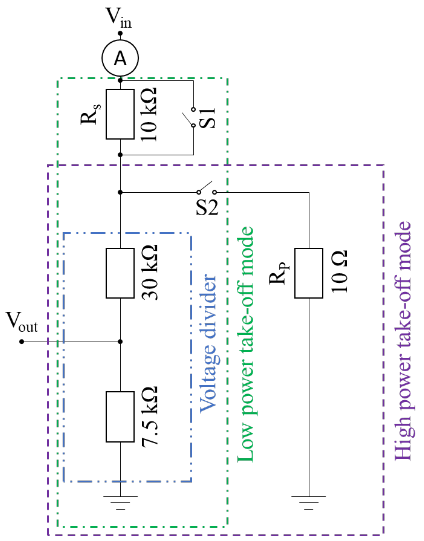

Figure 3.6: Circuit for the voltage divider with the loading resistors

is high $R_{\text{low}} = 47.5$ kΩ and therefore the observed current flow is low. Hence, the energy harvester operates in the low power take-off mode (green dashed dotted frame). The high power take-off mode (purple dotted frame) is reached by closing both switches. With this the series resistor is shorted and the current is divided between the two parallel branches of the circuit. The total resistance in the high power take-off mode has a value of $R_{\text{high}} = 9.997$ Ω. This small value results in a high current output and therefore a possible high power conversion as long as the voltage source, i.e. movement of the pendulum, is unchanged. The circuit in Figure 3.6 shows that the current is measured before all the resistors. The voltage output is measured at the shown position. The measured voltage output needs upscaling to determine the complete voltage output of the generator, see Equation (3.1).

$$V_{out} = \frac{7.5\ k\Omega}{7.5\ k\Omega + 30\ k\Omega} \times V_{in}. \tag{3.1}$$

Note that in the low power take-off mode (indicated by the green dash dotted frame) a series resistor of 10 $k\Omega$ is used and therefore this value needs to be added to the denominator of Equation (3.1) and therefore in the Arduino code. In the high power take-off mode (indicated by the dashed purple frame) the voltage divider values as defined in Equation 3.1 are used. With the microcontroller connected to the voltage bridge, see Figure 3.6, only positive voltage outputs can be measured. For negative voltage outputs the microcontroller shows a value of zero. Since, the two generators on each shaft are facing each their direction of rotation are oppositely signed. This in return also means that the voltage output of each of the generator on the shafts are oppositely signed. When one of the generators has a positive voltage output according to the pre-defined direction of excitation the other generator shows a negative output receptively. Since the negative voltage output cannot be measured with the described measurement setup and the microcontroller output shows no voltage output, the voltage output of each shaft can be artificially constructed[1]. This is done by subtracting the voltage output measured across generator 4 from the voltage output measured across generator 1, see Equation (3.2). The same procedure is applied with shaft 23, see Equation (3.3). This then gives an artificial constructed sine shaped output signal for the complete shaft which then can be used for the further post-processing.

$$V_{14}(t) = V_1(t) - V_4(t). \tag{3.2}$$

$$V_{23}(t) = V_2(t) - V_3(t). \tag{3.3}$$

The Arduino code developed for the experimental evaluation is uploaded to GitHub [138]. For the development of the Arduino code the following references were used [139–142].

---

[1] In other words the two generator voltage outputs on each shaft have a 180° phase shift towards each other.

It is important to investigate whether high frequency vibrations are prevailing in the structure of the energy harvesters since this is energy that cannot be transformed into motion energy of the pendulum bob and it therefore reduces the efficiency of the pendulum energy harvester. This is discussed in greater detail in Section 3.5. Examined are two points of importance, the pendulum bob and the flat bar in the power take-off sub-system. Therefore, two points were defined where the vibrations are measured see Figure 3.2b. Unfortunately, the only triaxial accelerometer that was available for the measurements is the inbuilt accelerometer of the iPhone XS Max. The large dimensions of the smartphone and the weight inevitably influence the vibration measurements, but this had to be accepted as there was no other triaxial accelerometer available. Moreover, the smartphone was only attached for the vibration measurements, and for the rest of the measurements it was removed and therefore did not increase the mass and mass moment of inertia of the rig for the other measurements. The directions of the accelerometer can be obtained from the developer website of Apple Inc. [143]. In the smartphone used an accelerometer of the company Bosch Sensortec GmbH is used, unfortunately the manufacturer of the smartphone does not give information on the exact model that is used but the BMA accelerometer series [144] was likely used. As a recording software the mobile application phyphox® developed by the RWTH Aachen University was used [145]. The acquisition rate of the smartphone is set to its maximum which is 100 Hz. Since there are unfortunately no construction schemes available for the smartphone, the position of the accelerometer is determined by observing dismantling plans of the smartphone. From which the position of the accelerometer on the logic board can be determined.

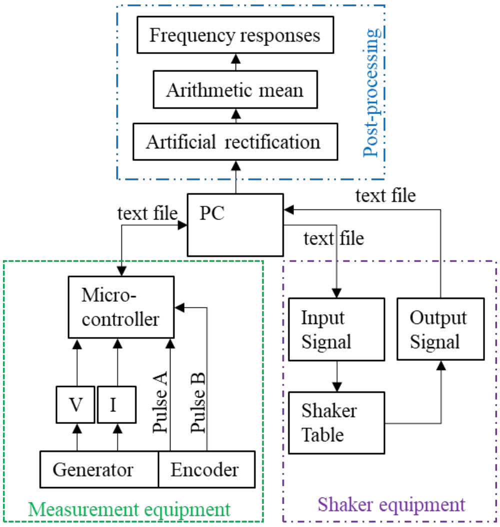

Figure 3.7: Block diagram of the microcontroller, shaker table, and post-processing process

A summary of the previously described experimental setup is shown in Figure 3.7. The computer is connected to the shaker table (purple dotted dashed frame) with a CAN to USB cable. With this cable an input signal file is transferred to the shaker table and the output file transferred back to the computer. This is plotted and discussed later in Figure 3.14. Additionally, the computer is connected to the microcontroller (green dashed frame) which is connected to the generators and encoders of the energy harvester. The output signals of the encoder and the voltage and current output signals, measured as shown in Figure 3.6, are stored in the microcontroller and subsequently transferred to the computer. An output text file from the microcontroller consists of columns with time, deflections, voltage, and current values. These files are then used for the post-processing process (blue double dotted frame) as described in Section 3.3.1.

3.3 Post-Processing and Validation of the Experimental Equipment

In the following sections the experimental equipment is validated and the post-processing of the experimental results is described.

3.3.1 Post-Processing of the Experimental Results

The Arduino gives an output signal for the angles and voltage output for all four motors/generators and the current output for two generators. This output is stored in form of a text file on the computer. To produce meaningful result the output text file needs careful treatment which is observed in the following starting with the deflection values. The two generators on each shaft face each other and therefore the direction of rotation is opposite towards each other or in other words a 180° phase shift between the deflection outputs of the symmetrically configured pairs of generators per axis can be observed. This means that the deflection of generator 1 has the additive inverse value of generator 4, see Figure 3.8, and the deflection value of generator 2 has the additive inverse value of generator 3. It is defined that the output values of generator 3 and generator 4 are additively inversed. Afterwards the deflection values of the two generators on each shaft are arithmetically averaged to get the artificially synchronised deflection values of each shafts θ_{14} and θ_{23} as a time dependent signal. Equations (3.4) and (3.5) show in equation

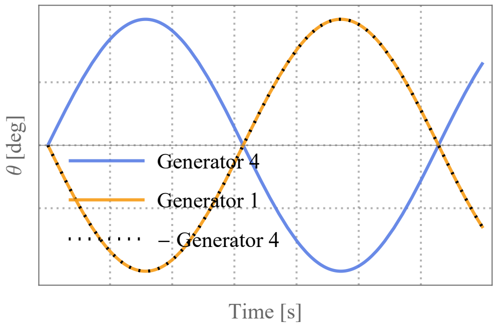

Figure 3.8: Qualitative deflection vales of generators 1 and 4

form the definitions of the coordinates θ_{14} and θ_{23}.

$$\theta_{14}(t) = \frac{\theta_1(t) + (-\theta_4(t))}{2}. \tag{3.4}$$

$$\theta_{23}(t) = \frac{\theta_2(t) + (-\theta_3(t))}{2}. \tag{3.5}$$

The experimental results in Chapter 6 are mainly analysed in the frequency domain. The experimental values however are recorded in the time domain and therefore need post-processing to create the frequency responses. Generally, it is distinguished between frequency responses that are measured with a steady-state signal and frequency responses that incorporate an excitation frequency sweep. Most of the experimental analysis observes frequency responses measured with a linear excitation frequency signal. This means that the omnidirectional energy harvester is excited over 200 s with a constant excitation frequency, see Figure 3.9b. Then subsequently the maximum deflection is arithmetically averaged over the last 20 s of the excitation period, see Figure 3.9. This ensures that the energy harvesters' deflection are observed in a steady-state, see Figure 3.9a. This is performed for different excitation frequencies several times and the results are arithmetically averaged and plotted in the frequency domain. Henceforth these frequency responses are referred to as linear frequency responses or linear part of the frequency response. The advantage of this is that transient responses are not present in any of the linear frequency responses.

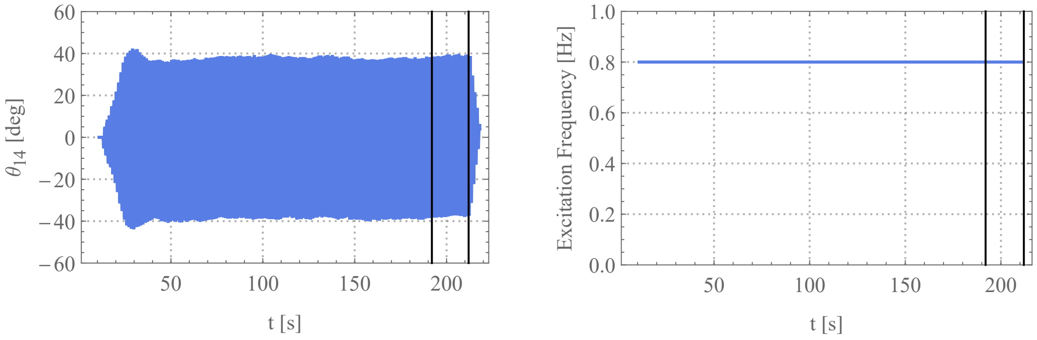

(a) Deflection of θ_{14} over time

(b) Excitation frequency over time

Figure 3.9: Definition of the time period over which the linear frequency responses are calculated

In Section 6.4 excitation frequency sweeps are included in the frequency responses to see a potential effect on the increase of the operational range of the omnidirectional pendulum energy harvester. The post-processing method of the frequency sweeps is slightly different from those for the linear frequency response. In Figure 3.10a time-domain response for the coordinate θ_{23} for the energy harvester excited with a frequency up-sweep from 0.82 Hz to

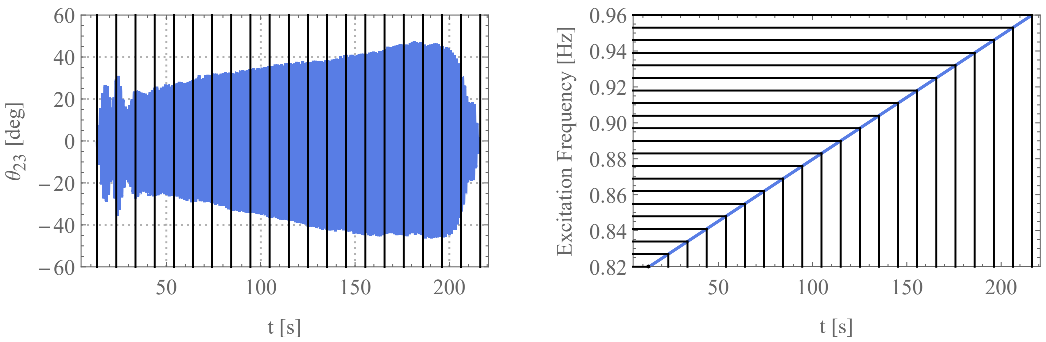

(a) θ_{23} over time

(b) Excitation frequency over time

Figure 3.10: Definition of the bandwidth elements during an excitation frequency up-sweep and down-sweeps, shown here exemplary an up-sweep from 0.82 Hz to 0.96 Hz

0.96 Hz is shown[2]. Additionally, vertical black lines are shown, where the horizontal distance between two neighbouring lines is defined as a bandwidth element. In this case the up-sweep is divided reasonably into 20 bandwidth elements of the same size of a length of 10 s. The size of a bandwidth element is dependent on the length of the excitation sweep and the amount of parts it is divided into. Since the frequency sweep function is linear the length of the bandwidth elements in the time domain is equal to the frequency range. Hence the name 'bandwidth' which is classically attributed to the frequency domain. In the shown case the length of a bandwidth element is 0.007 Hz, see Figure 3.10b. For each of these bandwidth elements the maximum and additive inversed deflections of the coordinates are stored and subsequently arithmetically averaged. These results are added to the linear frequency responses. The starting point or points of the frequency sweeps show transient dynamics. The definition of transient dynamics being a variation of the deflection over time and therefore they can show a lower or higher value than the steady-state. In this work the deflection values that are attributed to the transient response are shown and mentioned in the results section but are not discussed in greater detail since they do not influence the operational range of the energy harvester.

In Figure 3.11 the different parts of the frequency responses are defined. This definition has been chosen solely for the sake of better understanding. The linear operational range is the region in which the energy harvester can operate with a constant excitation frequency. This is defined as the area between the two local maxima of the coordinate θ_{14}. This is directly transferred to to the coordinate θ_{23} for reasons of simplicity. In this region the energy harvester is therefore considered as a linear device.

With the inclusion of up- and down-sweeps with slow sweep rates the energy harvesters operational range broadens. These areas are called lower and upper nonlinear jump regions see Figure 3.11. The increase of the operational range with the lower and upper nonlinear jump regions is here referred to a broadening. Two dimensionless variables are introduced to

---

[2] Here coordinate θ_{23} is used to show both coordinates, see Figures 3.9a and 3.10b.

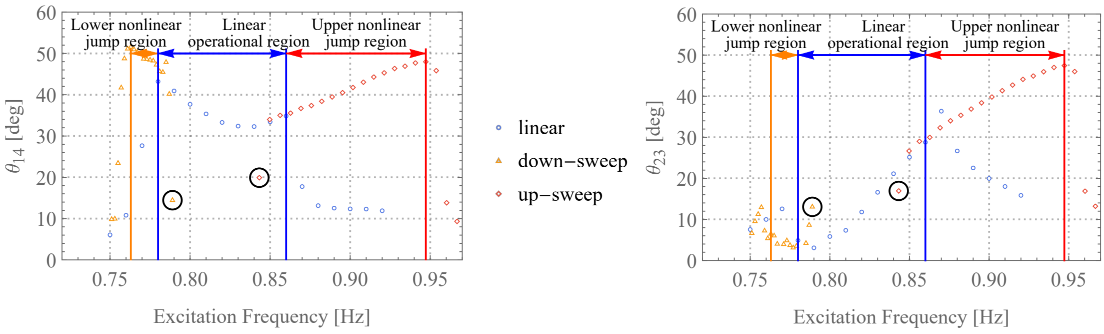

(a) Frequency resonse of θ_{14}

(b) Frequency response of θ_{23}

Figure 3.11: Definition of the linear operational range, lower nonlinear jump region, and upper nonlinear jump region of the omnidirectional pendulum energy harvester

calculate the broadening in a user-friendly per cent value, see Equations (3.6) and (3.7). For a pendulum length of 0.35 m the used base values for the analysis have a value of 0.08 Hz in the low power take-off mode and 0.11 Hz in the high power take-off mode. These values are used as the basis for the calculation of the broadening of the up-and down-sweeps in percentage terms.

$$\text{Broadening}_{\text{down-sweep}} = \frac{\text{Lower jump region}}{\text{Linear operational range}}\,100. \tag{3.6}$$

$$\text{Broadening}_{\text{up-sweep}} = \frac{\text{Upper jump region}}{\text{Linear operational range}}\,100. \tag{3.7}$$

The total broadening of the linear operational range is defined in Equation (3.8).

$$\text{Broadening}_{\text{total}} = \frac{\text{Upper jump region} + \text{Lower jump region}}{\text{Linear operational range}}\,100. \tag{3.8}$$

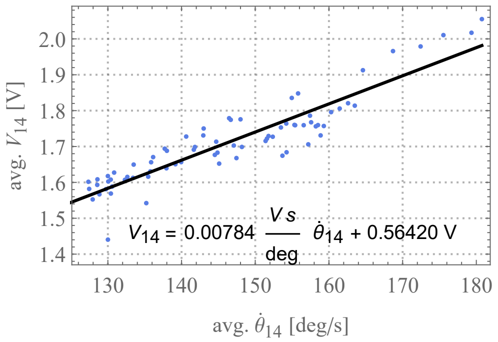

Figure 3.12: Arithmetic mean rectified voltage output over the arithmetic mean rectified of the velocity of θ_{14} with linear fitted equation

In a DC-generator the voltage output is dependent on the revolutions per unit time of the generator [146, 147]. This dependency on velocity is important to keep in mind when comparing the deflection of the shafts to the voltage output later on in this work. It is evident that the highest voltage output is not always at the same position as the highest deflection value. Therefore, later in the results section in Figure 6.21 the frequency responses for the velocity of the shafts are shown additionally to prove the described relationship. The relation between the arithmetic mean rectified voltage output and the arithmetic mean rectified velocity of θ_{14} in the high power take-off mode is shown in Figure 3.12. Note that the relationship is only observed in the operational region of the energy harvester. Therefore, voltage outputs that have a lower value than 1.4 V are not included in the calculation of the relationship between the variables.

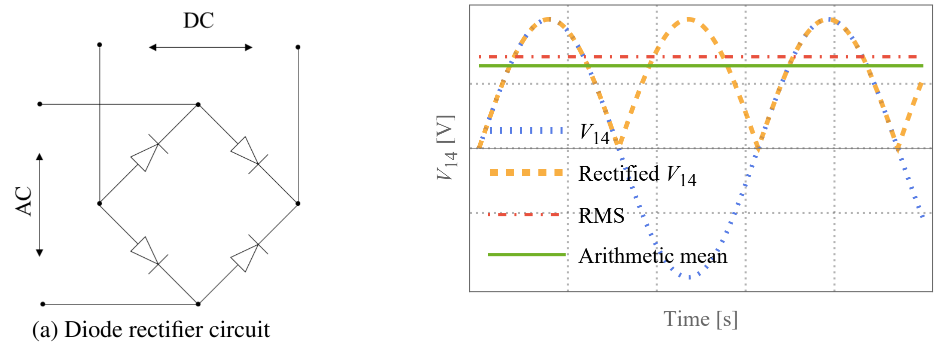

(a) Diode rectifier circuit

(b) Qualitative voltage output over time

Figure 3.13: Rectification of the voltage output of the energy harvester

The frequency responses in the result section for the voltage output do not show the peak voltage output but the arithmetic mean rectified voltage output. Note that is abbreviated with 'avg.'. The arithmetic mean rectified is used since it is assumed that in the power electronics of the energy harvester the low AC-voltage is converted into a DC-voltage with a full-wave diode rectifier circuit, see Figure 3.13a. The qualitative voltage output of V_{14} over time is shown in Figure 3.13b. The sine shaped oscillation of the voltage is rectified and subsequently arithmetically averaged. The commonly used root mean square (RMS) averaging results are shown as well. These are not used in this work. However, the arithmetic mean rectified voltage output can easily be converted into the RMS with the form factor [148–150] shown in Equation (3.9).

$$\mathrm{RMS}V_{14} = \frac{0.707}{0.637}\mathrm{avg.}V_{14} = 1.11\ \mathrm{avg.}V_{14}. \tag{3.9}$$

The current is measured once for each shaft right after the output of the generators 3 and 4 and in front of the shown circuit, see Figures 3.6 and 3.5. The power output of the energy harvester for each shaft is calculated with Equation (3.10).

$$P_{14} = 2\ V_{14}\ I_4, \quad P_{23} = 2\ V_{23}\ I_3. \tag{3.10}$$

It is important to observe the sweep rate of different frequency responses in the experimental result section, see Table 3.1. Because of the pre-defined length of the sweep of 200 s the sweep rate varies in the different figures. Even though this has the potential to affect the jumping down

Table 3.1: Sweep rate for excitation frequency sweeps in the different figures in the result section

Figures	**Sweep rate [Hz/min]**	
	down-sweep	up-sweep
6.18	-0.009	0.039
6.19	-0.012	0.039
6.20	-0.009	0.030
6.21	-0.024	0.042

point position in the frequency response this can be neglected since the sweep rate is sufficient small enough in all the cases shown.

3.3.2 Analysis of Experimental Inaccuracies

The determination of inaccuracies of the experimental equipment is extremely important for experimental work, this is carried out in the following. Without the electrical measurement equipment the length of the pendulum can reasonably be determined to an error of ± 0.5 mm. The mass of the pendulum bob is determined on a high accuracy scale to an error of ± 0.01 g. The time was measured by the Arduino board's included time module, this gives with the function 'millis()' a time output in milli seconds. The used crystal oscillator has an accuracy of 0.0005% and the time deviation is therefore insignificant over the measurement range of 200 s. There are several reasons for the measured inaccuracies of the rotational angle. They mostly come from the encoders and the spring coupling that is fitted prior to the encoder and therefore delays the rotation of the shaft slightly. This has a greater effect for small deflections but can be neglected for higher deflections. From the encoder an accuracy of ± 0.5° is expected. However, since the values of the two encoders on one shaft are arithmetically averaged and they are not physically connected the errors are in the range from ± 0 to 1.0°. The voltage sensor and current sensor have errors of ± 0.05 V and ± 0.1 A. The last one is unfortunately fairly high, for a high resistor this means that the current output is low and therefore the power output of a lightly damped energy harvester cannot be determined since the error that influences the result is too large. The offset angle has an accuracy of $\alpha_{offset} = \pm\, 0.25^\circ$. Figure 3.14 shows the input and output signal of the excitation amplitude of the shaker table over time. The input and output curves are almost identical and therefore can be considered accurate. It is therefore not likely that errors between the numerical and experimental results can be attributed to errors in the excitation.

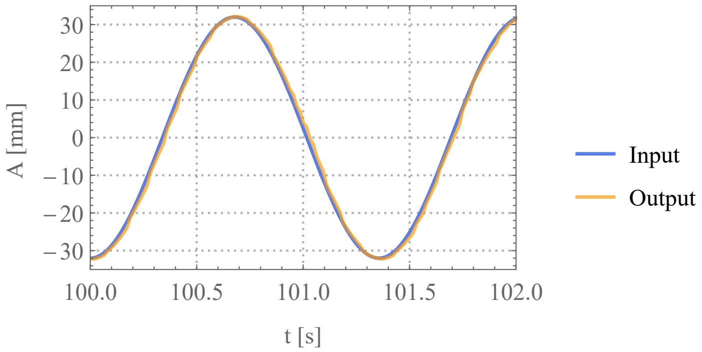

Figure 3.14: Input and output signal of the shaker table "CENTROTECNICA S.R.L. Lo.F.Hi.S." over time

Phyphox offers a sensor database [151] where the standard deviations of different smartphones are listed. For the acceleration measurements without g the standard deviation for the used accelerometer is 0.020 m/s^2 at an acquisition rate of 100 Hz.

3.4 Damping Ratios of the Omnidirectional Pendulum Energy Harvester

In this section the damping ratios of the pendulum energy harvester are determined. This is accomplished with an oscillation decay process of the different shafts of the pendulum energy harvester successively. The logarithmic decrement (3.11) is then used to calculate the damping ratio for the different shafts of the pendulum energy harvester. Since only one shaft at a time is observed these tests show the dynamics of the pendulum energy harvester in its rawest form. This is carried out for different pendulum lengths. The determination of the damping ratio was done with a load resistor value of 10 kΩ. This ensures that the current flow is minimal and therefore the electric power take-off is tiny and can therefore be neglected. The damping ratio is therefore solely attributed to the mechanical friction in the generators, bearings, and a tiny quantity of aerodynamic dissipation of the pendulum bob and pendulum rod.

$$\xi = \frac{\delta}{\sqrt{\delta^2 + (2\pi)^2}} \quad \text{where} \quad \delta = \ln \frac{x_0}{x_1} \tag{3.11}$$

Figure 3.15 shows plots for the energy harvester with a length of 0.75 m and a mass of 1.32 kg that is deflected in the angular direction of the shaft on which the generators 1 and 4 are connected to. The oscillation decay process of the coordinate θ_{14} is shown in Figure 3.15a. From this a damping ratio for the coordinate θ_{14} of $\xi_{14} = 0.0204$ is calculated. The coordinate θ_{23} does not show any deflection, see Figure 3.15b, this ensures that it does not affect the swing of the coordinate θ_{14}. The voltage output of the generators 1 and 4 is shown in Figure 3.15c,

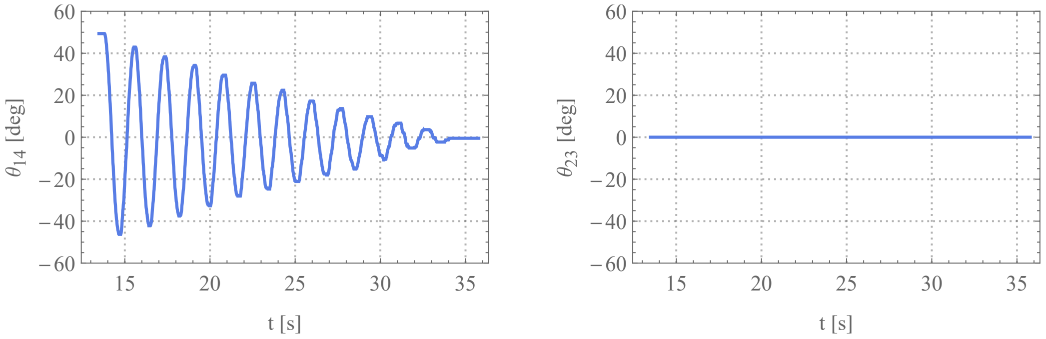

(a) θ_{14} over time

(b) θ_{23} over time

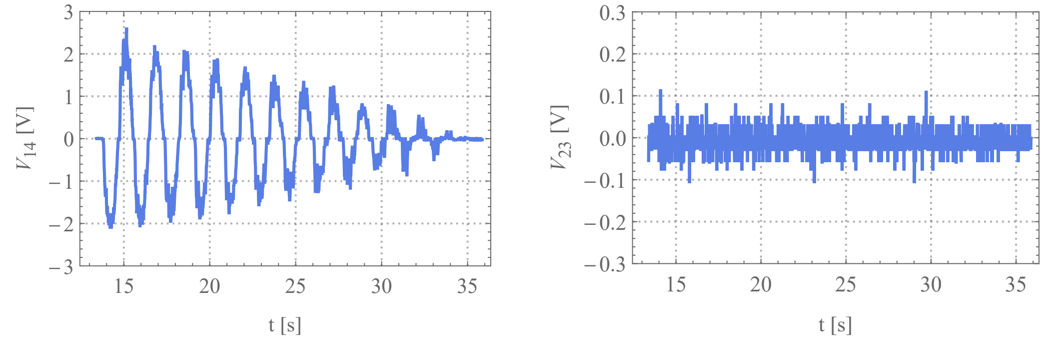

(c) Voltage output V_{14} over time

(d) Voltage output V_{23} over time

Figure 3.15: Experimental results of an oscillation decay process of the θ_{14} without excitation. The parameters of the pendulum energy harvester are: $l = 0.75$ m, $m = 1.32$ kg, $\xi_{14} = 0.0204$, $\xi_{23} = 0.0200$, $R_P =$ NC, and $R_S = 10$ kΩ.

the voltage output follows basically the velocity curve of θ_{14} with higher frequency noise visible in the main signal of the swing. Figure 3.15d shows the voltage output of θ_{23}. There is a general signal noise observed. This in return means that it is reasonable to assume that when the value of the voltage is lower than 0.05 V it is considered as background signal noise. The noise can be attributed to the errors of the voltage bridge and the microcontroller. It is noticeable that when the deflection of the pendulum becomes lower than around 10°, the measured values likewise become less accurate, this is mainly attributed to the spring coupling. Because with low deflection values the restoring force torque becomes smaller as well and therefore the damping within the spring coupling has a proportional higher effect on the deflection than for higher deflections. Figure 3.16 shows plots for the energy harvester with a length of 0.75 m and a mass of 1.32 kg that is deflected in the angular direction of the shaft 23. The mass moment of inertia of this shaft is lower compared to shaft 14 and the pillow blocks used have a different design. Therefore, a slightly different damping ratio from shaft 23 of $\xi_{23} = 0.020$ can be derived from Figure 3.16a. In Figure 3.16c the voltage output of θ_{23} is shown and it follows $\dot{\theta}_{23}$ well and the high frequency noise is observed. Figure 3.16d shows the voltage output of the resting coordinate θ_{14} that shows no deflection but as before the background signal noise can

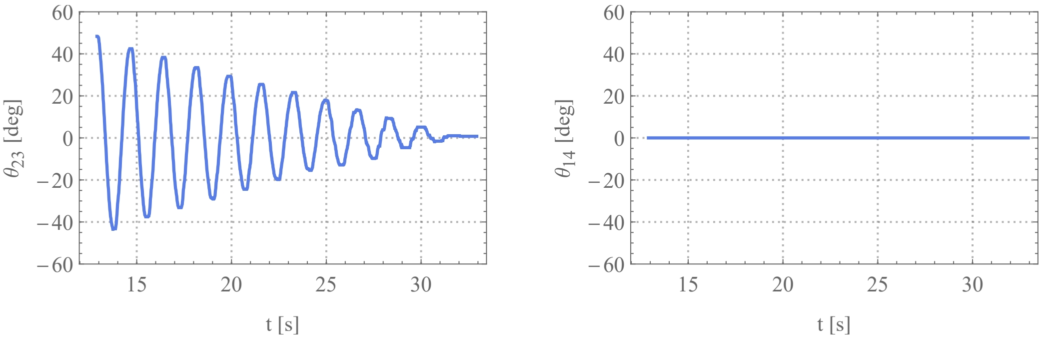

(a) θ_{23} over time (b) θ_{14} over time

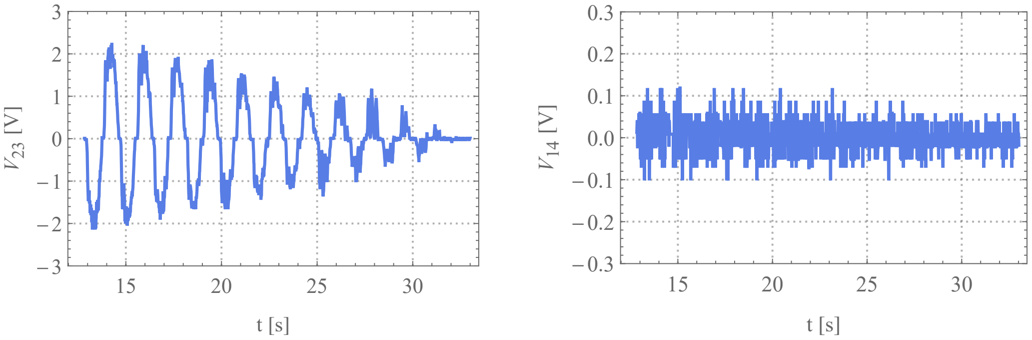

(c) Voltage output V_{23} over time (d) Voltage output V_{14} over time

Figure 3.16: Experimental results for an oscillation decay process of the coordinate θ_{23} without excitation. The parameters of the pendulum energy harvester are: $l = 0.75$ m, $m = 1.32$ kg, $\xi_{14} = 0.0204$, $\xi_{23} = 0.020$, $R_P = \text{NC}$, and $R_S = 10$ kΩ.

be observed. From Figures 3.15a and 3.16a the damping ratios for the energy harvester with a pendulum length of 0.75 m are determined.

Figure 3.17 shows rotational angle and voltage output for the energy harvester with a length of 0.5 m and a mass of 1.32 kg that is deflected in the angular direction of the coordinate θ_{14}. The oscillation decay process of the coordinate θ_{14} is shown in Figure 3.17a. From this a damping ratio for θ_{14} of $\xi_{14} = 0.0325$ is determined. This means that the damping ratio increased with decreasing of the pendulum length. As before it can be seen that the measurements of the angle become more inaccurate when the measured angle is below a value of 10°, for the mentioned reasons. As can be seen from Figure 3.17b the coordinate θ_{23} does not show any deflection and this ensures that it does not affect the swing of the coordinate θ_{14}. The voltage output of generators 1 and 4 is shown in Figure 3.17c. The voltage output follows, as expected, the velocity of the coordinate θ_{14}. Here as well the high frequency noise can be observed. Figure 3.17d shows the voltage output of the resting coordinate θ_{14} where the background noise signal can be observed.

Figure 3.18 shows diagrams for deflection of the coordinate θ_{23} of a pendulum energy harvester with a length of 0.5 m and a mass of 1.32 kg. In Figure 3.18a the deflection for the coordinate θ_{23} is shown and from this the damping ratio is calculated with a value of

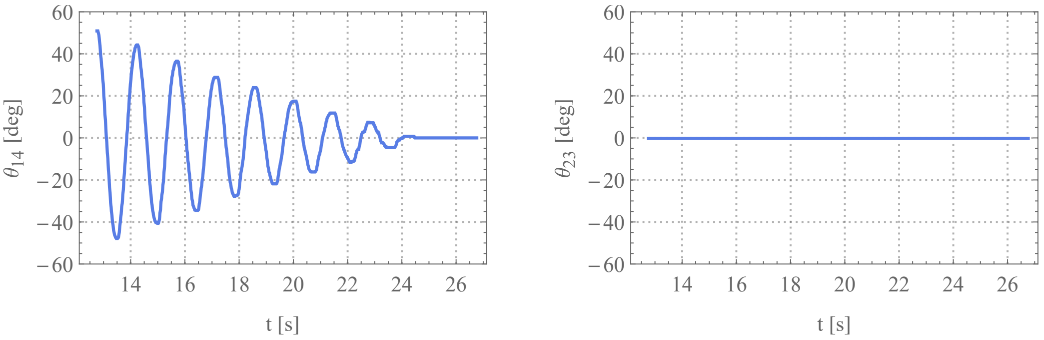

(a) θ_{14} over time

(b) θ_{23} over time

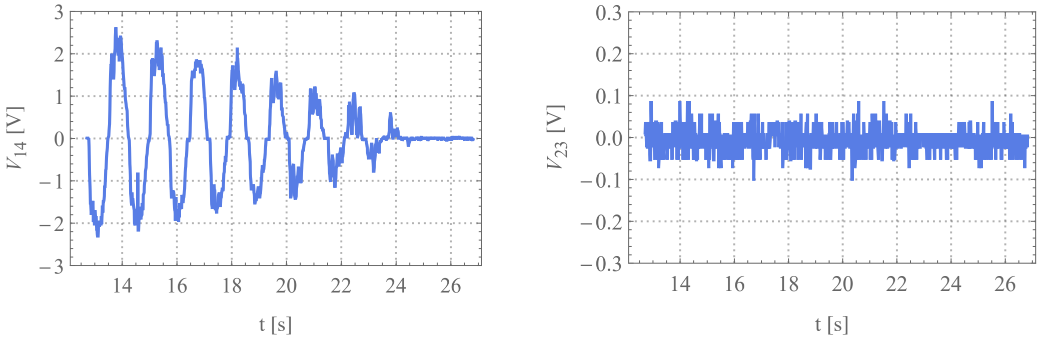

(c) Voltage output V_{14} over time

(d) Voltage output V_{23} over time

Figure 3.17: Experimental results for an oscillation decay process of the coordinate θ_{14} without excitation. The parameters of the pendulum energy harvester are: $l = 0.5$ m, $m = 1.32$ kg, $\xi_{14} = 0.0325$, $\xi_{23} = 0.0323$, $R_P = \mathrm{NC}$, and $R_S = 10$ kΩ.

$\xi_{23} = 0.0323$. The coordinate θ_{14} does as expected not show any deflections, see Figure 3.18b. In Figure 3.18c the voltage output V_{23} is shown with its peak being at $\theta_{23} = 0$, and therefore follows the velocity of the coordinate θ_{23} with high frequency noise that is observed on the oscillation. Figure 3.18d shows the voltage output of the resting coordinate θ_{14} where the background noise signal can be observed.

In Table 3.2 the damping ratios for different pendulum lengths are listed. These damping ratios are solely attributable to the mechanical friction in the bearings, gears and generators and a tiny quantity of aerodynamic dissipation. These values are used for the numerical calculation. The damping ratios were determined with at least three repeated measurements where the calculated damping ratio was arithmetically averaged. It generally can be seen that with a decreasing pendulum length the damping ratio increases.

In Figure 3.19 the damping ratios for shaft 14 and shaft 23 are plotted over the pendulum length. The relation between length and damping ratio is not linear and is approximately reminiscent of a $f(x) = 1/x$ function. For the smallest pendulum length of $l = 0.2$ m the damping ratio is over proportionally high and for the longest pendulum length of $l = 0.75$ m the damping ratio is the lowest. Interestingly the damping ratio for shaft 23 shows almost no increase from a pendulum length decrease from $l = 0.75$ m to 0.6 m. This effect can be seen in Section 6.17

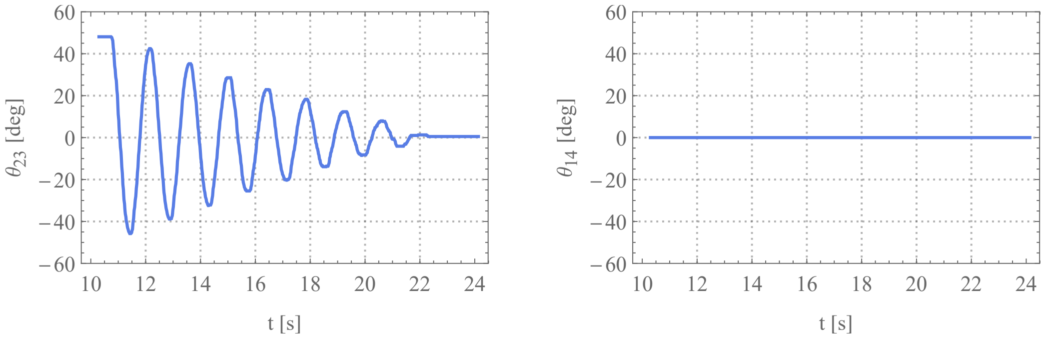

(a) θ_{23} over time

(b) θ_{14} over time

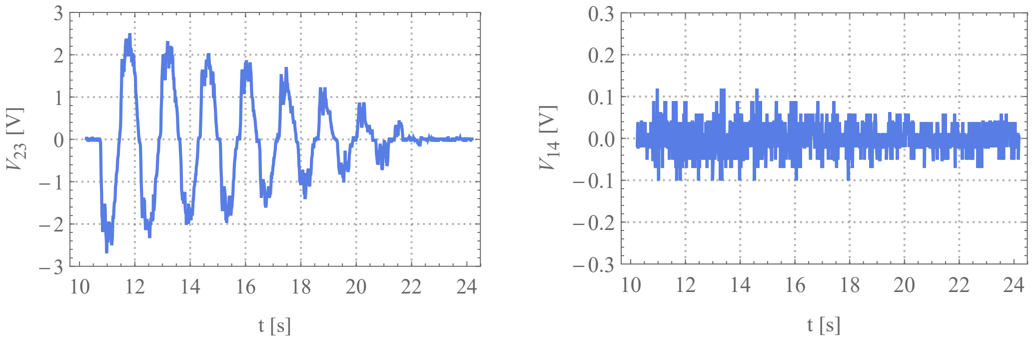

(c) Voltage output V_{23} over time

(d) Voltage output V_{14} over time

Figure 3.18: Experimental results for an oscillation decay process of the coordinate θ_{23} without excitation. The parameters of the pendulum energy harvester are: $l = 0.5$ m, $m = 1.32$ kg, $\xi_{14} = 0.0325$, $\xi_{23} = 0.0323$, $R_P = \text{NC}$, and $R_S = 10$ kΩ.

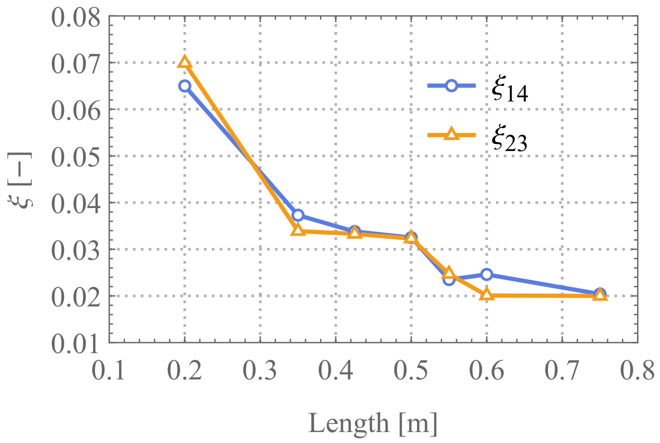

Figure 3.19: Damping ratios of the energy harvester of the different shafts over the pendulum length

when comparing the frequency responses for the different pendulum lengths. The difference between the damping ratios of the two shafts at the same pendulum length is within the margin

Table 3.2: Damping ratios of the energy harvester depending on the length of the pendulum

Length [m]	**Damping ratios**	
	ξ_{14}	ξ_{23}
0.2	0.0650	0.0699
0.35	0.0373	0.0339
0.425	0.0338	0.0333
0.5	0.0325	0.0323
0.55	0.0235	0.0247
0.6	0.0246	0.0201
0.75	0.0204	0.0200

of tolerance.

3.5 Higher Frequency Vibrations of the Structure of the Omnidirectional Pendulum Energy Harvester's Moving Parts

In the power take-off sub-system and the bob of the pendulum energy harvester high frequency vibrations can be seen. These need to be quantified, therefore the triaxial accelerometers as described in Section 3.2 are used to measure those.

Figure 3.20 shows the accelerations measured with a triaxial accelerometer at the pendulum bob. The Figures show the acceleration in the *x*, *y*, and *z*-directions over time and the FFT-analysis of the absolute acceleration. The used accelerometer is described in the methodology Chapter 3.2.3. The position of the accelerometer on the pendulum bob is described in Figure 3.2b and the coordinate system that is used for defining the acceleration directions is described in Figure 3.4.

The acceleration in the *x*-direction is shown in Figure 3.20a. It is evident that there are high frequencies present. The same applies to the other horizontal direction which is the acceleration in the *y*-direction in Figure 3.20b where higher frequency vibrations are existing. Since the pendulum energy harvester is a pre-prototype the pendulum rod consists of an M8 threaded rod. With respect to vibration optimisation this is clearly not an ideal design but it suits the purpose for this early stage of the development progress. For an improved version of the energy harvester it is definitely advisable to investigate an improved pendulum rod design with the goal of reducing the vibrations within the pendulum rod.

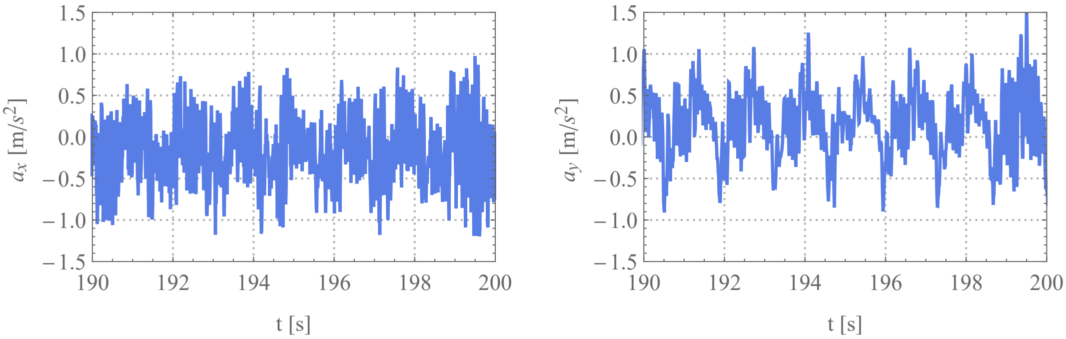

(a) Acceleration in the *x*-direction

(b) Acceleration in the *y*-direction

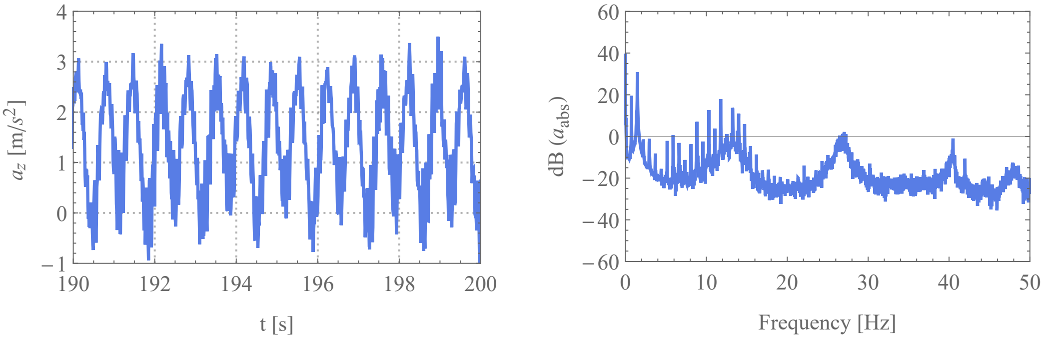

(c) Acceleration in the *z*-direction

(d) FFT of the absolute acceleration

Figure 3.20: Experimental results of the acceleration on the pendulum bob. The parameters of the pendulum energy harvester are: $l = 0.5$ m, $m = 1.32$ kg, $\xi_{14} = 0.0325$, $\xi_{23} = 0.0323$, $\Omega = 0.7375$ Hz, $A = 32$ mm, $R_P =$ NC, and $R_S = 10$ kΩ.

In Figure 3.20c the acceleration in the *z*-direction is shown. A general oscillation of the pendulum bob can be seen. Here as well higher frequency vibrations are observed.

The FFT analysis in Figure 3.20d shows the first peak at a frequency of 0.733 Hz which is almost at the excitation frequency. The following maxima are attributed to the parametric resonance and are therefore multipliers of the first peak. They are characterised by high peaks that can be detected up to a frequency of about 15 Hz. In addition, other frequencies can be observed which are not attributed to the swing of the pendulum bob. The first noticeable peak for this is observed at a frequency of 13.5 Hz and the parametric resonance of this frequency can be seen at 27 Hz. This shows that the higher frequency vibrations are present however, they have overall a relatively small impact on the movement of the pendulum bob. Nevertheless, this shows that not all of the input energy gets transformed to movement energy of the pendulum bob this therefore needs to be considered in the comparison of the numerical and experimental results. Thus it is defined that from a frequency higher than a value of 7 Hz (approximately 10 times the natural undamped frequency of the spherical pendulum) the output is defined as higher frequency vibrations in the pendulum bob and is therefore considered as unusable for the energy harvesting. The percentage of the higher frequency energy to the total energy at the pendulum bob has a value of 2.8 %.

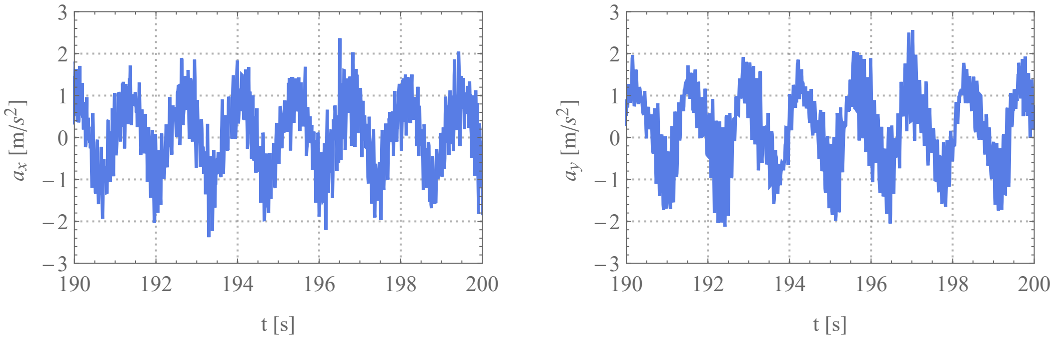

(a) Acceleration in the x-direction

(b) Acceleration in the y-direction

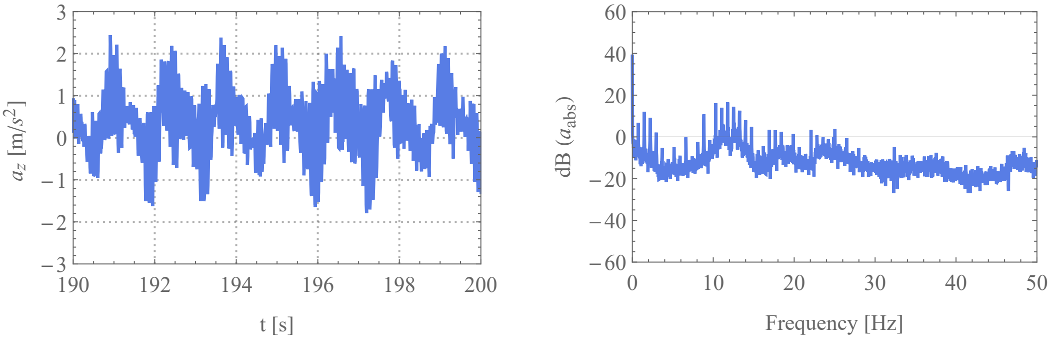

(c) Acceleration in the z-direction

(d) FFT of the absolute acceleration

Figure 3.21: Experimental results of the acceleration on the flat bar in the power take-off subsystem. The parameters of the pendulum energy harvester are: $l = 0.5$ m, $m = 1.32$ kg, $\xi_{14} = 0.0325$, $\xi_{23} = 0.0323$, $\Omega = 0.7375$ Hz, $A = 32$ mm, $R_P =$ NC, and $R_S = 10$ kΩ.

In Figure 3.21 the accelerations in the three directions and FFT analysis for the absolute acceleration are shown. The accelerometer is fitted on the lower flat bar of the power take-off subsystem for these measurements. The acceleration in the x-direction is shown in Figure 3.21a. The fundamental oscillation of the pendulum bob and the high frequency vibrations can be seen. These high frequency vibrations no longer have an effect on the movement of the pendulum bob and can therefore not be used to harvest energy. The acceleration in the y-direction is shown in Figure 3.21b. As in the acceleration in the x-direction in Figure 3.21a the oscillation of the pendulum bob and the high frequency vibrations of the flat bar can be seen in the y-direction as well. This indicates that the vibrations in the y-direction have an adverse effect on the energy harvesting. In Figure 3.21b the acceleration of the z-axis is shown. It can be seen that there is an overall positive offset in the y-direction of the diagram. The FFT of the absolute acceleration is shown in Figure 3.21d with the first peak at a frequency of 0.7371 Hz being attributed to the natural frequency of the pendulum energy harvester. The following peaks appear because of the parametric resonance. Two other local maxima are observed for the frequencies 11.46 Hz and 13.05 Hz. These are related to the higher frequency vibrations in the aluminium alloy flat bar. In a further development stage, the design of the flat bar should be examined as well with a special focus on reducing the vibrations. As before the percentage of the higher frequency oscillation above 7 Hz to the overall power of the vibrations is calculated with a value of 5.8 %.

Higher frequency vibrations within the design of the pendulum energy harvester can be seen, and it is certainly advisable to improve the design of the pendulum energy harvester in the following development step to minimise these effect. However, these vibrations do not effect the overall dynamics of the pendulum strongly and are therefore not further investigated here.

3.6 Comparison of the Numerical and Experimental Results

In Chapter 7 the numerical and experimental results are compared therefore clarifications are introduced here. Here the main points of the mathematical model are summarised. The detailed deviation of the mathematical model is shown in the following is discussed in greater detail in Chapter 4.

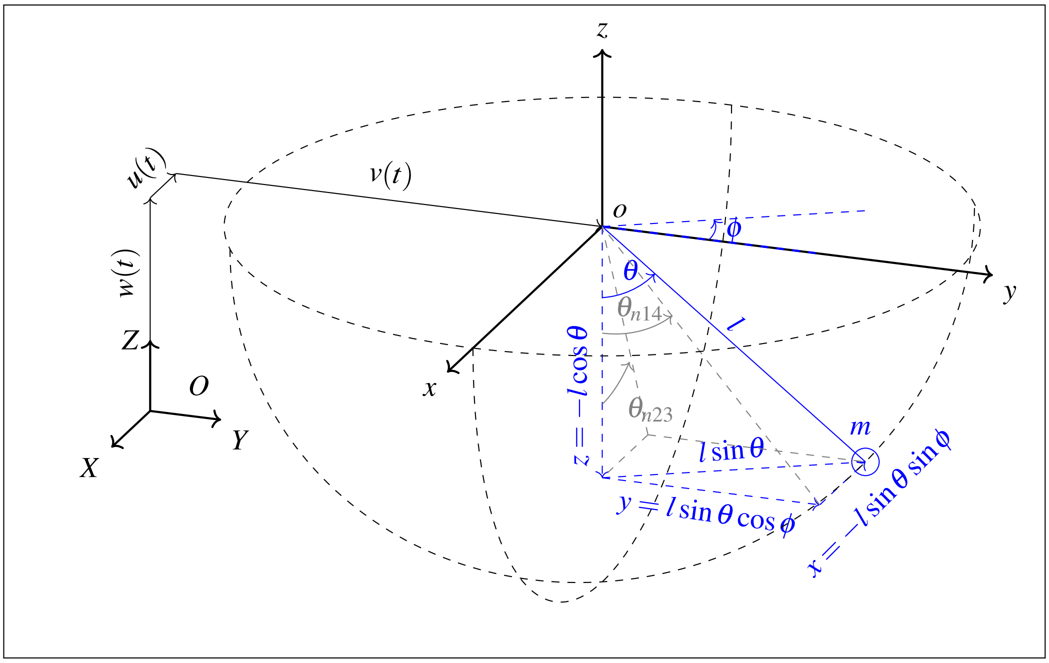

Figure 3.22: Diagram of a spherical pendulum with the kinematic relations and the conversion of numerical coordinates θ and ϕ to the numerically calculated and transformed experimental coordinates θ_{n14} and θ_{n23} and showing the limits of the spherical motion reached by the bob. Adapted from the previously published article related to this work [1]

In Figure 3.22 a schematic model of the omnidirectional pendulum energy harvester is shown. On the pivot of the pendulum the local coordinate system (o,x,y,z) is attached. The global coordinate system (O, X, Y, Z) is connected to the local coordinate system over the excitation force vectors $u(t)$, $v(t)$, and $w(t)$. For the numerical analysis the coordinates θ and ϕ are chosen. The are defined with the necessary kinematic relations. The other pair of shown coordinates θ_{n14} and θ_{n23} in Figure 3.22 relate directly to the experimental model, on the basis that the energy harvester uses two offset orthogonal shafts to provide the necessary geometrical freedom for spherical motion. The subscript n indicates that these coordinates are used for numerical analysis. When the subscript is absent this indicates that the coordinates are associated with the experimental system, see Figures 3.2a and 3.4. This notation is used throughout this work and allows a clear distinction between the experimental coordinates and the coordinates that are attributed to the numerical analysis. The relation between the numerical and experimental coordinates is shown in Equations (3.12) and (3.13).

$$\theta_{14} = \theta_{n14}. \tag{3.12}$$

$$\theta_{23} = \theta_{n23}. \tag{3.13}$$

To obtain the coordinates θ_{n14} and θ_{n23} the differential equations depending on the generalised coordinates θ and ϕ, described in greater detail in Chapter 4, are solved and then they are converted to the experimental coordinates in the next step with the Equations (3.14) and (3.15).

$$\theta_{n14} = \theta \sin(\phi). \tag{3.14}$$

$$\theta_{n23} = \theta \cos(\phi). \tag{3.15}$$

A similar conversion of the spherical coordinates has been considered by Ikeda, Harata, and Takeeda [114] as aleready described in the introduction Section 2.3.4.

Chapter 4

Mathematical Model of a Forced Spherical Pendulum with Active Power Take-Off

One of the aims of the work is to develop a mathematical model to determine the possibility of energy output from a spherical pendulum. For this purpose the spherical pendulum, introduced in Section 2.3.2, is extended by damping, excitation and active power take-off.

The calculation of the ordinary differential equations of the omnidirectional pendulum energy harvester was carried out by symbolic code written in *Wolfram Mathematica*® language and is uploaded to GitHub [138].

4.1 Development of the Mathematical Model of the Forced Spherical Pendulum

The mathematical model as described in Figure 4.1 is developed here as a damped forced system. The power take-off is developed later in Section 4.2.

In Figure 4.1 a schematic model of the spherical pendulum energy harvester is shown. The absolute frame (O,X,Y,Z) is connected to the local frame (o,x,y,z) by the vectors $u(t)$, $v(t)$, and $w(t)$, which excites the local system in the u, v, and w-directions (positive direction to the x, y, and z-axis). The coordinates θ and ϕ are the generalised coordinate chosen for the numerical analysis.

The kinematic relations from Figures 4.1, 4.2, and 4.3 are shown in Equations (4.1), (4.2), and (4.3). The kinematic relations are well known in the literature e.g. [57, 98, 111, 114].

$$x = -l \sin\theta \sin\phi, \tag{4.1}$$

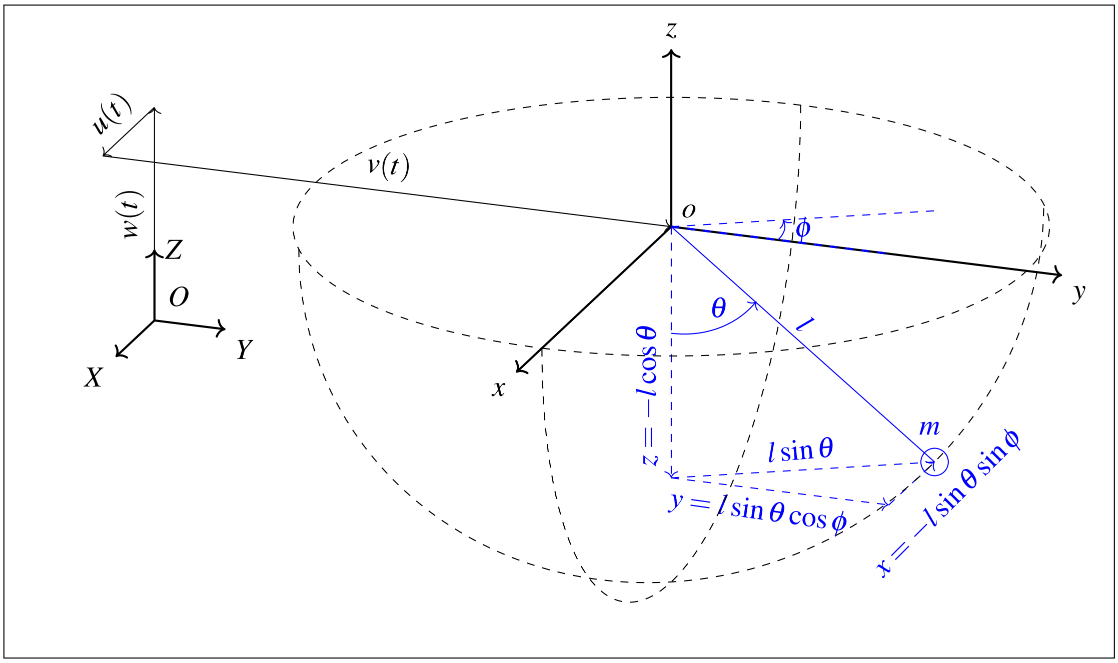

Figure 4.1: Diagram of a spherical pendulum with kinematics and excitation vectors. Adapted from the previously published work [1]

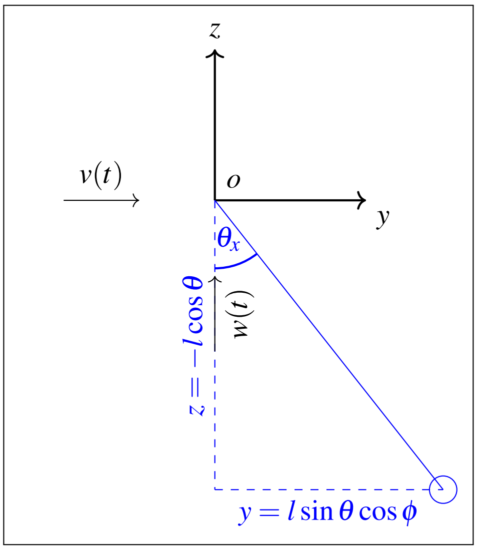

Figure 4.2: Diagram of a spherical pendulum in the yz-plane with kinematics and excitation vectors

$$y = l\sin\theta\cos\phi, \tag{4.2}$$

$$z = -l\cos\theta. \tag{4.3}$$

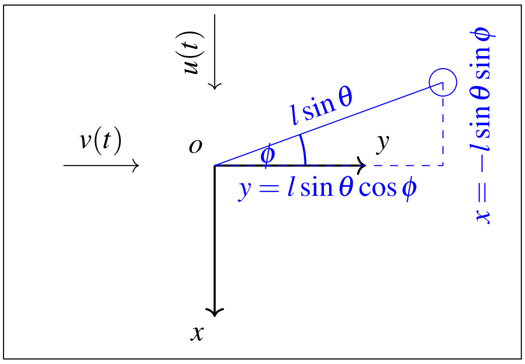

Figure 4.3: Diagram of a spherical pendulum in the xy-plane with kinematics and excitation vectors

Harmonic excitation functions of this sort are assumed, where U_0, V_0, and W_0 correspond to the peak excitation amplitudes and Ω_u, Ω_v, and Ω_w refer to the excitation frequencies.

$$u(t) = U_0\cos(\Omega_u t), \tag{4.4}$$

$$v(t) = V_0\cos(\Omega_v t), \tag{4.5}$$

$$w(t) = W_0\cos(\Omega_w t). \tag{4.6}$$

The linear undamped natural frequency (4.7) of a simple pendulum is introduced for the calculations.

$$\omega_n = \sqrt{\frac{g}{l}}. \tag{4.7}$$

After differentiating the kinematic relations in Equations (4.1) to (4.3) and the harmonic excitations functions in Equations (4.4) to (4.6) with respect to time, the functions are introduced into the equations for the potential and kinetic energy.

$$U = mgz(t) - mgw(t) = -mgl\cos\theta(t) + mgW_0\cos(\Omega_w t). \tag{4.8}$$

$$\begin{aligned} T &= 0.5m((\dot{x}(t)+\dot{u}(t))^2 + (\dot{y}(t)+\dot{v}(t))^2 + (\dot{z}(t)+\dot{w}(t))^2) \\ &= 0.5m\Bigg(\Big(l\dot{\theta}(t)\cos(\theta(t))\sin(\phi(t)) + l\sin(\theta(t))\dot{\phi}(t)\cos(\phi(t)) \\ &+ U_0\Omega_u\sin(\Omega_u t)\Big)^2 + \Big(-l\dot{\theta}(t)\cos(\theta(t))\cos(\phi(t)) \\ &+ l\sin(\theta(t))\dot{\phi}(t)\sin(\phi(t)) + V_0\Omega_v\sin(\Omega_v t)\Big)^2 \\ &+ \Big(-l\dot{\theta}(t)\sin(\theta(t)) + W_0\Omega_w\sin(\Omega_w t)\Big)^2\Bigg). \end{aligned} \tag{4.9}$$

In the following, the Lagrange equation of the second kind is shown.

$$\frac{d}{dt}\left(\frac{\partial T}{\partial \dot{q}}\right) - \frac{\partial T}{\partial q} + \frac{\partial U}{\partial q} = Q_q. \tag{4.10}$$

Therefore, Equation (4.9) is differentiated with respect to $\dot{\theta}(t)$.

$$\begin{aligned}\frac{\partial T}{\partial \dot{\theta}(t)} = lm\Big(& l\dot{\theta}(t) + U_0\Omega_u \cos(\theta(t))\sin(\phi(t))\sin(\Omega_u t) \\ & - V_0\Omega_v \cos(\theta(t))\cos(\phi(t))\sin(\Omega_v t) - W_0\Omega_w \sin(\theta(t))\sin(\Omega_w t)\Big).\end{aligned} \tag{4.11}$$

Differentiating Equation (4.11) with respect to time gives:

$$\begin{aligned}\frac{d}{dt}\left(\frac{\partial T}{\partial \dot{\theta}(t)}\right) = lm\Bigg(& l\ddot{\theta}(t) + U_0\Omega_u(\sin(\Omega_u t) \\ & \times \Big(\cos(\theta(t))\dot{\phi}(t)\cos(\phi(t)) - \dot{\theta}(t)\sin(\theta(t))\sin(\phi(t))\Big) \\ & + \Omega_u \cos(\theta(t))\sin(\phi(t))\cos(\Omega_u t)) \\ & + V_0\Omega_v(\sin(\Omega_v t)(\dot{\theta}(t)\sin(\theta(t))\cos(\phi(t)) \\ & + \cos(\theta(t))\dot{\phi}(t)\sin(\phi(t))) - \Omega_v\cos(\theta(t))\cos(\phi(t))\cos(\Omega_v t)) \\ & - W_0\Omega_w\dot{\theta}(t)\cos(\theta(t))\sin(\Omega_w t) - W_0\Omega_w^2\sin(\theta(t))\cos(\Omega_w t)\Bigg).\end{aligned} \tag{4.12}$$

Then differentiating Equation (4.9) with respect to the coordinate $\theta(t)$:

$$\begin{aligned}\frac{\partial T}{\partial \theta(t)} = lm\Big(& 0.5l\sin(2\theta(t))\dot{\phi}(t)^2 + U_0\Omega_u\sin(\Omega_u t)(\cos(\theta(t))\dot{\phi}(t)\cos(\phi(t)) \\ & - \dot{\theta}(t)\sin(\theta(t))\sin(\phi(t))) + V_0\Omega_v\sin(\Omega_v t)(\dot{\theta}(t)\sin(\theta(t))\cos(\phi(t)) \\ & + \cos(\theta(t))\dot{\phi}(t)\sin(\phi(t))) - W_0\Omega_w\dot{\theta}(t)\cos(\theta(t))\sin(\Omega_w t)\Big).\end{aligned} \tag{4.13}$$

The potential energy (4.8) is differentiated with respect to the coordinate $\theta(t)$.

$$\frac{\partial U}{\partial \theta(t)} = glm\sin(\theta(t)). \tag{4.14}$$

After introducing Equations (4.12), (4.13), and (4.14) into Equation (4.10) the equation of motion (EoM) with respect to the coordinate θ is obtained.

$$
\begin{aligned}
& glm\sin(\theta(t)) - lm(0.5l\sin(2\theta(t))\dot{\phi}(t)^2 + U_0\Omega_u\sin(\Omega_u t)\Big(\cos(\theta(t))\dot{\phi}(t)\cos(\phi(t)) \\
& - \dot{\theta}(t)\sin(\theta(t))\sin(\phi(t))\Big) + V_0\Omega_v\sin(\Omega_v t)\Big(\dot{\theta}(t)\sin(\theta(t))\cos(\phi(t)) \\
& + \cos(\theta(t))\dot{\phi}(t)\sin(\phi(t))\Big) - W_0\Omega_w\dot{\theta}(t)\cos(\theta(t))\sin(\Omega_w t)) \\
& + lm(l\ddot{\theta}(t) + U_0\Omega_u(\sin(\Omega_u t)\Big(\cos(\theta(t))\dot{\phi}(t)\cos(\phi(t)) - \dot{\theta}(t)\sin(\theta(t))\sin(\phi(t))\Big) \\
& + \Omega_u\cos(\theta(t))\sin(\phi(t))\cos(\Omega_u t)) + V_0\Omega_v(\sin(\Omega_v t)(\dot{\theta}(t)\sin(\theta(t))\cos(\phi(t)) \\
& + \cos(\theta(t))\dot{\phi}(t)\sin(\phi(t))) - \Omega_v\cos(\theta(t))\cos(\phi(t))\cos(\Omega_v t)) \\
& - W_0\Omega_w\dot{\theta}(t)\cos(\theta(t))\sin(\Omega_w t) - W_0\Omega_w^2\sin(\theta(t))\cos(\Omega_w t)) + Q_\theta \\
& = lm\Big(g\sin(\theta(t)) + l\ddot{\theta}(t) - 0.5l\sin(2\theta(t))\dot{\phi}(t)^2 + U_0\Omega_u^2\cos(\theta(t))\sin(\phi(t))\cos(\Omega_u t) \\
& - V_0\Omega_v^2\cos(\theta(t))\cos(\phi(t))\cos(\Omega_v t) - W_0\Omega_w^2\sin(\theta(t))\cos(\Omega_w t)\Big) + Q_\theta .
\end{aligned}
\tag{4.15}
$$

After collecting terms from Equation (4.15) and ordering them and subsequently dividing by ml^2 gives the equation of motion (4.16) for the coordinate θ.

$$
\begin{aligned}
& \ddot{\theta}(t) + \frac{g\sin(\theta(t))}{l} - \sin(\theta(t))\cos(\theta(t))\dot{\phi}(t)^2 \\
& \quad = -\frac{U_0\Omega_u^2\cos(\theta(t))\sin(\phi(t))\cos(\Omega_u t)}{l} + \frac{V_0\Omega_v^2\cos(\theta(t))\cos(\phi(t))\cos(\Omega_v t)}{l} \\
& \quad + \frac{W_0\Omega_w^2\sin(\theta(t))\cos(\Omega_w t)}{l} + \hat{Q}_\theta .
\end{aligned}
\tag{4.16}
$$

The damping term (4.17) is introduced in Equation (4.16) to make the equation more comparable to real life conditions.

$$
C_\theta = 2\xi_\theta\omega_n, \tag{4.17}
$$

This gives the equation of motion (4.18) with an included damping term for the coordinate θ.

$$
\begin{aligned}
& \ddot{\theta}(t) + 2\xi_\theta\omega_n\dot{\theta}(t) + \frac{g\sin(\theta(t))}{l} - \sin(\theta(t))\cos(\theta(t))\dot{\phi}(t)^2 \\
& \quad = -\frac{U_0\Omega_u^2\cos(\theta(t))\sin(\phi(t))\cos(\Omega_u t)}{l} + \frac{V_0\Omega_v^2\cos(\theta(t))\cos(\phi(t))\cos(\Omega_v t)}{l} \\
& \quad + \frac{W_0\Omega_w^2\sin(\theta(t))\cos(\Omega_w t)}{l} + \hat{Q}_\theta .
\end{aligned}
\tag{4.18}
$$

The kinematic energy (4.9) is derived with respect to the coordinate $\phi(t)$.

$$\begin{aligned} \frac{\partial T}{\partial \dot{\phi}(t)} = {} & lm\sin(\theta(t))(l\sin(\theta(t))\dot{\phi}(t) + U_0\Omega_u\cos(\phi(t))\sin(t\Omega_u) \\ & + V_0\Omega_v\sin(\phi(t))\sin(\Omega_v t)). \end{aligned} \tag{4.19}$$

Differentiating Equation (4.19) with respect to time gives:

$$\begin{aligned} \frac{d}{dt}\left(\frac{\partial T}{\partial \dot{\phi}(t)}\right) = {} & lm\Bigg(l\dot{\theta}(t)\sin(2\theta(t))\dot{\phi}(t) + l\sin^2(\theta(t))\ddot{\phi}(t) \\ & + U_0\Omega_u(\sin(\Omega_u t)(\dot{\theta}(t)\cos(\theta(t))\cos(\phi(t)) - \sin(\theta(t))\dot{\phi}(t)\sin(\phi(t))) \\ & + \Omega_u\sin(\theta(t))\cos(\phi(t))\cos(\Omega_u t)) \\ & + V_0\Omega_v\Big(\sin(\Omega_v t)(\theta'(t)\cos(\theta(t))\sin(\phi(t)) \\ & + \sin(\theta(t))\dot{\phi}(t)\cos(\phi(t))) + \Omega_v\sin(\theta(t))\sin(\phi(t))\cos(t\Omega_v)\Big)\Bigg). \end{aligned} \tag{4.20}$$

Then differentiating Equation (4.9) with respect to the coordinate $\phi(t)$:

$$\begin{aligned} \frac{\partial T}{\partial \phi(t)} = {} & lm\Bigg(U_0\Omega_u\sin(\Omega_u t)(\dot{\theta}(t)\cos(\theta(t))\cos(\phi(t)) \\ & - \sin(\theta(t))\dot{\phi}(t)\sin(\phi(t))) + V_0\Omega_v\sin(\Omega_v t)\Big(\dot{\theta}(t)\cos(\theta(t))\sin(\phi(t)) \\ & + \sin(\theta(t))\dot{\phi}(t)\cos(\phi(t))\Big)\Bigg). \end{aligned} \tag{4.21}$$

The potential energy (4.8) is derived with respect to the coordinate $\phi(t)$

$$\frac{\partial U}{\partial \phi(t)} = 0. \tag{4.22}$$

Introducing Equations (4.20), (4.21), and (4.22) into Equation (4.10) gives the EoM with respect to the coordinate ϕ.

$$\begin{aligned}
&lm\Bigg(l\dot{\theta}(t)\sin(2\theta(t))\dot{\phi}(t) + l\sin^2(\theta(t))\ddot{\phi}(t)\\
&+ U_0\Omega_u(\sin(\Omega_u t)\Big(\dot{\theta}(t)\cos(\theta(t))\cos(\phi(t)) - \sin(\theta(t))\dot{\phi}(t)\sin(\phi(t))\Big)\\
&+ \Omega_u\sin(\theta(t))\cos(\phi(t))\cos(\Omega_u t)) + V_0\Omega_v\Big(\sin(\Omega_v t)(\dot{\theta}(t)\cos(\theta(t))\sin(\phi(t))\\
&+ \sin(\theta(t))\dot{\phi}(t)\cos(\phi(t))) + \Omega_v\sin(\theta(t))\sin(\phi(t))\cos(\Omega_v t)\Big)\Bigg)\\
&- lm\Bigg(U_0\Omega_u\sin(\Omega_u t)(\dot{\theta}(t)\cos(\theta(t))\cos(\phi(t)) - \sin(\theta(t))\dot{\phi}(t)\sin(\phi(t)))\\
&+ V_0\Omega_v\sin(\Omega_v t)\Big(\dot{\theta}(t)\cos(\theta(t))\sin(\phi(t)) + \sin(\theta(t))\dot{\phi}(t)\cos(\phi(t))\Big)\Bigg) + Q_\phi\\
&= lm\sin(\theta(t))\Big(2l\dot{\theta}(t)\cos(\theta(t))\dot{\phi}(t) + l\sin(\theta(t))\ddot{\phi}(t) + U_0\Omega_u^2\cos(\phi(t))\cos(\Omega_u t)\\
&+ V_0\Omega_v^2\sin(\phi(t))\cos(\Omega_v t)\Big) + Q_\phi.
\end{aligned}\tag{4.23}$$

Thus, after ordering terms in Equation (4.23) and dividing by $ml^2\sin^2(\theta(t))$ the EoM for the coordinate ϕ is obtained.

$$\begin{aligned}
&\ddot{\phi}(t) + \frac{2\dot{\theta}(t)\cos(\theta(t))\dot{\phi}(t)}{\sin(\theta(t))}\\
&\qquad = -\frac{U_0\Omega_u^2\cos(\phi(t))\cos(\Omega_u t)}{l\sin(\theta(t))} - \frac{V_0\Omega_v^2\sin(\phi(t))\cos(\Omega_v t))}{l\sin(\theta(t))} + \hat{Q}_\phi.
\end{aligned}\tag{4.24}$$

The damping term (4.25) is introduced in Equation (4.24) to make the equations more comparable to the real life conditions.

$$C_\phi = 2\xi_\phi\omega_n, \tag{4.25}$$

This gives the equation of motion (4.26) with a damping term for the coordinate ϕ.

$$\begin{aligned}
&\ddot{\phi}(t) + \frac{2\xi_\phi\omega_n}{\sin^2(\theta(t))}\dot{\phi}(t) + \frac{2\dot{\theta}(t)\cos(\theta(t))\dot{\phi}(t)}{\sin(\theta(t))}\\
&\qquad = -\frac{U_0\Omega_u^2\cos(\phi(t))\cos(\Omega_u t)}{l\sin(\theta(t))} - \frac{V_0\Omega_v^2\sin(\phi(t))\cos(\Omega_v t))}{l\sin(\theta(t))} + \hat{Q}_\phi.
\end{aligned}\tag{4.26}$$

4.2 Introduction of an Active Power Take-Off Term

The literature shows different approaches for the modulation of active power take-off terms. In the following two sensible approaches with respect to this work are introduced.

4.2.1 Power Take-Off with a Sign Function

The square wave functions in Equation (4.27) applies a defined torque (T) in the opposite direction to the velocity. This models the force that is applied by the generator when energy is converted from the system. McRobb's thesis describes a power take-off with a square wave form for a planar pendulum [57]. Similar power take-off is introduced by Watt and Cartmell [152]

$$\begin{aligned} L_{\mathrm{sq}\theta} &= -T_\theta \operatorname{sgn}(\dot{\theta}(t)), \\ L_{\mathrm{sq}\phi} &= -T_\phi \operatorname{sgn}(\dot{\phi}(t)). \end{aligned} \tag{4.27}$$

The external torque in Equation (4.27), is introduced in Equations (4.18) and (4.26). For this Equations (4.27) are divided by ml^2 and by $ml^2 \sin^2(\theta(t))$, respectively. This gives the equations of motion for the coordinates θ (4.28) and the coordinate ϕ (4.29) with an active power take-off term.

$$\begin{aligned} &\ddot{\theta}(t) + 2\xi_\theta \omega_n \dot{\theta}(t) + \frac{g\sin(\theta(t))}{l} - \sin(\theta(t))\cos(\theta(t))\dot{\phi}(t)^2 \\ &\quad = -\frac{U_0\Omega_u^2 \cos(\theta(t))\sin(\phi(t))\cos(\Omega_u t)}{l} + \frac{V_0\Omega_v^2 \cos(\theta(t))\cos(\phi(t))\cos(\Omega_v t)}{l} \\ &\quad + \frac{W_0\Omega_w^2 \sin(\theta(t))\cos(\Omega_w t)}{l} - \frac{T_\theta \operatorname{sgn}(\dot{\theta}(t))}{ml^2}. \end{aligned} \tag{4.28}$$

$$\begin{aligned} &\ddot{\phi}(t) + \frac{2\xi_\phi \omega_n}{\sin^2(\theta(t))}\dot{\phi}(t) + \frac{2\dot{\theta}(t)\cos(\theta(t))\dot{\phi}(t)}{\sin(\theta(t))} \\ &\quad = -\frac{U_0\Omega_u^2 \cos(\phi(t))\cos(\Omega_u t)}{l\sin(\theta(t))} - \frac{V_0\Omega_v^2 \sin(\phi(t))\cos(\Omega_v t))}{l\sin(\theta(t))} \\ &\quad - \frac{T_\phi \operatorname{sgn}(\dot{\phi}(t))}{ml^2\sin^2(\theta(t))}. \end{aligned} \tag{4.29}$$

4.2.2 Power Take-Off with an Arctangent Function

In the appendix of McRobb's PhD thesis a different power take-off term is introduced [57] this procedure is similar to the power take-off term introduced by Watt and Cartmell [152]. It is basically a square wave function with rounded-off edges, mathematically this is represented with an Arctangent function (4.30). With the help of the torque T and the $\frac{2}{\pi}$ the amplitude of the power take-off is determined. The small parameter $\varepsilon_{\mathrm{r}} < 1$ and in most cases $\varepsilon_{\mathrm{r}} << 1$

determines the radius of the corners.

$$
\begin{aligned}
L_{\mathrm{arct}\theta} &= -\frac{2T_\theta}{\pi}\tan^{-1}\left(\frac{\dot{\theta}(t)}{\varepsilon_{\mathrm{r}}}\right),\\
L_{\mathrm{arct}\phi} &= -\frac{2T_\phi}{\pi}\tan^{-1}\left(\frac{\dot{\phi}(t)}{\varepsilon_{\mathrm{r}}}\right).
\end{aligned}
\tag{4.30}
$$

The external torque in Equation (4.30), is introduced in Equations (4.18) and (4.26). For this the Equations (4.30) are divided by ml^2 and by $ml^2\sin^2(\theta(t))$, respectively. This gives the equation of motion for the coordinate θ (4.31) and the coordinate ϕ (4.32) for a spherical pendulum with an active power take-off term.

$$
\begin{aligned}
&\ddot{\theta}(t) + 2\xi_\theta\omega_n\dot{\theta}(t) + \frac{g\sin(\theta(t))}{l} - \sin(\theta(t))\cos(\theta(t))\dot{\phi}(t)^2\\
&\quad = -\frac{U_0\Omega_u^2\cos(\theta(t))\sin(\phi(t))\cos(\Omega_u t)}{l} + \frac{V_0\Omega_v^2\cos(\theta(t))\cos(\phi(t))\cos(\Omega_v t)}{l}\\
&\quad + \frac{W_0\Omega_w^2\sin(\theta(t))\cos(\Omega_w t)}{l} - \frac{2T_\theta}{\pi ml^2}\tan^{-1}\left(\frac{\dot{\theta}(t)}{\varepsilon_{\mathrm{r}}}\right).
\end{aligned}
\tag{4.31}
$$

$$
\begin{aligned}
&\ddot{\phi}(t) + \frac{2\xi_\phi\omega_n}{\sin^2(\theta(t))}\dot{\phi}(t) + \frac{2\dot{\theta}(t)\cos(\theta(t))\dot{\phi}(t)}{\sin(\theta(t))}\\
&\quad = -\frac{U_0\Omega_u^2\cos(\phi(t))\cos(\Omega_u t)}{l\sin(\theta(t))} - \frac{V_0\Omega_v^2\sin(\phi(t))\cos(\Omega_v t))}{l\sin(\theta(t))}\\
&\quad - \frac{2T_\phi}{\pi ml^2\sin^2(\theta(t))}\tan^{-1}\left(\frac{\dot{\phi}(t)}{\varepsilon_{\mathrm{r}}}\right).
\end{aligned}
\tag{4.32}
$$

The power take-off in the direction of the coordinate ϕ is included for the sake of completeness. But a power take-off in the direction of the coordinate ϕ is highly limited in its usability in the numerical analysis and is therefore not considered here. This is attributed to the missing of the restoring force term in the ordinary differential equation of the coordinate ϕ.

4.3 Nondimensionalization

Introducing the dimensionless time and dimensionless parameters to reduce scaling effects.

$$
\begin{aligned}
&\tau = \omega_0 t, && \omega_0^2 = \tfrac{g}{l}, && \alpha_\theta = 2\xi_\theta\tfrac{\omega_n}{\omega_0}, && \alpha_\phi = 2\xi_\phi\tfrac{\omega_n}{\omega_0},\\
&a_u = \tfrac{U_0}{l}, && a_v = \tfrac{V_0}{l}, && a_w = \tfrac{W_0}{l}, && \beta_u = \tfrac{\Omega_u}{\omega_0},\\
&\beta_v = \tfrac{\Omega_v}{\omega_0}, && \beta_w = \tfrac{\Omega_w}{\omega_0}, && P_\theta = \tfrac{T_\theta}{ml^2\omega_0^2}, && P_\phi = \tfrac{T_\phi}{ml^2\omega_0^2}.
\end{aligned}
\tag{4.33}
$$

Equations (4.28) and (4.29) with the Sign power take-off term are transformed to the dimensionless form. This gives the following dimensionless equations of motion for the coordinate

θ (4.34) and the coordinate ϕ (4.35) for a spherical pendulum with an active power take-off term based on a sgn function.

$$\begin{aligned}
&\ddot{\theta}(\tau)+\alpha_\theta\dot{\theta}(\tau)-\sin(\theta(\tau))\cos(\theta(\tau))\dot{\phi}(\tau)^2+\sin(\theta(\tau))\\
&\quad=-a_u\beta_u^2\cos(\theta(\tau))\sin(\phi(\tau))\cos(\beta_u\tau)+a_v\beta_v^2\cos(\theta(\tau))\cos(\phi(\tau))\cos(\beta_v\tau)\\
&\quad+a_w\beta_w^2\sin(\theta(\tau))\cos(\beta_w\tau)-P_\theta\operatorname{sgn}(\dot{\theta}(\tau)).
\end{aligned}\tag{4.34}$$

$$\begin{aligned}
&\ddot{\phi}(\tau)+\frac{\alpha_\phi}{\sin^2(\theta(\tau))}\dot{\phi}(\tau)+\frac{2\dot{\theta}(\tau)\cos(\theta(\tau))\dot{\phi}(\tau)}{\sin(\theta(\tau))}\\
&\quad=-a_u\beta_u^2\frac{\cos(\phi(\tau))}{\sin(\theta(\tau))}\cos(\beta_u\tau)-a_v\beta_v^2\frac{\sin(\phi(\tau))}{\sin(\theta(\tau))}\cos(\beta_v\tau)\\
&\quad-P_\phi\frac{\operatorname{sgn}(\dot{\phi}(\tau))}{\sin^2(\theta(\tau))}.
\end{aligned}\tag{4.35}$$

Equations (4.31) and (4.32) with the arctangent power take-off term are transformed to the dimensionless form. This gives the alternative dimensionless equations of motion for the coordinate θ (4.36) and the coordinate ϕ (4.37) for a spherical pendulum with an active power take-off term applying the arctangent function.

$$\begin{aligned}
&\ddot{\theta}(\tau)+\alpha_\theta\dot{\theta}(\tau)-\sin(\theta(\tau))\cos(\theta(\tau))\dot{\phi}(\tau)^2+\sin(\theta(\tau))\\
&\quad=-a_u\beta_u^2\cos(\theta(\tau))\sin(\phi(\tau))\cos(\beta_u\tau)+a_v\beta_v^2\cos(\theta(\tau))\cos(\phi(\tau))\cos(\beta_v\tau)\\
&\quad+a_w\beta_w^2\sin(\theta(\tau))\cos(\beta_w\tau)-\frac{2P_\theta}{\pi}\tan^{-1}\left(\frac{\dot{\theta}(\tau)}{\varepsilon_\mathrm{r}}\right).
\end{aligned}\tag{4.36}$$

$$\begin{aligned}
&\ddot{\phi}(\tau)+\frac{\alpha_\phi}{\sin^2(\theta(\tau))}\dot{\phi}(\tau)+\frac{2\dot{\theta}(\tau)\cos(\theta(\tau))\dot{\phi}(\tau)}{\sin(\theta(\tau))}\\
&\quad=-a_u\beta_u^2\frac{\cos(\phi(\tau))}{\sin(\theta(\tau))}\cos(\beta_u\tau)-a_v\beta_v^2\frac{\sin(\phi(\tau))}{\sin(\theta(\tau))}\cos(\beta_v\tau)\\
&\quad-\frac{2P_\phi}{\pi\sin^2(\theta(\tau))}\tan^{-1}\left(\frac{\dot{\phi}(\tau)}{\varepsilon_\mathrm{r}}\right).
\end{aligned}\tag{4.37}$$

It should be noted that Equations (4.34) and (4.36) are completely identical, except for the power take-off term. The same applies to Equations (4.35) and (4.37).

Chapter 5

Numerical Analysis

Hereinafter, the dimensionless differential equations are solved with the NDSolve function available in the *Wolfram Mathematica*® language. The decision as to which power take-off term is more feasible for the numerical analysis is postponed to Section 5.2. For the numerical evaluation, the dimensionless differential Equations (4.36) and (4.37) were used if not indicated otherwise. Therefore, all shown figures in this section are with dimensionless parameters. In the following figures that consider ranges for the excitation amplitude a which correspond to $a = a_u = a_v = a_w$ and excitation frequency β which correspond to $\beta = \beta_u = \beta_v = 0.5\beta_w$ if not indicated otherwise. A variation occurs, for example, in Section 5.1.2 where the spherical pendulum is not excited in all directions. After a study of the initial conditions (ICs), this gives two critical cases which are to be avoided. The numerical analysis cannot be started at the equilibrium point for a value of $\theta = 0$ because of the existing singularity at this point. Another extreme case is when the ICs are selected too high, this results in a displacement of the coordinate θ by 2π and a displacement of π for the coordinate ϕ [1]. Therefore the initial conditions are set to the following somewhat arbitrary but practically achievable values: $\theta(0) = 0.42$, $\dot{\theta}(0) = 0.42$, $\phi(0) = 0.42$ and $\dot{\phi}(0) = 0.42$. The excitation amplitude, excitation frequency, and damping ratios are kept at the same value or in the general area as for the experiments to ensure comparability. Even though the experiments are limited to one excitation, the numerical analysis allows an excitation in more directions and to make use of the full potential of the mathematical model this is used whenever it is needed.

The content of the numerical analysis section is examining the dynamics of the system without power take-off, then the power take-off is introduced, and the same dynamics are compared with a switched on power take-off. Additionally, the potential power output of the energy harvester is compared over different forcing parameters and power take-off torques.

The numerical analysis section included a large parameter study to examine the effect of the changed parameters on the dynamics of the system. To increase the readability of the thesis summary paragraphs and paragraphs that compared the figures with and without power take-off were added to the end of each subsection.

5.1 Dynamics of the Spherical Pendulum without a Power Take-Off

The spherical pendulum without a power take-off is extensively investigated in this section. It is crucial to understand the dynamics of the system and to validate the mathematical model without a power take-off. Successively, a variation of the excitation direction, excitation amplitude, and excitation frequencies are examined. The section concludes with an investigation of the nonlinear dynamics of the system in terms of quasi-periodicity and chaotic dynamics.

5.1.1 Trajectories of the Spherical Pendulum

The spherical pendulum is represented by the generalised coordinates θ and ϕ which are basically polar coordinates. To get a first general overview the coordinates θ and ϕ can be transformed into Cartesian coordinates with Equations (4.4) to (4.6) and therefore the 2D and 3D trajectories of the pendulum bob can be illustrated. This then gives the trajectory in the *xy*-plane, see Figure 5.1a for a pendulum that is forced in one horizontal direction. The trajectory shows a flower-like shape with a change of the rotational angle ϕ with each swing. In Figure 5.1b the three-dimensional trajectory is shown. It can be seen that even though only one excitation in the horizontal direction is applied, the motion is not periodic.

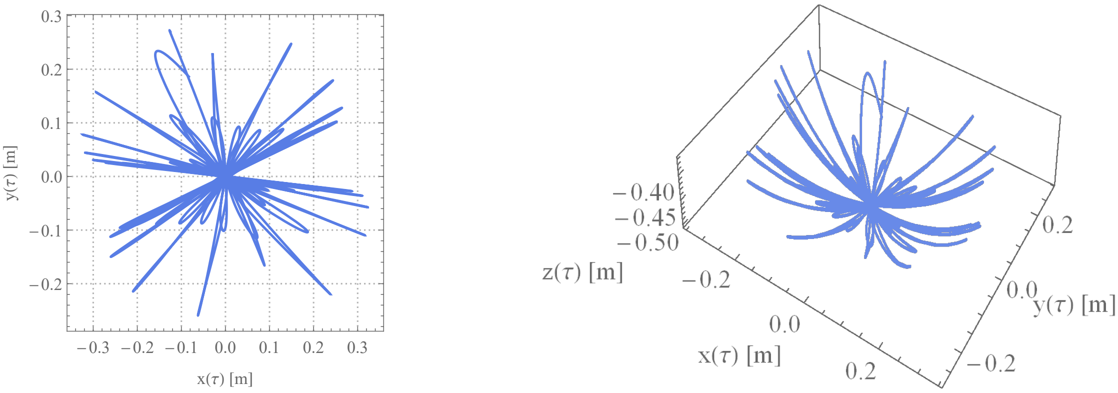

(a) Trajectory of the pendulum bob in the *xy*-plane

(b) 3D trajectory of the pendulum bob

Figure 5.1: Trajectory of the pendulum bob in different planes with the parameters set to: $l = 0.5$ kg, $m = 1.32$ kg, $g = 9.81\ \frac{\mathrm{m}}{\mathrm{s}^2}$, $\alpha_\theta = \alpha_\phi = 0.0648$, $a_u = 0.064$, $a_v = a_w = 0$, $\beta_u = 1$, $\beta_v = 0.5\beta_w = 0$, and $P_\theta = P_\phi = 0$.

5.1.2 Excitation in Different Directions

Although the experimental investigation of the energy harvester is limited to one horizontal degree of freedom for the excitation, it is advantageous to investigate a coupled excitation in the numerical analysis. But first the focus is on a single direction excited system. Figure 5.2

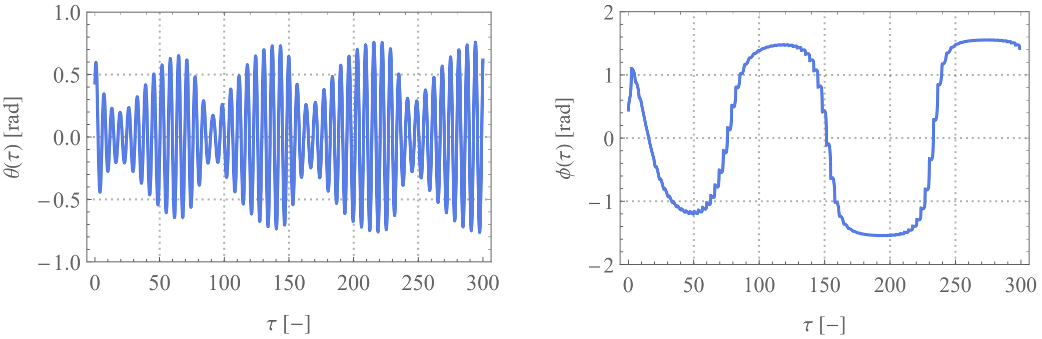

(a) θ over τ with $a_u = 0.064$ and $a_v = a_w = 0$ (b) ϕ over τ with $a_u = 0.064$ and $a_v = a_w = 0$

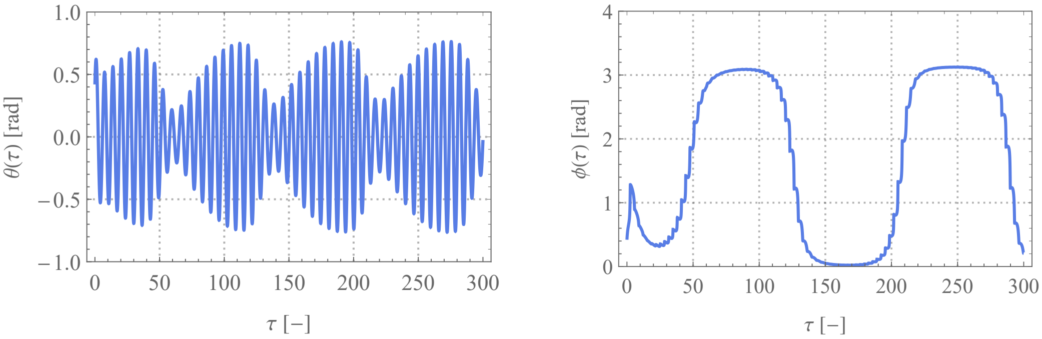

(c) θ over τ with $a_v = 0.064$ and $a_u = a_w = 0$ (d) ϕ over τ with $a_v = 0.064$ and $a_u = a_w = 0$

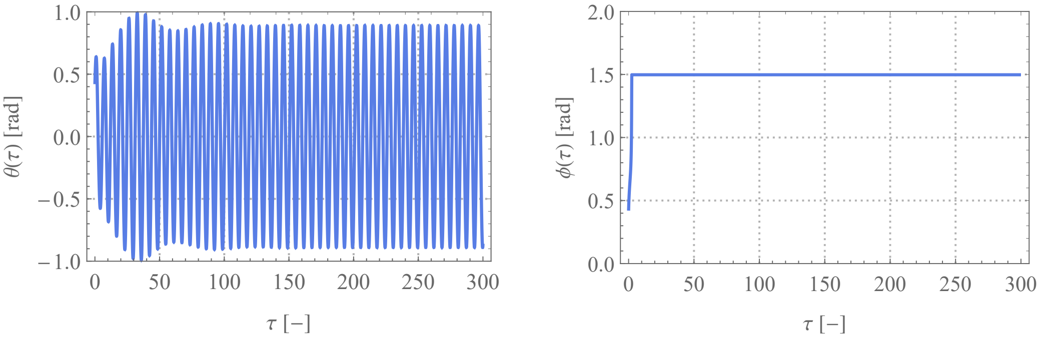

(e) θ over τ with $a_w = 0.064$ and $a_u = a_v = 0$ (f) ϕ over τ with $a_w = 0.064$ and $a_u = a_v = 0$

Figure 5.2: θ and ϕ over τ for a variation of the excitation direction with the parameters set to: $l = 0.5$ m, $m = 1.32$ kg, $g = 9.81\ \frac{\mathrm{m}}{\mathrm{s}^2}$, $\alpha_\theta = \alpha_\phi = 0.0648$, $\beta_u = \beta_v = 0.5\beta_w = 1$, and $P_\theta = P_\phi = 0$.

shows the diagrams for the generalised coordinates θ and ϕ of the spherical pendulum that is excited in all three directions subsequently. Figures 5.2a and 5.2b show the deflections of the coordinates θ and ϕ for an excitation along the x-axis (u-direction) of the coordinate system. This horizontal excitation leads to an oscillation of the coordinate θ that is not periodic but instead changes the level of the amplitude with a low frequency oscillation. Without further analysis it is not possible to directly identify the dynamics however it can be assumed that quasi-periodic dynamics are present. The missing restoring force term in the differential equations for the coordinate ϕ is the term that mainly influences the dynamics of coordinate ϕ. This gives interesting and sometimes even surprising movement patterns which will be discussed in the course of this section. For the coordinate ϕ in Figure 5.2b an oscillation-like movement is formed that shows movement with a very low frequency is prevailing. The results for the other horizontal excitation in direction of the y-axis (v-direction) of the coordinate system in Figures 5.2c and 5.2d show similar dynamics as the excitation in the x-direction.

When the spherical pendulum is forced only in the vertical direction (z-axis or w-direction), the dynamics of the system change, the coordinate θ in Figure 5.2f shows periodic dynamics after the transient response is decayed. The coordinate ϕ in Figure 5.2f shows a constant value of 1.5 rad when the steady-state response is reached.

Figure 5.3 shows the generalised coordinates θ and ϕ over the dimensionless time of the spherical pendulum with coupled excitation. In Figures 5.3a and 5.3b the spherical pendulum is forced in both horizontal directions u and v. The coordinate θ shows an oscillation where the deflection changes with each oscillation. The change in the amplitude resembles a low-frequency sinusoidal oscillation and this is an indication of quasi-periodicity. For the coordinate ϕ the dynamics show a low-frequency oscillation with abrupt changes in deflection. When the system is excited in one horizontal (u-direction) and one vertical direction (w-direction) the dynamics change to periodic dynamics after the transient response decayed for the coordinate θ see Figure 5.3c. The coordinate ϕ in Figure 5.3d shows a steady-state value of $\phi = -1.56$ rad. This indicates that the dynamics in the steady-state are those of a simple pendulum.

The excitation in three directions in Figure 5.3e shows similar results for the coordinate θ with periodic dynamics after the transient response decayed. In Figure 5.3f the dynamics of the coordinate ϕ are shown. At the beginning of the figure, it looks as if the value is approaching a fixed value, as can be seen in the figure above. However, the dynamics are very irregular and move with a high frequency harmonic along a line that appears to move with no clear structure. Generally, it can be stated that when the system is excited vertically, or coupled with a vertical part, it is in general more likely to show periodic dynamics compared to an excitation without a vertical component.

5.1.3 Variation of the Excitation Amplitude

To get a greater overview of the dynamics of the energy harvester, bifurcation diagrams are compared in the following. Figure 5.4 shows bifurcation diagrams with the excitation amplitude as control parameter. The bifurcation diagrams in the left column show the spherical pendulum that is excited in the u-direction and the figures in the right column show the spherical pendulum that is excited in the v-direction. In Figure 5.4a the system is excited with an excitation frequency of $\beta = 0.9$. With an increase in the excitation amplitude the deflection of the coordinate θ steadily increases, almost linearly. After the amplitude exceeds a value of $a_u = 0.15$ the sloped decreases and in the following when an excitation amplitude value of $a_u = 0.16$ is exceed the clearly periodic dynamics disappear and dynamics that suggest quasi-

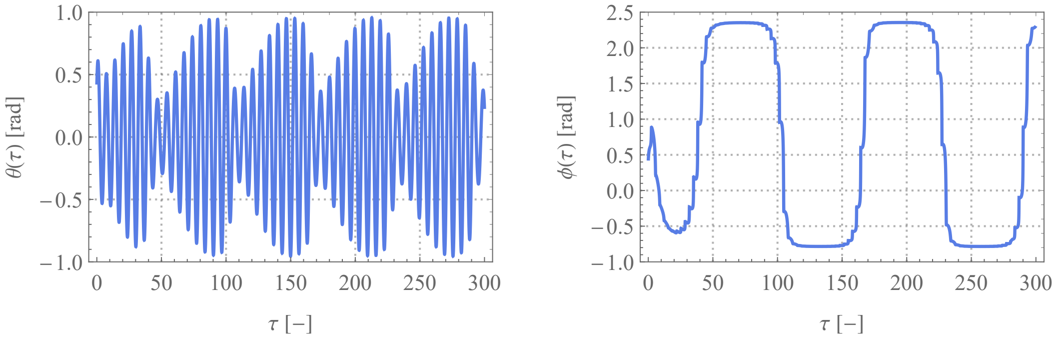

(a) θ over τ with $a_u = a_v = 0.064$ and $a_w = 0$ (b) ϕ over τ with $a_u = a_v = 0.064$ and $a_w = 0$

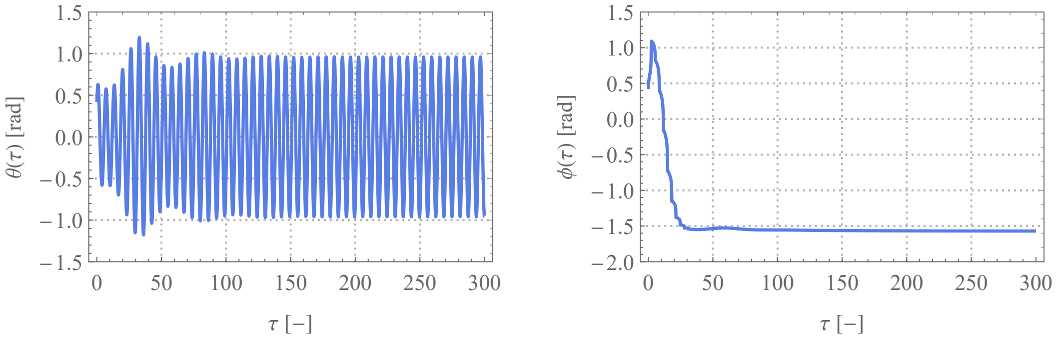

(c) θ over τ with $a_u = a_w = 0.064$ and $a_v = 0$ (d) ϕ over τ with $a_u = a_w = 0.064$ and $a_v = 0$

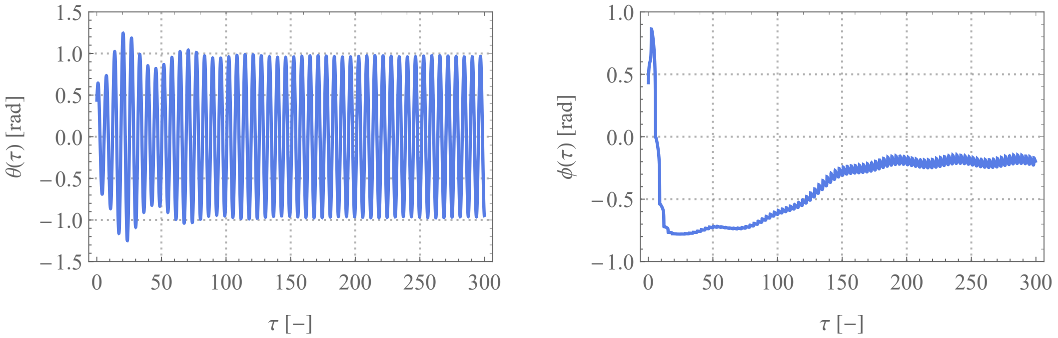

(e) θ over τ with $a_u = a_v = a_w = 0.064$ (f) ϕ over τ with $a_u = a_v = a_w = 0.064$

Figure 5.3: θ and ϕ over τ for a variation of the excitation direction with the parameters set to: $l = 0.5$ m, $m = 1.32$ kg, $g = 9.81\ \frac{\text{m}}{\text{s}^2}$, $\alpha_\theta = \alpha_\phi = 0.0648$, $\beta_u = \beta_v = 0.5\beta_w = 1$, and $P_\theta = P_\phi = 0$.

periodicity or chaos appear. For the excitation in the v-direction in Figure 5.4b the periodic dynamics are similar. Even after an excitation value of $a_v = 0.16$ is exceeded the coordinate θ shows periodic dynamics. For an excitation frequency with the natural undamped frequency of the simple pendulum the dynamics of the system differ drastically see Figure 5.4c. From a value of the excitation amplitude $a_u = 0$ to 0.05 the system shows periodic dynamics with a further increase in the excitation amplitude a jump to quasi-periodic or chaotic appearing dynamics is observed. The same dynamics are observed for the v-direction excited system in Figure 5.4d as well. The spherical pendulum is excited with an excitation frequency of $\beta = 1.1$ in the following. The dynamics of the spherical pendulum for the excitation in the u-direction are shown in

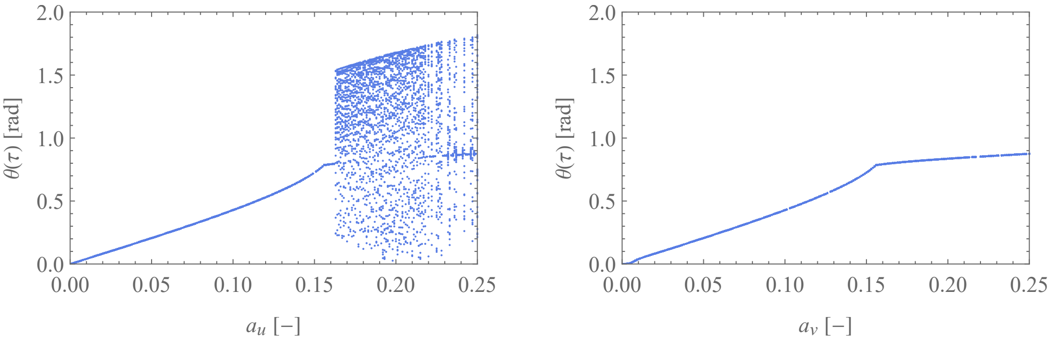

(a) θ over a_u with $a_v = a_w = 0$ and $\beta = 0.9$ (b) θ over a_v with $a_u = a_w = 0$ and $\beta = 0.9$

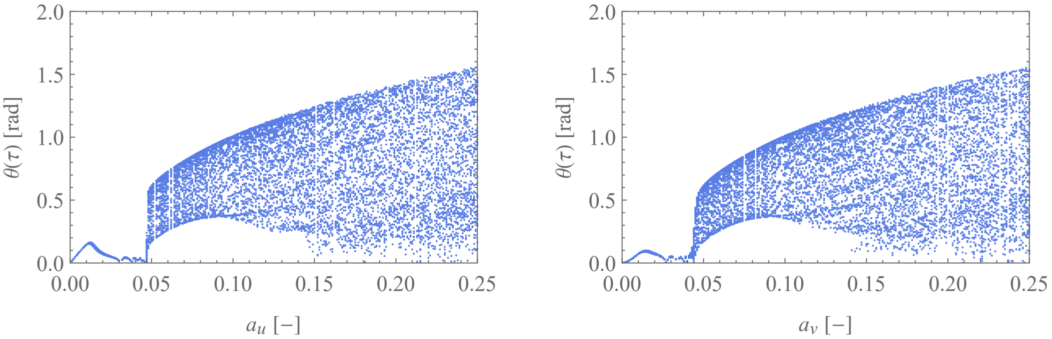

(c) θ over a_u with $a_v = a_w = 0$ and $\beta = 1.0$ (d) θ over a_v with $a_u = a_w = 0$ and $\beta = 1.0$

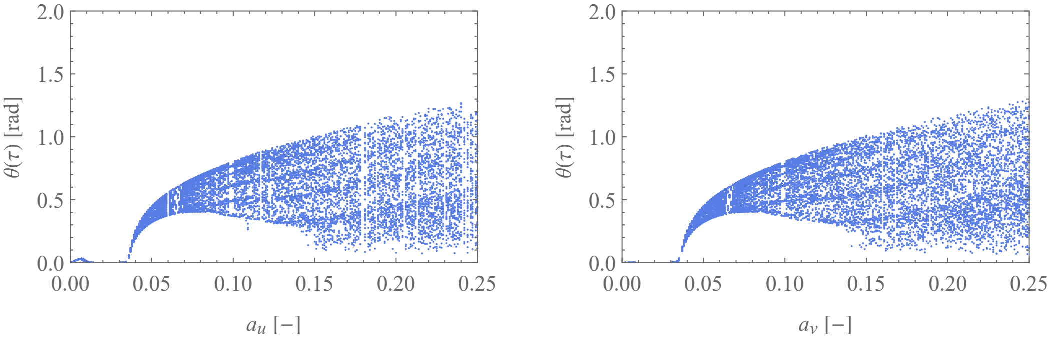

(e) θ over a_u with $a_v = a_w = 0$ and $\beta = 1.1$ (f) θ over a_v with $a_u = a_w = 0$ and $\beta = 1.1$

Figure 5.4: Bifurcation diagrams for θ over the excitation amplitude for a variation of the excitation direction and different excitation frequencies with the parameters set to: $l = 0.5$ m, $m = 1.32$ kg, $g = 9.81\ \frac{\mathrm{m}}{\mathrm{s}^2}$, $\alpha_\theta = \alpha_\phi = 0.0648$, and $P_\theta = P_\phi = 0$.

Figure 5.4e. At a low excitation amplitude the coordinate θ shows almost no displacement, but for an excitation amplitude higher than $a_u = 0.035$ the deflection of the coordinate θ increases steeply. From there on the deflections of the coordinate θ widen and suggest quasi-periodic or chaotic dynamics. Within these quasi-periodic or chaotic appearing areas there are stable periodic orbits observable e.g. at excitation amplitudes of $a_u = 0.65$ and $a_u = 0.95$. The bifurcation diagram for the excitation in the v-direction in Figure 5.4f shows similar dynamics to the u-direction excited pendulum in Figure 5.4e.

Figure 5.5 shows bifurcation diagrams for the coordinate θ for different excitation directions and excitation frequencies. The figures in the left column are exited in the vertical w-direction and the figures in the right column are excited with a coupled excitation in both horizontal directions u and v.

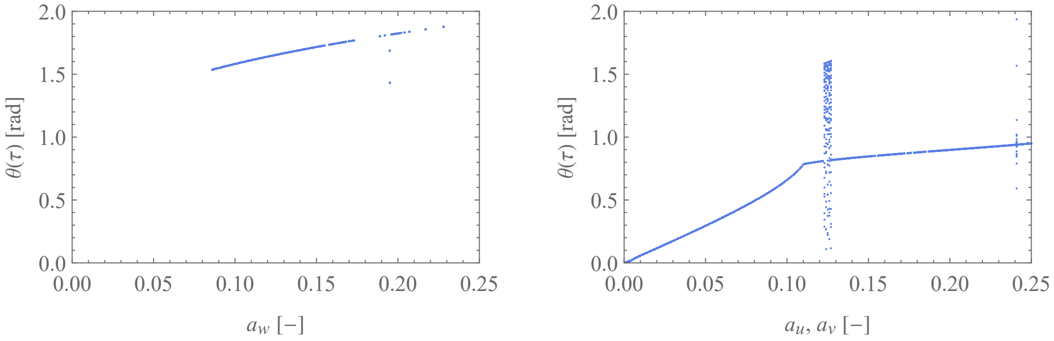

(a) θ over a_w with $a_u = a_v = 0$ and $\beta = 0.9$

(b) θ over a_u, a_v with $a_w = 0$ and $\beta = 0.9$

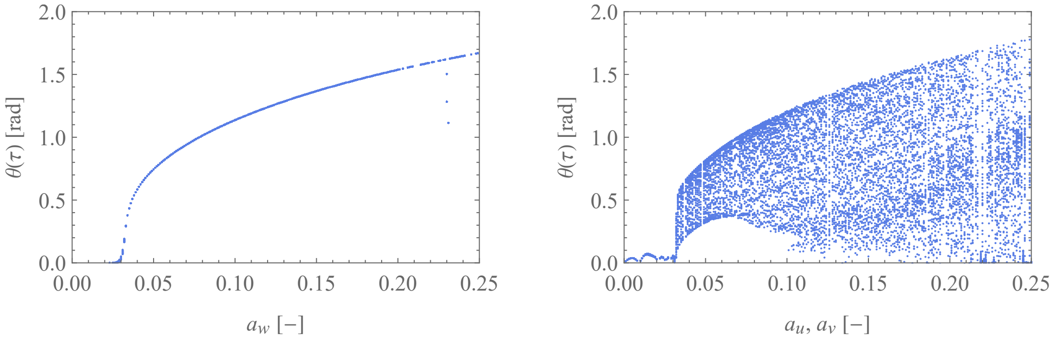

(c) θ over a_w with $a_u = a_v = 0$ and $\beta = 1.0$

(d) θ over a_u, a_v with $a_w = 0$ and $\beta = 1.0$

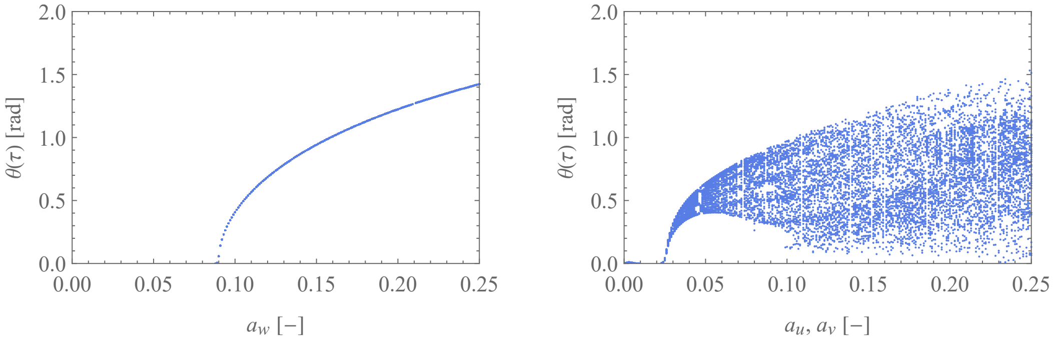

(e) θ over a_w with $a_u = a_v = 0$ and $\beta = 1.1$

(f) θ over a_u, a_v with $a_w = 0$ and $\beta = 1.1$

Figure 5.5: Bifurcation diagrams for θ over the excitation amplitude for a variation of the excitation direction and different excitation frequencies with the parameters set to: $l = 0.5$ m, $m = 1.32$ kg, $g = 9.81\ \frac{\mathrm{m}}{\mathrm{s}^2}$, $\alpha_\theta = \alpha_\phi = 0.0648$, and $P_\theta = P_\phi = 0$.

In Figure 5.5a the spherical pendulum is excited in the vertical direction with an excitation frequency of $\beta = 0.9$. The deflection of the coordinate θ shows a fixed point over the entire excitation amplitudes ranges shown whose slope decreases slightly with an increase of the excitation amplitude. However, there are some outliers and definition gaps where the calculation has stopped because of numerical issues before a steady-state was reached. The bifurcation diagram of the spherical pendulum for an excitation frequency of $\beta = 1.0$ and an excitation in the vertical direction is shown in Figure 5.5c. In the beginning, the fixed point of the coordinate θ rises almost abruptly but then flattens out sharply as the excitation amplitude increases. Here too there are some outliers to be observed. In Figure 5.5e the bifurcation diagram of the spherical pendulum for an excitation frequency of $\beta = 1.1$ for a vertical excitation is shown. The figure shows a fixed point over the whole portrayed area with the difference to Figure 5.5c being that the deflection starts at a higher excitation amplitude with a value of $a_w = 0.09$ rather than $a_w = 0.03$.

Figure 5.5b shows the bifurcation diagram for the spherical pendulum that is excited in both horizontal directions with an excitation frequency of $\beta = 0.9$. Most of the bifurcation diagram shows a fixed point that rises sharply at the beginning and then makes a bend at a value of the excitation amplitude of $a_u = a_v = 0.11$ from where the slope decreases. It is interesting to see that for a short period for the control parameter from $a_u = a_v = 0.122$ to 0.128 an area that suggests quasi-periodic or chaotic dynamics prevails. With an excitation frequency of $\beta = 1.0$ the dynamics of the system change drastically see Figure 5.5d. A fixed point with a low deflection of the coordinate θ can be seen until the excitation amplitude of $a_u = a_v = 0.0317$ is exceeded. From there, the system immediately jumps to dynamics that appear to be quasi-periodic or chaotic. In Figure 5.5f the bifurcation diagram for the spherical pendulum is shown with an excitation frequency of $\beta = 1.1$ and an excitation in both horizontal directions. Up to a value for the excitation amplitude of $a_u = a_v = 0.0259$ hardly any deflection of the coordinate θ is observed. After that, the fixed point rises sharply and expands without a clear bifurcation to a wide range of possible deflections. The bifurcation diagram appears to be chaotic from an excitation amplitude of $a_u = a_v = 0.05$ onwards.

Figure 5.6 shows bifurcation diagrams with different excitation amplitudes as the control parameters. The left column shows a coupled excitation in the u- and w-directions, synonymous with the x- and z-directions, for a variation of the excitation amplitude with $\beta = 0.9$, $\beta = 1.0$, and $\beta = 1.1$ in the different rows. The figures on the right side show bifurcation diagrams for the spherical pendulum that is excited in all directions in space with a variation of the excitation frequency for the different rows. The other parameters in Figure 5.6 are set to the values close to the experimental values and the power take-off is set to zero.

In Figure 5.6a the bifurcation diagram of the spherical pendulum for excitation amplitudes in the x- and z-directions as control parameters and for an excitation frequency of $\beta = 0.9$ is shown. Over the shown excitation amplitudes the bifurcation diagram shows a fixed point. For the low excitation amplitudes the deflection of the coordinate θ increases rapidly until the deflection of the coordinate θ jumps up to a value of 1.48 rad at a value of the excitation amplitudes of $a_u = a_w = 0.0595$. With a further increase in the excitation amplitudes the slope

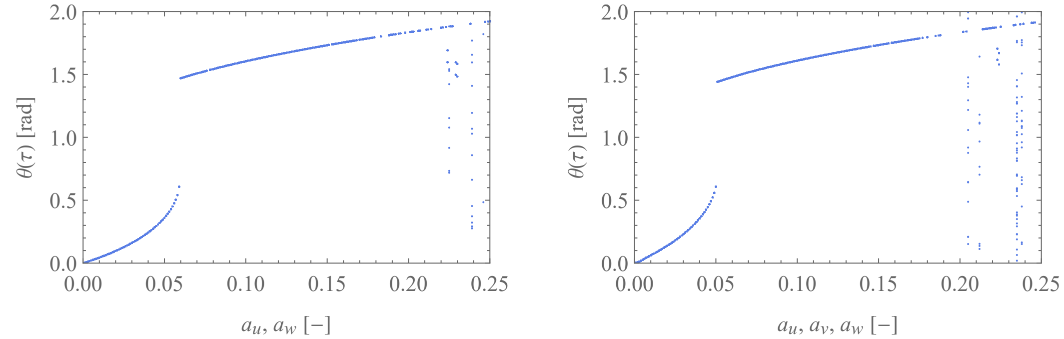

(a) θ over a_u, a_w with $a_v = 0$ and $\beta = 0.9$ (b) θ over a_u, a_v, a_w with $\beta = 0.9$

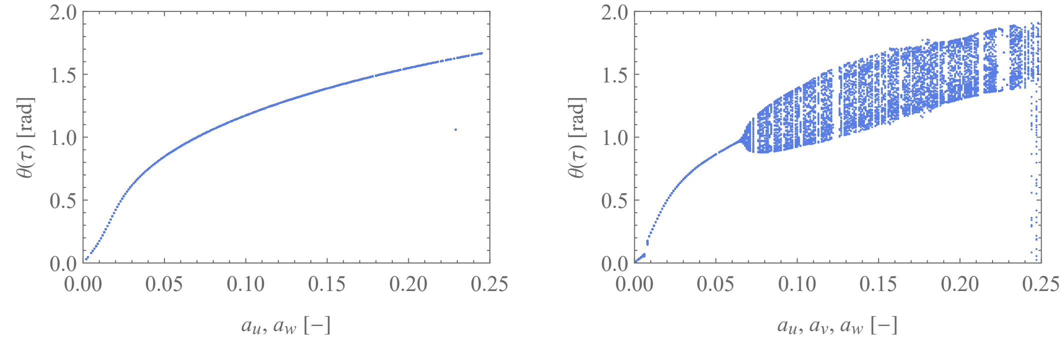

(c) θ over a_u, a_w with $a_v = 0$ and $\beta = 1.0$ (d) θ over a_u, a_v, a_w with $\beta = 1.0$

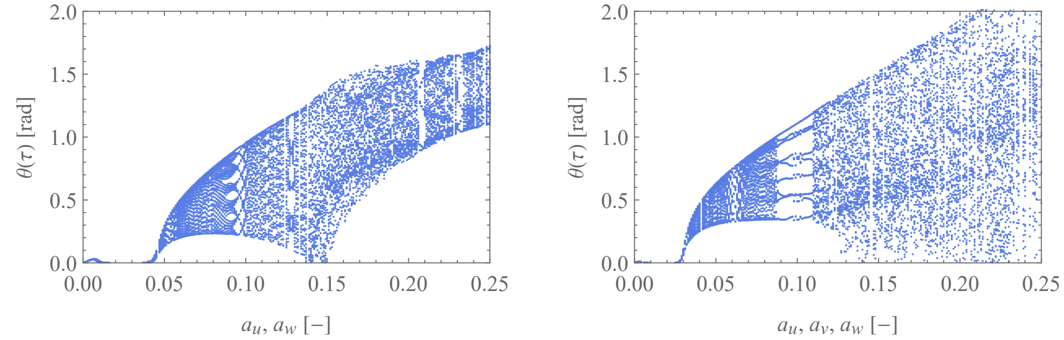

(e) θ over a_u, a_w with $a_v = 0$ and $\beta = 1.1$ (f) θ over a_u, a_v, a_w with $\beta = 1.1$

Figure 5.6: Bifurcation diagrams for θ over the excitation amplitude for a variation of the excitation direction and different excitation frequencies with the parameters set to: $l = 0.5$ m, $m = 1.32$ kg, $g = 9.81\ \frac{\mathrm{m}}{\mathrm{s}^2}$, $\alpha_\theta = \alpha_\phi = 0.0648$, and $P_\theta = P_\phi = 0$.

of the curve is strongly decreased. In the end range of the excitation amplitudes from 0.18 to 0.25, areas can be seen that do not show a fixed point.

The bifurcation diagram with the excitation amplitudes a_u and a_w as control parameters and the excitation frequency at the natural frequency $\beta = 1.0$ is shown in Figure 5.6c. The bifurcation diagram shows a fixed point over the plotted area of the excitation amplitude. Up to a value of the excitation amplitudes of $a_u = a_w = 0.034$ the slope of the graph is high but it decreases with a further increase in the excitation amplitudes gradually.

With a further increase in the excitation frequency of 10 % above the natural frequency the dynamics of the system change drastically see Figure 5.6e. Up to a value for the excitation amplitudes of $a_u = a_w = 0.04$ there is almost no deflection of the generalised coordinate θ observable. But afterwards the observed deflections of the coordinate θ blow up almost instantly. Within these areas that appear to be quasi-periodic or chaotic there are areas of stable periodic orbits observed, for example for ranges of the excitation amplitudes of $a_u = a_w = 0.093$ to 0.1, $a_u = a_w = 0.127$ to 0.13, and $a_u = a_w = 0.205$ to 0.21.

The bifurcation diagram with the excitation amplitudes a_u, a_v, and a_w as control parameters and an excitation frequency of $\beta = 0.9$ is shown in Figure 5.6b. At first glance the bifurcation diagram looks similar to those on the left in Figure 5.6a. The differences being that the jump up to the higher deflection of the coordinate $\theta = 1.45$ rad happens slightly earlier at a value for the excitation amplitudes of $a_u = a_v = a_w = 0.0499$.

In Figure 5.6d the bifurcation diagram for the spherical pendulum with the excitation amplitudes a_u, a_v, and a_w as control parameters and an excitation frequency of $\beta = 1.0$ is shown. The bifurcation diagram shows a fixed point up to a value of the excitation amplitudes of $a_u = a_v = a_w = 0.064$. From there on a range of deflections for the coordinate θ is observed. This margin remains relatively constant over the further shown control parameters, however, the absolute values slowly increase with an increase in the excitation amplitudes.

Figure 5.6f shows the bifurcation diagram for the spherical pendulum with the excitation amplitudes a_u, a_v, and a_w as control parameters and an excitation frequency with a value of $\beta = 1.1$. For a value of the excitation amplitudes from $a_u = a_v = a_w = 0$ to 0.029 the coordinate θ shows no significant deflection. With a further increase in the excitation amplitudes the generalised coordinate θ shows dynamics that appear to be chaotic or quasi-periodic. For a value of the excitation amplitudes from $a_u = a_v = a_w = 0.088$ to 0.11 the bifurcation diagram shows stable periodic orbits.

5.1.3.1 Summary of Section 5.1.3

When comparing Figures 5.4, 5.5, and 5.6 four main trends can be identified. Firstly, with the lowest excitation frequency of $\beta = 0.9$ the dynamics of the spherical pendulum are generally more periodic compared to the higher excitation frequencies $\beta = 1.0$ and $\beta = 1.1$. Secondly, there generally is a steep increase in the deflection of the coordinate θ at the lower excitation amplitudes, which flattens over a further increase in the excitation amplitude. This nonlinear behaviour must be taken into account in the experiments to find an optimum operational range for the energy harvester. Thirdly, a coupled excitation in the x- and y-directions and therefore only horizontal excitation suggest more chaotic dynamics than a coupled excitation in the x- and z-directions (horizontal and vertical). Fourthly, a coupled excitation that includes an excitation in the z-direction generally has higher deflections for the coordinate θ.

5.1.4 Variation of the Excitation Frequency

Figure 5.7 shows different bifurcation diagrams with the excitation frequency as a control parameter for different excitation amplitudes and directions. The figures in the left column show an excitation in the x-direction and the bifurcation diagrams in the right column show the response of the system that is excited in the y-direction.

In Figure 5.7a the bifurcation diagram with an excitation amplitude of $a_u = 0.064$ is shown. For a value of the excitation frequency below $\beta = 0.957$ the output shows a fixed point and

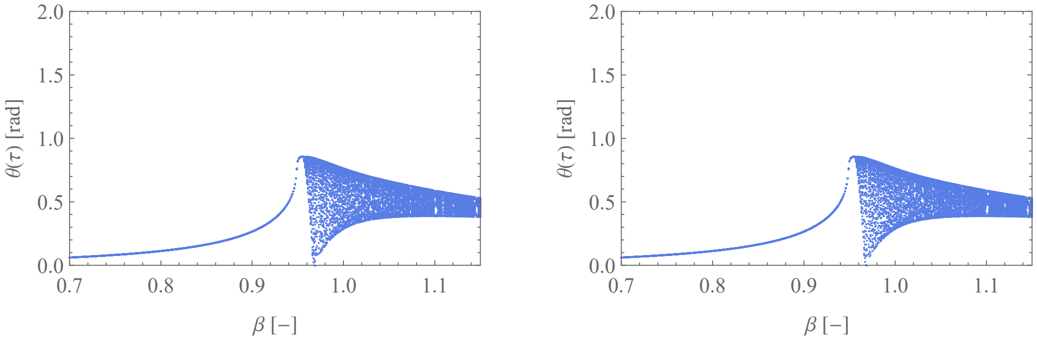

(a) θ over β with $a_u = 0.064$ and $a_v = a_w = 0$ (b) θ over β with $a_v = 0.064$ and $a_u = a_w = 0$

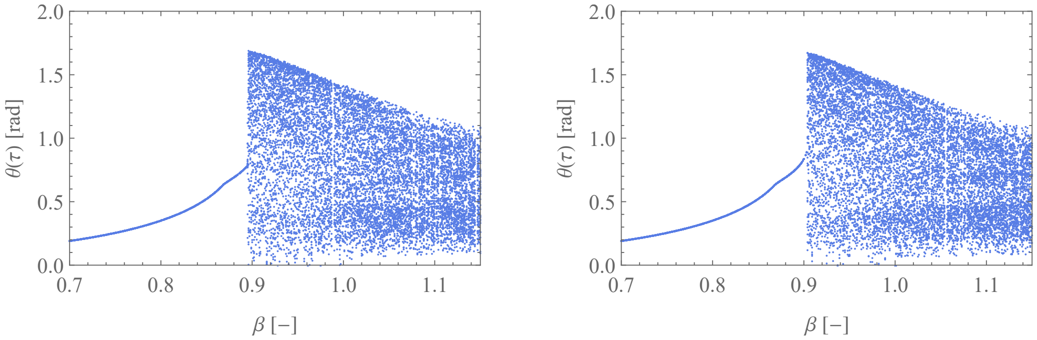

(c) θ over β with $a_u = 0.2$ and $a_v = a_w = 0$ (d) θ over β with $a_v = 0.2$ and $a_u = a_w = 0$

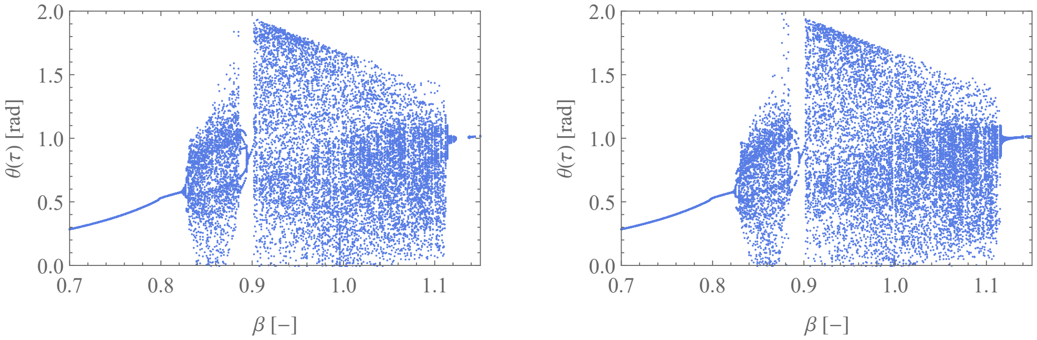

(e) θ over β with $a_u = 0.3$ and $a_v = a_w = 0$ (f) θ over β with $a_v = 0.3$ and $a_u = a_w = 0$

Figure 5.7: Bifurcation diagrams for θ over the excitation frequency for a variation of the excitation direction and different excitation amplitudes with the parameters set to: $l = 0.5$ m, $m = 1.32$ kg, $g = 9.81\ \frac{\text{m}}{\text{s}^2}$, $\alpha_\theta = \alpha_\phi = 0.0648$, and $P_\theta = P_\phi = 0$.

therefore the system shows periodic dynamics in this area. When this excitation frequency is exceeded a broad range of displacement of the coordinate θ is observed which narrows with an increasing excitation frequency. The narrowing is observed at the lower and upper limits of the coordinate θ. For an excitation frequency higher than $\beta = 0.957$ the coordinate θ shows dynamics that suggest quasi-periodicity or chaos.

Figure 5.7c shows a bifurcation diagram with an increased excitation amplitude of $a_u = 0.2$. For an excitation frequency of $\beta = 0.7$ to 0.89 a fixed point can be observed. With a further increase in the excitation frequency a broad range of deflections of the coordinate θ can be seen where the maximum possible value of θ decreases with a further increase in the excitation frequency. In the area for an excitation frequency from $\beta = 0.89$ to $\beta = 1.15$ the dynamics of the spherical pendulum suggest quasi-periodic or chaotic dynamics.

The bifurcation diagram for an excitation amplitude of $a_u = 0.3$ is shown in Figure 5.7e. For an excitation amplitude from $\beta = 0.7$ to 0.82 a fixed point can be seen. Followed by an area that suggests quasi-periodic or chaotic dynamics which develops in an area of unstable periodic orbits for an excitation frequency from $\beta = 0.89$ to 0.90. Afterwards, an area where chaotic or quasi-periodic dynamics can be assumed is dominant until the excitation frequency of $\beta = 1.12$ is exceeded. For the remaining range of excitation frequencies the coordinate θ shows a fixed point.

In Figure 5.7b shows a bifurcation diagram for the spherical pendulum that is excited in the y-direction with an excitation amplitude of $a_v = 0.064$. The bifurcation diagram is nearly identical to the one in Figure 5.7a. It shows a fixed point up to a value of the excitation frequency of $\beta = 0.957$. From there on the bifurcation diagram shows dynamics that suggest quasi-periodic or chaotic dynamics until the end of the plotted excitation frequency.

The bifurcation diagram with an excitation amplitude of $a_v = 0.2$ in Figure 5.7d has a similar appearance to the bifurcation diagram that is excited in the x-direction in Figure 5.7b. The fixed point can be seen for an excitation amplitude from $\beta = 0.7$ to 0.9 afterwards a wide range of deflections for the coordinate θ is shown that suggests quasi-periodic or chaotic dynamics.

The bifurcation diagram for an excitation amplitude of $a_v = 0.3$ in Figure 5.7f is similar to its counterpart on the left side in Figure 5.7e. The main difference being that for an excitation frequency of $\beta = 1.11$ to 1.15 Figure 5.7f shows a fixed point where Figure 5.7e shows a fixed point with numerical faulty computation gaps instead.

Figure 5.8 shows bifurcation diagrams for different excitation frequencies and excitation amplitudes and directions for the spherical pendulum with the excitation frequency acting as the control parameter. The bifurcation diagram for an excitation amplitude of $a_w = 0.064$ is shown in Figure 5.8a. A fixed point is observed for a value from the excitation frequency from

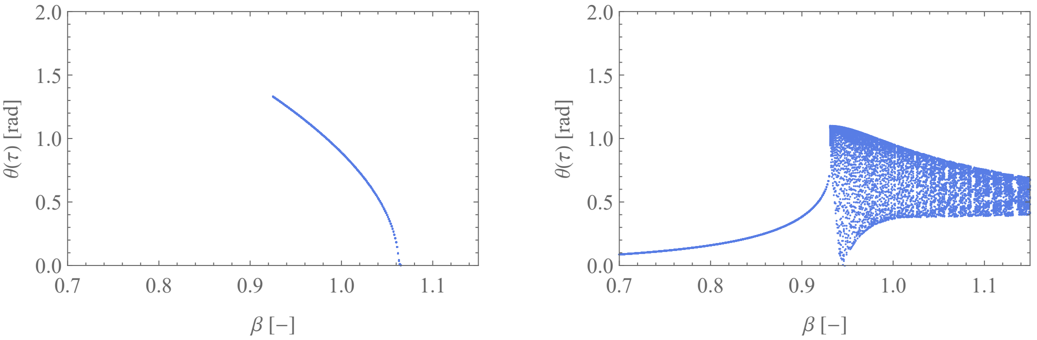

(a) θ over β with $a_w = 0.064$ and $a_u = a_v = 0$ (b) θ over β with $a_u = a_v = 0.064$ and $a_w = 0$

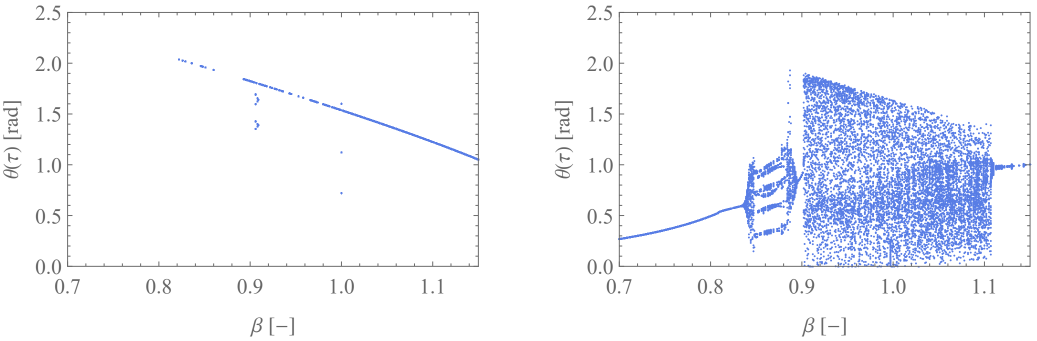

(c) θ over β with $a_w = 0.2$ and $a_u = a_v = 0$ (d) θ over β with $a_u = a_v = 0.2$ and $a_w = 0$

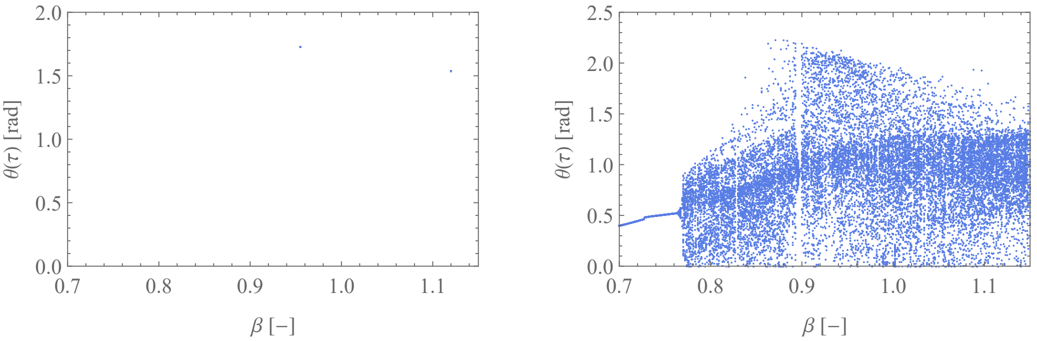

(e) θ over β with $a_w = 0.3$ and $a_u = a_v = 0$ (f) θ over β with $a_u = a_v = 0.3$ and $a_w = 0$

Figure 5.8: Bifurcation diagrams for θ over the excitation frequency for a variation of the excitation direction and different excitation amplitudes with the parameters set to: $l = 0.5$ m, $m = 1.32$ kg, $g = 9.81\ \frac{\mathrm{m}}{\mathrm{s}^2}$, $\alpha_\theta = \alpha_\phi = 0.0648$, and $P_\theta = P_\phi = 0$.

$\beta = 0.92$ to 1.07. In the remaining area of the excitation frequency the spherical pendulum does not show a deflection.

In Figure 5.8c the excitation amplitude is increased to a value of $a_w = 0.2$. For an excitation frequency from $\beta = 0.82$ to 1.15 the system shows a fixed point. In an area for the excitation frequency from $\beta = 0.9$ to 0.901 the system shows two small triangle shaped bifurcations.

With a further increase in the excitation amplitude to a value of $a_w = 0.3$ the numerical calculation gets unstable and therefore the bifurcation diagram in Figure 5.8e shows no significant output.

The bifurcation diagram in Figure 5.8b shows the deflection of the coordinate θ for a coupled excitation in the x- and y-directions with a value of the excitation amplitudes of $a_u = a_v = 0.064$. For an excitation frequency from $\beta = 0.7$ to 0.93 the bifurcations diagram shows a fixed point. With a further increase in the excitation frequency a range of deflection values of the coordinate θ can be seen. But with a further increase in the excitation frequency the minimum and maximum values of the shown deflections for θ converge.

In Figure 5.8d the bifurcation diagram for increased values excitation amplitudes of $a_u = a_v = 0.2$ is shown. At the beginning of the illustrated range up to an excitation frequency of $\beta = 0.835$, a fixed point can be seen which then bifurcates. This is followed by an area that shows stable periodic orbits which converges back to a fixed point for an excitation frequency range from $\beta = 0.896$ to 0.9. Followed by an area that suggests quasi-periodic or chaotic dynamics. This area returns to a fixed point at an excitation frequency higher than $\beta = 1.11$.

Figure 5.8f shows a bifurcation diagram for increased values of the excitation amplitudes of $a_u = a_v = 0.3$. This increase in the excitation amplitudes generally shows less periodic dynamics. For an excitation frequency in an area from $\beta = 0.7$ to 0.763 the system shows a fixed point which afterwards bifurcates and rapidly transforms in an area that suggests quasi-periodic or chaotic dynamics. This area is briefly interrupted by a stable periodic orbit for a value of the excitation frequency from $\beta = 0.893$ to $\beta = 0.901$.

Figure 5.9 shows bifurcation diagrams for different coupled excitation modes and excitation amplitudes with the excitation frequency as the control parameter. The left column shows bifurcation diagrams for a coupled excitation in the x- and z-directions and the right column shows bifurcation diagrams that are obtained with a coupled excitation in the x-, y-, and z-directions.

In Figure 5.9a the bifurcation diagram of the spherical pendulum for a value of the excitation amplitudes $a_u = a_w = 0.064$ is shown. The bifurcation diagram shows a jump up for a value of the excitation frequency of $\beta = 0.893$ which indicates the classical softening characteristics. Within the area from $\beta = 0.7$ to 1.038 the bifurcation diagram shows a fixed point. Afterwards, the fixed point bifurcates and shows an area where the dynamics suggest chaotic or quasi-periodic dynamics. At an area around the excitation frequency of $\beta = 1.07$ the maximum value of θ decreases abruptly and increases abruptly as well after the local minimum is exceeded.

Figure 5.9c shows a bifurcation diagram for the spherical pendulum with increased excitation amplitudes $a_u = a_w = 0.2$. For an excitation frequency from $\beta = 0.7$ to 0.78 the figure shows a fixed point that jumps up to a higher deflection for the coordinate θ of 2.15 rad with a further increase in the excitation frequency. The bifurcation shows a fixed point after the up jump until the excitation frequency of $\beta = 1.02$ is exceeded where the fixed point bifurcates

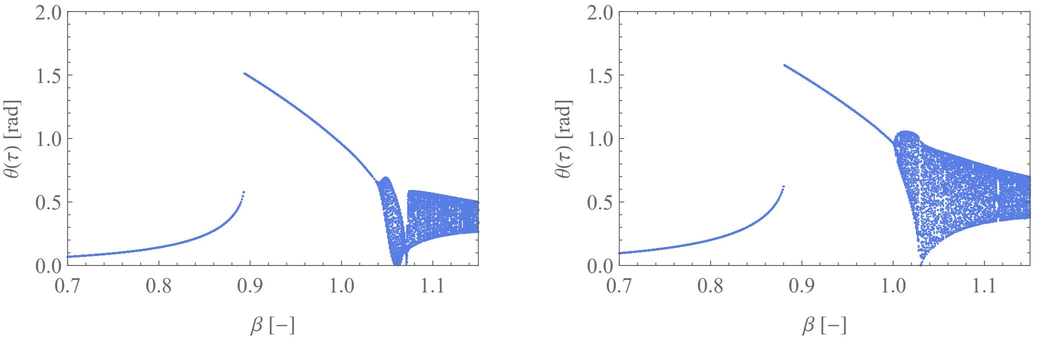

(a) θ over β with $a_u = a_w = 0.064$ and $a_v = 0$ (b) θ over β with $a_u = a_v = a_w = 0.064$

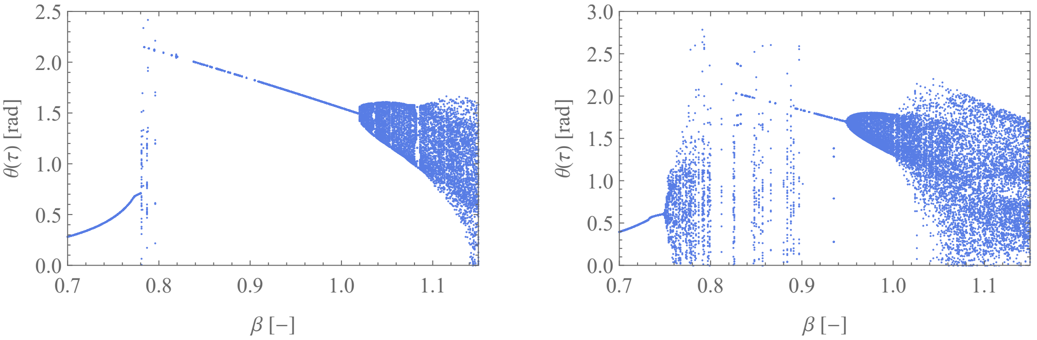

(c) θ over β with $a_u = a_w = 0.2$ and $a_v = 0$ (d) θ over β with $a_u = a_v = a_w = 0.2$

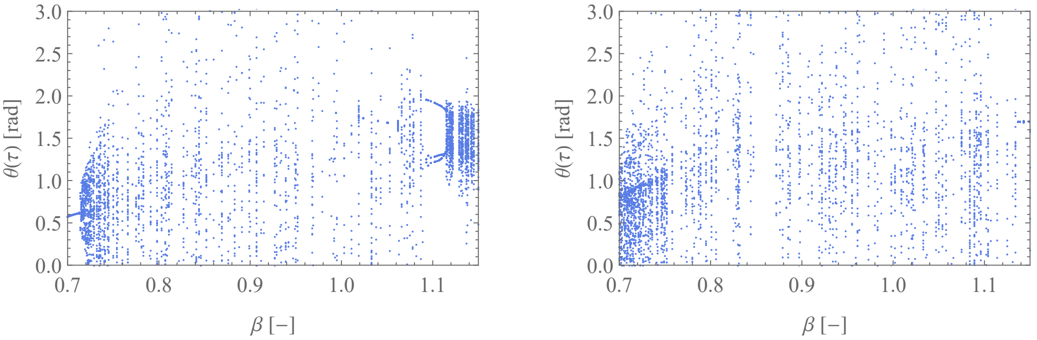

(e) θ over β with $a_u = a_w = 0.3$ and $a_v = 0$ (f) θ over β with $a_u = a_v = a_w = 0.3$

Figure 5.9: Bifurcation diagrams for θ over the excitation frequency for a variation of the excitation direction and different excitation amplitudes with the parameters set to: $l = 0.5$ m, $m = 1.32$ kg, $g = 9.81\ \frac{\text{m}}{\text{s}^2}$, $\alpha_\theta = \alpha_\phi = 0.0648$, and $P_\theta = P_\phi = 0$.

and an area can be seen that suggest quasi-periodic or chaotic dynamics which can be seen for the remaining excitation frequency.

In Figure 5.9f the bifurcation diagram for the spherical pendulum for a value of the excitation amplitudes of $a_u = a_w = 0.3$ is shown. The bifurcation diagram shows a fixed point for an excitation frequency from $\beta = 0.7$ to 0.715 and stable periodic orbits for an excitation frequency from $\beta = 1.09$ to 1.12. For the remaining area, the bifurcation diagram shows dynamics that suggest quasi-periodic or chaotic behaviour.

Figure 5.9b shows the bifurcation diagram for the spherical pendulum that is excited in all three directions with an excitation amplitudes of $a_u = a_v = a_w = 0.064$. The diagram shows a fixed point until the excitation frequency of $\beta = 1.0$ is reached. In between this area for an excitation frequency of $\beta = 0.88$ there is a up jump observed that gives evidence of the softening properties of the system. In an area of the excitation frequency from $\beta = 1.0$ to 1.15 the dynamics of the pendulum suggest quasi-periodic or chaotic dynamics.

The bifurcation diagram of the spherical pendulum for the increased values of the excitation amplitudes of $a_u = a_v = a_w = 0.2$ is shown in Figure 5.9d. With the increase in the excitation amplitudes the system generally becomes less periodic. Fixed points can be seen for shorter ranges for an excitation frequency from $\beta = 0.7$ to 0.75 and from $\beta = 0.822$ to 0.95. The other areas show dynamics that suggest quasi-periodic or chaotic dynamics.

In Figure 5.9f the bifurcation diagram for an excitation amplitudes of $a_u = a_v = a_w = 0.3$ is shown. The system shows no fixed points or stable periodic orbits for the increased excitations amplitudes. The points that are shown do not indicate any specific dynamics.

5.1.4.1 Summary of Section 5.1.4

Several general conclusions can be drawn from the bifurcation diagrams in Figures 5.7, 5.8, and 5.9. The softening characteristics of the spherical pendulum can be seen in all bifurcation diagrams, this is evident because the highest deflection of the coordinate θ can always be seen for an excitation frequency lower than one. In other words the highest deflection of the coordinate θ is at an excitation frequency value lower than the natural frequency. Additionally, with an increase in the excitation amplitude the value for the max deflection can be seen at a lower excitation frequency. As before, here again it can be seen that when an excitation in the z-direction is included the system is overall more periodic than without an excitation in the vertical direction.

5.1.5 Poincaré Sections

To quantify the dynamics of the spherical pendulum further Poincaré sections are used. Figure 5.10 shows Poincaré sections for different excitation amplitudes and frequencies. The left column shows an excitation in the x-direction with an excitation amplitude of $a_u = 0.064$, the right column shows an excitation in the x-direction with an increased excitation amplitude of $a_u = 0.3$, and the different rows show an excitation frequency of $\beta = 0.9$, $\beta = 1.0$, and $\beta = 1.1$ from top to bottom.

The Poincaré section in Figure 5.10a shows the dynamics of the system for an excitation frequency of $\beta = 0.9$ shows one single point which confirms the fixed point of the bifurcation diagram in Figure 5.7a. This shows that the dynamics of the system are periodic for a excitation amplitude of $a_u = 0.064$ and an excitation frequency of $\beta = 0.9$.

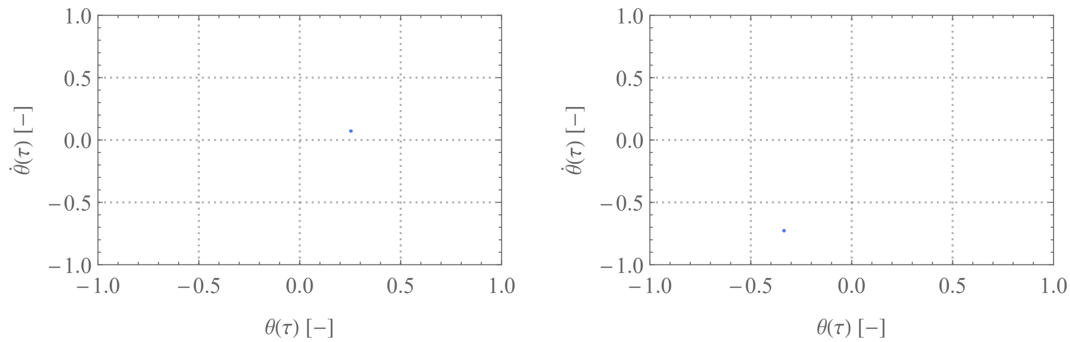

(a) Poincaré section with $a_u = 0.064$ and $\beta = 0.9$ (b) Poincaré section with $a_u = 0.3$ and $\beta = 0.9$

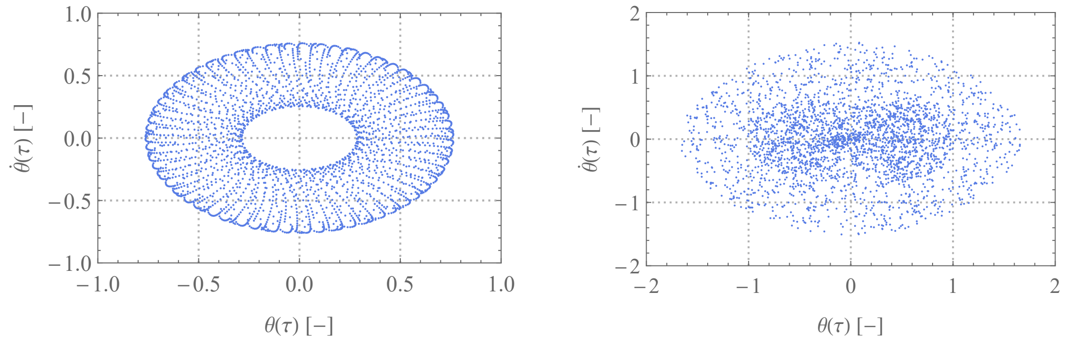

(c) Poincaré section with $a_u = 0.064$ and $\beta = 1.0$ (d) Poincaré section with $a_u = 0.3$ and $\beta = 1.0$

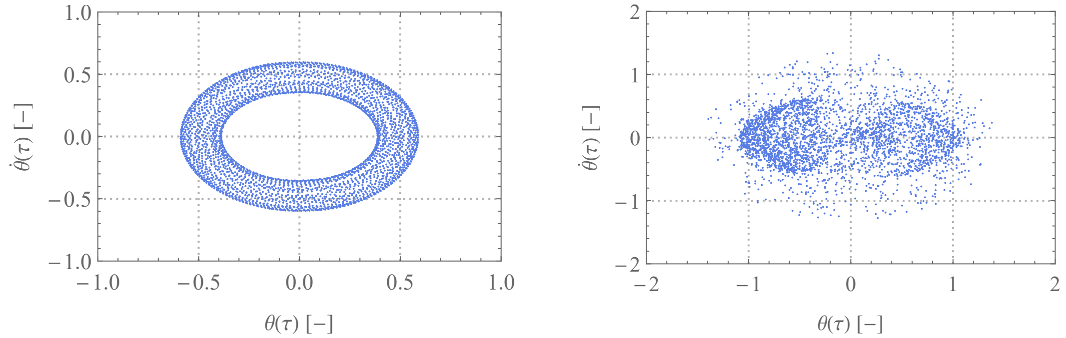

(e) Poincaré section with $a_u = 0.064$ and $\beta = 1.1$ (f) Poincaré section with $a_u = 0.3$ and $\beta = 1.1$

Figure 5.10: Poincaré sections for a variation of the excitation amplitudes and different excitation frequencies with the parameters set to: $l = 0.5$ m, $m = 1.32$ kg, $g = 9.81\ \frac{\mathrm{m}}{\mathrm{s}^2}$, $\alpha_\theta = \alpha_\phi = 0.0648$, $a_v = a_w = 0$, and $P_\theta = P_\phi = 0$.

With a further increase in the excitation frequency to a value of $\beta = 1.0$ the dynamics of the system change see Figure 5.10c. The Poincaré section shows a ring-shaped pattern that is showing a regular pattern. It looks as if the ring consists of individual pieces that are strung together. It can be assumed that this is a stage where the dynamics of the system change from quasi-periodic dynamics to chaotic dynamics.

In Figure 5.10e the Poincaré section is shown for an excitation amplitude of $a_u = 0.064$ and an excitation frequency of $\beta = 1.1$. The diagram shows a circular pattern that is ring-shaped which can be seen as a transition between quasi-periodic dynamics to chaotic dynamics.

Figure 5.10b shows the Poincaré section for a increased excitation amplitude of $a_u = 0.3$ and an excitation frequency of $\beta = 0.9$. The diagram shows a fixed point and is therefore in accordance with the bifurcation diagram in Figure 5.7f which shows a fixed point for a short moment after the stable periodic orbits have passed which confirms the periodic dynamics.

The excitation frequency is further increased to a value of $\beta = 1.0$ in Figure 5.10d. For these values the Poincaré section suggests chaotic dynamics. Additionally, the diagram has a concentration of points in the inner area.

In Figure 5.10f the Poincaré section for a excitation frequency of $\beta = 1.1$ is shown. The dynamics suggest a chaotic behaviour, and there is a concentration of points in the middle of the diagram observed with two attractors on the left and right side of the y-axis.

Poincaré sections for different coupled excitations and excitation frequencies are shown in Figure 5.11. The Poincaré section in the left column are excited in the u- and w-directions with values of the excitation amplitudes of $a_u = a_w = 0.064$ and those in the right column are excited with increased values of the excitation amplitudes $a_u = a_w = 0.3$.

In Figure 5.11a the Poincaré section for an excitation frequency of $\beta = 0.9$ and excitation amplitudes of $a_u = a_w = 0.064$ is shown. For these forcing conditions a fixed point is shown in the Poincaré section which indicated that the spherical pendulum shows periodic dynamics.

With an increase in the excitation frequency to a value of $\beta = 1.0$ the dynamics of the system change. The Poincaré section shows circular pattern Figure 5.11d. Where the single points within the Poincaré section form a line-like pattern the dynamics of the system are therefore quasi-periodic.

Figure 5.11e shows the Poincaré section for an excitation frequency of $\beta = 1.1$ and excitation amplitudes $a_u = a_w = 0.064$. The figure shows a ring shaped form that consists of smaller ring shaped movements.

In Figure 5.11b the Poincaré section for an excitation frequency of $\beta = 0.9$ and a value for the excitation amplitudes of $a_u = a_w = 0.2$ is shown. The figure shows a fixed point that indicates periodic dynamics of the spherical pendulum for the shown excitation parameters.

Figure 5.11d shows the Poincaré section for an excitation frequency of $\beta = 1.0$ and excitation amplitudes of $a_u = a_w = 0.2$. The figure shows an oval-shaped shape where the single point of the Poincaré section all form one line. This clearly indicates that the dynamics of the spherical pendulum are quasi-periodic for the shown excitation parameters.

With a further increase in the excitation frequency to a value of $\beta = 1.1$ the Poincaré section shows a ring-shaped form see Figure 5.11f. This could be considered as a transitional stage from quasi-periodic dynamics to chaotic dynamics.

With the help of the Poincaré section it can be concluded that the spherical pendulum shows quasi-periodic dynamics and chaotic dynamics depending on the excitational parameters. Ad-

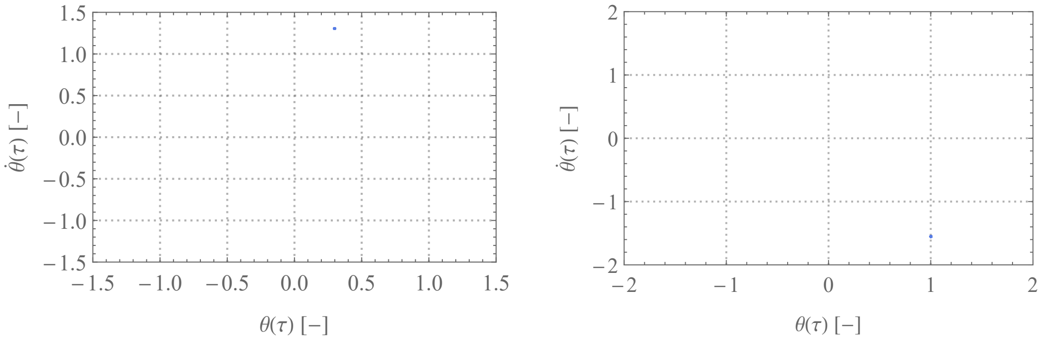

(a) Poincaré section with $a_u = a_w = 0.064$ and $\beta = 0.9$ (b) Poincaré section with $a_u = a_w = 0.2$ and $\beta = 0.9$

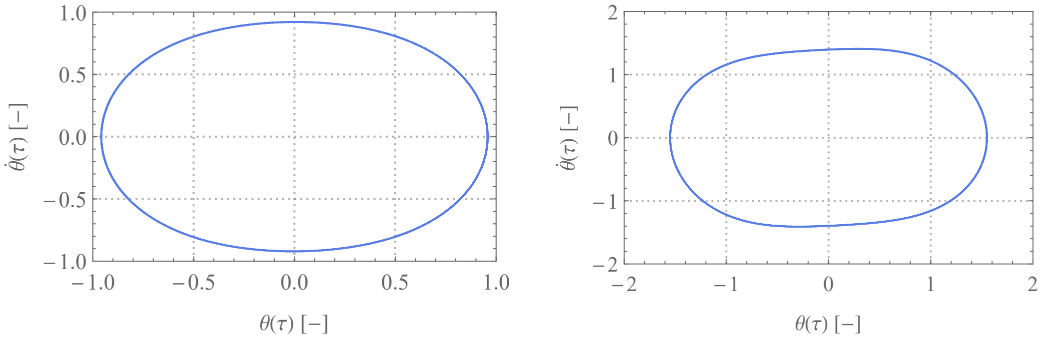

(c) Poincaré section with $a_u = a_w = 0.064$ and $\beta = 1.0$ (d) Poincaré section with $a_u = a_w = 0.2$ and $\beta = 1.0$

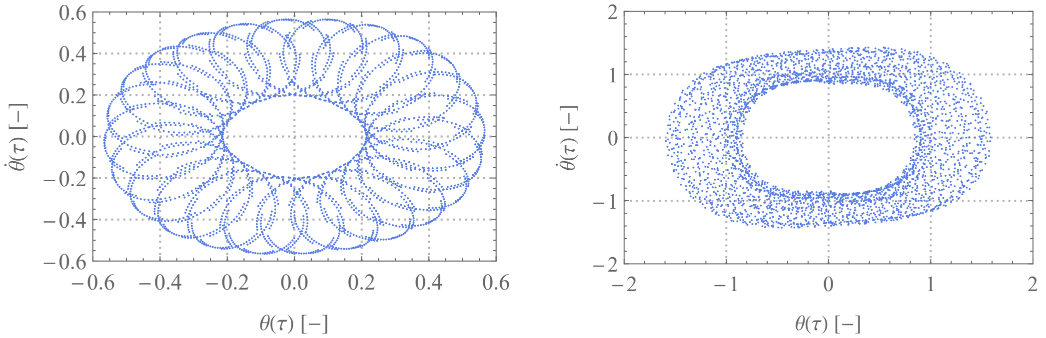

(e) Poincaré section with $a_u = a_w = 0.064$ and $\beta = 1.1$ (f) Poincaré section with $a_u = a_w = 0.2$ and $\beta = 1.1$

Figure 5.11: Poincaré sections for a variation of the excitation amplitudes and different excitation frequencies with the parameters set to: $l = 0.5$ m, $m = 1.32$ kg, $g = 9.81\ \frac{\mathrm{m}}{\mathrm{s}^2}$, $\alpha_\theta = \alpha_\phi = 0.0648$, $a_v = 0$, and $P_\theta = P_\phi = 0$.

ditional fixed points and transitioning processes between quasi-periodic and chaotic dynamics can be observed.

5.2 Numerical Representation of Power Take-Off Methods

The mathematical model of the spherical pendulum has to have some kind of power take-off term to operate as an omnidirectional energy harvester. The power take-off is only applied in the direction of the generalised coordinate θ. Two main approaches are commonly used for that, a sign function and an arctangent function [57]. The mathematical description of the functions for these power take-off terms can be found in Section 4.2. In this section it is examined which power take-off method is advantageous for the following numerical analysis. Thus, the power take-off torque is plotted over the time for a variation of the different power take-off parameters.

5.2.1 Power Take-Off with a Sign Function

With the sign function a square wave function can be produced. The parameter that can be controlled here is the dimensionless power take-off torque P_θ which controls the amplitude of the power take-off. The direction of the power take-off is defined by the velocity of the coordinate θ.

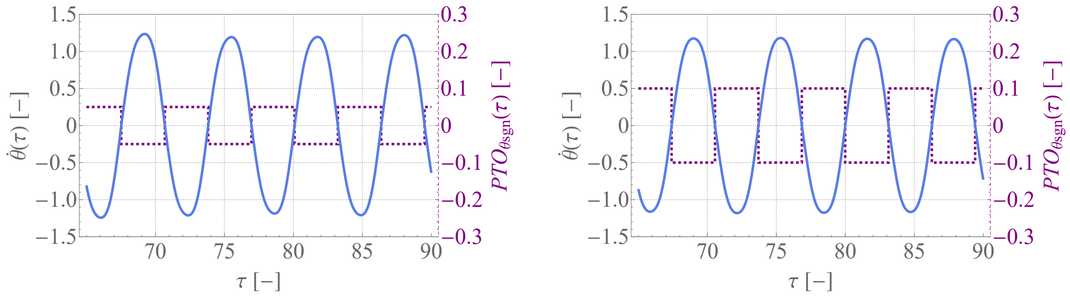

(a) $P_\theta = 0.05$

(b) $P_\theta = 0.1$

Figure 5.12: Power take-off and velocity of the coordinate θ over τ the parameters set to: $l = 0.5$ m, $m = 1.32$ kg, $g = 9.81\ \frac{\text{m}}{\text{s}^2}$, $\alpha_\theta = \alpha_\phi = 0.0648$, $a_u = a_v = a_w = 0.128$, $\beta = 1.0$, and $P_\phi = 0$.

Figure 5.12 shows two different power take-off torques for an excitation in all directions with an arbitrary selected value for the excitation amplitudes $a_u = a_v = a_w = 0.128$ and an excitation frequency of $\beta = 1.0$. In Equation (5.1) the power take-off function over time is shown.

$$PTO_{\theta sgn}(\tau) = -P_\theta \operatorname{sgn}(\dot{\theta}(\tau)). \tag{5.1}$$

In Figure 5.12a the velocity of the coordinate θ and the square wave function of the power take-off according to Equation (4.34) with a value of $P_\theta = 0.05$ are shown. It can be seen that the deflection of these two parameters is always in the opposite direction which is the requirement for the power take-off. If that was not the case the power take-off term would add power to the system instead of taking it off. The value of $P_\theta = 0.05$ defines the amplitude of the power take-off torque which can be observed with the purple square wave function. In Figure 5.12b the power take-off torque is increased to a value of $P_\theta = 0.1$. With that increase in the power take-off torque the maximum deflection of the velocity of the coordinate θ decreases slightly by 0.055. It is important to mention that with a further increase of the power take-off torque the maximum deflection of the coordinate θ decreases slightly until the power take-off torque reaches a value where the whole deflection is completely absorbed. For the shown parameters of the energy harvester this occurs for a value of the power take-off torque higher than $P_\theta = 0.1667$. The maximum value for the power take-off torque depends on the parameters of the pendulum energy harvester and the excitation parameters that are applied to the system.

5.2.2 Power Take-Off with an Arctangent Function

Another option to simulate a power take-off is with an arctangent function as mathematically described in Section 4.2.2. This function is similar to the sign function with the major difference being that an additional tuning parameter is introduced which is the radiusing parameter ε_r. With this parameter the roundness of the corners is defined. In theory it can be selected freely to any positive infinitesimal value, however, it is more sensible to restrict the range from a value close to positive infinitesimal to one. The smaller the value is selected the smaller is the radius. The arctangent power take-off over time is shown in Equation (5.2).

$$PTO_{\theta arc}(\tau) = -\frac{2P_\theta}{\pi}\tan^{-1}\left(\frac{\dot{\theta}(\tau)}{\varepsilon_\mathrm{r}}\right). \tag{5.2}$$

Figure 5.13 shows the velocity of the coordinate θ and the arctangent power take-off function in the time domain for different values of the radiusing parameters ε_r. In Figure 5.13a the value for ε_r is set to 0.01. This small value rounds off the edges of the arctangent slightly and almost does not influence the amplitude of the power take-off. With a further increase of the radiusing parameter to a value of 0.1 in Figure 5.13b the radius of the edges increases and at the same time the pre-defined dimensionless power take-off torque P_θ is not reached anymore. This becomes even more visible after the radiusing parameter is increased to a value of 0.2 in Figure 5.13c and to a value of 1 in Figure 5.13d. In the latter case, only half of the power take-off torque amplitude can be seen. From these figures it is clear that when the radiusing parameter selected is too high this reduces the power take-off drastically and to that end a reasonable value for $\varepsilon_r = 0.01$ is selected for the following analysis if not indicated otherwise.

5.2.3 Comparison of the Different Power Take-Off Methods

It remains to select which power take-off term is to be used for further analysis. The sign function is in principle the simpler mathematical description, but due to the missing adjustment parameters it is not suitable for fine-tuning. In addition, it was noticed during the numerical analysis that the sign function generates more numerical errors than the arctangent function in the numerical analysis and numerical problems occur earlier and more frequently. In contrast, the arctangent function can be fine-tuned very well with the radiusing parameter. And with a small selected value of 0.01, it is hardly possible to distinguish its overall power output from

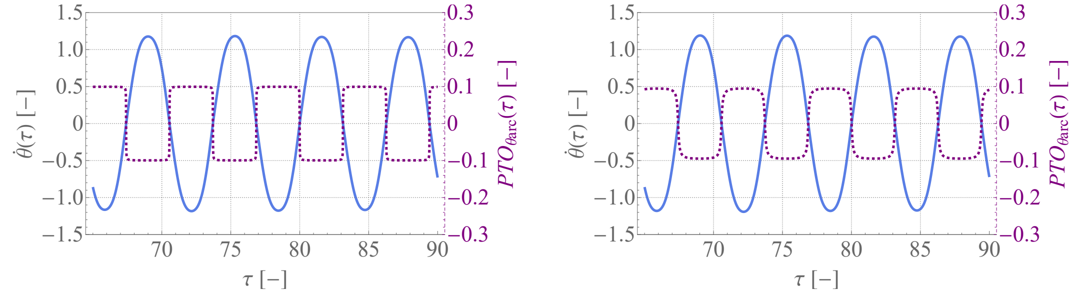

(a) $\varepsilon_r = 0.01$

(b) $\varepsilon_r = 0.1$

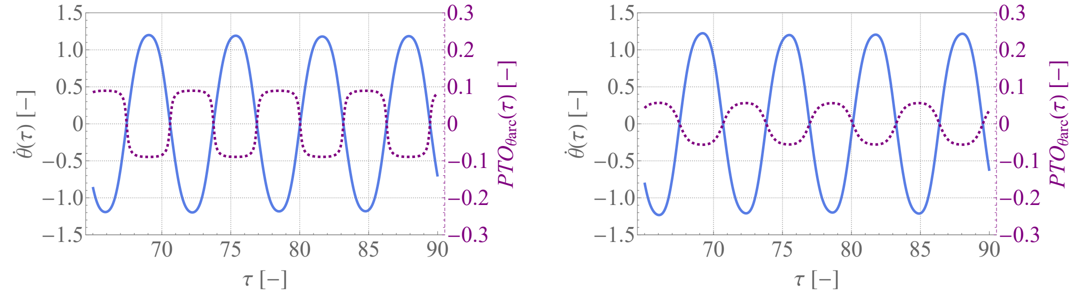

(c) $\varepsilon_r = 0.2$

(d) $\varepsilon_r = 1$

Figure 5.13: Power take-off and velocity of the coordinate θ over τ the parameters set to: $l = 0.5$ m, $m = 1.32$ kg, $g = 9.81\ \frac{\mathrm{m}}{\mathrm{s}^2}$, $\alpha_\theta = \alpha_\phi = 0.0648$, $a_u = a_v = a_w = 0.128$, $\beta = 1.0$, and $P_\theta = 0.1$, $P_\phi = 0$.

the sign function. However, because of the advantage of increased numerical reliability during the computation the arctangent power take-off term was chosen for the further analysis.

5.3 Dynamics of the Spherical Pendulum with a Power Take-Off

In this section the power take-off is switched on an the dynamics of the omnidirectional energy harvester are discussed. The plots are similar to those in Section 5.1 where the power take-off is switched off. This allows a direct comparison between a switched on and switched off power take-off.

5.3.1 Variation of the Excitation Amplitude

Figure 5.14 shows bifurcation diagrams of the pendulum energy harvester for an excitation in one direction for different excitation frequencies and a power take-off torque of $P_\theta = 0.05$. The figures in the left column are excited in the u-direction and the figures in the right column are

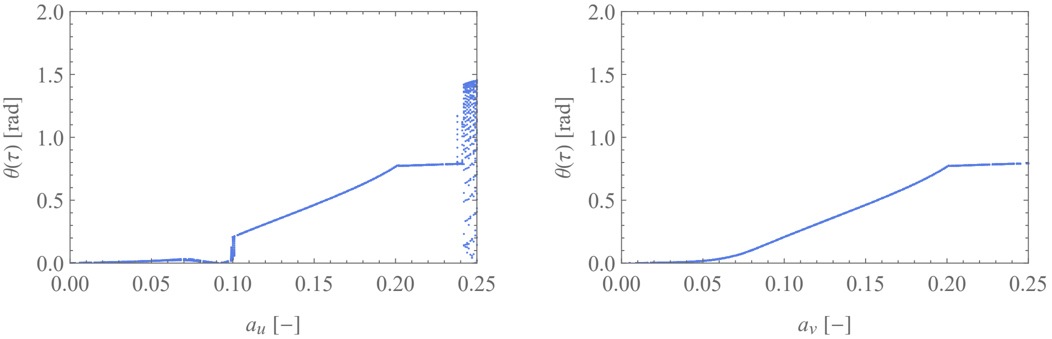

(a) θ over a_u with $a_v = a_w = 0$ and $\beta = 0.9$ (b) θ over a_v with $a_u = a_w = 0$ and $\beta = 0.9$

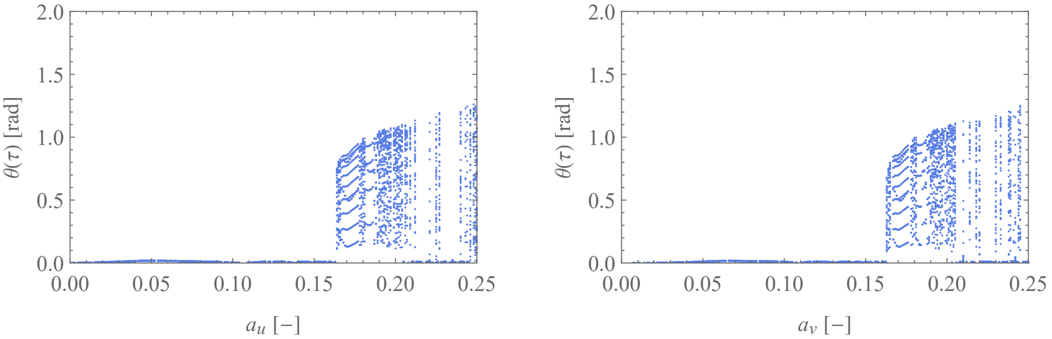

(c) θ over a_u with $a_v = a_w = 0$ and $\beta = 1.0$ (d) θ over a_v with $a_u = a_w = 0$ and $\beta = 1.0$

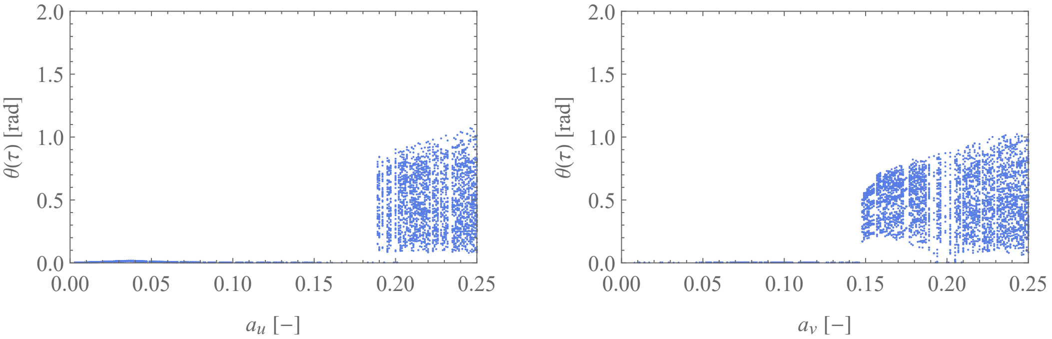

(e) θ over a_u with $a_v = a_w = 0$ and $\beta = 1.1$ (f) θ over a_v with $a_u = a_w = 0$ and $\beta = 1.1$

Figure 5.14: Bifurcation diagrams for θ over the excitation amplitude for a variation of the excitation direction and different excitation frequencies with the parameters set to: $l = 0.5$ m, $m = 1.32$ kg, $g = 9.81\ \frac{\text{m}}{\text{s}^2}$, $\alpha_\theta = \alpha_\phi = 0.0648$, $\varepsilon_r = 0.01$, $P_\theta = 0.05$, and $P_\phi = 0$.

excited in the v-direction and the different rows are excited with an excitation frequency of 0.9, 1.0, and 1.1.

In Figure 5.14a the bifurcation diagram for an excitation in the u-direction with an excitation frequency of $\beta = 0.9$ is shown. The diagram shows almost no deflection until the excitation amplitude of $a_u = 0.1$ is passed where the deflection jumps up to a value of 0.22 rad. Between that jump up and the excitation amplitude of $a_u = 0.237$ the bifurcation diagram shows a fixed point that is increasing over the whole area which has a slope change at a value of the excitation amplitude of $a_u = 0.20$. At the end of the shown area the dynamics of the spherical pendulum change to more chaotic appearing dynamics.

Figure 5.14c shows the bifurcation diagram for an excitation in the u-direction and an excitation frequency of $\beta = 1.0$. Until the excitation amplitude of $a_u = 0.16$ is exceeded the system shows no deflection. In this area the power take-off is stronger than the energy input with the excitation this results in a non-existing deflection of the coordinate θ. For the rest of the shown range the spherical pendulum shows dynamics that suggest quasi-periodic or chaotic dynamics. Within this area stable periodic orbits can be seen.

The bifurcation diagram for an excitation in the u-direction and an excitation frequency of $\beta = 1.1$ is shown in Figure 5.14e. Until the excitation amplitude of $a_u = 0.188$ is exceeded the coordinate θ shows no deflection. Afterwards the system shows dynamics that suggest chaotic or quasi-periodic dynamics.

In Figure 5.14b the bifurcation diagram for an excitation in the v-direction and an excitation frequency of $\beta = 0.9$ is shown. Compared to the excitation in the u-direction this bifurcation diagram shows a fixed point over the complete excitation area and there is no initial jump at an excitation amplitude of $a_u = 0.1$ observed. Additionally, the chaotic and quasi-periodic dynamics at the end of the range of the shown excitation amplitude cannot be seen anymore.

Figure 5.14d shows the bifurcation diagram for an excitation in the v-direction and an excitation frequency of $\beta = 1.0$. The bifurcation diagram looks similar to the bifurcation diagram that is excited in the u-direction in Figure 5.14c.

The bifurcation diagram for an excitation in the v-direction and an excitation frequency of 1.1 is shown in Figure 5.14f. The diagram shows no deflection until the excitation amplitude of $a_v = 0.148$ is exceeded. From there on the dynamics of the coordinate θ change and suggest quasi-periodic or chaotic dynamics.

When comparing the figures with the power take-off with those without the power take-off in Figure 5.4 it is evident the system becomes more periodic with a switched on power take-off. Additionally, the possible operational range in which the coordinate θ shows a deflection decreases with an inclusion of a power take-off.

In Figure 5.15 bifurcation diagrams for an excitation direction in vertical direction (left column) and a coupled excitation in the u- and v-directions (right column) is shown.

The excitation in the w-direction for an excitation frequency of $\beta = 0.9$ is shown in Figure 5.15a. For the most part the coordinate θ shows no deflection. In an area for the excitation amplitude from $a_w = 0.137$ to 0.215 the spherical pendulum however shows a fixed point.

With an increase in the excitation frequency to a value of 1.0 the area in which a fixed point can be seen increases, see Figure 5.15c. The fixed point can be seen for an area of the excitation amplitude from $a_w = 0.096$ to 0.238. The remaining area does not show a deflection of the coordinate θ.

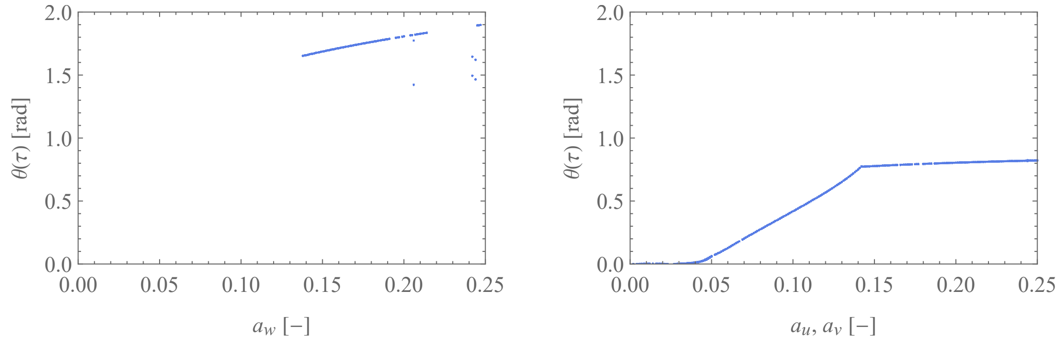

(a) θ over a_w with $a_u = a_v = 0$ and $\beta = 0.9$ (b) θ over a_u, a_v with $a_w = 0$ and $\beta = 0.9$

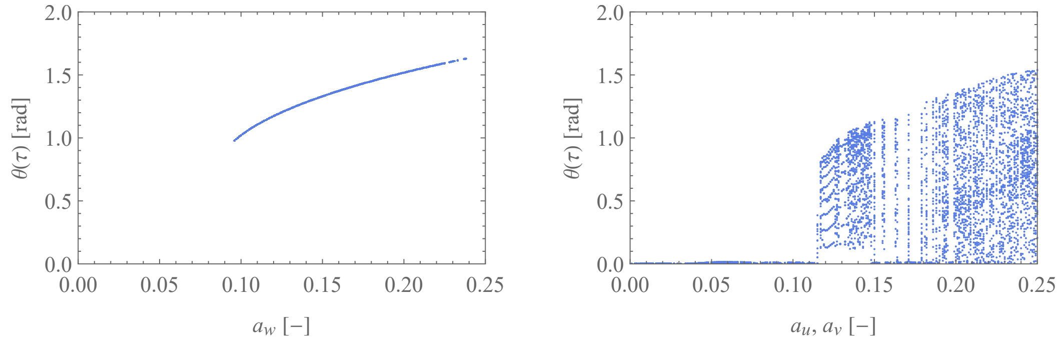

(c) θ over a_w with $a_u = a_v = 0$ and $\beta = 1.0$ (d) θ over a_u, a_v with $a_w = 0$ and $\beta = 1.0$

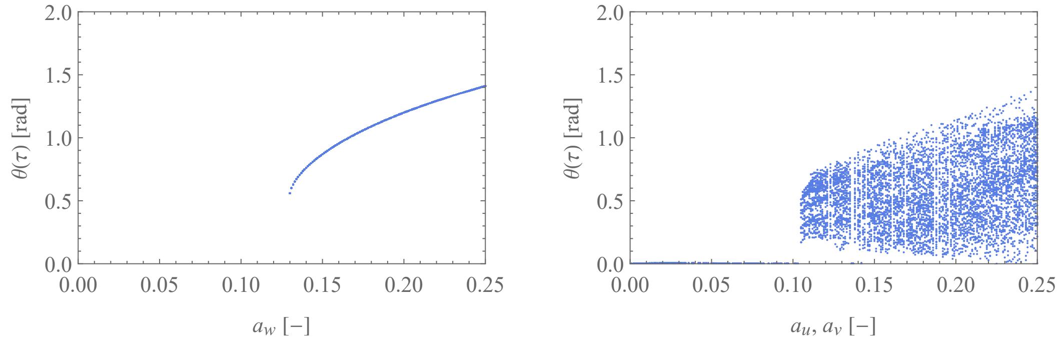

(e) θ over a_w with $a_u = a_v = 0$ and $\beta = 1.1$ (f) θ over a_u, a_v with $a_w = 0$ and $\beta = 1.1$

Figure 5.15: Bifurcation diagrams for θ over the excitation amplitude for a variation of the excitation direction and different excitation frequencies with the parameters set to: $l = 0.5$ m, $m = 1.32$ kg, $g = 9.81\ \frac{\text{m}}{\text{s}^2}$, $\alpha_\theta = \alpha_\phi = 0.0648$, $\varepsilon_r = 0.01$, $P_\theta = 0.05$, and $P_\phi = 0$.

Figure 5.15e shows the bifurcation diagram for an excitation in vertical direction with an excitation frequency of $\beta = 1.1$. The generalised coordinate θ shows a fixed point for a range of excitation amplitude from 0.13 to 0.25. For a value of the excitation amplitude lower than 0.13 the coordinate θ shows no deflection.

In Figure 5.15b the bifurcation diagram for a coupled excitation in both horizontal directions and an excitation frequency of 0.9 is shown. Over the whole shown range of the control parameter the coordinate θ shows a fixed point. This fixed point has a value close to zero until an excitation amplitude of $a_u = a_v = 0.04$ where the slope increases and the deflection of the coordinate θ increases gradually. At a value of the excitation amplitudes of $a_u = a_v = 0.14$ the fixed point bends and the slope of the fixed point decreases.

Figure 5.15d shows the bifurcation diagram for a coupled excitation in the u- and v-directions with an excitation frequency of $\beta = 1.0$. Until the excitation amplitudes reach a value of 0.11 the coordinate θ shows no deflection. With a further increase in the excitation amplitudes the dynamics of the system suggest quasi-periodic or chaotic dynamics with stable stable periodic orbits that are observed in-between.

The excitation frequency is further increased to a value of 1.1 which is shown in the bifurcation diagram in Figure 5.15f. Until the excitation amplitudes of 0.105 is reached the coordinate θ of the spherical pendulum shows no deflection. As the excitation amplitudes are increase further the system shows dynamics that suggest quasi-periodic or chaotic dynamics.

In Figure 5.16 bifurcation diagrams for coupled excitation in the u- and w-directions in the left column and a coupled excitation in the u-, v-, and w-directions in the right column for different excitation frequencies and a power take-off torque of $P_\theta = 0.05$ are shown.

A coupled excitation in the u- and w-directions and an excitation frequency of $\beta = 0.9$ is shown in Figure 5.16a. The bifurcation diagram shows almost no deflection of the coordinate θ until the excitation amplitudes exceed a value of 0.073. From there on the fixed point shows a steep rise until a value for the excitation amplitudes of 0.082 is exceeded where the deflection jumps up to $\theta = 1.5$ rad. With a further increase in the excitation amplitudes the system shows a fixed point that gradually increases.

With a decrease of the excitation frequency to a value of $\beta = 1.0$ the dynamics of the system change see Figure 5.16c. For small excitation amplitudes up to a value of 0.071 the coordinate θ shows none to small deflections. This is followed by a jump up to a value of the coordinate θ of 0.89 rad. The further development of the coordinate θ shows a fixed point that continuously increases.

For a value of the excitation frequency of $\beta = 1.1$ the system shows no deflection until the excitation amplitudes exceed a value of 0.09 see Figure 5.16e. This is followed by a small jump up to a value of the deflection of $\theta = 0.32$ rad. The bifurcation diagram shows a fixed point that constantly increases for the following range of excitation amplitudes shown.

In Figure 5.16b the omnidirectional pendulum energy harvester is excited in all three orthogonal directions in space with an excitation frequency of 0.9. For low excitation amplitudes the deflection of the coordinate θ shows a fixed point that increases with approximately exponential characteristics until it jumps up to a higher deflection of $\theta = 1.44$ rad at a value of the excitation amplitudes of 0.07. The bifurcation diagram shows a fixed point where the deflection gradually increases with an increase in the excitation amplitudes. When the excitation amplitudes pass a threshold of $a_u = a_v = a_w = 0.2$ the fixed point ceases to exist and the dynamics of the system change to a pattern that appears to be chaotic.

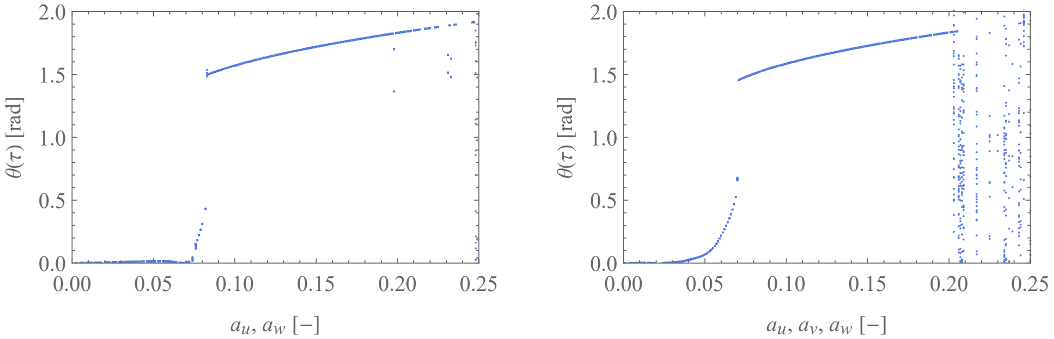

(a) θ over a_u, a_w with $a_v = 0$ and $\beta = 0.9$ (b) θ over a_u, a_v, a_w with $\beta = 0.9$

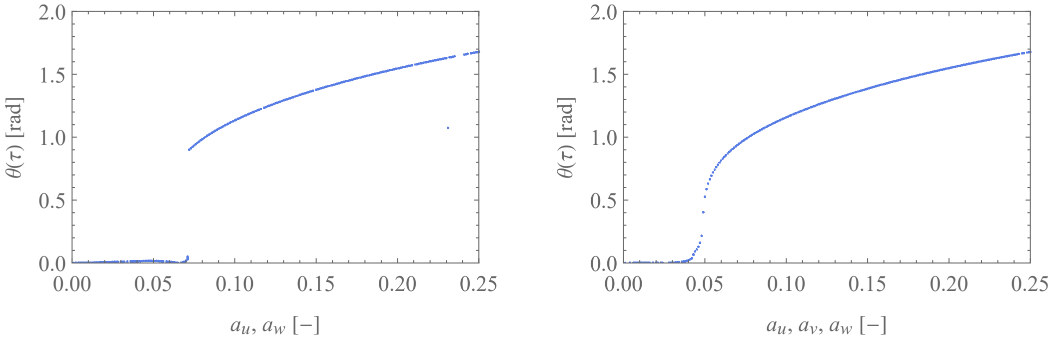

(c) θ over a_u, a_w with $a_v = 0$ and $\beta = 1.0$ (d) θ over a_u, a_v, a_w with $\beta = 1.0$

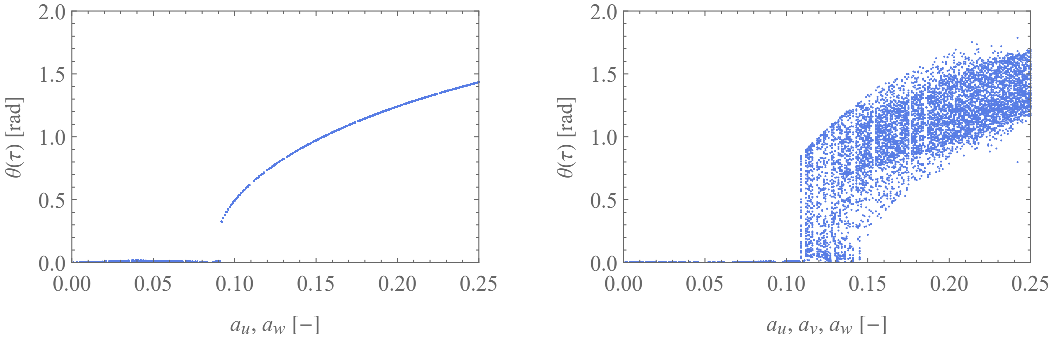

(e) θ over a_u, a_w with $a_v = 0$ and $\beta = 1.1$ (f) θ over a_u, a_v, a_w with $\beta = 1.1$

Figure 5.16: Bifurcation diagrams for θ over the excitation amplitude for a variation of the excitation direction and different excitation frequencies with the parameters set to: $l = 0.5$ m, $m = 1.32$ kg, $g = 9.81\ \frac{\text{m}}{\text{s}^2}$, $\alpha_\theta = \alpha_\phi = 0.0648$, $\varepsilon_r = 0.01$, $P_\theta = 0.05$, and $P_\phi = 0$.

Figure 5.16d shows a bifurcation diagram for an excitation in the u-, v-, and w-directions for an excitation frequency of $\beta = 1.0$. The bifurcation diagram shows a fixed point for the whole area shown that constantly increases with an increase in the excitation amplitudes. At a value for the excitation amplitudes of 0.049 the deflection of the generalised coordinate θ shows a small jump up while the fixed point undergoes an inflection point. With a further increase in the excitation amplitudes the deflection of the coordinate θ increases likewise.

With a further increase in the excitation frequency to a value of $\beta = 1.1$ the dynamics of the system change drastically, see Figure 5.16f. For low values of the excitation amplitudes lower than 0.109 the coordinate θ shows almost no deflection. With a further increase in the excitation amplitudes the predominant fixed point, of the two figures above with a lower excitation frequency, disappears completely and the bifurcation diagram of the system suggest quasi-periodic or chaotic dynamics.

5.3.1.1 Summary of Section 5.3.1

The comparison of the Figures 5.14, 5.15, and 5.16 shows similar results to those in Section 5.1.3. Firstly, when using a coupled excitation the coordinate θ shows a deflection for a lower excitation amplitude than for a single direction excitation. Secondly, with an inclusion of a vertical excitation the dynamics of the system are more periodic than a system that is excited solely in a horizontal direction. Thirdly, within the shown operational range the system does not show linear behaviour, there are areas in which the deflection of the coordinate θ increases at a stronger rate than in others. Therefore, it is important to keep that in mind for the following experimental evaluation to find the optimal operating point for the omnidirectional energy harvester.

5.3.1.2 Comparison of figures without and with power take-off from Section 5.1.3 and 5.3.1

When comparing the results in this section with a power take-off with the figures in Section 5.1.3 where the same figures are observed without a power take-off it can be observed that with a power take-off the system shows generally more periodic dynamics. In return this means that the existence of more fixed points makes the system is overall less quasi-periodic or chaotic.

5.3.2 Variation of the Excitation Frequency

Figure 5.17 shows bifurcation diagrams for the pendulum energy harvester with the excitation frequency as the control parameter for an excitation in the u-direction in the left column and an excitation in the v-direction in the right column for different values of the excitation amplitudes and a power take-off torque of $P_\theta = 0.05$.

In Figure 5.17a the spherical pendulum energy harvester is excited with a small excitation amplitude of $a_u = 0.064$. The bifurcation diagram shows a fixed point of the coordinate θ with almost no deflection over the whole shown area.

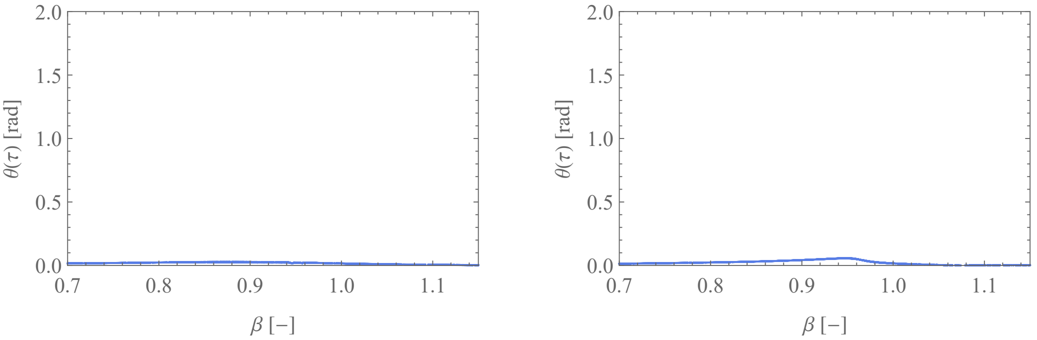

(a) θ over β with $a_u = 0.064$ and $a_v = a_w = 0$ (b) θ over β with $a_v = 0.064$ and $a_u = a_w = 0$

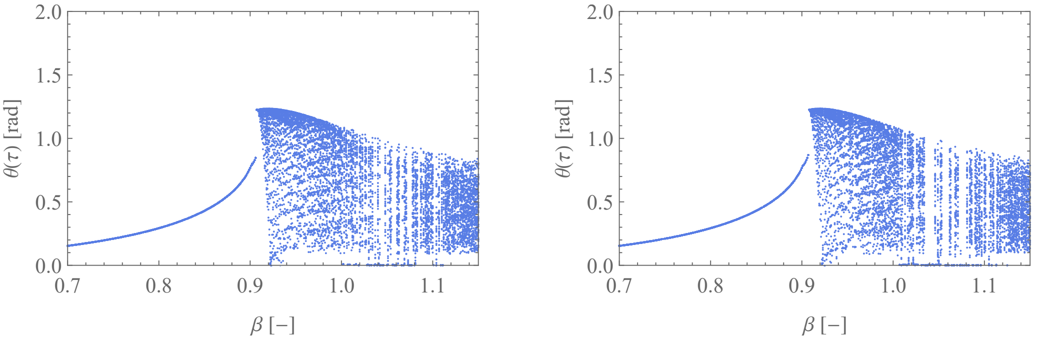

(c) θ over β with $a_u = 0.2$ and $a_v = a_w = 0$ (d) θ over β with $a_v = 0.2$ and $a_u = a_w = 0$

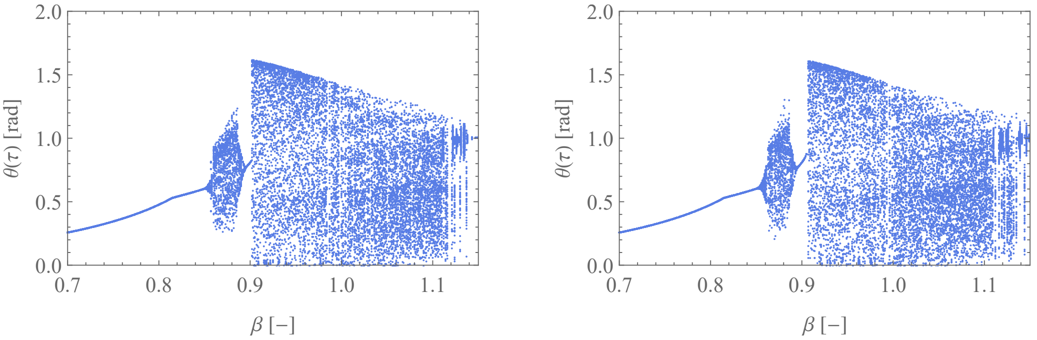

(e) θ over β with $a_u = 0.3$ and $a_v = a_w = 0$ (f) θ over β with $a_v = 0.3$ and $a_u = a_w = 0$

Figure 5.17: Bifurcation diagrams for θ over the excitation frequency for a variation of the excitation direction and different excitation amplitudes with the parameters set to: $l = 0.5$ m, $m = 1.32$ kg, $g = 9.81\ \frac{\mathrm{m}}{\mathrm{s}^2}$, $\alpha_\theta = \alpha_\phi = 0.0648$, $\varepsilon_r = 0.01$, $P_\theta = 0.05$, and $P_\phi = 0$.

With an increase in the excitation amplitude to a value of $a_u = 0.2$ the coordinate θ shows higher deflections see Figure 5.17c. For an excitation frequency from $\beta = 0.7$ to 0.907 the system shows a fixed point for the coordinate θ that increases with approximately exponential characteristics with an increase in the excitation frequency. With a further increase in the excitation frequency the system shows a jump up to dynamics that suggest quasi-periodic or chaotic dynamics. The maximum deflection likewise decreases with an increase in the excitation frequency.

Figure 5.17e shows a bifurcation diagram with a value for the excitation amplitude of $a_u = 0.3$. For an excitation frequency from $\beta = 0.7$ to 0.85 the coordinate θ shows a fixed point which then bifurcates and an area that suggests quasi-periodic or chaotic dynamics emerge. This area is interrupted by an area that shows a fixed point for an excitation frequency from $\beta = 0.89$ to 0.90. With an excitation frequency higher than 0.9 the system shows an area that suggest quasi-periodic or chaotic dynamics.

The bifurcation diagram in Figure 5.17b is excited in the v-direction with a small excitation amplitude of $a_v = 0.064$. For this excitation amplitude the coordinate θ shows a fixed point with a small almost not existing deflection.

In Figure 5.17d the excitation amplitude is increased to a value of $a_v = 0.2$. The bifurcation diagram shows a fixed point that increases with approximately exponential characteristics for a value of the excitation frequency of $\beta = 0.7$ to 0.907. With a further increase in the excitation frequency the system shows an area that suggests quasiperiodicity or chaos.

Figure 5.17f shows the bifurcation diagram with a value for the excitation amplitude of $a_v = 0.3$. Similarly to the bifurcation diagram with the excitation in the u-direction this figure shows initially a fixed point until the excitation frequency of 0.85 is exceeded where the fixed point bifurcates in an area that suggests quasi-periodic or chaotic dynamics. This area abruptly changes back to a fixed point for a value of the excitation frequency from $\beta = 0.89$ to 0.907. With a further increase in the excitation frequency the bifurcation diagram for the coordinate θ suggests quasi-periodic or chaotic dynamics for the remaining frequency range.

In Figure 5.18 bifurcation diagrams for an excitation in the w-direction and in the u- and v-directions with an power take-off torque of $P_\theta = 0.05$ and the excitation frequency β as control parameter are shown.

Figure 5.18a shows an excitation in the w-direction with an excitation amplitude of $a_w = 0.064$. It can be seen that the numerical analysis for this set of parameters does not show any output. A similar behaviour can be observed in Figure 5.18e for a value of the excitation amplitude of $a_w = 0.3$.

In Figure 5.18c the bifurcation diagram for an excitation amplitude of $a_w = 0.2$ is shown. The analysis shows no numerical result until the excitation frequency of 0.848 is exceeded where the pendulum energy harvester shows a fixed point that gradually decreases with an increase in the excitation frequency.

The bifurcation diagram for the system that is excited in the two horizontal directions with a value for the excitation amplitudes of $a_u = a_v = 0.064$ is shown in Figure 5.18b. The system shows a fixed point that increases in value with an increase in the excitation frequency. When a value for the excitation frequency of 0.989 is exceeded the fixed point performs a down jump to a value of the coordinate θ close to zero which is observed till the end of the shown excitation frequency.

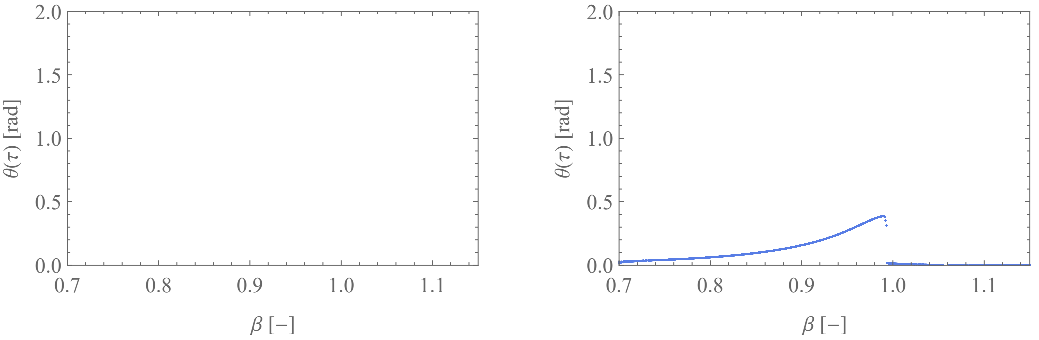

(a) θ over β with $a_w = 0.064$ and $a_u = a_v = 0$

(b) θ over β with $a_u = a_v = 0.064$ and $a_w = 0$

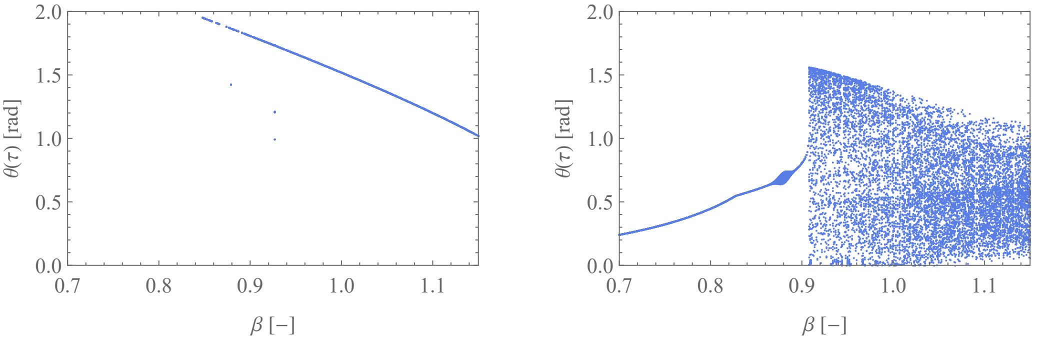

(c) θ over β with $a_w = 0.2$ and $a_u = a_v = 0$

(d) θ over β with $a_u = a_v = 0.2$ and $a_w = 0$

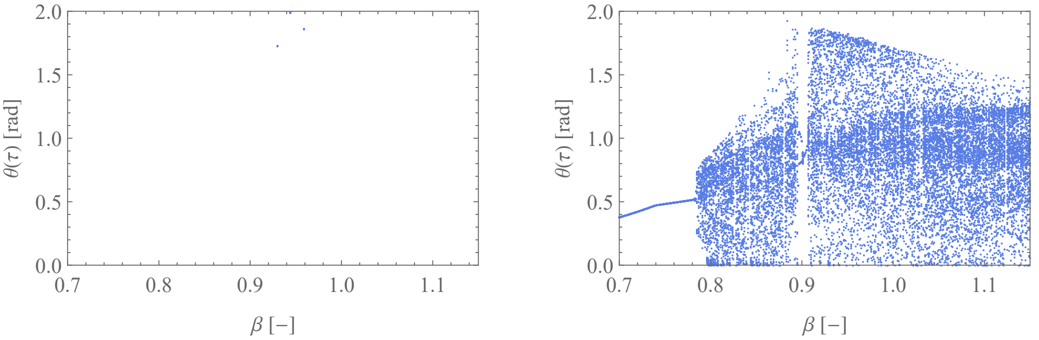

(e) θ over β with $a_w = 0.3$ and $a_u = a_v = 0$

(f) θ over β with $a_u = a_v = 0.3$ and $a_w = 0$

Figure 5.18: Bifurcation diagrams for θ over the excitation frequency for a variation of the excitation direction and different excitation amplitudes with the parameters set to: $l = 0.5$ m, $m = 1.32$ kg, $g = 9.81\ \frac{\mathrm{m}}{\mathrm{s}^2}$, $\alpha_\theta = \alpha_\phi = 0.0648$, $\varepsilon_r = 0.01$, $P_\theta = 0.05$, and $P_\phi = 0$.

The excitation amplitudes are increased to a value of $a_u = a_v = 0.2$ in Figure 5.18d. The figure shows a fixed point until the excitation frequency of 0.907 is exceeded with a short exception for an excitation frequency from $\beta = 0.866$ to 0.89 where the fixed point bifurcates and merges again shortly after. For a value of the excitation frequency higher than 0.807 the dynamics of the system suggest quasi-periodicity or chaos.

Figure 5.18f shows a bifurcation diagram for the omnidirectional pendulum energy harvester that is excited with values for the excitation amplitudes of $a_u = a_v = 0.3$. For an excitation frequency of $\beta = 0.7$ to 0.78 the deflection of the coordinate θ shows a fixed point that subsequently bifurcates. This is followed by an area that suggests quasi-periodicity or chaos. For an excitation frequency of $\beta = 0.896$ to 0.906 the system shows stable periodic orbits which return to an area that suggests quasi-periodic or chaotic dynamics. For this configuration of excitation amplitudes areas can be seen within the quasi-periodic or chaotic dynamics in which the single points of the bifurcation diagram are denser than in others, these are the so-called veins.

In Figure 5.19 bifurcation diagrams with the excitation frequency β as control parameter for coupled excitations in the u- and w-directions and in the u-, v-, and w-directions are shown for different excitation amplitudes and a power take-off torque of $P_\theta = 0.05$.

The excitation amplitudes are set to a value of $a_u = a_w = 0.064$ see Figure 5.19a. With this low excitation the coordinate θ shows a fixed point with a very small deflection.

In Figure 5.19c the excitation amplitudes are increased to a value of $a_u = a_w = 0.2$. With this the deflection of the generalised coordinate θ increases. The bifurcation diagram shows a fixed point for a value of the excitation frequency from $\beta = 0.7$ to 0.796. Afterwards, it comes to a jump up to a higher deflection value of the fixed point at an excitation frequency of $\beta = 0.81$. During this jump up the system shows dynamics that suggest quasi-periodicity or chaos. For an excitation frequency from $\beta = 0.81$ to 1.12 the coordinate θ shows a fixed point with the occasional missing deflection value because of issues in the numerical analysis. For a value of the excitation frequency from 0.94 to 0.956 there is a trapezium-shaped area in addition to the fixed point can be seen with a deflection value lower than those of the fixed point. At the end of the shown area of the excitation frequency with a value higher than 1.12 the fixed point bifurcates.

Figure 5.19e shows the bifurcation diagram for a value of the excitation amplitudes of $a_u = a_w = 0.3$. It is important to mention that for this configuration of the coupled excitation it is possible that the pendulum bob performs a looping and therefore the values of the deflection of the coordinate θ could in fact be outside of the displayed range of the y-axis. For a value of the excitation frequency from $\beta = 0.7$ to 0.73 the bifurcation diagram shows a fixed point that subsequently bifurcates and an area that suggests quasi-periodicity or chaos emerges. This area is interrupted by an area of stable periodic orbits for an excitation frequency from $\beta = 1.08$ to 1.19. It is possible that there is a fixed point observed in the area of $\beta = 0.98$ to 1.15. However, this cannot be confirmed because of the full rotation of the pendulum bob and thus the resulting missing data points.

In Figure 5.19b the omnidirectional pendulum energy harvester is excited in all three directions of space with a value of the excitation amplitudes set to $a_u = a_v = a_w = 0.064$. The bifurcation diagram shows a fixed point of the whole range of the control parameter. The fixed point shows clear softening characteristics with a jump up to a higher deflection of 1.36 rad at a value of the excitation frequency of 0.91. With a further increase in the excitation frequency

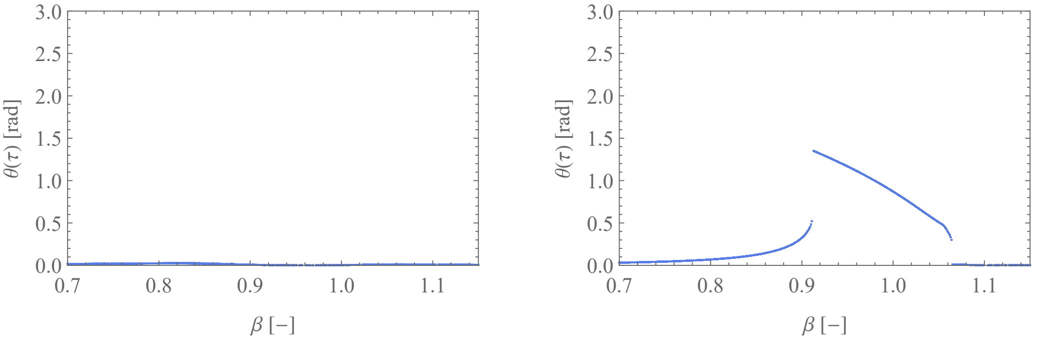

(a) θ over β with $a_u = a_w = 0.064$ and $a_v = 0$ (b) θ over β with $a_u = a_v = a_w = 0.064$

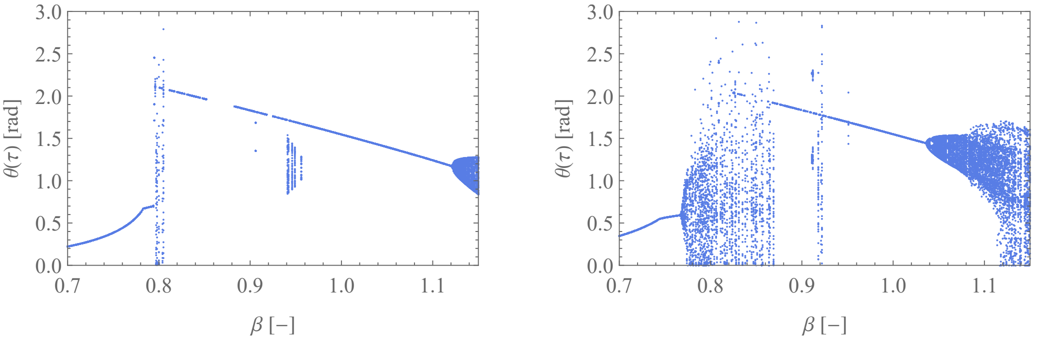

(c) θ over β with $a_u = a_w = 0.2$ and $a_v = 0$ (d) θ over β with $a_u = a_v = a_w = 0.2$

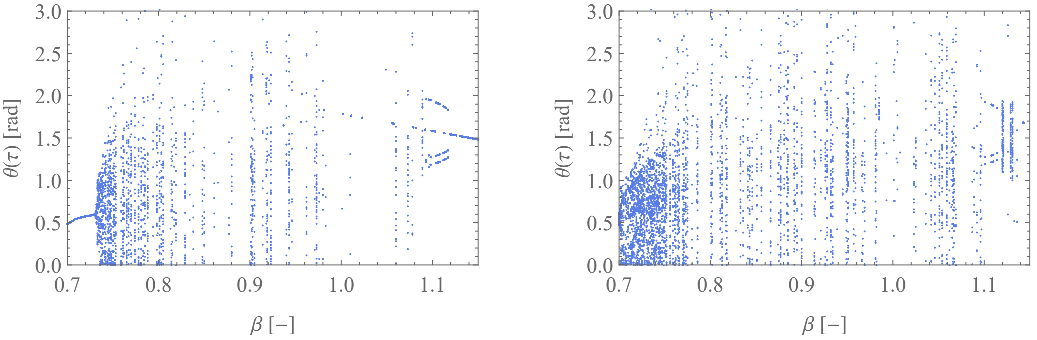

(e) θ over β with $a_u = a_w = 0.3$ and $a_v = 0$ (f) θ over β with $a_u = a_v = a_w = 0.3$

Figure 5.19: Bifurcation diagrams for θ over the excitation frequency for a variation of the excitation direction and different excitation amplitudes with the parameters set to: $l = 0.5$ m, $m = 1.32$ kg, $g = 9.81\ \frac{\mathrm{m}}{\mathrm{s}^2}$, $\alpha_\theta = \alpha_\phi = 0.0648$, $\varepsilon_r = 0.01$, $P_\theta = 0.05$, and $P_\phi = 0$.

the deflection of the coordinate θ gradually decreases until jumping down to a value close to zero at an excitation frequency of 1.06.

The excitation amplitudes are increased to a value of $a_u = a_v = a_w = 0.2$ see Figure 5.19d. For an excitation frequency of $\beta = 0.7$ to 0.766 the coordinate θ shows a fixed point. This fixed point then bifurcates and an area that suggests quasi-periodic or chaotic dynamics emerges. At an excitation frequency of 0.868 a fixed point suddenly appears that remains until the excitation frequency of 1.04 is exceeded. Here the fixed point bifurcates again and an area that suggest quasi-periodicity or chaos emerges.

Figure 5.19f shows the bifurcation diagram for a value of the excitation amplitudes of $a_u = a_v = a_w = 0.3$. The dynamics for these high excitation amplitudes are hardly quantifiable solely an area of stable periodic orbits can be seen for an excitation frequency from $\beta = 1.09$ to 1.119.

5.3.2.1 Summary of Section 5.3.2

When comparing Figures 5.17, 5.18, and 5.19 a few general observations can be made. Generally, the softening characteristics of the system can be seen in the bifurcation diagrams. This is proven by the fact that the highest deflection for the coordinate θ is always reached at a value for the excitation frequency lower than the natural frequency. In other words the highest deflection is reached at a value for β lower than one. Additionally, it can be seen that with an increase in the excitation amplitude the defection of the coordinate θ generally increases. When the pendulum energy harvester is excited with a coupled excitation configuration that includes a vertical component that is parametrically excited the dynamics of the coordinate θ are generally more periodic than without the counterpart. It can be observed that in the numerically calculated results with an included power take-off an excitation amplitude of 0.064 is to low too see a deflection of the coordinate θ.

5.3.2.2 Comparison of the figures without and with power take-off from Sections 5.1.4 and 5.3.2

Comparing Figures 5.17, 5.18, and 5.19 to those in Section 5.1.4 which are the same figures but without a power take-off it is evident that generally a lower deflection of the coordinate θ can be observed. Additionally, it can be seen that the power take-off seems to increase the periodicity of the system. And in some cases a switched on power take-off completely cancels out the motion of the pendulum bob of the energy harvester.

5.3.3 Poincaré Sections

Figure 5.20 shows Poincaré sections for an excitation in the u-direction for different excitation amplitudes and excitation frequencies and a power take-off torque of $P_\theta = 0.05$.

In Figure 5.20a the Poincaré section for an excitation amplitude of $a_u = 0.064$ and an excitation frequency of $\beta = 0.9$ is shown. Generally it can be observed that the deflections for this low excitation amplitude are low as well. The Poincareé section shows a line that is processing towards the centre of the coordinate system.

With an increase in the excitation frequency to a value of $\beta = 0.9$ the Poincaré section shows a sun-like shape whose beams are spiralling towards the middle as if they are forming a circle see Figure 5.20c.

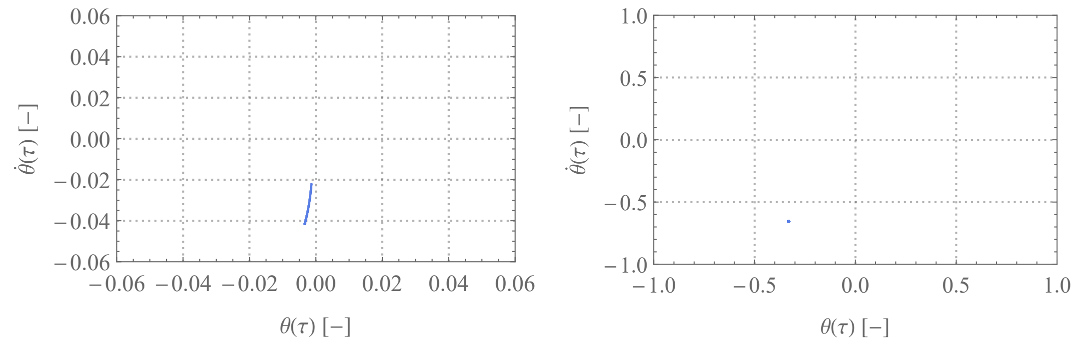

(a) Poincaré section with $a_u = 0.064$ and $\beta = 0.9$ (b) Poincaré section with $a_u = 0.3$ and $\beta = 0.9$

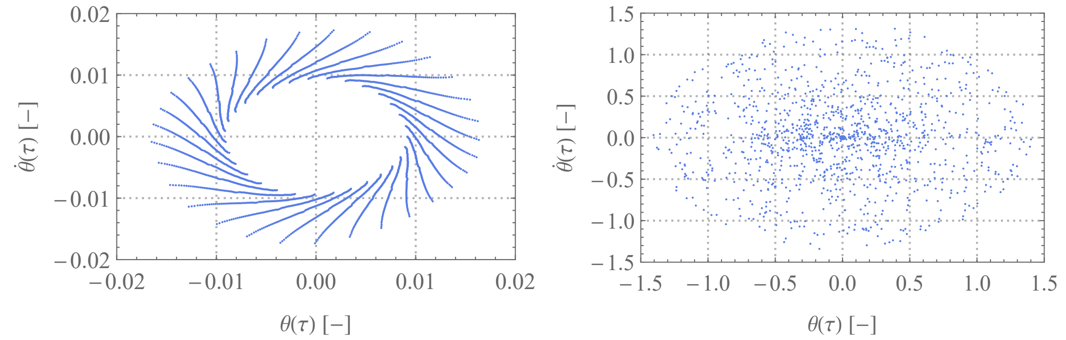

(c) Poincaré section with $a_u = 0.064$ and $\beta = 1.0$ (d) Poincaré section with $a_u = 0.3$ and $\beta = 1.0$

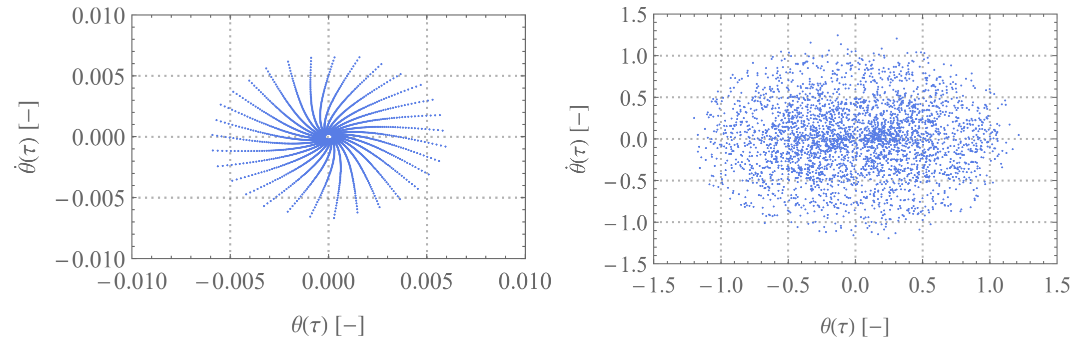

(e) Poincaré section with $a_u = 0.064$ and $\beta = 1.1$ (f) Poincaré section with $a_u = 0.3$ and $\beta = 1.1$

Figure 5.20: Poincaré sections for a variation of the excitation amplitudes and different excitation frequencies with the parameters set to: $l = 0.5$ m, $m = 1.32$ kg, $g = 9.81\ \frac{\mathrm{m}}{\mathrm{s}^2}$, $\alpha_\theta = \alpha_\phi = 0.0648$, $a_v = a_w = 0$, $\varepsilon_r = 0.01$, $P_\theta = 0.05$, and $P_\phi = 0$.

Figure 5.20e shows the Poincaré section for the omnidirectional pendulum energy harvester that is excited with the excitation amplitude being $a_u = 0.064$ and the excitation frequency being $\beta = 1.1$. The figure shows a sun-like shaped figure whose rays are spiralling towards the middle. Here however the middle has a lower radius than for the Poincaré section with an excitation frequency of 1.0.

With an increase in the excitation amplitude to a value of $a_u = 0.3$ and a value for the excitation frequency of $\beta = 0.9$ the Poincaré section shows a fixed point see Figure 5.20b. This shows that the dynamics of the spherical pendulum are periodic for this configuration of the excitational parameters.

Figure 5.20d shows the Poincaré section for an excitation amplitude of $a_u = 0.3$ and an excitation frequency of $\beta = 1.0$. The Poincaré section suggests chaotic dynamics for the shown configuration of excitation parameters.

In Figure 5.20f the Poincaré section for the system that is excited with an excitation amplitude of $a_u = 0.3$ and an excitation frequency of $\beta = 1.1$ is shown. The system shows dynamics that suggest chaos.

Figure 5.21 shows Poincaré sections for different variations of coupled excitations with different excitation frequencies and a power take-off torque of $P_\theta = 0.05$.

The Poincaré section with a value for the excitational parameters $a_u = a_w = 0.2$, $a_v = 0$ and $\beta = 0.9$ in Figure 5.21a shows a single point and therefore indicates that the dynamics of the coordinate θ are periodic. This is in line with the fixed point that is shown in the bifurcation diagram in Figure 5.19e.

In Figure 5.21c the Poincaré section with a value for the excitation amplitudes of $a_u = a_w = 0.2$ and $a_v = 0$ and a value for the excitation frequency of $\beta = 1.0$ is shown. The figure shows an elliptical trajectory which consists of a great number of single points that connect together in a way that it appears to be a line. This shape indicates quasi-periodic dynamics.

Figure 5.21e shows the Poincaé section for an value for the excitational parameters of $a_u = a_w = 0.2$, $a_v = 0$, and $\beta = 1.1$. Figure 5.21e shows quasi-periodicity for the shown excitational parameters.

For the next figures the omnidirectional pendulum energy harvester is excited in all three directions of space. The Poincaré section in Figure 5.21b shows the results for the system that is excited with the parameters being $a_u = a_v = a_w = 0.2$ and $\beta = 0.9$. The Poincaré section shows one single point which indicates that the dynamics of the coordinate θ are periodic for the shown excitational parameters.

In Figure 5.21d the Poincaré section for a value for the excitation amplitudes of $a_u = a_v = a_w = 0.2$ and an excitation frequency of $\beta = 1.0$ is shown. The elliptical shape in the Poincaré section shows that the coordinate θ is quasi-periodic for the shown excitational parameters.

Figure 5.21f shows the Poincaré section for a value of the excitation amplitudes of $a_u = a_v = a_w = 0.2$ and a value for the excitation frequency of $\beta = 1.1$. The Poincaré sections shows dynamics that show an elliptical shape however the single points are not placed next to each other anymore but instead form some kind of belt around the centre of the coordinate system. This would indicate that the coordinate θ is in some kind of transitioning progress from quasi-periodicity to chaos.

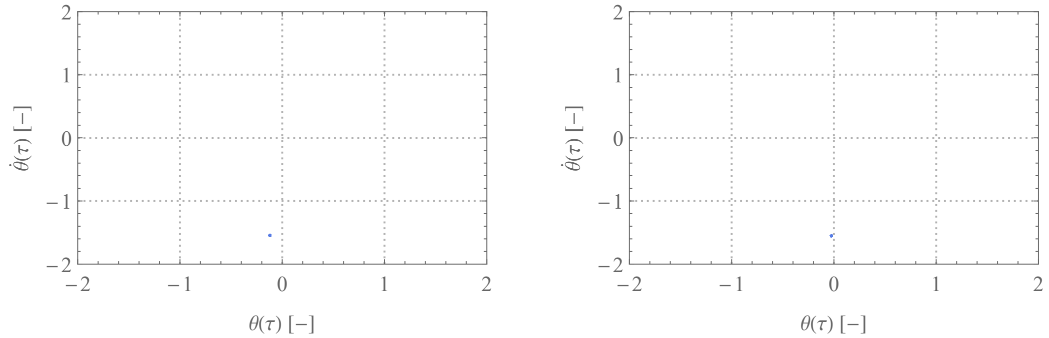

(a) Poincaré section with $a_u = a_w = 0.2$, $a_v = 0$ and $\beta = 0.9$

(b) Poincaré section with $a_u = a_v = a_w = 0.2$ and $\beta = 0.9$

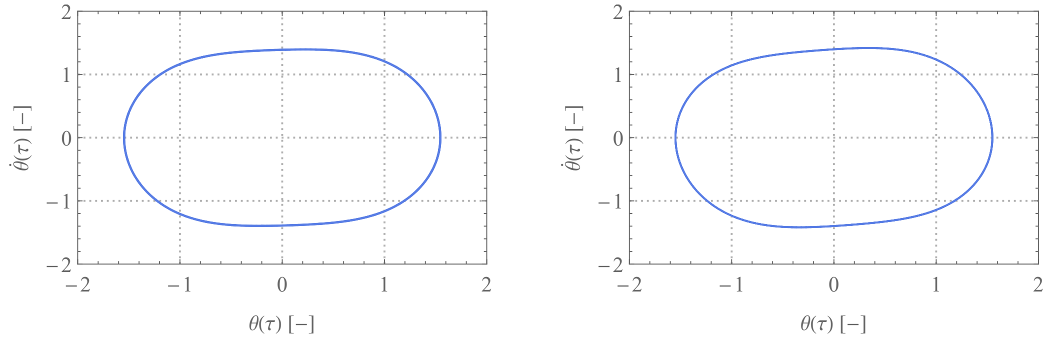

(c) Poincaré section with $a_u = a_w = 0.2$, $a_v = 0$, and $\beta = 1.0$

(d) Poincaré section with $a_u = a_v = a_w = 0.2$ and $\beta = 1.0$

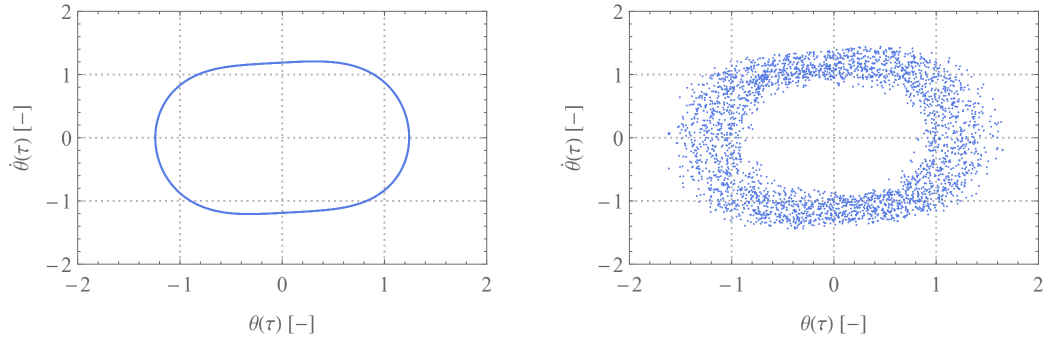

(e) Poincaré section with $a_u = a_w = 0.2$, $a_v = 0$, and $\beta = 1.1$

(f) Poincaré section with $a_u = a_v = a_w = 0.2$ and $\beta = 1.1$

Figure 5.21: Poincaré sections for a variation of the excitation amplitudes and different excitation frequencies with the parameters set to: $l = 0.5$ m, $m = 1.32$ kg, $g = 9.81\ \frac{\mathrm{m}}{\mathrm{s}^2}$, $\alpha_\theta = \alpha_\phi = 0.0648$, $\varepsilon_r = 0.01$, $P_\theta = 0.05$, and $P_\phi = 0$.

5.4 Power Output of the Omnidirectional Pendulum Energy Harvester

This section observes the dimensionless arithmetic mean rectified power output P_{avg} over variations of the excitation amplitude, excitation frequency, and the power take-off torque. This allows a discussion of the optimal operational point or area of the energy harvester. The power output is generated by introducing a power take-off torque in the direction of the generalised coordinate θ since the power that can be taken-off of the coordinate ϕ is highly limited and would cause issues with the numerical analysis. The dimensionless arithmetic mean rectified power output P_{avg} is a good indicator to determine the efficiency of the omnidirectional energy harvester. Figures similar to those in this section were previously published [1] and this section can be seen as an extension to the publication. The difference is that the pendulum energy harvester is excited in all orthogonal directions of space in the journal article and in this section the energy harvester is excited in the u- and in u-, w-directions.

In the publication a few remarks were made to clarify the procedure. These apply here as well and are therefore summarised. To calculate the actual power output in Watts Equation (5.3) can used. The parameters $ml^2\omega_0^2$ come from the dimensionalisation of the power take-off term and the parameter ω_0 is attributed to the dimensionless time.

$$P_{act} = P_{avg} m l^2 \omega_0^3. \tag{5.3}$$

For the power output the sign shaped signal is rectified and arithmetically averaged to see the arithmetic mean rectified power output. The numerical analysis arithmetically averages the power output for a time period from $\tau = 800 - 900$ this ensures that the transient response is fully decayed. It is possible that the numerical computation stops within the pre-defined range for τ. This results in a lower value for P_{avg} than is actually the case. These inaccuracies however are easy to identify and therefore do not pose any problem.

Figure 5.22 shows diagrams for the arithmetic mean rectified power output over the dimensionless power take-off torque for different values of the excitation amplitudes and frequencies.

In Figure 5.22a the spherical pendulum is excited in the u-direction with an excitation amplitude of $a_u = 0.064$. For an excitation frequency of 0.9 (blue circles) the arithmetic mean rectified power output P_{avg} shows a local maximum of 0.0024 at a value of the power take-off torque of $P_\theta = 0.027$. With a further increase in the power take-off torque the arithmetic mean rectified power output decreases. An increase in the excitation frequency to a value of 1.0 (orange triangles) decreases the overall power output. For the excitation frequency of 1.1 (red diamonds) the arithmetic mean rectified power output shows an initial deflection at $P_\theta = 0.01$. With a further increase of the power take-off torque the arithmetic mean rectified power output decreases.

The excitation amplitude is increased to a value of $a_u = 0.2$ in Figure 5.22c. For an excitation frequency of 0.9 the arithmetic mean rectified power output sees a steep rise for an increase of the power take-off torque until it reaches a maximum for a value for the power take-off torque of 0.079. From there on the arithmetic mean rectified power output gradually decreases until jumping down to a value close to zero at a value of the power take-off torque of 0.1. The excitation of the omnidirectional pendulum harvester at the natural frequency shows a

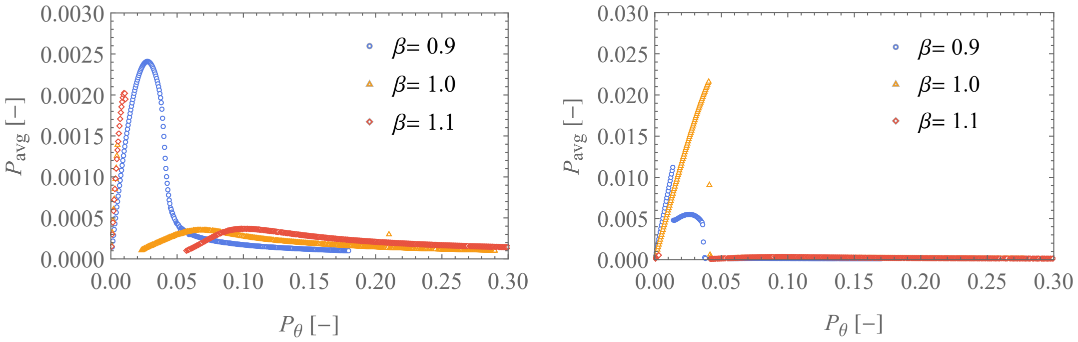

(a) P_{avg} over P_θ with $a_u = 0.064$ and $a_w = 0$

(b) P_{avg} over P_θ with $a_u = a_w = 0.064$

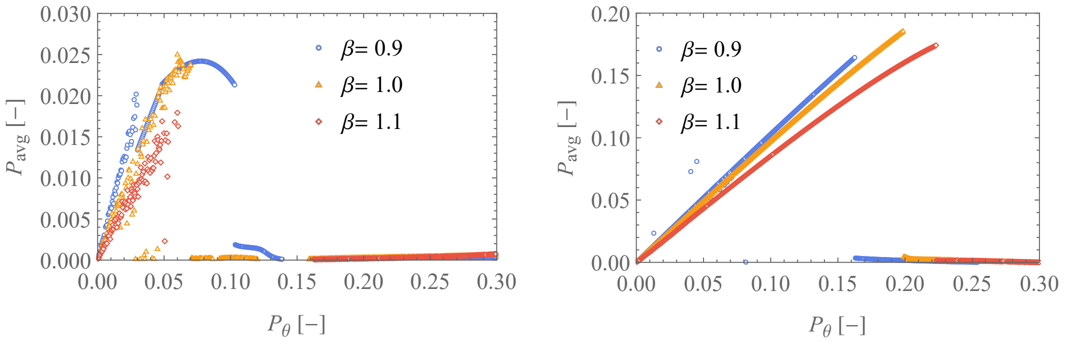

(c) P_{avg} over P_θ with $a_u = 0.2$ and $a_w = 0$

(d) P_{avg} over P_θ with $a_u = a_w = 0.2$

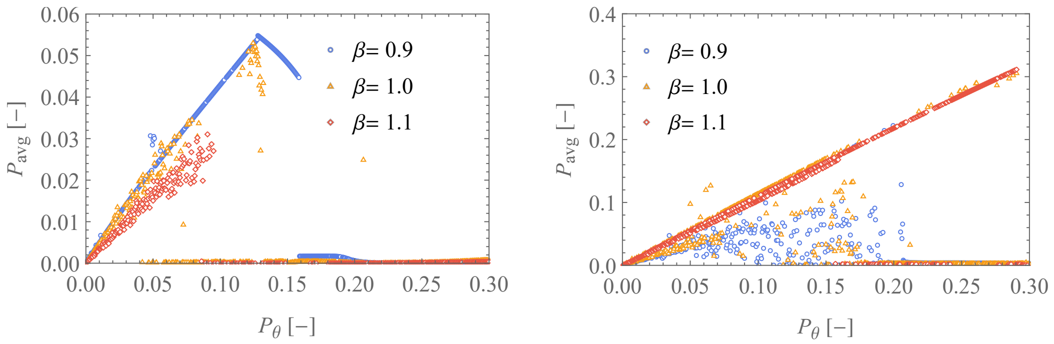

(e) P_{avg} over P_θ with $a_u = 0.3$ and $a_w = 0$

(f) P_{avg} over P_θ with $a_u = a_w = 0.3$

Figure 5.22: Arithmetic mean rectified power output over the power take-off torque for a variation of the excitation direction and different excitation frequencies with the parameters set to: $l = 0.5$ m, $m = 1.32$ kg, $g = 9.81\ \frac{\mathrm{m}}{\mathrm{s}^2}$, $\alpha_\theta = \alpha_\phi = 0.0648$, $a_v = 0$, $\varepsilon_r = 0.01$, and $P_\phi = 0$.

steep rise at the beginning for low power take-off torques and then jumps down to a value close to zero for a power take-off torque of $P_\theta = 0.069$. The excitation frequency of 1.1 shows the lowest overall arithmetic mean rectified power output. The maximum power output is reached for a value of the power take-off torque of 0.058.

In Figure 5.22e the excitation amplitude is increased to a value of $a_u = 0.3$. This increase in the excitation amplitude generally increases the arithmetic mean rectified power output of the energy harvester. The system that is excited with an excitation frequency of 0.9 shows a maximum value of the arithmetic mean rectified power output of $P_{avg} = 0.054$ for a power take-off torque of 0.129. For an excitation frequency of 1.0 the maximum power output can be observed for a value slightly lower than the one for $\beta = 0.9$. The omnidirectional pendulum energy harvester that is excited with an excitation frequency of 1.1 shows a steep increase of the power output a for low power take-off torques and reaches its maximum 0.0547 for a value of the power take-off torque of 0.093.

Figure 5.22b shows the arithmetic mean rectified power output of the omnidirectional pendulum energy harvester that is excited with different excitation frequencies and excitation amplitudes with a value of $a_u = a_w = 0.064$. For an excitation frequency of $\beta = 0.9$ the power output increases steeply at the beginning until a power take-off torque of 0.014 is exceeded. With a further increase of the power take-off torque the arithmetic mean rectified power output jumps down to a lower value of 0.005 and increases slightly in the following until jumping down to zero eventually at a value for the power take-off torque of 0.037. For an excitation frequency of 1.0 a maximum value of the arithmetic mean rectified power output of 0.022 is reached at a power take-off torque of 0.04. This is the highest reachable power output for this shown configuration of excitation parameters. For an excitation frequency of 1.1 the spherical pendulum shows no power output.

The excitation amplitudes are increased to a value of $a_u = a_w = 0.2$ in Figure 5.22d. For an excitation frequency of 0.9 the arithmetic mean rectified power output sees an almost linear increase with an increase of the power take-off torque. The maximum value of the arithmetic mean rectified power output of 0.16 is reached for a power take-off torque of 0.16. With a further increase in the power take-off torque the arithmetic mean rectified power output jumps down to a value close to zero. For an excitation frequency of 1.0 the maximum value of the arithmetic mean rectified power output of 0.19 is reached at a power take-off torque of 0.2. Here as well the arithmetic mean rectified power output jumps down to a value close to zero with a further increase of the power take-off torque. The maximum value for the arithmetic mean rectified power output of 0.17 is reached at a power take-off torque of 0.22 for a system that is excited with an excitation frequency of 1.1.

With an increase in the excitation amplitudes to $a_u = a_w = 0.3$ significant changes in the average power output curves can be observed in Figure 5.22f. For an excitation frequency of 0.9 the arithmetic mean rectified power output unfortunately follows no clear pattern over the power take-off torque. The excitation frequencies of 1.0 and 1.1 show an almost linear increase of the arithmetic mean rectified power output over the power take-off torque. The maximum value of the arithmetic mean rectified power output 0.31 for $\beta = 1.1$ is reached at an power take-off torque of 0.29. For an excitation frequency of $\beta = 1.0$ the maximum power output of 0.37 is reached for a power take-off torque of 0.355 and is therefore unfortunately outside of the shown range of the diagram. The difference between the two excitation frequencies is that $\beta = 1.1$ shows fewer numerical errors in the area of the power take-off torque higher than 0.15.

It is evident that the arithmetic mean rectified power output of the energy harvester is highly dependent on the excitation amplitudes, excitation frequencies, and the power take-off torque. For the numerical analysis only the results of Figures 5.22d and 5.22f show adequate power outputs.

Figure 5.23 shows plot that show the arithmetic mean rectified power output over the power take-off torque for a variation of the excitation frequency and the excitation amplitudes.

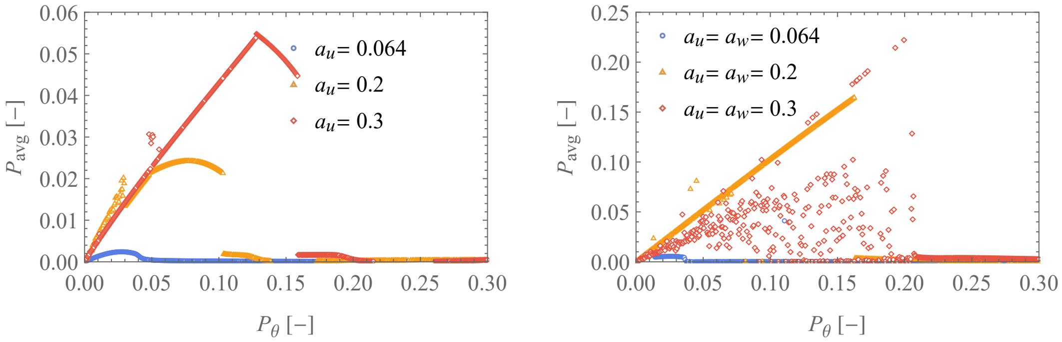

(a) P_{avg} over P_θ with $\beta = 0.9$ and $a_w = 0$

(b) P_{avg} over P_θ with $\beta = 0.9$

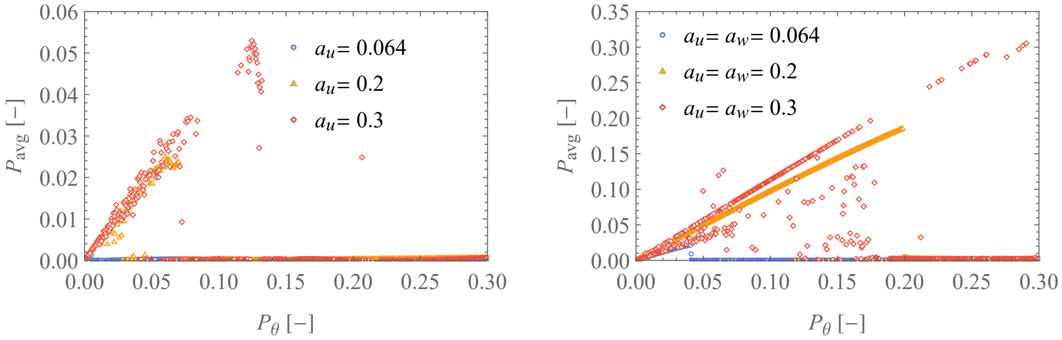

(c) P_{avg} over P_θ with $\beta = 1.0$ and $a_w = 0$

(d) P_{avg} over P_θ with $\beta = 1.0$

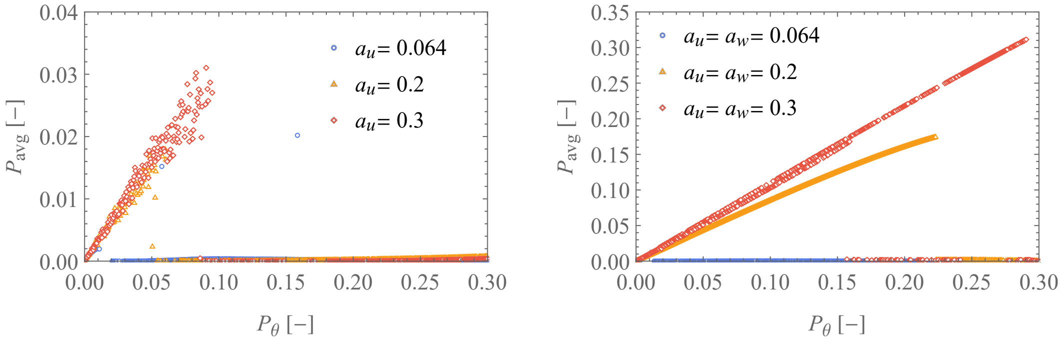

(e) P_{avg} over P_θ with $\beta = 1.1$ and $a_w = 0$

(f) P_{avg} over P_θ with $\beta = 1.1$

Figure 5.23: Arithmetic mean rectified power output over the power take-off torque for a variation of the excitation direction and amplitude and different excitation frequencies with the parameters set to: $l = 0.5$ m, $m = 1.32$ kg, $g = 9.81\ \frac{\mathrm{m}}{\mathrm{s}^2}$, $\alpha_\theta = \alpha_\phi = 0.0648$, $a_v = 0$, $\varepsilon_r = 0.01$, and $P_\phi = 0$.

In Figure 5.23a the omnidirectional pendulum energy harvester is excited in the u-direction with an excitation frequency of 0.9. For an excitation amplitude of $a_u = 0.064$ the energy harvester shows almost no arithmetic mean rectified power output. With an increase in the excitation amplitude to a value of $a_u = 0.2$ the arithmetic mean rectified power output rises steeply for a low power take-off torque. It reaches its maximum arithmetic mean rectified power output of 0.024 for a value of the power take-off torque of 0.079. From there on the power output decreases slightly with an increase of the power take-off torque until jumping down to a value close to zero for a value of the power take-off torque of 0.104. For a value of the excitation amplitude of $a_u = 0.3$ the arithmetic mean rectified power output shows an almost linear rise for an increase of the power take-off torque. It reaches its maximum of 0.055 for a value of the power take-off torque of 0.13. With a further increase in the torque the power output decreases until jumping down to a value close to zero for a value of the power take-off torque of 0.159.

Figure 5.23c shows the arithmetic mean rectified power output over the power take-off torque for an excitation frequency of 1.0. For an excitation amplitude of $a_u = 0.064$ a power output cannot be seen. With an increase in the excitation frequency to a value of $a_u = 0.2$ the power output shows an increase until reaching a maximum of 0.023 for a value of the power take-off torque of 0.069. For a value of the excitation amplitude of $a_u = 0.3$ the power output shows a steep rise and reaches a maximum of 0.053 for a value of the power take-off torque of 0.12. For an area of the power take-off torque from 0.083 to 0.11 the power output shows no value which can be attributed to numerical issues where the computation stops before reaching the pre-defined $\tau > 800$.

The energy harvester that is excited with an excitation frequency of 1.1 is shown in Figure 5.23e. When the system is excited with an excitation amplitude of $a_u = 0.064$ a power output cannot be seen. With an increase in the excitation amplitude to a value of $a_u = 0.2$ the maximum value of the arithmetic mean rectified power output of 0.0176 is reached at a value of the power take-off torque of 0.058. For a value of the excitation amplitude of $a_u = 0.3$ the maximum power output of 0.029 is reached at a power take-off torque of 0.092.

In Figure 5.23b the arithmetic mean rectified power output over the power take-off torque for an excitation frequency of 0.9 is shown. For a value of the excitation amplitudes of $a_u = a_w = 0.064$ the power output is close to zero. With an increase in the excitation amplitudes to a value of $a_u = a_w = 0.2$ the arithmetic mean rectified power output shows a linear increase with the maximum power output of 0.164 reached at a value of the power take-off of 0.163. With a further increase in the power take-off torque the power output jumps down to a value close to zero. The power output for the system that is excited with a value for the excitation amplitudes of $a_u = a_w = 0.3$ shows various measurement points that do not indicate any clear pattern. This can be attributed to numerical issues.

The omnidirectional energy harvester is excited with an excitation frequency of 1.0 in Figure 5.23d. For a value of the excitation amplitudes $a_u = a_w = 0.064$ the power output is close to a value of zero. With an increase in the excitation amplitudes $a_u = a_w = 0.2$ the power output rises almost linearly and reaches its maximum power output of 0.185 for a value of the power take-off torque of 0.198. For a value of the excitation amplitudes of $a_u = a_w = 0.3$ the power output shows an overall maximum deflection of 0.31 for a power take-off torque of 0.29. However, the path to this maximum power output is full of gaps that appear because of issues in the numerical analysis where the computation stops before reaching the pre-defined $\tau > 800$.

In Figure 5.23f the omnidirectional energy harvester is excited with an excitation frequency of 1.1. For a value of the excitation amplitudes of $a_u = a_w = 0.064$ the system shows an average power output close to zero. With an increase in the excitation amplitudes to a value of $a_u = a_w = 0.2$ the power output increases almost linearly and reaches its maximum of 0.174 at a value of the power take-off torque of 0.224. For a value of the excitation amplitudes of $a_u = a_w = 0.3$ the maximum value of the arithmetic mean rectified power output of 0.31 is reached at a value for the power take-off torque of 0.29.

In Figure 5.24 the arithmetic mean rectified power output is plotted over the excitation amplitude for a variation of the excitation frequency. Figure 5.24a shows the arithmetic mean rectified power output of the energy harvester with a power take-off torque of $P_\theta = 0.05$ for different excitation frequencies over the excitation amplitude in the u-direction. With an excitation frequency of 0.9 the arithmetic mean rectified power output is close to zero for a value from the excitation amplitude lower than $a_u = 0.1$. With a further increase in the excitation amplitude the arithmetic mean rectified power output increases almost linearly. The slope of the arithmetic mean rectified power output decreases to almost zero with an excitation amplitude value higher than $a_u = 0.2$. For an excitation frequency of 1.0 the arithmetic mean rectified power output shows an output with a value for the excitation amplitude higher than $a_u = 0.17$. From there on an arithmetic mean rectified power output in the area of 0.02 can be observed for the rest of the shown excitation amplitude range. With an excitation frequency of 1.1 the arithmetic mean rectified power output is close to zero until the excitation amplitude of $a_u = 0.18$ is reached. For the rest of the shown range of the excitation amplitude the arithmetic mean rectified power output remains in the region of 0.015.

The power take-off torque is increased to a value of $P_\theta = 0.1$ in Figure 5.24c. For the excitation frequencies of 1.0 and 1.1 the omnidirectional pendulum energy harvester shows a power output close to zero. With an excitation frequency of 0.9 the system shows a small arithmetic mean rectified power output for an excitation amplitude from $a_u = 0.16$ to 0.19 which then jumps up to a higher arithmetic mean rectified power output value and steeply rises for the rest of the shown excitation amplitude area.

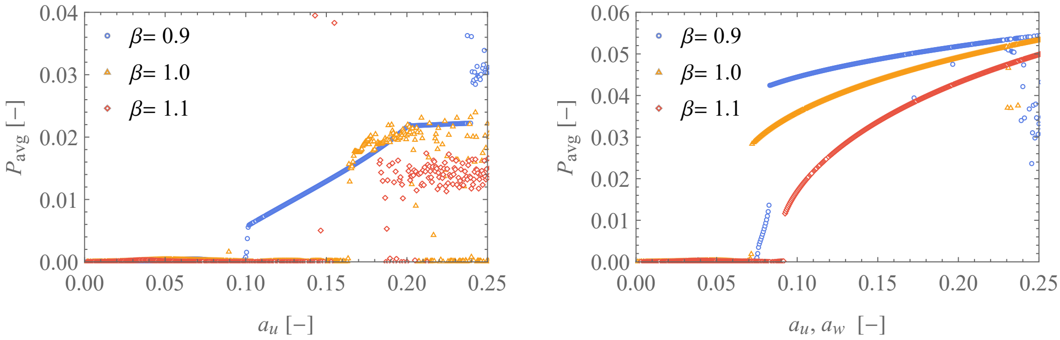

(a) P_{avg} over a_u with $P_\theta = 0.05$ and $a_w = 0$ (b) P_{avg} over a_u, a_w with $P_\theta = 0.05$

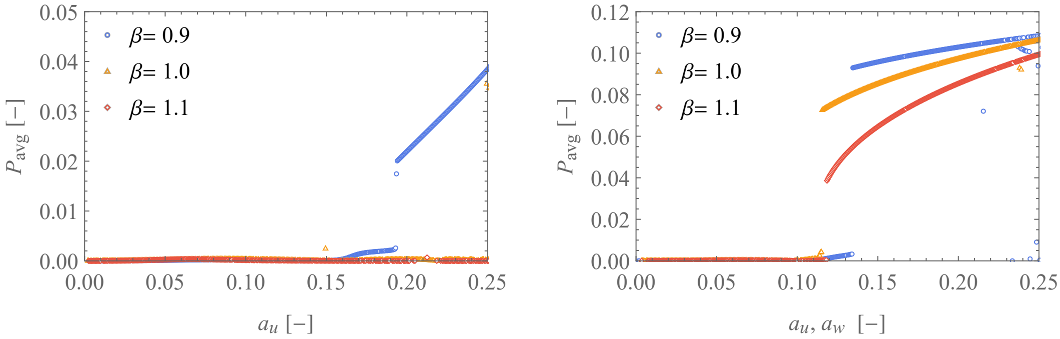

(c) P_{avg} over a_u with $P_\theta = 0.1$ and $a_w = 0$ (d) P_{avg} over a_u, a_w with $P_\theta = 0.10$

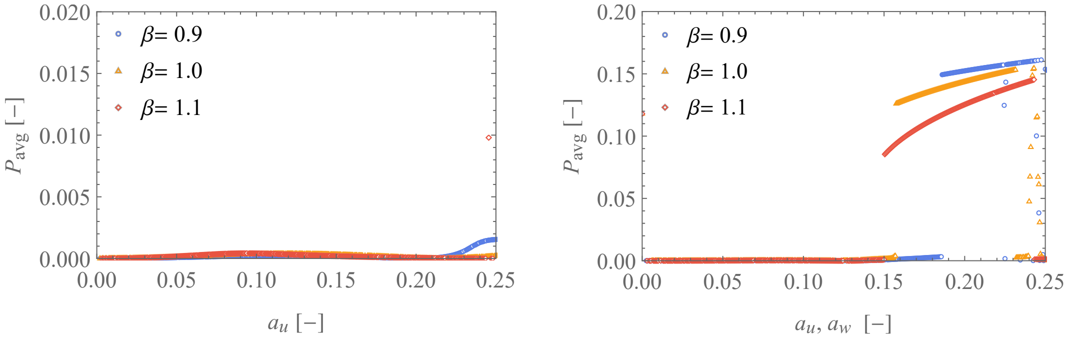

(e) P_{avg} over a_u with $P_\theta = 0.15$ and $a_w = 0$ (f) P_{avg} over $a_u = a_w$ with $P_\theta = 0.15$

Figure 5.24: Arithmetic mean rectified power output over the excitation amplitude for a variation of the excitation direction, different excitation frequencies, and different power take-off torques with the parameters set to: $l = 0.5$ m, $m = 1.32$ kg, $g = 9.81\ \frac{\text{m}}{\text{s}^2}$, $\alpha_\theta = \alpha_\phi = 0.0648$, $a_v = 0$, $\varepsilon_r = 0.01$, and $P_\phi = 0$.

With a further increase in the power take-off torque to a value of $P_\theta = 0.15$ the arithmetic mean rectified power output of the energy harvester drastically decreases see Figure 5.24e. The excitation frequencies 1.0 and 1.1 do not show any power output. Only for an excitation frequency of 0.9 a small power output can be observed for an excitation amplitude higher than $a_u = 0.22$.

In Figure 5.24b the pendulum energy harvester is excited with a coupled excitation in the u- and w-directions. For an excitation frequency of 0.9 the first power output can be seen for the excitation amplitudes higher than $a_u = a_w = 0.076$. The arithmetic mean rectified power output increases rapidly for a further increase in the excitation amplitudes until jumping up to a higher arithmetic mean rectified power output of 0.04 at a value of the excitation amplitudes of $a_u = a_w = 0.083$. With a further increase in the excitation amplitudes the arithmetic mean rectified power output increases as well. For a value of the excitation frequency of 1.0 the arithmetic mean rectified power output shows no deflection until the arithmetic mean rectified power output jumps up to a value of 0.028 at a value of the excitation amplitudes of $a_u = a_w = 0.072$. In the following the graph the arithmetic mean rectified power output gradually increases with an increase in the excitation amplitudes. The arithmetic mean rectified power output shows a jump up to 0.011 at a value of the excitation amplitudes of $a_u = a_w = 0.093$ and then gradually increases with an increase in the excitation amplitudes.

The power take-off torque is increased to a value of $P_\theta = 0.1$ in Figure 5.24d. For a value of the excitation frequency of 0.9 the arithmetic mean rectified power output sees a jump up to a value of 0.09 for a value of the excitation amplitudes of $a_u = a_w = 0.13$. With a further increase in the excitation amplitudes the arithmetic mean rectified power output increases as well. With an increase in the excitation frequency to a value of 1.0 the jump up of the arithmetic mean rectified power output to a value of 0.072 appears at a value of the excitation amplitudes of $a_u = a_w = 0.11$. With a further increase in the excitation amplitudes the arithmetic mean rectified power output increases. The arithmetic mean rectified power output of the energy harvester that is excited with an excitation frequency of 1.1 shows a jump up to a value of the arithmetic mean rectified power output of 0.038 for a value of the excitation amplitudes of $a_u = a_w = 0.118$. From there on the arithmetic mean rectified power output increases with an increase in the excitation amplitudes.

In Figure 5.24f the power take-off torque is increased to a value of $P_\theta = 0.15$. The energy harvester sees a jump up to a power output of 0.149 for a value of the excitation amplitudes of $a_u = a_w = 0.186$ when excited with an excitation frequency of 0.9. With a further increase in the excitation amplitudes the arithmetic mean rectified power output increases slightly. For an excitation frequency of 1.0 the arithmetic mean rectified power output sees a jump up to a value of 0.125 for a value of the excitation amplitudes of $a_u = a_w = 0.158$ and the arithmetic mean rectified power output increases further with an increase in the excitation amplitudes. For a value of the excitation frequency of 1.1 the up jump appears at a value of the excitation amplitudes of $a_u = a_w = 0.15$ and an arithmetic mean rectified power output of 0.085 is reached at this value. With a further increase in the excitation amplitudes the arithmetic mean rectified power output increases as well.

In Figure 5.25 frequency responses for different power take-off torques and a variation of the excitation amplitudes are shown.

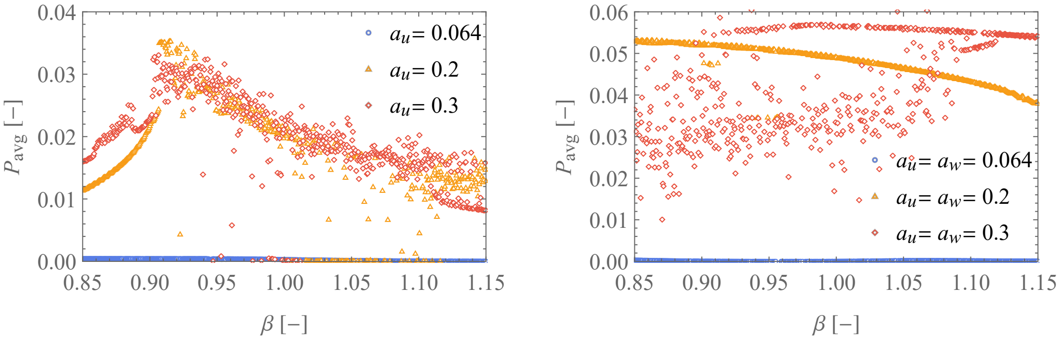

(a) P_{avg} over β with $P_\theta = 0.05$ and $a_w = 0$ (b) P_{avg} over β with $P_\theta = 0.05$

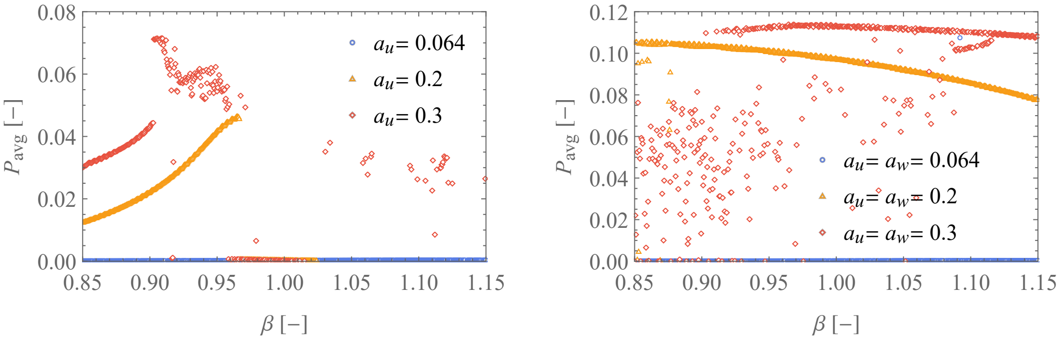

(c) P_{avg} over β with $P_\theta = 0.1$ and $a_w = 0$ (d) P_{avg} over β with $P_\theta = 0.1$

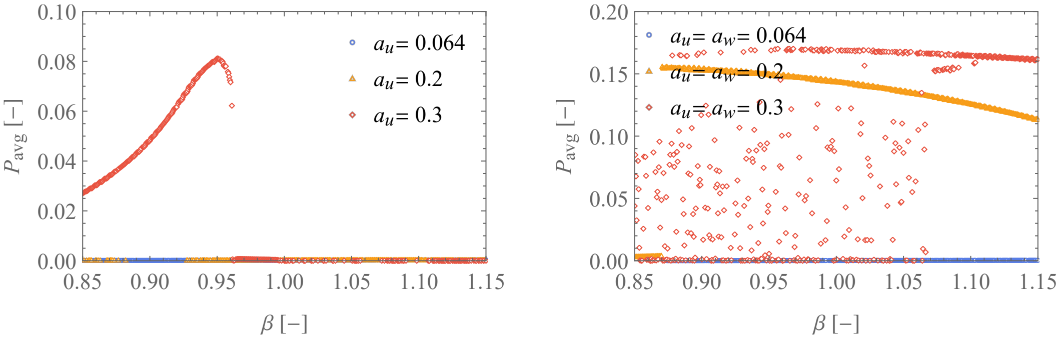

(e) P_{avg} over β with $P_\theta = 0.15$ and $a_w = 0$ (f) P_{avg} over β with $P_\theta = 0.15$

Figure 5.25: Arithmetic mean rectified power output over the excitation frequency β for a variation of the excitation direction, different excitation amplitudes, and different power take-off torques with the parameters set to: $l = 0.5$ m, $m = 1.32$ kg, $g = 9.81\ \frac{\text{m}}{\text{s}^2}$, $\alpha_\theta = \alpha_\phi = 0.0648$, $a_v = 0$, $\varepsilon_r = 0.01$, and $P_\phi = 0$.

The energy harvester is loaded with a power take-off torque of $P_\theta = 0.05$ in Figure 5.25a. The arithmetic mean rectified power output of the energy harvester is close to zero for an excitation amplitude of $a_u = 0.064$. With an increase in the excitation amplitude to a value of $a_u = 0.2$ the power output shows a steep rise followed by a jump up to the maximum value of the arithmetic mean rectified power output of 0.035 for a value of the excitation frequency of 0.91. The arithmetic mean rectified power output decreases with a further increase in the excitation amplitude. The different points do not form a neat curve anymore, since for this area of the excitation frequency the bifurcation diagram already suggested quasi-periodic or chaotic dynamics. When the system that is excited with an excitation amplitude of $a_u = 0.3$ shows a slightly lower overall maximum power output of 0.033 at the same excitation frequency as the system that is excited with an excitation amplitude of $a_u = 0.2$.

In Figure 5.25c the power take-off torque of the omnidirectional energy harvester is increased to a value of $P_\theta = 0.1$. For a value of the excitation amplitude of $a_u = 0.064$ the system does not show any power output. With an increased value of the excitation amplitude $a_u = 0.2$ the power output rises steeply to a value of 0.046 for a value of the excitation frequency of 0.97. When the excitation frequency increases further the arithmetic mean rectified power output jumps down to a value close to zero. For an excitation amplitude of $a_u = 0.3$ the arithmetic mean rectified power output increases for a value of the excitation frequency from 0.85 to 0.9. With a further increase in the excitation frequency the arithmetic mean rectified power output jumps up to its maximum value of 0.07. The power output shows a bowl-shaped trajectory for a further increase in the excitation frequency until jumping down to a value close to zero for an excitation frequency of $\beta = 0.97$.

The frequency response for the omnidirectional energy harvester with a power take-off torque of $P_\theta = 0.15$ is shown in Figure 5.25e. For a value of the excitation amplitude of $a_u = 0.064$ and $a_u = 0.2$ a power output of the energy harvester is not possible. With an excitation amplitude of $a_u = 0.3$ the arithmetic mean rectified power output shows a steep rise for an excitation frequency from 0.85 to 0.95. The maximum value of the arithmetic mean rectified power output of 0.08 is reached for an excitation frequency of $\beta = 0.95$. With a further increase in the excitation frequency the arithmetic mean rectified power output decreases until eventually the power output jumps down suddenly at a value of the excitation frequency of 0.96.

In Figure 5.25b the energy harvester is excited in the u- and w-directions and is loaded with a power take-off torque of $P_\theta = 0.05$. For a value of the excitation amplitudes of $a_u = a_w = 0.064$ the energy harvester does not produce any power output. With an increase of the excitation amplitudes to a value of $a_u = a_w = 0.2$ the power outputs are all aligned. The highest arithmetic mean rectified power output of 0.053 is reached for the lowest shown excitation frequency of 0.85. For an increase in the excitation frequency the arithmetic mean rectified power output decreases. With an increase in the excitation amplitudes $a_u = a_w = 0.3$ the arithmetic mean rectified power output shows a fixed point for a value of the excitation frequency from $\beta = 0.915$ to 1.15. This is accompanied by power output values that appear to have a chaotic pattern.

Figure 5.25d shows the frequency response for the omnidirectional energy harvester that is loaded with a power take-off torque of $P_\theta = 0.1$. The energy harvester does not show any power output when the system is excited with the excitation amplitudes of $a_u = a_w = 0.064$. With an increase in the excitation amplitudes to a value of $a_u = a_w = 0.2$ the maximum value of the power output of 0.105 is reached at an excitation frequency of 0.85. For a further increase in the excitation frequency the arithmetic mean rectified power output decreases. With a further increase in the excitation amplitudes $a_u = a_w = 0.3$ the power output of the system increases further to a value of 0.114. A constant power output is feasible for a value of the excitation frequency from $\beta = 0.9$ to 1.15. For a value of the excitation frequency lower than 0.9 the power output follows no clear trend.

The power take-off torque is increased to a value of $P_\theta = 0.15$ in Figure 5.25f. For a value of the excitation amplitudes $a_u = a_w = 0.064$ the energy harvester does not show any power output. With an increase in the excitation amplitudes to a value of $a_u = a_w = 0.2$ the maximum value for the arithmetic mean rectified power output of 0.155 is reached for an excitation frequency of $\beta = 0.87$. When the excitation frequency is increased further the arithmetic mean rectified power output decreases. For a value of the excitation amplitudes of $a_u = a_w = 0.3$ the maximum value of the arithmetic mean rectified power output is 0.17. It is possible to harvest energy from the omnidirectional energy harvester for an excitation frequency from $\beta = 0.878$ to 1.15.

5.4.0.1 Summary of Section 5.4

It is evident that the omnidirectional pendulum energy harvester's power output is highly dependent on the excitation frequency, excitation amplitudes, damping ratio, and the power take-off torque. And it gets even more complex when the dimensions of the pendulum energy harvester e.g. length and mass area included as well. Since the different figures in Section 5.4 show no clear overall trend is important that an optimisation process of the energy harvester is a single case selection. The article [1] that is published related to this work gives an optimisation process flow chart to simplify the optimisation process. In Chapter 8 a controlled switching off and switching on power take-off is examined numerically.

5.5 Approximate Analytical Solution for a Simple Pendulum with a Power Take-Off using the Perturbation Method of Multiple Scales

This section is concerned with the perturbation method of multiple scales for a forced damped simple pendulum with power take-off. A further analysis of the spherical pendulum with the method of multiple scales can be found in the appendix, in a nutshell, it can be said that this calculation was unfortunately abandoned because of the cyclic behaviour of the coordinate ϕ and because of the fractions by which the generalised coordinates are divided by each other.

With the latter, the problem arises of finding the secular terms that are solvable. For more details please see the notes in Appendix A.

A literature search shows a lack of perturbation analysis by the method of multiple scales for a spherical pendulum. Only Olsson [98] used the Lindstedt-Poincaré perturbation method to calculate the dynamics of a spherical pendulum. However, the author is interested in small deflections and therefore did not obtain the differential equations in polar coordinates but transformed them with a small angle assumption to Cartesian coordinates instead. With this reasonable assumption, the author removes the cyclic dynamics of the coordinate ϕ and in addition the fractions with different generalised coordinates in the numerators and denominators. This gives Olsson the possibility to avoid the two issues that emerged in the analysis of the spherical pendulum in Appendix A. However, the transformation of the polar in Cartesian coordinates cannot be used for this work, since this work is concerned with large deflections in the direction of the coordinate θ since these are directly related to an effective energy harvester. Moreover, it is evident that from the coordinate ϕ, that is defining the rotation of the planar pendulum, no power can be extracted. After careful consideration of all the advantages and disadvantages, it was decided that for the calculation of the method of multiple scales a scaled-down version of the spherical pendulum with one degree of freedom would be sufficient. This system still represents the important dynamics of the energy harvester including the most important part, the power take-off over the planar coordinate θ. The sketch of the simple pendulum is shown in Figure 5.26, it should be noted that the coordinate system is not a standard (o,x,y)-coordinate system, but instead, a (o,y,z)-coordinate system was chosen. This is done because the results are compared with the numerical and experimental results and thus the axes and the excitations should match.

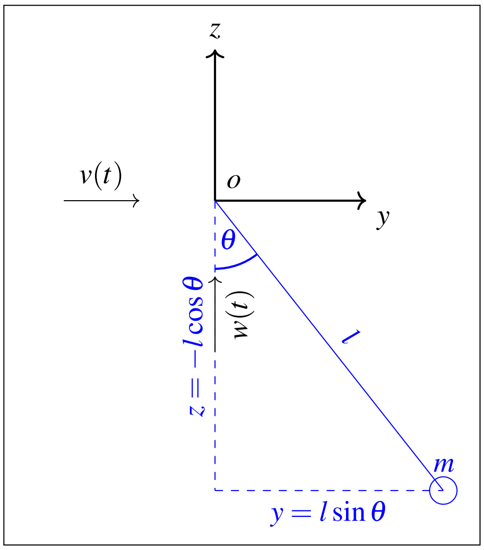

Figure 5.26: Diagram of a simple pendulum in yz-coordinate system with kinematics and excitations.

In the dimensionless differential Equations (4.36) and (4.37) of the spherical pendulum, the coordinate ϕ and its derivatives are set to zero and the differential Equation (5.5) for the simple pendulum is obtained. Additionally, a parameter ω^2 for the $\sin(\theta(\tau))$ term is introduced, see Equation (5.4). The value for ω^2 is equal to one, this parameter is solely introduced to make the equation mathematically more consistent.

$$\omega^2 = \frac{\omega_n^2}{\omega_0^2} = 1. \tag{5.4}$$

With this the dimensionless ordinary differential equation for the forced damped simple pendulum with power take-off is obtained.

$$\begin{aligned}\ddot{\theta}(\tau) + \alpha_\theta \dot{\theta}(\tau) + \omega^2 \sin(\theta(\tau)) - a_v \beta_v^2 \cos(\theta(\tau)) \cos(\beta_v \tau) \\ - a_w \beta_w^2 \sin(\theta(\tau)) \cos(\beta_w \tau) = -\frac{2P_\theta}{\pi} \tan^{-1}\left(\frac{\dot{\theta}(\tau)}{\varepsilon_{\mathrm{r}}}\right).\end{aligned} \tag{5.5}$$

Subsequently, the trigonometric terms are expanded one after another with the Maclaurin expansions.

$$\sin\theta(\tau) = \theta(\tau) - \frac{\theta(\tau)^3}{6} + \frac{\theta(\tau)^5}{120} - ... \tag{5.6}$$

$$\cos\theta(\tau) = 1 - \frac{\theta(\tau)^2}{2} + \frac{\theta(\tau)^4}{24} - ... \tag{5.7}$$

The Maclaurin expansion of the power take-off term gives

$$\tan^{-1}\left(\frac{\dot{\theta}(\tau)}{\varepsilon_r}\right) = \frac{\dot{\theta}(\tau)}{\varepsilon_r} - \frac{\dot{\theta}(\tau)^3}{3\varepsilon_r^3} + ... \tag{5.8}$$

Introducing the Maclaurin expansions (5.6) to (5.8) in the ordinary differential Equation (5.5) gives.

$$\begin{aligned}\ddot{\theta}(\tau) + \alpha_\theta \dot{\theta}(\tau) + \omega^2 \left(\theta(\tau) - \frac{\theta(\tau)^3}{6} + ...\right) - a_v \beta_v^2 \cos(\beta_v \tau) \left(1 - \frac{\theta(\tau)^2}{2} + ...\right) \\ - a_w \beta_w^2 \cos(\beta_w \tau) \left(\theta(\tau) - \frac{\theta(\tau)^3}{6} + ...\right) = -\frac{2P_\theta}{\pi} \left(\frac{\dot{\theta}(\tau)}{\varepsilon_r} - \frac{\dot{\theta}(\tau)^3}{3\varepsilon_r^3} + ...\right).\end{aligned} \tag{5.9}$$

Equation (5.9) can be made to a plausible ordering scheme. Generally, the MacLaurin expansions were used up to the third order, this ensures that the nonlinearities of the terms were adequately represented in the calculation therefore the small parameter $\varepsilon (\varepsilon < 1)$ is introduced. The general requirement for the perturbation hierarchy is that the lowest order can be solved analytically which requires a linear ODE at the lowest order. This so-called generation equation should be of the form $\ddot{\theta} + \omega^2 \theta = 0$. This gives the linear solution in complementary function form $\theta_0 = Ae^{i\omega T_0} + \bar{A}e^{-i\omega T_0}$. The damping, excitation and loading terms can then be ordered in the equations of the perturbation hierarchy with $O(\varepsilon^1)$ and $O(\varepsilon^2)$. The nonlinear stiffness term is controlled by $-\frac{\theta(\tau)^3}{6}$ and should be scaled to $O(\varepsilon^1)$. Likewise the term $-\frac{\theta(\tau)^2}{2}$ is scaled to $O(\varepsilon^1)$. This ensures that the nonlinearities are represented in the first order of the perturbation hierarchy. Additional relations (5.10) are introduced to get a plausible ordering scheme.

$$\begin{aligned} &\alpha_\theta = \varepsilon\bar{\alpha}_\theta, && \frac{1}{6} = \varepsilon\bar{\gamma}, && P_\theta = \varepsilon\bar{P}_\theta, \\ &a_v = \varepsilon\bar{a}_v, && a_w = \varepsilon\bar{a}_w, && \frac{1}{3} = \varepsilon\bar{\sigma}, \\ &-\frac{\theta(\tau)^2}{2} = -\varepsilon\bar{\eta}\,\theta(\tau)^2. \end{aligned} \tag{5.10}$$

Introducing the relations (5.10) into Equation (5.9) gives:

$$\begin{aligned} &\ddot{\theta}(\tau) + \bar{\alpha}_\theta\dot{\theta}(\tau) + \omega^2\theta(\tau) - \omega^2\varepsilon\bar{\gamma}\theta(\tau)^3 - a_v\beta_v^2\cos(\beta_v\tau)\left(1 - \varepsilon\bar{\eta}\,\theta(\tau)^2\right) \\ &\quad - a_w\beta_w^2\cos(\beta_w\tau)\left(\theta(\tau) - \varepsilon\bar{\gamma}\theta(\tau)^3\right) = -\frac{2\varepsilon P_\theta}{\pi}\left(\frac{\dot{\theta}(\tau)}{\varepsilon_r} - \bar{\sigma}\varepsilon\frac{\dot{\theta}(\tau)^3}{\varepsilon_r^3} + \dots\right). \end{aligned} \tag{5.11}$$

Introducing the independent variables according to the well-known procedure in the literature [153–157].

$$T_n = \varepsilon^n\tau, \qquad \text{for} \qquad n = 0, 1, 2, \dots \tag{5.12}$$

Followed by the derivatives with respect to τ.

$$\begin{aligned} \frac{d}{d\tau} &= \frac{dT_0}{d\tau}\frac{\partial}{\partial T_0} + \frac{dT_1}{d\tau}\frac{\partial}{\partial T_1} + \dots = \frac{\partial}{\partial T_0} + \varepsilon\frac{\partial}{\partial T_1} + \dots = D_0 + \varepsilon D_1 + \dots \\ \frac{d^2}{d\tau^2} &= \frac{\partial^2}{\partial T_0^2} + 2\varepsilon\frac{\partial^2}{\partial T_0\partial T_1} + \varepsilon^2\left(2\frac{\partial^2}{\partial T_0\partial T_2} + \frac{\partial^2}{\partial T_1^2}\right) + \dots \\ &= D_0^2 + 2\varepsilon D_0 D_1 + \varepsilon^2(D_1^2 + 2D_0D_2) + \dots \end{aligned} \tag{5.13}$$

It can be assumed that θ is represented by the series:

$$\theta(\tau) = \theta_0(T_0, T_1, T_2) + \varepsilon\theta_1(T_0, T_1, T_2) + \dots \tag{5.14}$$

Introducing Equations (5.12) to (5.14) in the ordinary differential Equation (5.11) gives the perturbation hierarchy for order $O(0)$ to $O(2)$:

$$D_0^2\theta_0 + \omega^2\theta_0 = 0. \tag{5.15}$$

$$\begin{aligned} D_0^2\theta_1+\omega^2\theta_1 = &-2\left(D_0D_1\theta_0\right)+\omega^2\bar{\gamma}\theta_0^3-\bar{\alpha}_\theta\left(D_0\theta_0\right)+\bar{a}_v\beta_v^2\cos\left(\beta_v\tau\right)\\ &+\bar{a}_w\beta_w^2\cos\left(\beta_w\tau\right)\theta_0-\frac{\left(2\bar{P}_\theta\right)\left(D_0\theta_0\right)}{\pi\varepsilon_r}. \end{aligned} \tag{5.16}$$

The second order of the perturbation hierarchy is shown for completeness but will not be used during the calculations since all the nonlinearities, forcing terms and power take-off terms are represented adequately in the first-order terms.

$$\begin{aligned} D_0^2\theta_2+\omega^2\theta_2 = &-2\left(D_0D_2\theta_0\right)-2\left(D_0D_1\theta_1\right)-D_1^2\theta_0+3\omega^2\bar{\gamma}\theta_0^2\theta_1-\bar{\alpha}_\theta\left(D_1\theta_0\right)\\ &-\bar{\alpha}_\theta\left(D_0\theta_1\right)-\bar{\eta}\bar{a}_v\beta_v^2\cos\left(\beta_v\tau\right)\theta_0^2-\bar{\gamma}\bar{a}_w\beta_w^2\cos\left(\beta_w\tau\right)\theta_0^3\\ &+\bar{a}_w\beta_w^2\cos\left(\beta_w\tau\right)\theta_1-\frac{2\bar{P}_\theta\left(D_1\theta_0\right)}{\pi\varepsilon_r}-\frac{2\bar{P}_\theta\left(D_0\theta_1\right)}{\pi\varepsilon_r}+\frac{2\bar{\sigma}\bar{P}_\theta\left(D_0\theta_0\right)^3}{\pi\varepsilon_r^3}. \end{aligned} \tag{5.17}$$

By solving Equation (5.15) the generating solution is obtained. Where $A(T_1)$ is a constant of the complementary function that is dependent on the slower time scale and $\bar{A}(T_1)$ is the complex conjugate of $A(T_1)$.

$$\theta_0=A(T_1)e^{i\omega T_0}+\bar{A}(T_1)e^{-i\omega T_0}. \tag{5.18}$$

Introducing the solution for θ_0 (5.18) in the first-order of the perturbation hierarchy Equation (5.16) gives Equation (5.19). Note that the slower time was omitted from the amplitude $A(T_1)$ to improve clarity. However, this does not remove the arguments dependency on the slower time scale T_1.

$$\begin{aligned} D_0^2\theta_1+\omega^2\theta_1 = &-2i\omega D_1Ae^{i\omega T_0}+2i\omega D_1\bar{A}e^{-i\omega T_0}\\ &-\bar{\alpha}_\theta i\omega Ae^{i\omega T_0}+\bar{\alpha}_\theta i\omega\bar{A}e^{-i\omega T_0}\\ &+\bar{\gamma}\omega^2A^3e^{3i\omega T_0}+3\bar{\gamma}\omega^2A^2\bar{A}e^{i\omega T_0}+3\bar{\gamma}\omega^2\bar{A}^2Ae^{-i\omega T_0}+\bar{\gamma}\omega^2\bar{A}^3e^{-3i\omega T_0}\\ &+\bar{a}_v\beta_v^2\cos\left(\beta_v\tau\right)\\ &+\bar{a}_w\beta_w^2\cos\left(\beta_w\tau\right)\left(Ae^{i\omega T_0}+\bar{A}e^{-i\omega T_0}\right)\\ &-\frac{2\bar{P}_\theta i\omega A}{\pi\varepsilon_r}e^{i\omega T_0}+\frac{2\bar{P}_\theta i\omega\bar{A}}{\pi\varepsilon_r}e^{-i\omega T_0}. \end{aligned} \tag{5.19}$$

In the following, the secular equations in Equation (5.19) are identified. Therefore the excitation terms are expanded with the following exponential expression.

$$\cos(\beta T_0)=\frac{1}{2}e^{i\beta T_0}+\frac{1}{2}e^{-i\beta T_0}\quad\text{where}\quad\tau\approx T_0. \tag{5.20}$$

Introducing Equation (5.20) into Equation (5.19) gives:

$$\begin{aligned}D_0^2\theta_1+\omega^2\theta_1 =&-2i\omega D_1 A e^{i\omega T_0}+2i\omega D_1\bar{A}e^{-i\omega T_0}\\&-\bar{\alpha}_\theta i\omega A e^{i\omega T_0}+\bar{\alpha}_\theta i\omega\bar{A}e^{-i\omega T_0}\\&+\bar{\gamma}\omega^2A^3e^{3i\omega T_0}+3\bar{\gamma}\omega^2A^2\bar{A}e^{i\omega T_0}+3\bar{\gamma}\omega^2\bar{A}^2Ae^{-i\omega T_0}+\bar{\gamma}\omega^2\bar{A}^3e^{-3i\omega T_0}\\&+\frac{1}{2}\bar{a}_v\beta_v^2e^{i\beta_v T_0}+\frac{1}{2}\bar{a}_v\beta_v^2e^{-i\beta_v T_0}\\&+\frac{1}{2}\bar{a}_w\beta_w^2\bar{A}e^{-i\omega T_0+i\beta_w T_0}+\frac{1}{2}\bar{a}_w\beta_w^2Ae^{i\omega T_0-i\beta_w T_0}\\&+\frac{1}{2}\bar{a}_w\beta_w^2Ae^{i\omega T_0+i\beta_w T_0}+\frac{1}{2}\bar{a}_w\beta_w^2\bar{A}e^{-i\omega T_0-i\beta_w T_0}\\&-\frac{2\bar{P}_\theta i\omega A}{\pi\varepsilon_r}e^{i\omega T_0}+\frac{2\bar{P}_\theta i\omega\bar{A}}{\pi\varepsilon_r}e^{-i\omega T_0}.\end{aligned}\tag{5.21}$$

5.5.1 Numerical Solution of the Secular Terms

The system will be excited close to the natural frequency ω which means that the excitation frequency β_v can be set to ω. The excitation frequency β_w is excited at the condition of principal of parametric resonance and therefore is set to 2ω. Note that this approach does not allow any detuning. The calculation of the secular terms with a detuning parameter can be found in Section 5.5.2.

$$D_1A=-\frac{1}{2}\bar{\alpha}_\theta A-\frac{3}{2}\bar{\gamma}\omega iA^2\bar{A}-\frac{1}{4}\bar{a}_v\omega i-\bar{a}_w\omega i\bar{A}-\frac{\bar{P}_\theta A}{\pi\varepsilon_r}.\tag{5.22}$$

The following polar notation is introduced. The polar coordinates a_p and α_p are real functions of the slow time scale T_1.

$$A=\frac{a_p}{2}e^{i\alpha_p},\qquad \bar{A}=\frac{a_p}{2}e^{-i\alpha_p},\qquad a_p=a_p(T_1),\qquad \alpha_p=\alpha_p(T_1).\tag{5.23}$$

The derivative of A with respect to T_1 is.

$$D_1A=\frac{a_p'}{2}e^{i\alpha_p}+\frac{a_p}{2}i\alpha_p'e^{i\alpha_p}.\tag{5.24}$$

Introducing the polar coordinates (5.23) and its derivative (5.24) in Equation (5.22) and splitting the secular governing terms into real and imaginary parts gives:

$$a_p' =2\left(-\frac{1}{4}\omega\sin\left(\alpha_p\right)\bar{a}_v-\frac{1}{2}\omega\sin\left(2\alpha_p\right)a_p\bar{a}_w-\frac{a_p\bar{P}_\theta}{\pi\varepsilon_r}-\frac{1}{4}a_p\bar{\alpha}_\theta\right).\tag{5.25}$$

$$a_p\alpha_p' =2\left(-\frac{3}{16}\omega\bar{\gamma}a_p^3-\frac{1}{4}\omega\cos\left(\alpha_p\right)\bar{a}_v-\frac{1}{2}\omega\cos\left(2\alpha_p\right)a_p\bar{a}_w\right).\tag{5.26}$$

The first-order differential Equations (5.25) and (5.26) unfortunately cannot be solved analytically. Therefore, they are solved with a suitable procedure of numerical integration. The results are shown in Figure 5.27. From Figures 5.27 the steady-state values for $a_p = 1.61$ and $\alpha_p = -1.65$ are obtained. These values are being introduced in the polar equations for the constant A and $\bar{A}$ in Equation (5.23). And subsequently they are introduced in the assumed solution of the coordinate θ in Equation (5.14). This gives an analytical steady-state solution of the coordinate θ:

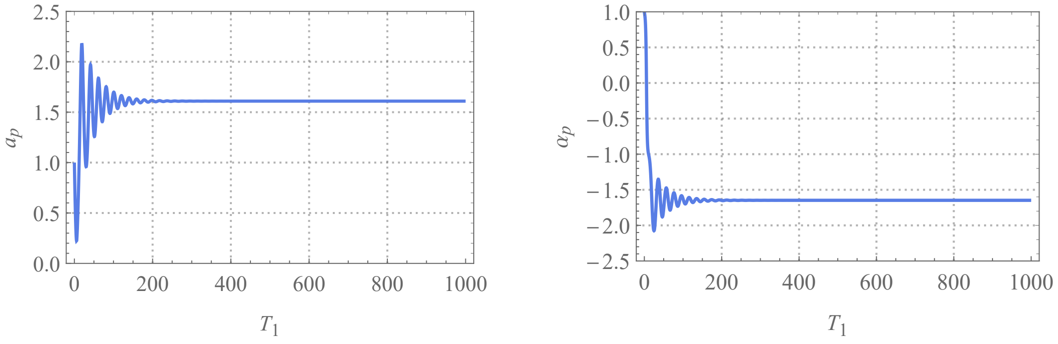

(a) Amplitude a_p over T_1

(b) Phase of motion α_p over T_1

Figure 5.27: Numerical analysis of the amplitude a_p and phase of motion α_p of the secular terms. With the variables set to: $\omega = 1$, $\bar{a}_v = 0.16$, $\bar{a}_w = 0.16$, $\bar{\alpha}_\theta = 0.05$, $\bar{P}_\theta = 0.0$, $\bar{\gamma} = \frac{1}{6}$, ICs $= 1$, and $\varepsilon_r = 0.01$

$$\theta(\tau) = \frac{1.61}{2} e^{-i1.65} e^{i\omega\tau} + \frac{1.61}{2} e^{i1.65} e^{-i\omega\tau} \quad \text{where} \quad \tau \approx T_0. \tag{5.27}$$

In Figure 5.28a the analytical results for the coordinate θ are shown. The coordinate θ is plotted over τ and the system shows periodic dynamics. The numerical results of the coordinate θ in Figure 5.28b shows periodic dynamics well however the amplitudes are slightly lower than in the method of multiple scales. The first-order differential Equations (5.25) and (5.26) are solved

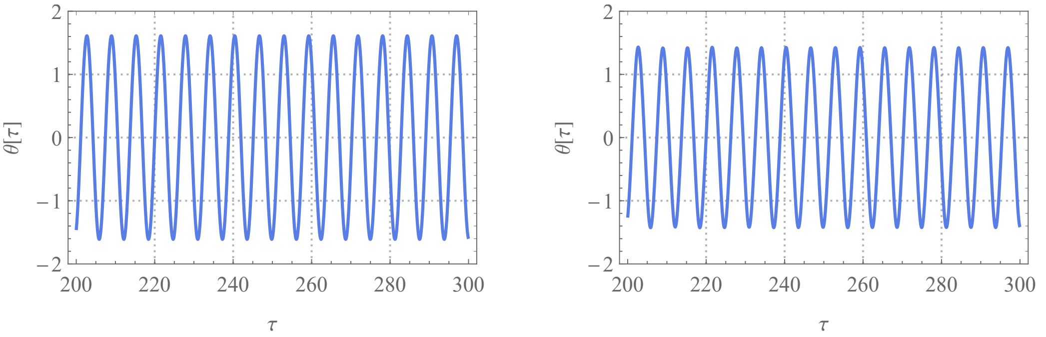

(a) Multiple scales results of θ over τ

(b) Numerical results of θ over τ

Figure 5.28: Results for the coordinate θ. With the variables set to: $\omega = 1$, $\bar{a}_v = 0.16$, $\bar{a}_w = 0.16$, $\bar{\alpha}_\theta = 0.05$, $\bar{P}_\theta = 0.0$, $\bar{\gamma} = \frac{1}{6}$, and $\varepsilon_r = 0.01$

with a suitable procedure for numerical integration with values close to the experimentally determined parameters. Figure 5.29 shows the numerical results with the steady-state values being $a_p = 0.71$ and $\alpha_p = -2.33$.

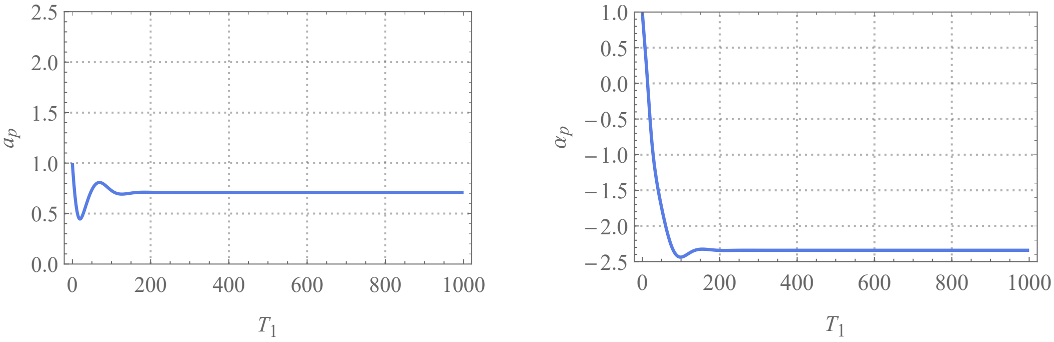

(a) Amplitude a_p over T_1

(b) Phase of motion α_p over T_1

Figure 5.29: Numerical analysis of the amplitude a_p and phase of motion α_p of the secular terms. With the variables set to: $\omega = 1$, $\bar{a}_v = 0.064$, $\bar{a}_w = 0$, $\bar{\alpha}_\theta = 0.0648$, $\bar{P}_\theta = 0.0$, $\bar{\gamma} = \frac{1}{6}$, ICs $= 1$, and $\varepsilon_r = 0.01$

The effect of the power take-off on the movement of the pendulum is examined in the following. Therefore, Equations (5.25) and (5.26) are being numerically integrated with a reasonable selected medium high power take-off of $\bar{P}_\theta = 0.15$. Before calculating the results of the equations it is crucial to observe the effect of the radiusing variable ε_r. Recalling that the parameter was introduced to produce a slightly rounded-off square wave power take-off function to make the calculation less vulnerable to numerical errors [1]. The variable was set to a value of $\varepsilon_r = 0.01$ which ensured that the power take-off function is slightly rounded off. However, when the radiusing variable is kept at $\varepsilon_r = 0.01$ for the approximate solution the power take-off term increases significantly by a factor of 100. This results in the fact that the numerical calculation of the amplitude a_p gets to close to zero and therefore the resulting approximation of θ shows a small deflection which is not close to reality. Therefore the radiusing parameter ε_r will be set to one in the following calculations. This changes the power take-off function from a square wave function to an Arctangent function. In return, this means that the power take-off in the method of multiple scales is slightly lower than in the numerical analysis. This is in contrast to a power take-off that is 100 times too high and therefore the choice of $\varepsilon_r = 1$ is a reasonable assumption for this work. The numerical analysis of the Equations (5.25) and (5.26) are shown in Figure 5.30. When comparing the solutions with power take-off Figure 5.30 to the solutions without power take-off in Figure 5.27 it can be seen that the steady-state value is reached faster when the power take-off is switched on. This in accordance with the higher damping that is induced because of the switched on power take-off. Additionally, it is observed that the amplitude a_p reduces slightly and the phase α_p gets bigger.

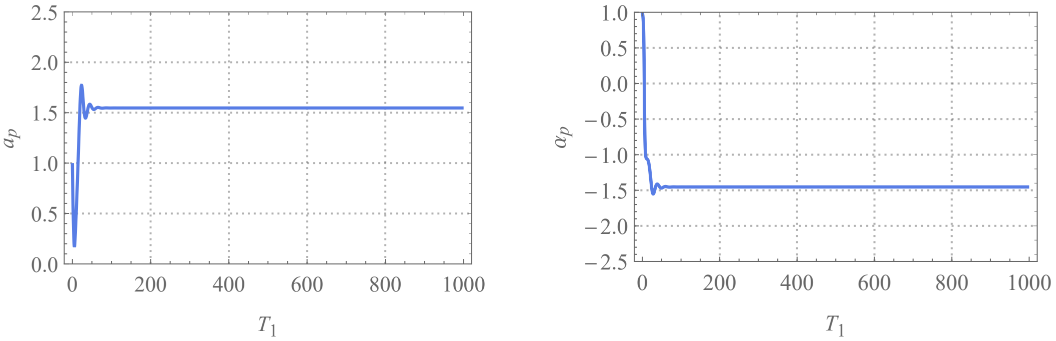

(a) Amplitude a_p over T_1

(b) Phase of motion α_p over T_1

Figure 5.30: Numerical analysis of the amplitude a_p and phase of motion α_p of the secular terms. With the variables set to: $\omega = 1$, $\bar{a}_v = 0.16$, $\bar{a}_w = 0.16$, $\bar{\alpha}_\theta = 0.05$, $\bar{P}_\theta = 0.15$, $\bar{\gamma} = \frac{1}{6}$, ICs $= 1$, and $\varepsilon_r = 1$

From Figure 5.30 the steady-states values $a_p = 1.55$ and $\alpha_p = -1.45$ are obtained. These values are introduced in the polar equations for the complex amplitude A and $\bar{A}$ in Equation (5.23). And subsequently, they are introduced in the assumed solution of the coordinate θ in Equation (5.14). In Figure 5.31a the results from the approximation of the coordinate θ are shown and Figure 5.31b shows the numerical results for the coordinate θ. When comparing Figures 5.28 and 5.31, it can be seen that the amplitude drops slightly when the power take-off is switched on. This is in accordance with the numerical results.

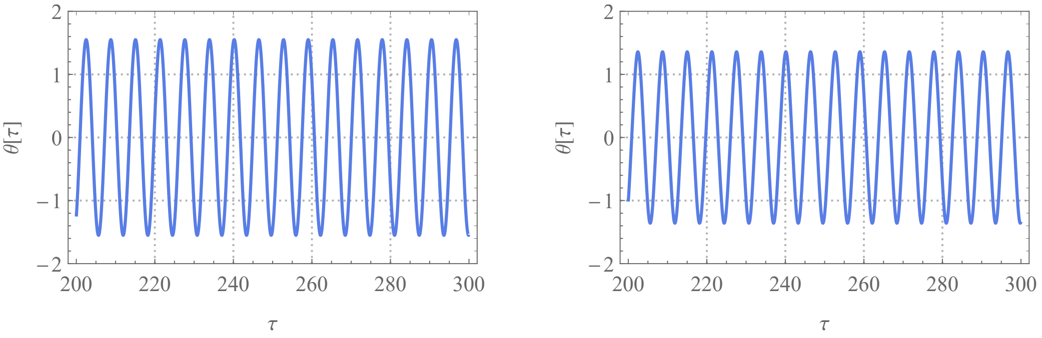

(a) Multiple scales results of θ over τ with $\varepsilon_r = 1$

(b) Numerical results of θ over τ with $\varepsilon_r = 1$

Figure 5.31: Results for the coordinate θ. With the variables set to: $\omega = 1$, $\bar{a}_v = 0.16$, $\bar{a}_w = 0.16$, $\bar{\alpha}_\theta = 0.05$, $\bar{P}_\theta = 0.15$, and $\bar{\gamma} = \frac{1}{6}$

The first-order differential Equations (5.25) and (5.26) are solved with a suitable procedure for numerical integration for the experimentally determined parameters. Figure 5.32 shows the numerical results with the steady-state values being $a_p = 0.25$ and $\alpha_p = -1.6$.

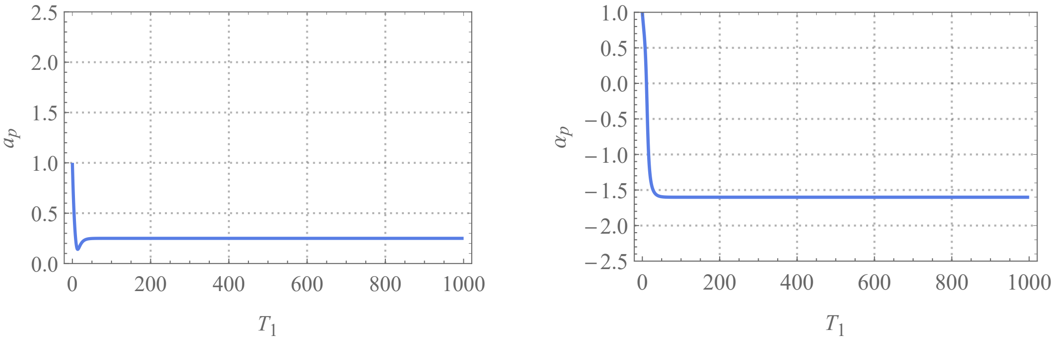

(a) Amplitude a_p over T_1

(b) Phase of motion α_p over T_1

Figure 5.32: Numerical analysis of the amplitude a_p and phase of motion α_p of the secular terms. With the variables set to: $\omega = 1$, $\bar{a}_v = 0.064$, $\bar{a}_w = 0$, $\bar{\alpha}_\theta = 0.0648$, $\bar{P}_\theta = 0.15$, $\bar{\gamma} = \frac{1}{6}$, ICs $= 1$, and $\varepsilon_r = 1$

5.5.2 Frequency Response Equation

In the following, a frequency response equation with a detuning parameter is derived. Recalling Equation (5.21) and introducing principal parametric resonance with a detuning parameter $\beta_w = 2\omega + \varepsilon\sigma_p$ and likewise introducing $\beta_v = \omega + \varepsilon\sigma_d$. Note that as in related works [156, 158] the detuning parameter is introduced into the exponential function. The excitation frequencies outside the exponential function are considered as constants and are therefore replaced with ω and 2ω, see Equation (5.28).

$$\begin{aligned}
D_0^2\theta_1 + \omega^2\theta_1 = & -2i\omega D_1 A e^{i\omega T_0} + 2i\omega D_1 \bar{A} e^{-i\omega T_0} \\
& - \bar{\alpha}_\theta i\omega A e^{i\omega T_0} + \bar{\alpha}_\theta i\omega \bar{A} e^{-i\omega T_0} \\
& + \bar{\gamma}\omega^2 A^3 e^{3i\omega T_0} + 3\bar{\gamma}\omega^2 A^2 \bar{A} e^{i\omega T_0} + 3\bar{\gamma}\omega^2 \bar{A}^2 A e^{-i\omega T_0} + \bar{\gamma}\omega^2 \bar{A}^3 e^{-3i\omega T_0} \\
& + \frac{1}{2}\bar{a}_v \beta_v^2 e^{i(\omega+\varepsilon\sigma_d)T_0} + \frac{1}{2}\bar{a}_v \beta_v^2 e^{-i(\omega+\varepsilon\sigma_d)T_0} \\
& + \frac{1}{2}\bar{a}_w \beta_w^2 \bar{A} e^{-i\omega T_0 + i(2\omega+\varepsilon\sigma_d)T_0} + \frac{1}{2}\bar{a}_w \beta_w^2 A e^{i\omega T_0 - i(2\omega+\varepsilon\sigma_d)T_0} \\
& + \frac{1}{2}\bar{a}_w \beta_w^2 A e^{i\omega T_0 + i(2\omega+\varepsilon\sigma_d)T_0} + \frac{1}{2}\bar{a}_w \beta_w^2 \bar{A} e^{-i\omega T_0 - i(2\omega+\varepsilon\sigma_d)T_0} \\
& - \frac{2\bar{P}_\theta i\omega A}{\pi\varepsilon_r} e^{i\omega T_0} + \frac{2\bar{P}_\theta i\omega \bar{A}}{\pi\varepsilon_r} e^{-i\omega T_0}.
\end{aligned} \tag{5.28}$$

This gives the following secular terms:

$$D_1 A = -\frac{1}{2}\bar{\alpha}_\theta A - \frac{3}{2}\bar{\gamma}\omega i A^2 \bar{A} - \frac{1}{4}\bar{a}_v \omega i e^{i\varepsilon\sigma_p T_0} - \bar{a}_w \omega i \bar{A} e^{i\varepsilon\sigma_p T_0} - \frac{\bar{P}_\theta A}{\pi\varepsilon_r}. \tag{5.29}$$

Introducing the polar notation from Equations (5.23) and (5.24) in Equation (5.29) and subsequently splitting the equation into real and imaginary parts gives:

$$a_p' = 2\left(-\frac{1}{4}\omega\sin\left(\alpha_p - \sigma_p\right)\bar{a}_v - \frac{1}{2}\omega\sin\left(2\alpha_p - \sigma_p\right)a_p\bar{a}_w - \frac{a_p\bar{P}_\theta}{\pi\varepsilon_r} - \frac{1}{4}a_p\bar{\alpha}_\theta\right). \tag{5.30}$$

$$a_p\alpha_p' = 2\left(-\frac{3}{16}\omega\bar{\gamma}a_p^3 - \frac{1}{4}\omega\cos\left(\alpha_p - \sigma_p\right)\bar{a}_v - \frac{1}{2}\omega\cos\left(2\alpha_p - \sigma_p\right)a_p\bar{a}_w\right). \tag{5.31}$$

Introducing a transformed phase angle ψ for the parametric resonance to make Equations (5.30) and (5.31) autonomous, see Equation (5.32).

$$\psi = \varepsilon\sigma_p T_0 - 2\alpha_p = \sigma_p T_1 - 2\alpha_p. \tag{5.32}$$

To obtain steady-state solution $a_p' = \psi' = 0$ is introduced which gives $\sigma_p = 2\alpha_p$. Since in Equations (5.30) and (5.31) the system is excited both parametrically and in primary resonance the same procedure is used for the primary resonance subsequently. This expression is introduced on the left hand side of Equation (5.31). Subsequently Equations (5.30) and (5.31) are squared and added which gives the frequency response equation.

$$\left(\frac{3}{8}\omega\bar{\gamma}a_p^3 + \frac{a_p\sigma_p}{2}\right)^2 + \frac{1}{4}a_p^2\left(\frac{4\bar{P}_\theta}{\pi\varepsilon_r} + \bar{\alpha}_\theta\right)^2 = \frac{1}{4}\omega^2\bar{a}_v^2 + \omega^2 a_p^2\bar{a}_w^2. \tag{5.33}$$

Figure 5.33 shows the frequency response of the pendulum as described by Equation (5.33). There are eight different cases shown, for various excitation configurations, damping ratios, and power take-off cases. The vertically excited simple pendulum is shown in Figure 5.33a, the pendulum shows softening characteristics due to the cubic nonlinearities. Cartmell [156] and Xu and Wiercigroch [158] observed similar results for their vertical excited simple pendulums.

In Figure 5.33b the pendulum is forced in the horizontal and vertical directions. This excitation configuration shows the softening character of the pendulum. However, for an amplitude a_p below 0.5 the detuning parameter goes to plus-minus infinity. Similar dynamics can be observed in Figure 5.33c where the pendulum is solely excited in the horizontal direction.

Figure 5.33d shows the frequency response diagram for the experimentally determined parameters. The system shows softening characteristics.

In the next step the power take-off was set to a value of $\bar{P}_\theta = 0.15$, see Figures 5.33e to 5.33h. For the vertical excited system in Figure 5.33e, the two branches move closer to the zero point (closer to the y-axis) when compared to the switched off power take-off. The same occurs when the system is excited in both directions see Figure 5.33f. The frequency response for the horizontally excited pendulum, in Figure 5.33g, shows a maximum amplitude $a_p = 0.65$ for a value of the detuning parameter slightly lower than zero. Figure 5.33h shows the frequency response diagram for the experimentally determined damping ratios and excitation amplitudes.

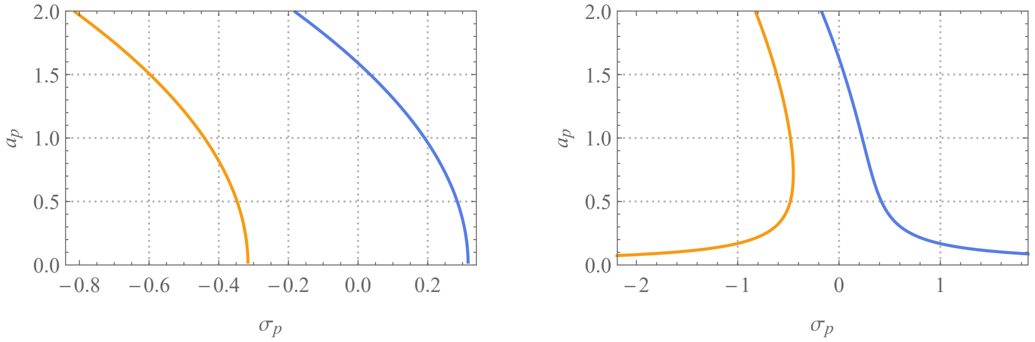

(a) Excitation $\bar{a}_v = 0.0$, $\bar{a}_w = 0.16$, and $\bar{P}_\theta = 0$

(b) Excitation $\bar{a}_v = 0.16$, $\bar{a}_w = 0.16$, and $\bar{P}_\theta = 0$

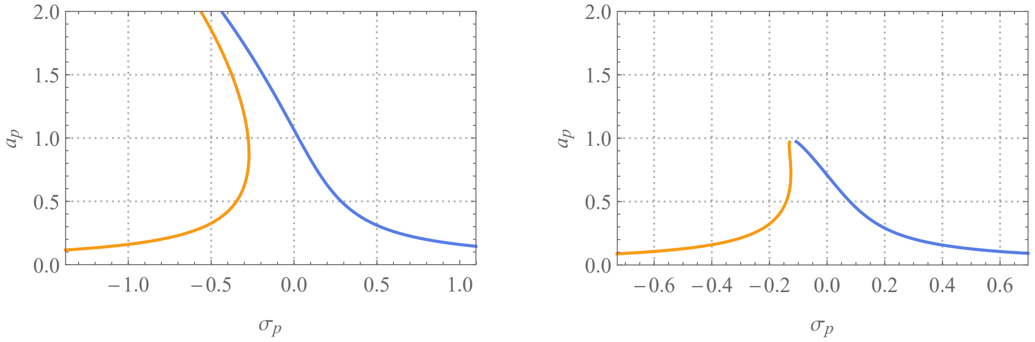

(c) Excitation $\bar{a}_v = 0.16$, $\bar{a}_w = 0.0$, and $\bar{P}_\theta = 0$

(d) Excitation $\bar{a}_v = 0.064$, $\bar{a}_w = 0.0$, damping ratio changed to $\bar{\alpha}_\theta = 0.0648$, and $\bar{P}_\theta = 0$

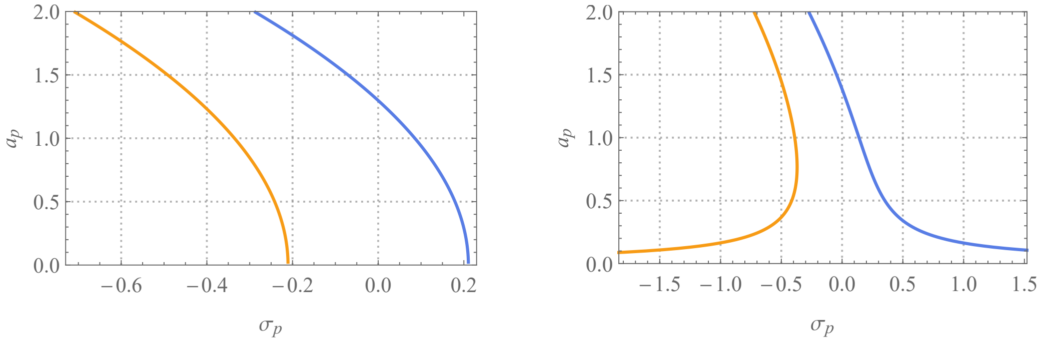

(e) Excitation $\bar{a}_v = 0.0$, $\bar{a}_w = 0.16$, and $\bar{P}_\theta = 0.15$

(f) Excitation $\bar{a}_v = 0.16$, $\bar{a}_w = 0.16$, and $\bar{P}_\theta = 0.15$

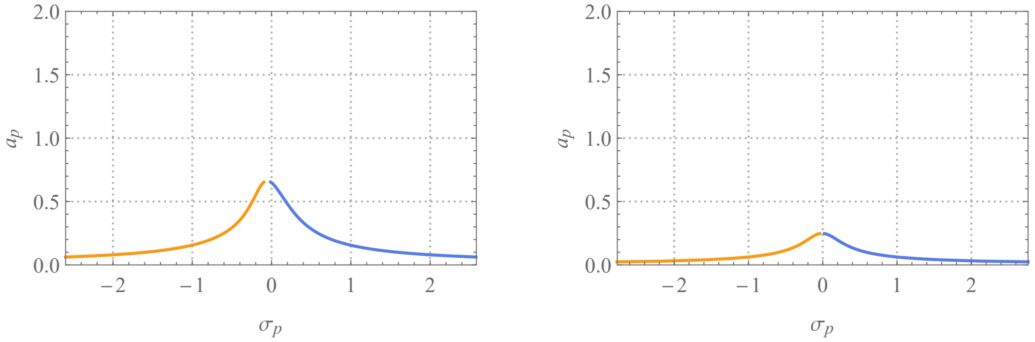

(g) Excitation $\bar{a}_v = 0.16$, $\bar{a}_w = 0.0$, and $\bar{P}_\theta = 0.15$

(h) Excitation $\bar{a}_v = 0.064$, $\bar{a}_w = 0.0$, damping ratio changed to $\bar{\alpha}_\theta = 0.0648$, and $\bar{P}_\theta = 0.15$

Figure 5.33: Frequency response diagrams with the variables set to: $\omega = 1$, $\bar{\alpha}_\theta = 0.05$, $\bar{\gamma} = \frac{1}{6}$, $\varepsilon_r = 1$, and ICs $= 1$

Chapter 6

Experimental Analysis

This section examines the experimental results of the omnidirectional pendulum energy harvester. The design is introduced in Section 3.2. The results presented in this section are given with dimensions to clearly distinguish them from the numerical results. In the experimental analysis section the dynamics of the two shafts are examined separately. The experimental analysis section is initially observing linear frequency responses, since the likelihood of a constant excitation frequency is higher in possible areas of application. The section concludes with the inclusion of excitation frequency sweeps to observe a possible broadening of the operational range of the energy harvester.

Several excitation conditions for the energy harvester have been uploaded to YouTube to give the reader a better overall picture of the energy harvester [3]. The uploaded videos are those that are examined in Section 6.4.

6.1 Omnidirectional Pendulum Energy Harvester with a Pendulum Length of 0.5 m

The dynamics, voltage, and power output of the energy harvester with a pendulum length 0.5 m are examined in the following section. The measurements are conducted with and without a power take-off.

6.1.1 Dynamics of the Omnidirectional Pendulum Energy Harvester in the Low Power Take-Off Mode

The pendulum energy harvester presented here is limited to a frequency range where the optimum operational region lies. It is therefore crucial to know the precise operational range for the pendulum energy harvester. Therefore, in this section the figures shown are for the most part not time-dependent but the excitation frequency or excitation amplitude is used as a control parameter. This allows the parameters to be determined over several measurements, to compare and take the arithmetic mean the results with each other to obtain statistically more accurate results. This is achieved with frequency responses and deflections over excitation amplitude responses. In this section the energy harvester is examined in the low power power take-off mode. This means that a high value series resistor of 10 kΩ was included in the electrical circuit to decrease the current and therefore the damping ratios are determined with a value of $\xi_{14} = 0.0325$ and $\xi_{23} = 0.0323$ which is mainly attributed to the friction within the generators and bearings and a tiny amount of aerodynamic dissipation. The calculated undamped natural frequency of a simple pendulum with a length of 0.5 m has a value of 0.70 Hz. This can be assumed as the natural frequency of the spherical pendulum energy harvester.

In Figure 6.1 the pendulum energy harvester is placed on the shaker table with an offset of $\alpha_{offset} = 0°$ and is excited with an excitation amplitude of $A = 24$ mm for which the coordinate θ_{14} does not show any deflection. This offset angle is one of the two extrema of the operational energy harvester where the dynamics of the harvester are similar to those of a simple pendulum. The energy input is converted to the movement of the coordinate θ_{23}. This means that the omnidirectional energy harvester degenerates to a simple pendulum energy harvester for an angle $\alpha_{offset} = 0°$ or $\alpha_{offset} = 90°$ and every following 90° angle. The excitation amplitude $A = 24$ mm is the maximum achievable value for this configuration before the pendulum bob hits the cage. The frequency response and the arithmetic mean rectified voltage output over the excitation frequency are shown in Figure 6.1a and Figure 6.1b. Both Figures show the expected softening characteristics of the simple pendulum. The global maximum amplitude of the coordinate θ_{23} is reached at an excitation frequency of 0.68 Hz. Unfortunately, one of the pins was disconnected from the microcontroller during this measurements and therefore the voltage measurement failed at and is therefore cannot be seen. However, it is safe to assume that the a

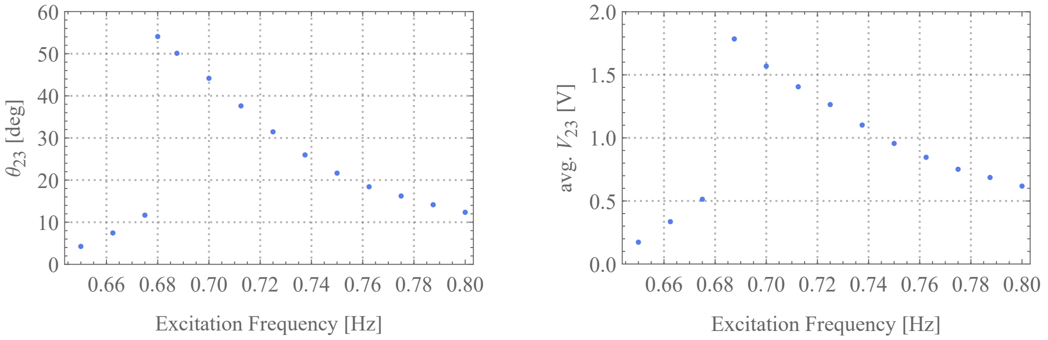

(a) Frequency response of the coordinate θ_{23}

(b) Arithmetic mean rectified voltage output avg. V_{23} over the excitation frequency Ω

Figure 6.1: Frequency response and voltage output over excitation frequency Ω for the pendulum energy harvester in the low power take-off mode. The parameters of the pendulum energy harvester are: $l = 0.5$ m, $m = 1.32$ kg, $\alpha_{offset} = 0°$, $A = 24$ mm, $\xi_{14} = 0.0325$, $\xi_{23} = 0.0323$, $R_P =$ NC, and $R_S = 10$ kΩ.

maximum arithmetic mean rectified voltage output is observed at this excitation frequency.

Figure 6.2 shows the frequency response and the arithmetic mean rectified voltage output over the excitation frequency with an excitation amplitude of $A = 24$ mm for the energy harvester with an offset angle of $\alpha_{offset} = 90°$. As mentioned before, this configuration only allows a rotation of the coordinate θ_{14} and the coordinate θ_{23} does not respond. These plots show softening characteristics for the coordinate θ_{14} and the arithmetic mean rectified voltage output as well. The global maximum is reached at an excitation frequency of 0.68 Hz with the maximum values being $\theta_{14} = 47.7°$ and avg. $V_{14} = 1.52$ V.

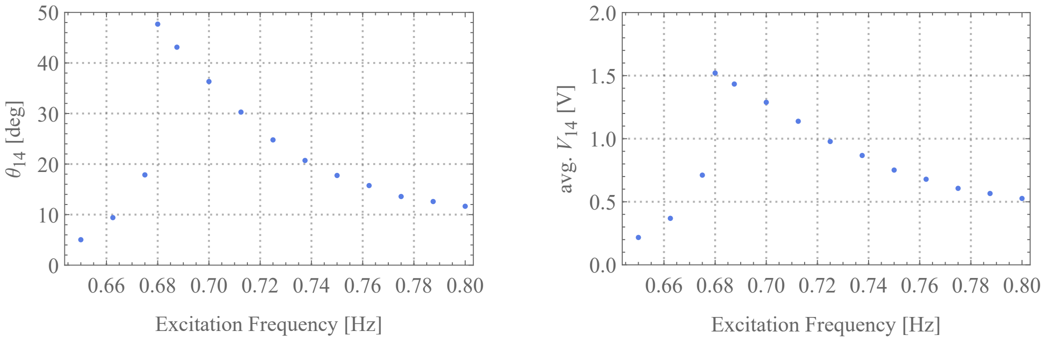

(a) Frequency response of the coordinate θ_{14}

(b) Arithmetic mean rectified voltage output avg. V_{14} over the excitation frequency Ω

Figure 6.2: Frequency response and voltage output over excitation frequency Ω for the pendulum energy harvester in the low power take-off mode. The parameters of the pendulum energy harvester are: $l = 0.5$ m, $m = 1.32$ kg, $\alpha_{offset} = 90°$, $A = 24$ mm, $\xi_{14} = 0.0325$, $\xi_{23} = 0.0323$, $R_P =$ NC, and $R_S = 10$ kΩ.

When comparing Figure 6.1 to Figure 6.2 it is seen that even though the system is excited with the same excitation amplitude the maximal deflection of the coordinate θ_{23} is slightly larger than the amplitude of coordinate θ_{14}. This agrees with the previously determined damping ratios which are slightly lower for the coordinate θ_{23} compared to the coordinate θ_{14}.

For an omnidirectional energy harvester it is indispensable that power can be generated from the system regardless of the excitation direction. Therefore an offset angle of $\alpha_{offset} = 45°$ is selected to ensure participation of both shafts. The results for the frequency response and arithmetic mean rectified voltage output over excitation frequency for an excitation amplitude of $A = 24$ mm are shown in Figure 6.3. At first glance it can be seen that the deflection of the coordinates θ_{14} and θ_{23} are lower compared to the simple pendulums with the same configuration. Therefore, higher excitation amplitudes are achievable for this configuration before the pendulum bob collides with the supporting structure. Additionally, the dynamics are generally different and not as neat as for the simple pendulum and this needs to be looked at more closely for correct interpretation of the results.

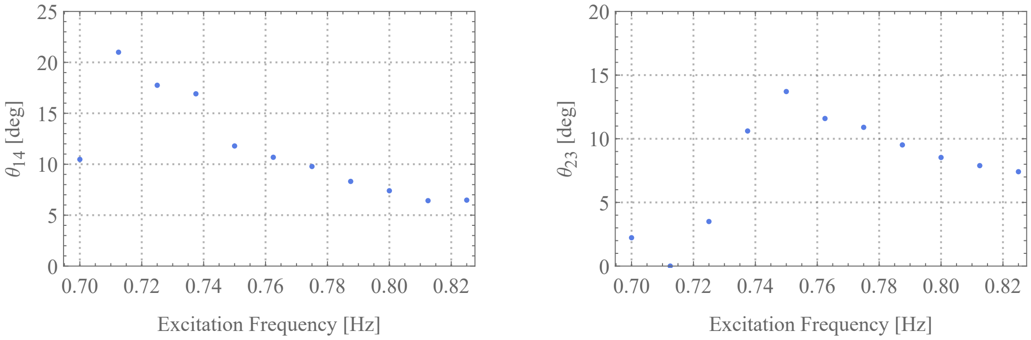

(a) Frequency response of the coordinate θ_{14}

(b) Frequency response of the coordinate θ_{23}

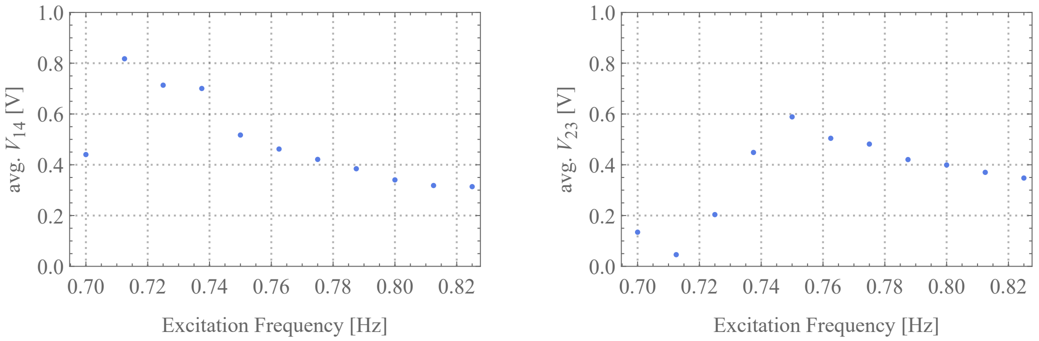

(c) Arithmetic mean rectified voltage output avg. V_{14} over the excitation frequency Ω

(d) Arithmetic mean rectified voltage output avg. V_{23} over the excitation frequency Ω

Figure 6.3: Frequency responses and voltage output over excitation frequency Ω for the pendulum energy harvester in the low power take-off mode. The parameters of the pendulum energy harvester are: $l = 0.5$ m, $m = 1.32$ kg, $\alpha_{offset} = 45°$, $A = 24$ mm, $\xi_{14} = 0.0325$, $\xi_{23} = 0.0323$, $R_P = \text{NC}$, and $R_S = 10\ \text{k}\Omega$.

The frequency response of the coordinate θ_{14} as shown in Figure 6.3a is close to the expected softening characteristics as they are for a simple pendulum. The maximum of θ_{14} is reached at an excitation frequency of $\Omega = 0.7125$ Hz with a value of $\theta_{14} = 20.0°$. The value for the maximum voltage output at the same excitation frequency has a value of avg. $V_{14} = 0.82$ V. However, these results were the first ones measured, and therefore only a few points have been measured to see that the value of the coordinate θ_{14} will increase again for a value of the excitation frequency $\Omega = 0.74$ Hz and then abruptly jump down to the next measured point. These dynamics can be observed in the following figures where the density of measurements points was increased in the important areas. The coordinate θ_{23} in Figure 6.3b starts with a slight deflection and jumps down to zero after that, then the deflection angle rises steeply and reaches its maximum $\theta_{23} = 13.7°$ for a value of the excitation frequency of $\Omega = 0.75$ Hz. The value for the maximum at the same excitation frequency has a value of avg. $V_{23} = 0.59$ V. After the maximum is passed the value for the coordinate θ_{23} slowly decreases with an increase in the excitation frequency. The arithmetic mean rectified voltage output in Figure 6.3c and Figure 6.3d shows the same overall characteristics as the frequency responses of the coordinates

θ_{14} and θ_{23}.

In Figure 6.4 the amplitude is increased to a value of $A = 32$ mm. This is the maximum achievable amplitude for the system before the pendulum bob collides with the supporting structure for a value of the excitation frequency of $\Omega = 0.68$ Hz. When comparing Figures 6.3 and 6.4, it is evident that more measurement points have been added at key positions. With this higher resolution it can be observed that for the coordinate θ_{14} the deflection in Figure 6.4a jumps up to a global maximum value of $\theta_{14} = 46.9°$ with a value of the excitation frequency of $\Omega = 0.68$ Hz. At the same time, the coordinate θ_{23} hardly deflects, so for this frequency range simple pendulum dynamics can be assumed, and, as expected, the softening properties are observed. In the following the value for the coordinate θ_{14} decreases up to a value of the excitation frequency of $\Omega = 0.725$ Hz where it reaches a local minimum. Then θ_{14} rises again until eventually jumping down to a lower value when exceeding an excitation the local maximum at a frequency of $\Omega = 0.75$ Hz. This results in a broadening of the operational range

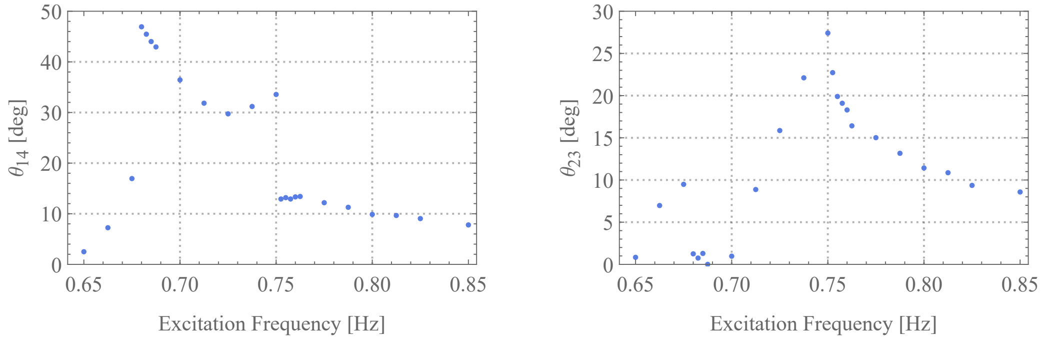

(a) Frequency response of of the coordinate θ_{14}

(b) Frequency response of the coordinate θ_{23}

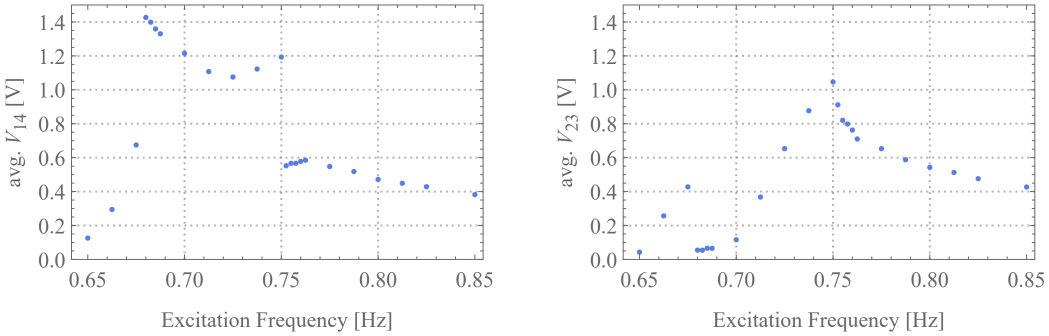

(c) Arithmetic mean rectified voltage output over avg. V_{14} the excitation frequency Ω

(d) Arithmetic mean rectified voltage output avg. V_{23} over the excitation frequency Ω

Figure 6.4: Frequency responses and voltage output over excitation frequency Ω for the pendulum energy harvester in the low power take-off mode. The parameters of the pendulum energy harvester are: $l = 0.5$ m, $m = 1.32$ kg, $\alpha_{offset} = 45°$, $A = 32$ mm, $\xi_{14} = 0.0325$, $\xi_{23} = 0.0323$, $R_P = \text{NC}$, and $R_S = 10\ \text{k}\Omega$.

of the pendulum energy harvester for the coordinate θ_{14} with a hardening effect that is observed at the end of the operating range.

The dynamics of θ_{23} are more complicated at first glimpse and therefore need to be observed with caution. Figure 6.4b shows the angular displacement of the coordinate θ_{23}. When increasing the excitation frequency, it can be seen that over the first three measurement points the value of θ_{23} increases and then immediately drops to a value close to zero and holds this value until it starts rising again after the excitation frequency of $\Omega = 0.7$ Hz is exceeded. It can be assumed that the interaction between the two shafts has an influence here. In the following the coordinate θ_{23} undergoes a frequency response as one would expect from a linear system. The global maximum is reached for an excitation frequency of $\Omega = 0.75$ Hz with a value of $\theta_{23} = 27.3^\circ$. It is worth mentioning that at this excitation frequency the trajectory of the pendulum bob is of almost perfect circular shape and can therefore be considered to be operating as a conical pendulum. The same applies for the preceding excitation frequency of $\Omega = 0.7375$ Hz. The arithmetic mean rectified voltage output again shows similar dynamics to those of the coordinate. With the local maximum arithmetic mean rectified voltage outputs being: avg. $V_{14} = 1.42$ V, avg. $V_{14} = 1.18$ V, avg. $V_{23} = 0.43$ V, and avg. $V_{23} = 1.04$ V (from left to right).

Figure 6.5 shows the frequency response and the arithmetic mean rectified voltage output over the excitation frequency for an excitation amplitude of $A = 32$ mm and an offset angle of $\alpha_{offset} = 135^\circ$. The offset angle was chosen to determine whether the characteristic dynamics of the coordinate θ_{14} depend on the orientation of the energy harvester towards the excitational force or whether this is a design characteristic. The global maximum amplitude is reached at an excitation frequency of $\Omega = 0.675$ Hz with it being $\theta_{14} = 51.3^\circ$. At the end of the operational range for the coordinate θ_{14} the local maximum has a value of $\theta_{14} = 33.9^\circ$ at an excitation frequency of $\Omega = 0.75$ Hz. Since there is hardly any difference between Figure 6.4 and Figure 6.5, it can be assumed that shaft 14 shows dynamic properties due to design properties and the slightly higher damping ratio. One significant difference between the offset angle of $\alpha_{offset} = 45^\circ$ and $\alpha_{offset} = 135^\circ$ can be seen in Figure 6.5b where the deflection angle θ_{23} drops directly to a lower value after reaching its local maximum amplitude at $\Omega = 0.75$ Hz with a value of $\theta_{23} = 28.4^\circ$, compared to Figure 6.4b where an intermediate step can be seen.

The arithmetic mean rectified voltage output of the coordinate θ_{14} in Figure 6.5c shows local maxima with a value of avg. $V_{14} = 1.43$ V and avg. $V_{14} = 1.12$ V. In Figure 6.5d the arithmetic mean rectified voltage output of the coordinate θ_{23} has two local maxima which are avg. $V_{23} = 0.29$ V and avg. $V_{23} = 0.99$ V.

Furthermore, the quasi-periodic dynamics of the pendulum energy harvesters within the frequency response in Figure 6.5 can be found. It should be noted that these dynamics can be found at the same position in all frequency responses with an offset angle $\alpha_{offset} = 45^\circ$

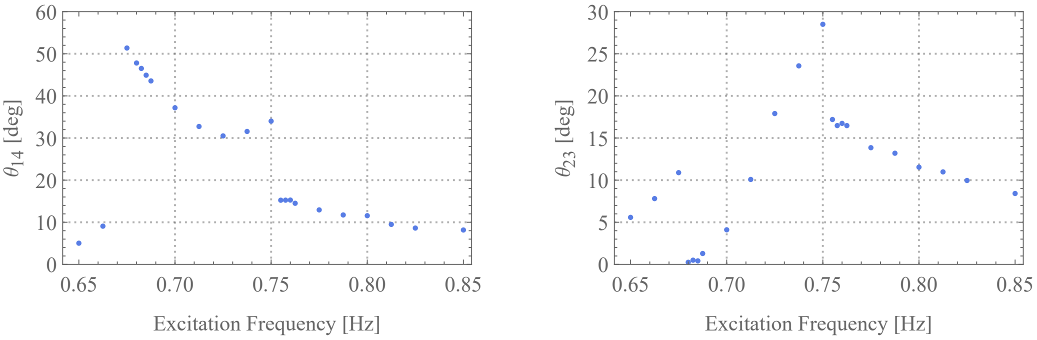

(a) Frequency response of the coordinate θ_{14}

(b) Frequency response of the coordinate θ_{23}

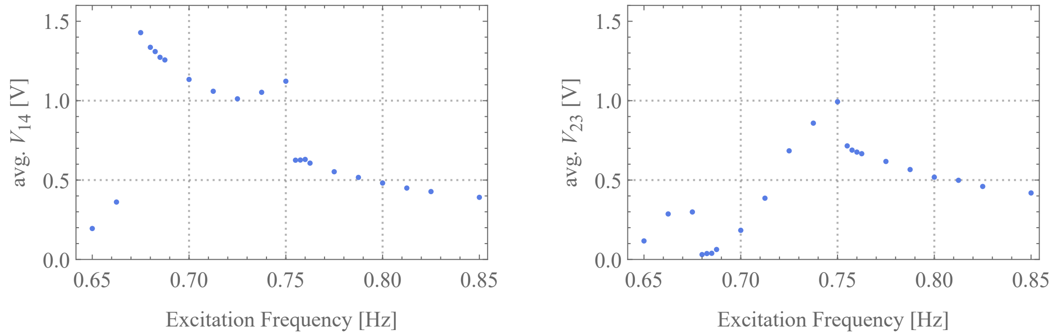

(c) Arithmetic mean rectified voltage output avg. V_{14} over the excitation frequency Ω

(d) Arithmetic mean rectified voltage output avg. V_{23} over the excitation frequency Ω

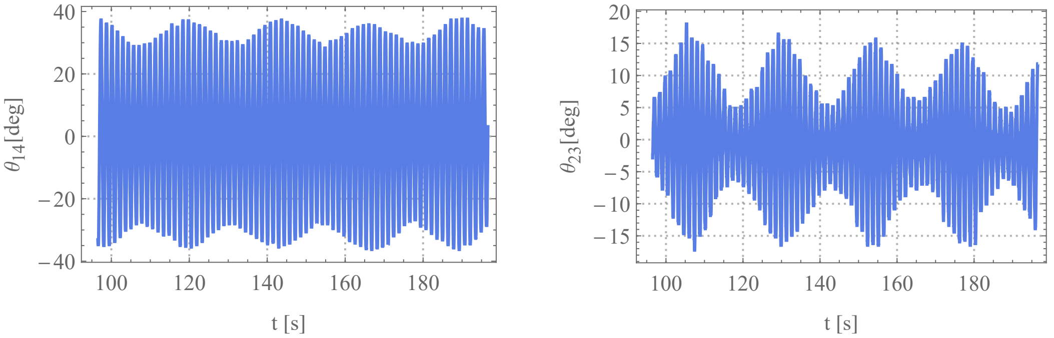

(e) θ_{14} over time for an excitation frequency of $\Omega =$ 0.7125 Hz

(f) θ_{23} over time for an excitation frequency of $\Omega =$ 0.7125 Hz

Figure 6.5: Frequency responses, voltage output over excitation frequency Ω, and deflection angles over time for the pendulum energy harvester in the low power take-off mode. The parameters of the pendulum energy harvester are: $l = 0.5$ m, $m = 1.32$ kg, $\alpha_{offset} = 135°$, $A = 32$ mm, $\xi_{14} = 0.0325$, $\xi_{23} = 0.0323$, $R_P =$ NC, and $R_S = 10$ kΩ.

and $\alpha_{offset} = 135°$. Figures 6.5e and 6.5f show the time domain responses for an excitation frequency of $\Omega = 0.7125$ Hz for the two coordinates θ_{14} and θ_{23}. The time domain clearly suggests quasi-periodic dynamics.

The dynamics of the energy harvester show a repeating pattern. This is with the assistance of Figures 6.5a and 6.5b. For this the energy harvester is observed from the top view. Before the first local maximum of the coordinate θ_{14} is reached the pendulum bob moves parallel to the direction of excitation. Therefore, both shafts are engaged in the movement in equal parts. When the first local maximum of the coordinate θ_{14} is reached the whole motion is observed in shaft 14. The coordinate θ_{23} does not show any oscillation at this point. With a further increase in excitation frequency the trajectory of the pendulum bob becomes more oval and eventually becomes almost circular when the second local maximum of the coordinate θ_{14} is reached. With a further increase the trajectory of the bob oscillates parallel to the direction of excitation again.

Figure 6.6 shows the angular displacement and the arithmetic mean rectified voltage output for a variation of the excitation amplitude for an excitation frequency of $\Omega = 0.7375$ Hz. The

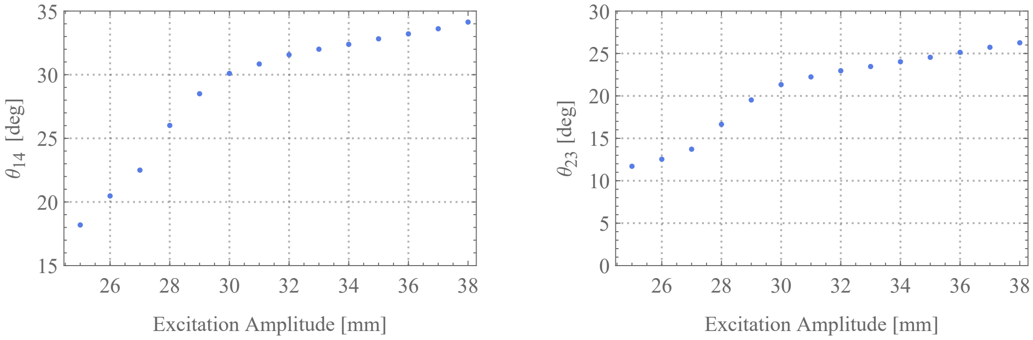

(a) θ_{14} over the excitation amplitude A

(b) θ_{23} over the excitation amplitude A

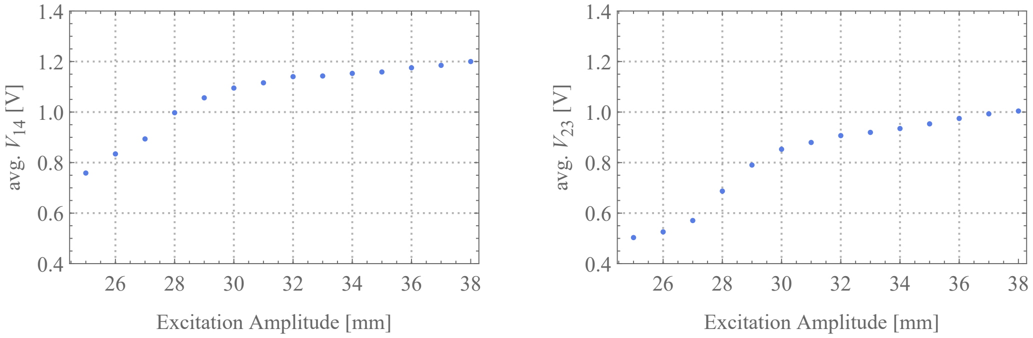

(c) Arithmetic mean rectified voltage output avg. V_{14} over the excitation amplitude A

(d) Arithmetic mean rectified voltage output avg. V_{23} over the excitation amplitude A

Figure 6.6: Variation of the excitation amplitude A of the pendulum energy harvester in the low power take-off mode. The parameters of the pendulum energy harvester are: $l = 0.5$ m, $m = 1.32$ kg, $\alpha_{offset} = 45°$, $\Omega = 0.7375$ Hz, $\xi_{14} = 0.0325$, $\xi_{23} = 0.0323$, $R_P =$ NC, and $R_S = 10$ kΩ.

excitation frequency was chosen because the bob here shows a circular motion and therefore both coordinates show a deflection. The coordinate θ_{14} shows a steep rise with an increase of the excitation amplitude until it reaches a point at an excitation amplitude of $A = 30$ mm where the graph bends and afterwards the slope of the coordinate θ_{14} is smaller. This trend can be observed for the arithmetic mean rectified voltage output avg. V_{14} as well, see Figure 6.6c.

For the coordinate θ_{23} in Figure 6.6b, the system shows an inflection point at an excitation amplitude of $A = 28$ mm. Within the area of the infection point the slope is slightly increased but afterwards the slope decreases again to pre-inflection point values. The arithmetic mean rectified voltage output V_{23} in Figure 6.6d shows similar characteristics to the deflection of the coordinate θ_{23}.

This shows that not only the excitation frequency but also the excitation amplitude shows nonlinear properties. For an effective energy harvester it is advantageous to operate the system above an excitation amplitude of $A = 30$ mm to utilise the previously completed steep slope.

6.1.2 Dynamics of the Omnidirectional Pendulum Energy Harvester in the High Power Take-Off Mode

In this section the power take-off load is increased electrically. This is achieved by removal of the series resistor and inclusion of a 10 Ω resistor parallel to the voltage sensor see Figure 3.5. This gives a higher current output and and therefore a higher electrical power output. The damping ratios of the two coordinates remain the same as in the low power output and have a value of $\xi_{14} = 0.0325$ and $\xi_{23} = 0.0323$. Since the current output is now physically larger and over surpasses the background noise of the current sensor the current can be measured and therefore the power output of the energy harvester can be determined.

Figure 6.7 shows the frequency response and arithmetic mean rectified voltage output of the pendulum energy harvester with an offset angle of $\alpha_{offset} = 45°$ and an excitation amplitude of $A = 32$ mm. Therefore, the measurements in Figure 6.7 are basically the measurements in Figure 6.4 with an increased power take-off. Therefore, it is not surprising that the amplitudes observed in the high power take-off mode are generally lower. Additionally, it can be seen that the previously clear jumps become less clear as the power take-off increases. The coordinate θ_{14} shows a global maximum deflection of $\theta_{14} = 31.86°$ at an excitation frequency of $\Omega = 0.6875$ Hz. The global maximum arithmetic mean rectified voltage output of the coordinate θ_{14} is observed at the same excitation frequency and has a value of avg. $V_{14} = 0.95$ V. In Figure 6.7b the local maximum deflections of the coordinate θ_{23} are at excitation frequencies of $\Omega = 0.68$ Hz and $\Omega = 0.76$ Hz and have values of $\theta_{23} = 9.32°$ and $\theta_{23} = 12.29°$. The arithmetic mean rectified voltage output at these positions gives values of avg. $V_{23} = 0.18$ V and avg. $V_{14} = 0.51$ V.

Next, the excitation amplitude is increased to its maximum possible value of $A = 44$ mm. With a higher excitation amplitude the pendulum bob would collide with the supporting structure. The excitation amplitude $A = 44$ mm is therefore the maximum possible excitation amplitude for the shown parameters of the pendulum energy harvester. This is carried out to show the maximum feasible power output of the harvester with a pendulum length of 0.5 m.

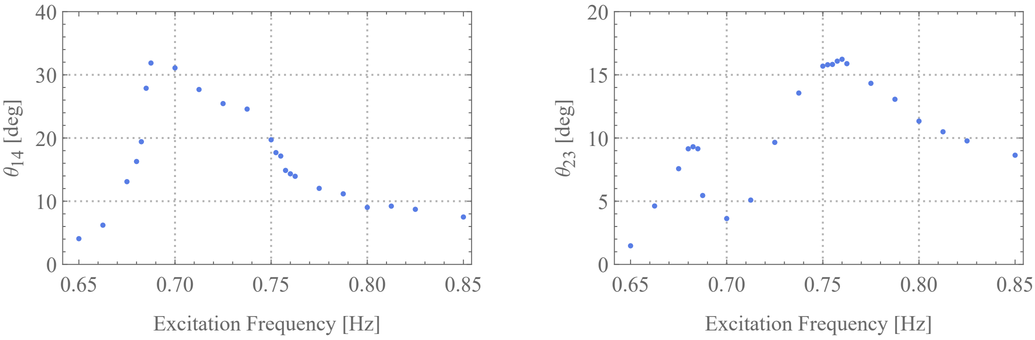

(a) Frequency response of the coordinate θ_{14}

(b) Frequency response of the coordinate θ_{23}

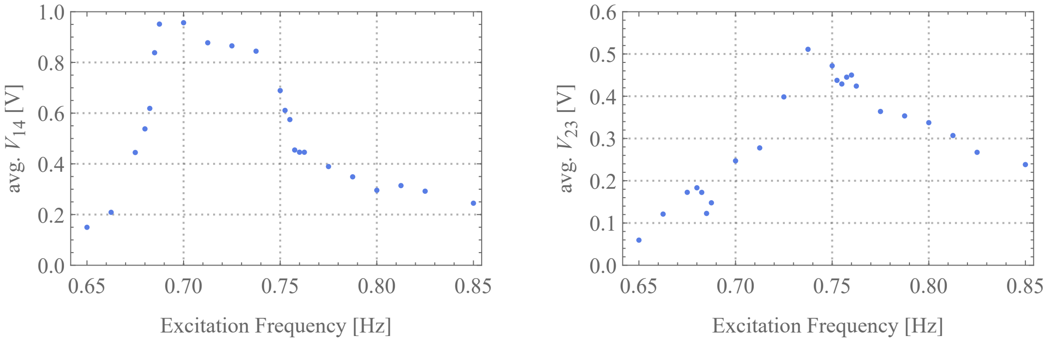

(c) Arithmetic mean rectified voltage output avg. V_{14} over the excitation frequency Ω

(d) Arithmetic mean rectified voltage output avg. V_{23} over the excitation frequency Ω

Figure 6.7: Frequency responses and arithmetic mean rectified voltage output over excitation frequency Ω for the pendulum energy harvester in the high power take-off mode. The parameters of the pendulum energy harvester are: $l = 0.5$ m, $m = 1.32$ kg, $\alpha_{offset} = 45°$, $A = 32$ mm, $\xi_{14} = 0.0325$, $\xi_{23} = 0.0323$, $R_P = 10\ \Omega$, and $R_S = 0\ \Omega$.

Figure 6.8 shows the rotational angles, the arithmetic mean rectified voltage, and the arithmetic mean rectified power output over the excitation frequency. Firstly, it can be observed that the jumps within the frequency response can clearly be seen again with an increased excitation amplitude. In Figure 6.8a θ_{14} shows a frequency response similar to the previously observed plots with the characteristic softening properties and the light hardening effect at the end of the operational range. The global maximum deflections of the coordinate θ_{14} being at excitation frequencies of $\Omega = 0.675$ Hz and $\Omega = 0.7625$ Hz with the values for the amplitudes being $\theta_{14} = 49.45°$ and $\theta_{14} = 37.4°$. Likewise, the frequency response for θ_{23} is similar to the previously observed figures with a global maximum deflection reached at an excitation frequency of $\Omega = 0.7625$ Hz with a value of $\theta_{23} = 31.7°$. The other local maximum is observed at an excitation frequency of $\Omega = 0.6625$ Hz with a value of $\theta_{23} = 12.78°$. The arithmetic mean rectified voltage output mostly verifies the angular displacement diagrams. The local maximum voltage outputs of the coordinate θ_{14} in Figure 6.8c being avg. $V_{14} = 1.37$ V and avg. $V_{14} = 1.27$ V. For the coordinate θ_{23} the arithmetic mean rectified voltage outputs at the positions of the maximal deflection are avg. $V_{23} = 0.33$ V and avg. $V_{23} = 1.5$ V see Figure 6.8d.

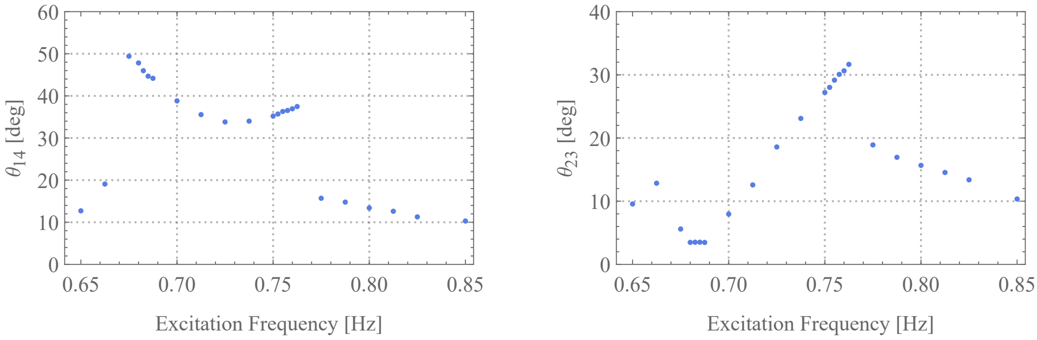

(a) Frequency response of the coordinate θ_{14}

(b) Frequency response of the coordinate θ_{23}

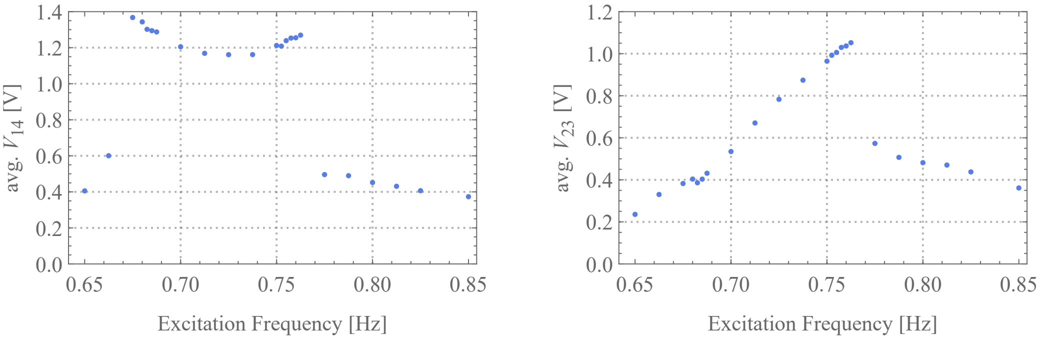

(c) Arithmetic mean rectified voltage output avg. V_{14} over the excitation frequency Ω

(d) Arithmetic mean rectified voltage output avg. V_{23} over the excitation frequency Ω

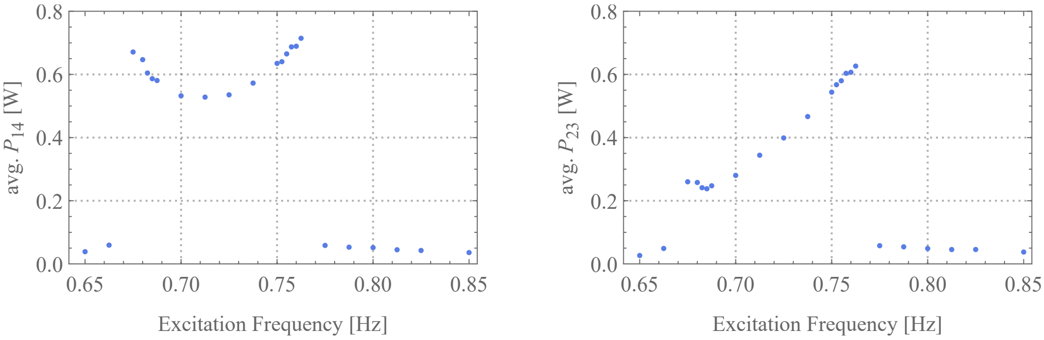

(e) Arithmetic mean rectified power output P_{14} over the excitation frequency Ω

(f) Arithmetic mean rectified power output P_{23} over the excitation frequency Ω

Figure 6.8: Frequency responses, voltage output over excitation frequency Ω, and arithmetic mean rectified power output over excitation frequency Ω for the pendulum energy harvester in the high power take-off mode. The parameters of the pendulum energy harvester are: $l = 0.5$ m, $m = 1.32$ kg, $\alpha_{offset} = 45°$, $A = 44$ mm, $\xi_{14} = 0.0325$, $\xi_{23} = 0.0323$, $R_P = 10\ \Omega$, and $R_S = 0\ \Omega$.

The coordinate θ_{14} has an arithmetic mean rectified power output of 0.67 W that can be produced for an excitation frequency of $\Omega = 0.675$ Hz. The right branch of the power output in Figure 6.8e is higher with a value of $P_{14} = 0.71$ W. This is because the velocity of the pendulum is higher on the right branch compared to the left branch. And with an increase in velocity the power output increases. The maximum power output of the coordinate θ_{23} has a value of

0.63 W at an excitation frequency of $\Omega = 0.7625$ Hz see Figure 6.8f .

Figure 6.9 shows the amplitudes of the two generator coordinates, the arithmetic mean rectified voltage output, and the power output over the excitation amplitude with an excitation frequency of $\Omega = 0.7375$ Hz. The excitation frequency was chosen because the bob here shows

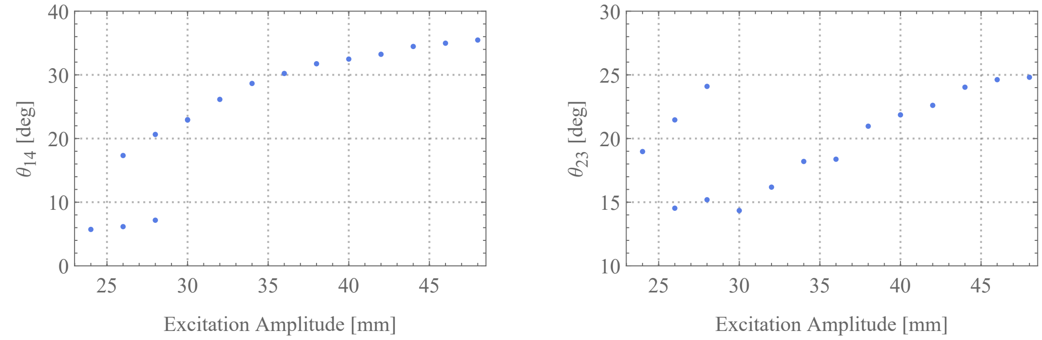

(a) θ_{14} over the excitation amplitude A

(b) θ_{23} over the excitation amplitude A

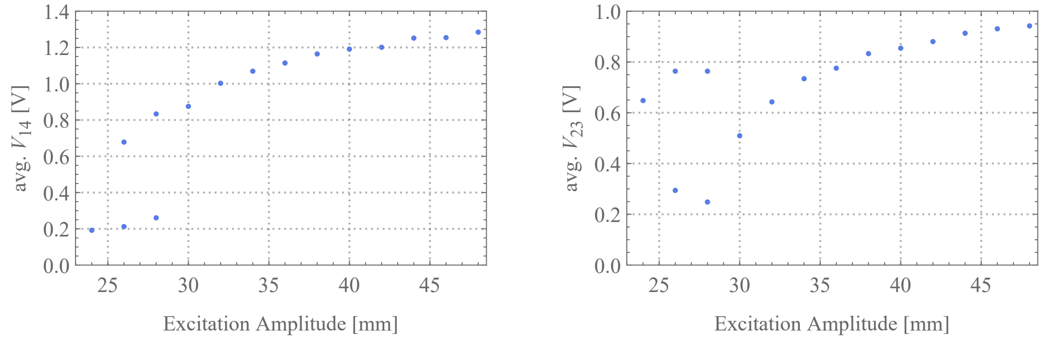

(c) Arithmetic mean rectified voltage output avg. V_{14} over the excitation amplitude A

(d) Arithmetic mean rectified voltage output avg. V_{23} over the excitation amplitude A

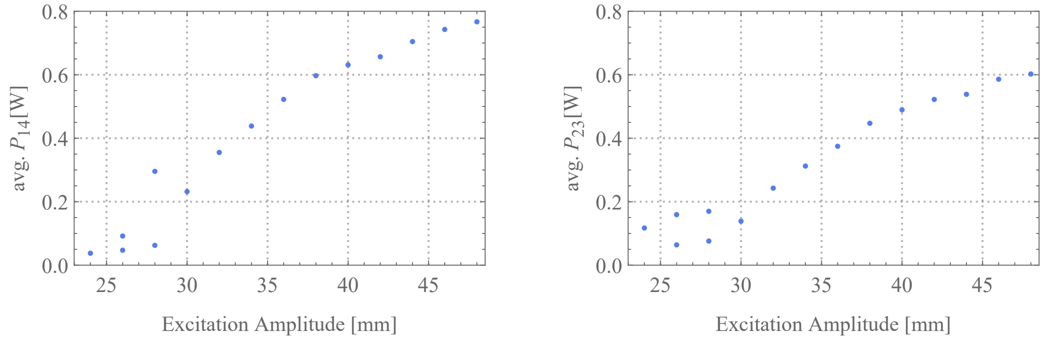

(e) Arithmetic mean rectified power output P_{14} over the excitation amplitude A

(f) Arithmetic mean rectified power output P_{23} over the excitation amplitude A

Figure 6.9: Deflection of the coordinates θ_{14} and θ_{23}, arithmetic mean rectified voltage output avg. V_{14} and avg. V_{23}, and arithmetic mean rectified power output P_{14} and P_{23} over the excitation amplitude A of the pendulum energy harvester in the high power take-off mode. The parameters of the pendulum energy harvester are: $l = 0.5$ m, $m = 1.32$ kg, $\alpha_{offset} = 45°$, $\Omega = 0.7375$ Hz, $\xi_{14} = 0.0325$, $\xi_{23} = 0.0323$, $R_P = 10\ \Omega$, and $R_S = 0\ \Omega$.

an almost circular motion and therefore both coordinates show a physically large deflection. In Figure 6.9a the deflection of the coordinate θ_{14} over the excitation amplitude is shown. For excitation amplitudes $A = 26$ mm and $A = 28$ mm the deflection shows two measurement points that have a large physical difference to each other. Therefore, the measurement was repeated several times to confirm the correctness of the measured points. Since the additional measurements confirmed the fact that they are in fact two individual points, it is not reasonable to take the arithmetic mean value for these measurements and instead it must be assumed that this shows an unstable branch with softening characteristics. For an excitation amplitude of $A = 26$ mm, this means that an amplitude for the coordinate θ_{14} of $6.1°$ or $17.2°$ can occur at the same time. At an excitation amplitude of $A = 28$ mm the two deflections have values of $\theta_{14} = 7.17°$ and $\theta_{14} = 20.6°$. It is important to mention that the same approach was used for the coordinate θ_{23}. As the excitation amplitude continues to increase further than an excitation amplitude of $A = 28$ mm, the deflection of the coordinate θ_{14} increases as well, but the slops flattens over time. The global maximum is reached with a value of $\theta_{14} = 35.5°$ for an excitation amplitude of $A = 48$ mm. Investigating a higher excitation amplitude is not possible, before internal collisions occur during the transient response, but it is safe to assume that a higher excitation amplitude would increase the deflection of the coordinate θ_{14}.

The arithmetic mean rectified voltage output avg. V_{14} is shown in Figure 6.9c and it follows the coordinate θ_{14} well and the global maximum arithmetic mean rectified voltage output has a value of avg. $V_{14} = 1.3$ V for an excitation amplitude of $A = 48$ mm. The values for the arithmetic mean rectified voltage output at an excitation amplitude of $A = 26$ mm are avg. $V_{14} = 0.21$ V and avg. $V_{14} = 0.68$ V and for an excitation amplitude of $A = 26$ mm they have the values avg. $V_{14} = 0.26$ V and avg. $V_{14} = 0.83$ V.

In Figure 6.9e the power output P_{14} over the excitation amplitude is shown. The global maximum power output of $P_{14} =$ 0.77 W at an excitation amplitude of $A = 48$ mm is observed.

The coordinate θ_{23} over the excitation amplitude is shown in Figure 6.9b. As in the case of the coordinate θ_{14}, the measured values of the excitation amplitude $A = 26$ mm and $A = 28$ mm have measurement points that are far from each other and are therefore confirmed as different points after repeated measurement. The value for an excitation amplitude of $A = 26$ mm are $\theta_{23} = 14.5°$ and $\theta_{23} = 21.5°$ and for an excitation amplitude of $A = 28$ mm they have values of $\theta_{23} = 15.2°$ and $\theta_{23} = 24.1°$. The global maximum has a deflection of $\theta_{23} = 24.8°$ at an excitation amplitude of $A = 48$ mm.

The arithmetic mean rectified voltage output avg. V_{23} follows the coordinate θ_{23}. The value for an excitation amplitude of $A = 26$ mm are $V_{23} = 0.29$ V and $V_{23} = 0.76$ V and for an excitation amplitude of $A = 28$ mm they have are $V_{23} = 0.25$ V and $V_{23} = 0.76$ V. The global maximum arithmetic mean rectified voltage output has a value of avg. $V_{23} = 0.94$ V for an excitation amplitude of $A = 48$ mm.

The power output P_{23} over the excitation amplitude is shown in Figure 6.9f. The global maximum power output at an excitation amplitude of $A = 48$ mm has a value of $P_{23} =$ 0.6 W.

6.2 Omnidirectional Pendulum Energy Harvester with a Pendulum Length of 0.75 m

The dynamics, voltage, and power output of the omnidirectional pendulum energy harvester with a pendulum length 0.75 m is examined in the following section. The experiments were carried out with and without a power take-off. It is generally known that the natural frequency of a simple pendulum can be calculated over the length of the pendulum see Equation (4.7). In principle, the longer the pendulum arm the lower the natural frequency becomes. Thus, the operational range of the pendulum energy harvester can be moved and optimised by deliberate selection of the pendulum length. A pendulum length of 0.75 m with a calculated linear undamped natural frequency of 0.576 Hz is tested in this section. This natural frequency is assumed for the spherical pendulum.

6.2.1 Dynamics of the Omnidirectional Pendulum Energy Harvester in the Low Power Take-Off Mode

The damping ratios with a pendulum length of 0.75 m show values of $\xi_{14} = 0.0204$ and $\xi_{23} = 0.020$. In Figure 6.10 the frequency response and the arithmetic mean rectified voltage output over the excitation frequency of the pendulum energy harvester with an offset angle of $\alpha_{offset} = 0°$ and with an excitation amplitude of $A = 24$ mm are both examined. Because of the selected offset angle the coordinate θ_{14} does not deflect and only a deflection of the

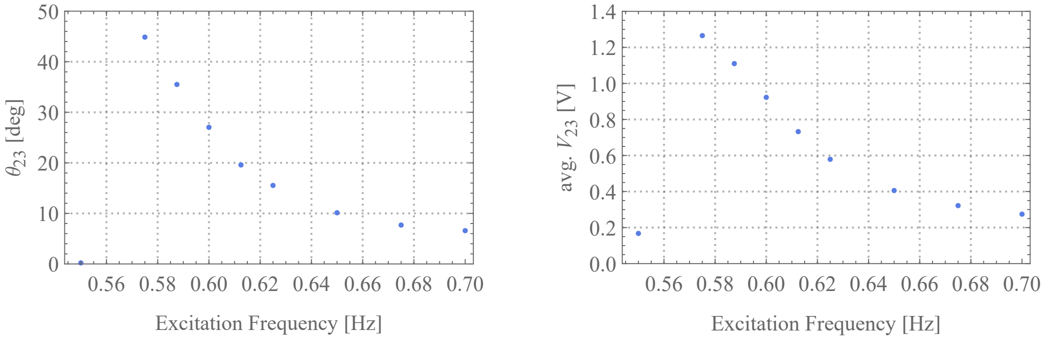

(a) Frequency response of the coordinate θ_{23}

(b) Arithmetic mean rectified voltage output avg. V_{23} over the excitation frequency Ω

Figure 6.10: Frequency response and arithmetic mean rectified voltage output over excitation frequency Ω for the pendulum energy harvester in the low power take-off mode with the parameters set to: $l = 0.75$ m, $m = 1.32$ kg, $\alpha_{offset} = 0°$, $A = 24$ mm, $\xi_{14} = 0.0204$, $\xi_{23} = 0.020$, $R_P =$ NC, and $R_S = 10\ k\Omega$.

coordinate θ_{23} is observed. The coordinate θ_{23} shows a classical frequency response of a system with softening properties with its maximum close to the calculated natural frequency at $\Omega = 0.575$ Hz with a global maximum amplitude of $\theta_{23} = 44.8°$ see Figure 6.10a. The same applies to the arithmetic mean rectified voltage output in the frequency domain with the global maximum arithmetic mean rectified voltage output being avg. $V_{23} = 1.26$ V see Figure 6.10b.

Figure 6.11 shows the frequency response and the arithmetic mean rectified voltage output over the excitation frequency for the pendulum energy harvester with an offset angle of $\alpha_{offset} = 90°$ and with an excitation amplitude of $A = 24$ mm. In this configuration only the coordinate θ_{14} is oscillating and is therefore exclusively shown. As expected for a simple pendulum the angle θ_{14} and the arithmetic mean rectified voltage output show softening characteristics. With the global maximum deflection being at an excitation frequency of $\Omega = 0.575$ Hz see Figure 6.11a. The global maximum amplitude of the coordinate θ_{14} has a value of $\theta_{14} = 41.4°$ and the maximum arithmetic mean rectified voltage output has a value of avg. $V_{14} = 1.21$ V see Figure 6.11b.

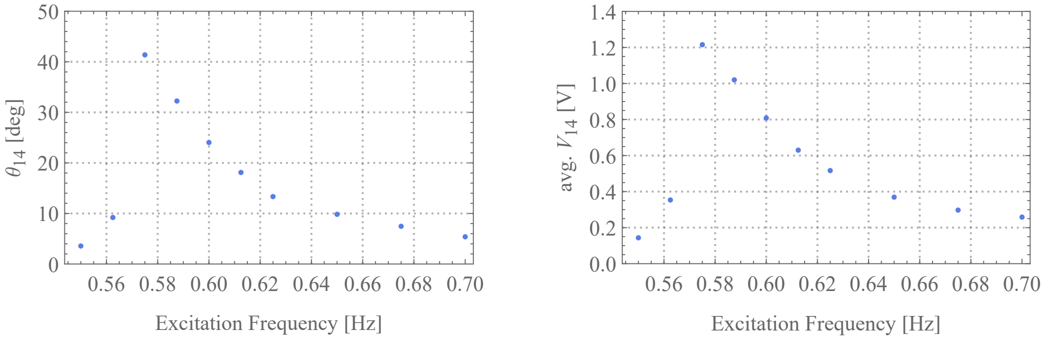

(a) Frequency response of the coordinate θ_{14}

(b) Arithmetic mean rectified voltage output avg. V_{14} over the excitation frequency Ω

Figure 6.11: Frequency response and voltage output over excitation frequency Ω for the pendulum harvester in the low power take-off mode. The parameters of the energy harvester are: $l = 0.75$ m, $m = 1.32$ kg, $\alpha_{offset} = 90°$, $A = 24$ mm, $\xi_{14} = 0.0204$, $\xi_{23} = 0.020$, $R_P = \text{NC}$, and $R_S = 10$ kΩ.

Since this work is concerned with an omnidirectional energy harvester, the offset angle is set to a value of $\alpha_{offset} = 45°$ for the following figures. Figure 6.12 shows the frequency response and the arithmetic mean rectified voltage output over the excitation frequency for the coordinate θ_{14} and the coordinate θ_{23} with an excitation amplitude of $A = 32$ mm. Firstly, it is noticeable that a significantly larger excitation amplitude is required to obtain similar deflections of θ_{14} compared to the simple pendulum. It can be seen that, apart from the displacement along the x-axis of the frequency response due to the change in length, the frequency responses are very similar in shape to those with a pendulum length of 0.5 m. The coordinate θ_{14} in

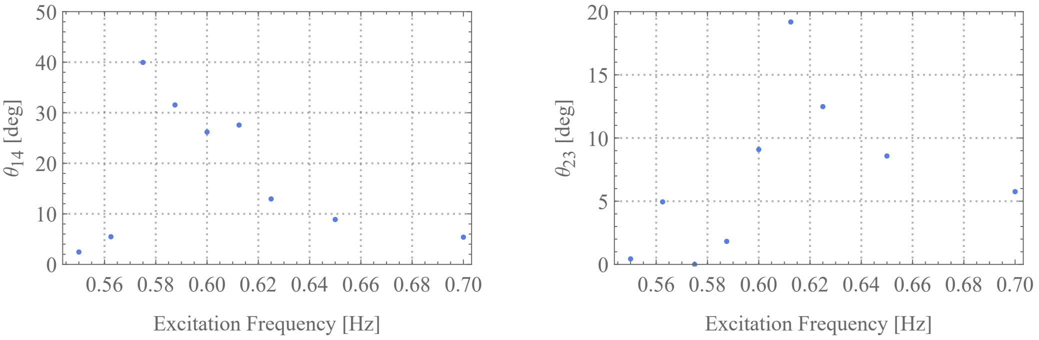

(a) Frequency response of the coordinate θ_{14}

(b) Frequency response of the coordinate θ_{23}

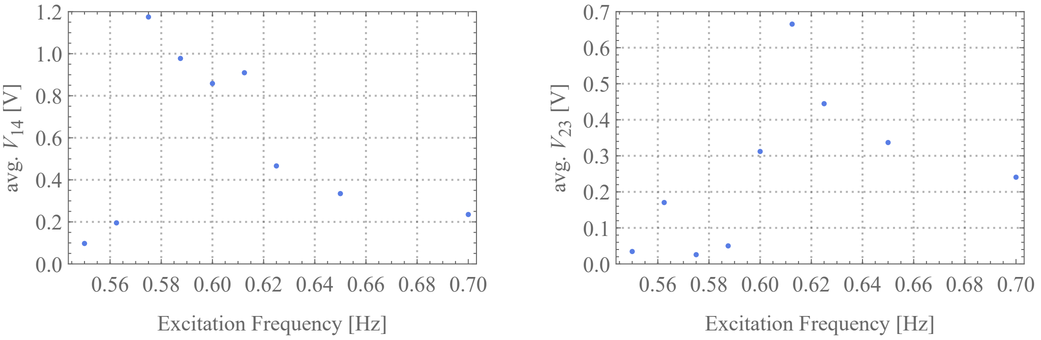

(c) Arithmetic mean rectified voltage output avg. V_{14} over the excitation frequency Ω

(d) Arithmetic mean rectified voltage output avg. V_{23} over the excitation frequency Ω

Figure 6.12: Frequency responses and voltage output over excitation frequency Ω for the pendulum energy harvester in the low power take-off mode. The parameters of the pendulum energy harvester are: $l = 0.75$ m, $m = 1.32$ kg, $\alpha_{offset} = 45°$, $A = 32$ mm, $\xi_{14} = 0.0204$, $\xi_{23} = 0.020$, $R_P = \text{NC}$, and $R_S = 10\ \text{k}\Omega$.

Figure 6.12a shows the same softening and hardening characteristics that show a favourable effect on the operational range. The global maximum deflection of $\theta_{14} = 39.9°$ is reached at an excitation frequency of $\Omega = 0.575$ Hz with the corresponding arithmetic mean rectified global maximum arithmetic mean rectified voltage output being avg. $V_{14} = 1.18$ V. The deflection of the coordinate θ_{23} in Figure 6.12b shows an initial deflection for an excitation frequency of 0.5625 Hz with a deflection of $\theta_{23} = 4.9°$ and afterwards drops toward a value close to zero. Then the frequency response shows a classical linear resonance curve with its global maximum reached at a value of the excitation frequency of 0.6125 Hz with a deflection of $\theta_{23} = 19.2°$. The arithmetic mean rectified voltage output at this position has a value of avg. $V_{23} = 0.66$ V see Figure 6.12d.

Since these measurements were conducted with a series resistor with a physically high value of 10 kΩ the ground potential is not affected by the movement of the coordinates, therefore the voltage outputs in Figures 6.12c and 6.12d confirm the measured rotational angle values.

In Figure 6.13 the values for the coordinates θ_{14} and θ_{23} and the arithmetic mean rectified voltage output avg. V_{14} and avg. V_{23} are plotted over a variation of the excitation amplitude. The excitation frequency is set to a value of $\Omega = 0.612$ Hz and for this value both coordinates have a fairly high deflection because when observing the pendulum bob from the top view it follows an almost circular trajectory. The amplitude values for the coordinate θ_{14} are shown in Figure 6.13a. For the first four measurement points the deflection rises sharply. However, when the value for the excitation amplitude of $A = 25$ mm is exceeded the slope decreases rapidly and the deflection hardly increases with an increase in the excitation amplitude. The global maximum deflection is reached at an excitation amplitude of $A = 36$ mm and has a value of $\theta_{14} = 29.7°$. The arithmetic mean rectified voltage output avg. V_{14} in Figure 6.13c follows the same trend as the deflection of the coordinate θ_{14}. With the global maximum value being avg. $V_{14} = 0.97$ V at a value of the excitation amplitude of $A = 36$ mm see Figure 6.13c. A higher excitation amplitude cannot be examined since the pendulum bob would collide with the supporting structure of the energy harvester during the transient response.

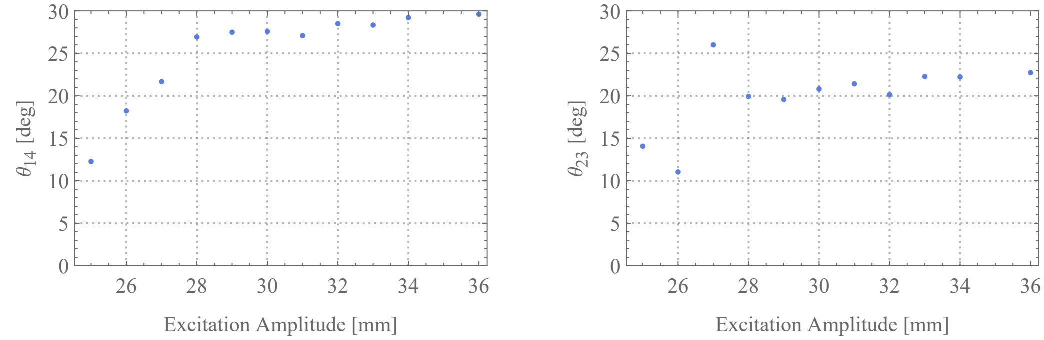

(a) θ_{14} over the excitation amplitude A

(b) θ_{23} over the excitation amplitude A

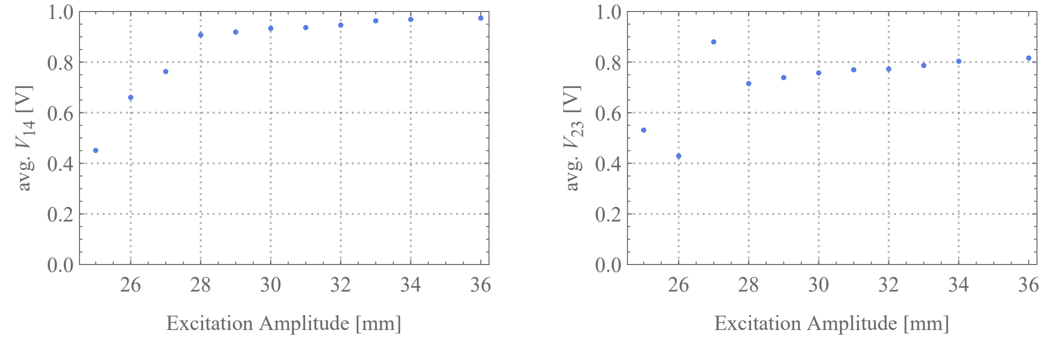

(c) Arithmetic mean rectified voltage output avg. V_{14} over the excitation amplitude A

(d) Arithmetic mean rectified voltage output avg. V_{23} over the excitation amplitude A

Figure 6.13: θ_{14}, θ_{23}, avg. V_{14}, and avg. V_{23} for a variation of the excitation amplitude A of the pendulum energy harvester in the low power take-off mode. The parameters of the energy harvester are: $l = 0.75$ m, $m = 1.32$ kg, $\alpha_{offset} = 45°$, $\Omega = 0.612$ Hz, $\xi_{14} = 0.0204$, $\xi_{23} = 0.020$, $R_P =$ NC, and $R_S = 10$ kΩ.

The coordinate θ_{23} over the excitation amplitude is shown in Figure 6.13b. Contrary to expectations, the first three measuring points do not show a constant increase of the deflection. At an excitation amplitude of $A = 25$ mm a deflection of $\theta_{23} = 14.1°$ is reached, then the amplitude slightly decreases to a value of $\theta_{23} = 11.0°$ with the next measurement point. For an excitation amplitude with a value of $A = 27$ mm the coordinate θ_{23} increases strongly to a value of $\theta_{23} = 25.9°$. After that, the deflection decreases again and, similar to the final phase of the coordinate θ_{14}, and hardly increases with increasing excitation amplitude. The global maximum deflection is not reached at the highest excitation amplitude but instead at an excitation amplitude of $A = 27$ mm with a value of $\theta_{23} = 25.9°$. The arithmetic mean rectified voltage output avg. V_{23} follows the deflection of the coordinate θ_{23} well and reaches its global maximum for an excitation amplitude of $A = 27$ mm with a value of avg. $V_{23} = 0.88$ V see Figure 6.13d.

6.2.2 Dynamics of the Omnidirectional Pendulum Energy Harvester in the High Power Take-Off Mode

The power take-off is now increased to determine the maximal power output of the pendulum energy harvester with a length of 0.75 m. This is achieved by including a parallel resistor with a physically low value of 10 Ω. A detailed description of the measurement circuit can be found in Section 3.2.3. With this the electrical power output of the energy harvester increases. The damping ratios continue to have values of $\xi_{14} = 0.0204$ and $\xi_{23} = 0.0200$.

Figure 6.14 shows the frequency response, arithmetic mean rectified voltage output over the excitation frequency, and the mean rectified power output over the excitation frequency for the different coordinates with an increased power take-off with an excitation amplitude of $A = 32$ mm and an offset angle of $\alpha_{offset} = 45°$. The coordinate θ_{14} shows a gradual increase over the excitation frequency until it reaches a value of $\Omega = 0.575$ Hz where it jumps up to the global maximum deflection of $\theta_{14} = 36.5°$. Over the next four measurement points the deflection slowly decreases until it slightly increases after a value for the excitation frequency of $\Omega = 0.6$ Hz is exceeded. At the excitation frequency $\Omega = 0.6125$ Hz a local maximum is reached with a value of $\theta_{14} = 26.6°$ afterwards the deflection jumps down to a lower deflection value. From there on the coordinate slowly converges towards zero. The arithmetic mean rectified voltage output avg. V_{14} follows the trend of the coordinate θ_{14} with two maximum voltage outputs being avg. $V_{14} = 0.96$ V and avg. $V_{14} = 0.86$ V. The two maximum power outputs from the coordinates θ_{14} are at excitation frequencies mentioned above and have values of $P_{14} = 0.33$ W and $P_{14} = 0.25$ W.

Figure 6.14b shows the frequency response of the coordinate θ_{23}. The first four measurement points show a steady increase with the local maximum reached at an excitation frequency of $\Omega = 0.57$ Hz with a deflection of $\theta_{23} = 11.5°$. This is followed by a sudden jump down close

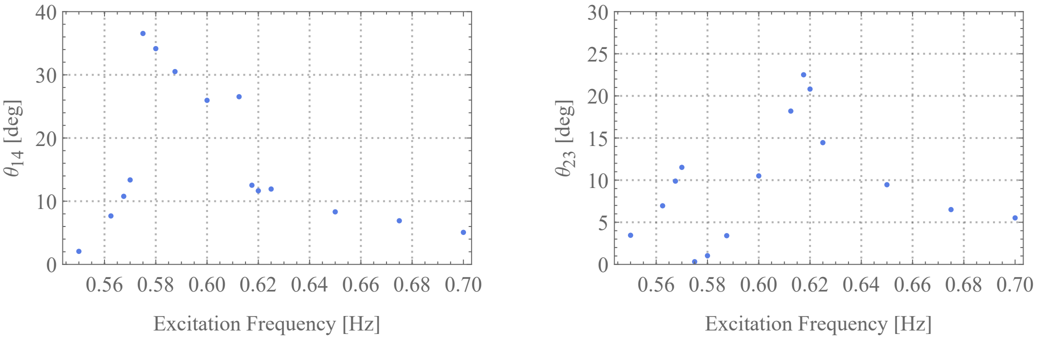

(a) Frequency response of the coordinate θ_{14}

(b) Frequency response of the coordinate θ_{23}

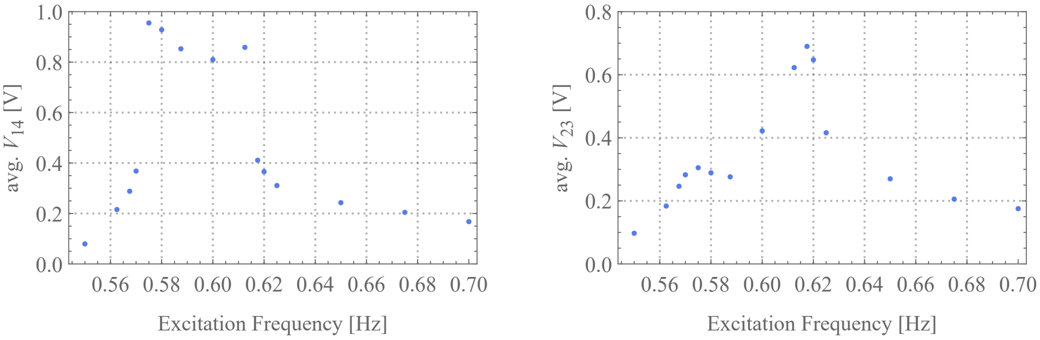

(c) Arithmetic mean rectified voltage output avg. V_{14} over the excitation frequency Ω

(d) Arithmetic mean rectified voltage output avg. V_{23} over the excitation frequency Ω

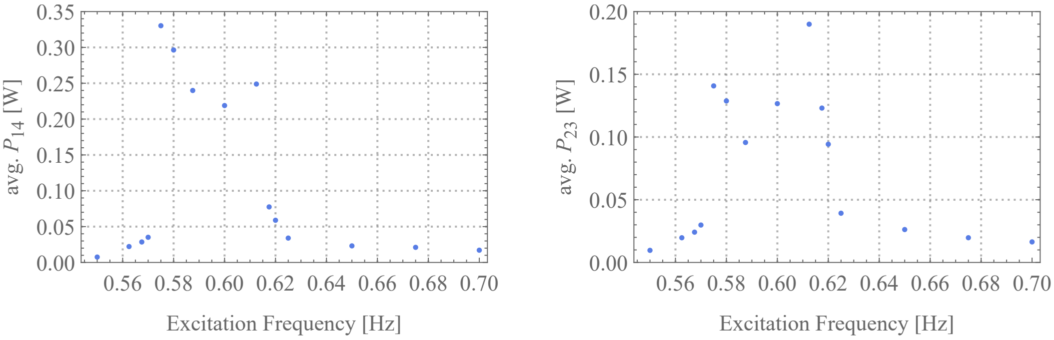

(e) Arithmetic mean rectified power output P_{14} over the excitation frequency Ω

(f) Arithmetic mean rectified power output P_{23} over the excitation frequency Ω

Figure 6.14: Frequency responses, arithmetic mean rectified voltage output over excitation frequency Ω, and arithmetic mean rectified power output over excitation frequency Ω for the pendulum energy harvester in the high power take-off mode. The parameters of the pendulum energy harvester are: $l = 0.75$ m, $m = 1.32$ kg, $\alpha_{offset} = 45°$, $A = 32$ mm, $\xi_{14} = 0.0204$, $\xi_{23} = 0.0200$, $R_P = 10\ \Omega$, and $R_S = 0\ \Omega$.

to zero. From there on the deflection gradual increases with an increasing excitation frequency until it reaches a global maximum at an excitation frequency of $\Omega = 0.6175$ Hz with a value of $\theta_{23} = 22.5°$. When the global maximum is passed the amplitude slowly decreases.

Comparing Figures 6.14b and 6.14d, it can be seen that the voltage output mostly matches the amplitude of θ_{23}, however, in a region for the excitation frequency of $\Omega = 0.575 - 0.5875$ Hz the arithmetic mean rectified voltage output shows values that are directly influenced by the high levels of deflections of the coordinate θ_{14} and therefore need to be observed with caution. In fact the voltage output at this range is too high. But at the global maximum deflection of the coordinate θ_{23} the deflection is fairly small and therefore the voltage and current output at this position is correct and an arithmetic mean rectified voltage output avg. $V_{23} = 0.69$ V and a global maximum power output of $P_{23} = 0.19$ W are observed.

In Figure 6.15 the excitation amplitude is increased to a value of $A = 38$ mm. This value corresponds to the maximum achievable excitation amplitude that is give by the physical restrictions of the cage in which the pendulum oscillates. The coordinate θ_{14} is plotted over the excitation amplitude in Figure 6.15a. Here, the classical dynamics of the harvester with an offset angle of $\alpha_{offset} = 45°$ can be observed with the softening properties at the beginning of the operational range and the slight hardening effect at the end. The local maxima are observed at values for the excitation frequency $\Omega = 0.5675$ Hz with a deflection of $\theta_{14} = 45.6°$ and $\Omega = 0.62$ Hz with a amplitude of $\theta_{14} = 30.76°$. The arithmetic mean rectified voltage output V_{14} shows a similar development as the coordinate θ_{14}. The maximum arithmetic mean rectified voltage outputs have values of avg. $V_{14} = 0.99$ V and avg. $V_{14} = 0.94$ V see Figure 6.15c. Therefore, the global maximum arithmetic mean rectified power output from the coordinate θ_{14} can be given as $P_{14} = 0.47$ W at an excitation frequency of 0.5675 Hz and the local maximum power output has a value of $P_{14} = 0.35$ W at an excitation frequency of $\Omega = 0.62$ Hz see Figure 6.15d.

The deflections of the coordinate θ_{23} over the excitation frequency are shown in Figure 6.15b. The maxima are observed at excitation frequencies of $\Omega = 0.5625$ Hz, $\Omega = 0.5875$ Hz, and $\Omega = 0.62$ Hz with the maximum deflection values being $\theta_{23} = 13.3°$, $\theta_{23} = 16.61°$, and $\theta_{23} = 28.6°$. From Figure 6.15d the arithmetic mean rectified voltage output of these points can be observed with the values being avg. $V_{23} = 0.28$ V, avg. $V_{23} = 0.596$ V, and avg. $V_{23} = 0.84$ V. The maximum power output on these three excitation frequencies has a value of $P_{23} = 0.028$ W, $P_{23} = 0.15$ W, and $P_{23} = 0.36$ W see Figure 6.15f.

Figure 6.16 shows the deflections of the coordinates θ_{14} and θ_{23}, arithmetic mean rectified voltage output avg. V_{14} and avg. V_{23}, and arithmetic mean rectified power output P_{14} and P_{23} over the excitation amplitude. The pendulum harvester is excited with an excitation frequency of $\Omega = 0.612$ Hz. For this excitation frequency the trajectory of the pendulum bob (observed from the top view) follows an almost circular pattern. This ensures that both shafts show high deflection values. In Figure 6.16a the coordinate θ_{14} is shown over the excitation amplitude. For the first five measurement points the deflection gradually decreases with a decrease in the excitation amplitude. For a value of $A = 34$ mm the deflection shows two values $\theta_{14} = 17.8°$ and $\theta_{14} = 27.4°$ that have a great distance towards each other. This is confirmed with several

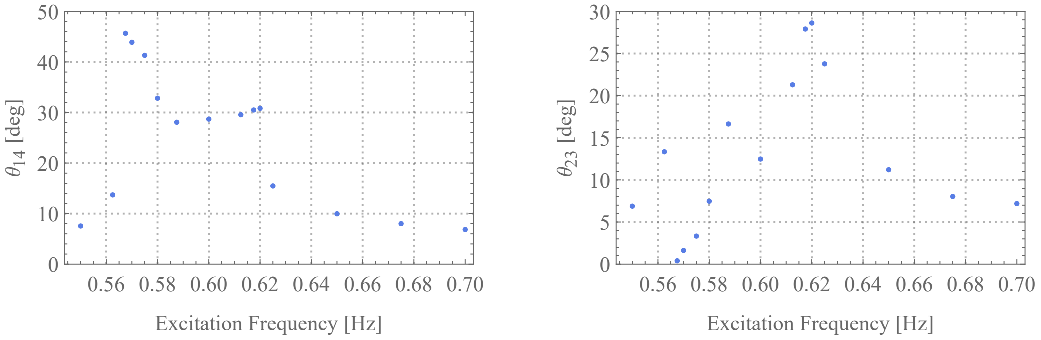

(a) Frequency response of the coordinate θ_{14}

(b) Frequency response of the coordinate θ_{23}

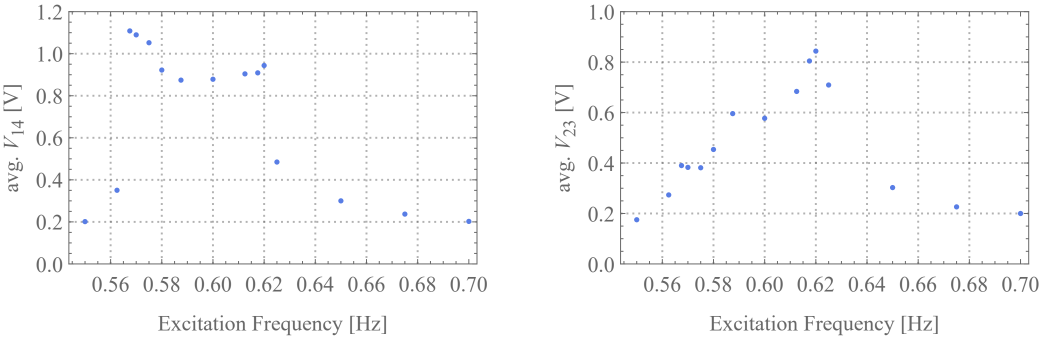

(c) Arithmetic mean rectified voltage output avg. V_{14} over the excitation frequency Ω

(d) Arithmetic mean rectified voltage output avg. V_{23} over the excitation frequency Ω

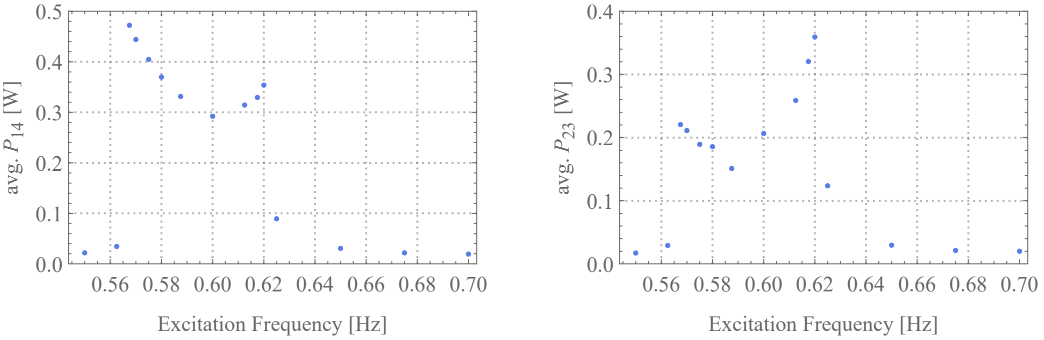

(e) Arithmetic mean rectified power output P_{14} over the excitation frequency Ω

(f) Arithmetic mean rectified power output P_{23} over the excitation frequency Ω

Figure 6.15: Frequency responses, arithmetic mean rectified voltage output over excitation frequency Ω, and arithmetic mean rectified power output over excitation frequency Ω for the pendulum energy harvester in the high power take-off mode. The parameters of the pendulum energy harvester are: $l = 0.75$ m, $m = 1.32$ kg, $\alpha_{offset} = 45°$, $A = 38$ mm, $\xi_{14} = 0.0204$, $\xi_{23} = 0.0200$, $R_P = 10\ \Omega$, and $R_S = 0\ \Omega$.

measurements and the steady-state solution settles to either of these two values. This again shows the nonlinearity that occurs with a variation of the excitation amplitude. From then on, the deflection of the coordinate θ_{14} increases steadily, but the slope is no longer as steep as before the jump. The global maximum deflection is reached with an excitation amplitude of $A = 40$ mm with a value of $\theta_{14} = 29.9°$.

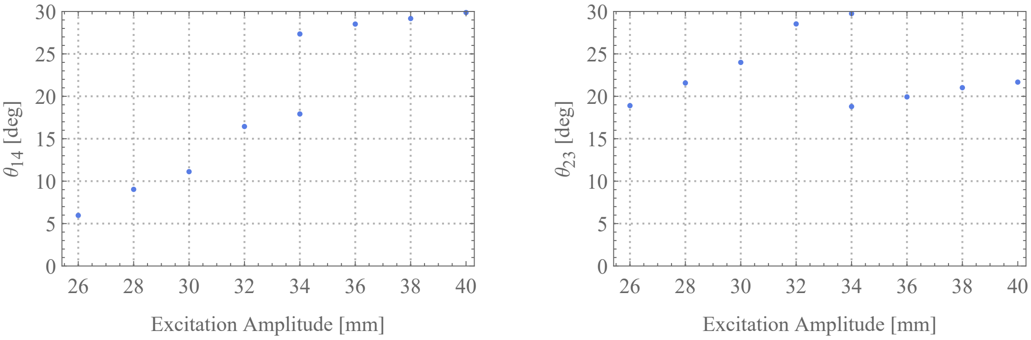

(a) θ_{14} over the excitation amplitude A

(b) θ_{23} over the excitation amplitude A

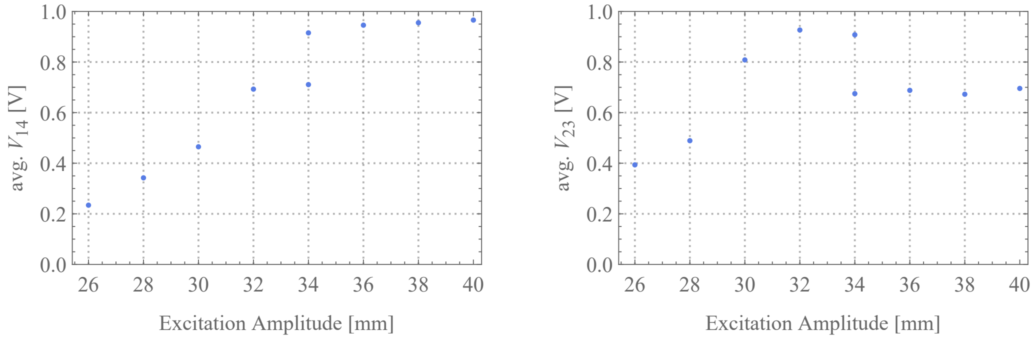

(c) Arithmetic mean rectified voltage output avg. V_{14} over the excitation amplitude A

(d) Arithmetic mean rectified voltage output avg. V_{23} over the excitation amplitude A

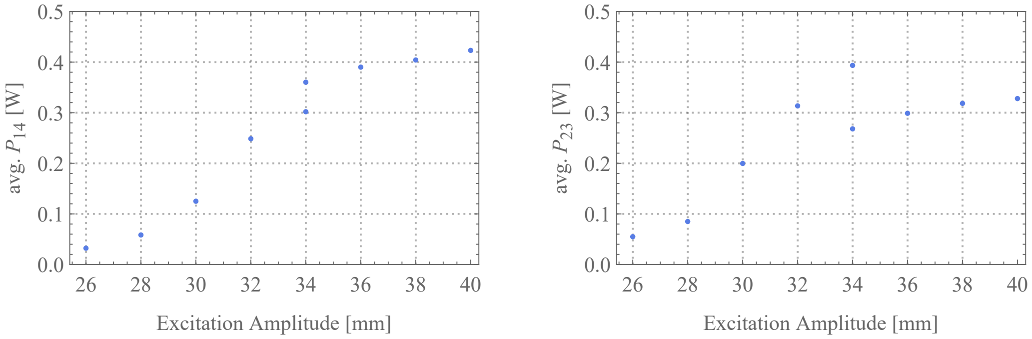

(e) Arithmetic mean rectified power output P_{14} over the excitation amplitude A

(f) Arithmetic mean rectified power output P_{23} over the excitation amplitude A

Figure 6.16: Deflection of the coordinates θ_{14} and θ_{23}, arithmetic mean rectified voltage output avg. V_{14} and avg. V_{23}, and arithmetic mean rectified power output P_{14} and P_{23} over the excitation amplitude A of the pendulum energy harvester in the high power take-off mode. The parameters of the pendulum energy harvester are: $l = 0.75$ m, $m = 1.32$ kg, $\alpha_{offset} = 45°$, $\Omega = 0.612$ Hz, $\xi_{14} = 0.0204$, $\xi_{23} = 0.0200$, $R_P = 10\ \Omega$, and $R_S = 0\ \Omega$.

The arithmetic mean rectified voltage output avg. V_{14} in Figure 6.16c shows similar characteristics as the coordinate θ_{14}. Here too a jump up is observed at an excitation amplitude of $A = 34$ mm, the two corresponding voltages have a value of avg. $V_{14} = 0.71$ V and avg. $V_{14} = 0.92$ V. The global maximum arithmetic mean rectified voltage output of avg. $V_{14} = 0.96$ V is reached at an excitation amplitude of $A = 40$ mm.

In Figure 6.16e the power output P_{14} of the coordinate θ_{14} is shown over the excitation amplitude. The graph follows the coordinate θ_{14} well and the jump up at an excitation amplitude of $A = 34$ mm is observed as well with the two values being $P_{14} = 0.30$ W and $P_{14} = 0.36$ W. The global maximum power output is reached at an excitation amplitude of $A = 40$ mm with a value of $P_{14} = 0.42$ W.

The coordinate θ_{23} over the excitation amplitude is shown in Figure 6.16b. Over the first 5 measuring points the amplitude gradually increases. At an excitation amplitude of $A = 34$ mm, two points whose values are $\theta_{23} = 18.8^\circ$ and $\theta_{23} = 29.7^\circ$ are shown. The deflection of $\theta_{23} = 29.7^\circ$ corresponds to the global maximum amplitude of the displayed area. After the excitation amplitude of $A = 34$ mm is exceeded, the deflection continues to increase, but the slope is not as steep as before and the overall deflection is lower than before the jump.

Figure 6.16d shows the arithmetic mean rectified voltage output avg. V_{23} of the coordinate θ_{23} over the excitation amplitude. The voltage output shows similar characteristics to the deflection of the coordinate θ_{23}. The arithmetic mean rectified voltage output is rising and then the two different arithmetic mean rectified voltage output values can be seen for an excitation amplitude of $A = 34$ mm. Afterwards the arithmetic mean rectified voltage output stays constant for a further increase in excitation amplitude.

In Figure 6.16f the power output P_{23} of the coordinate θ_{23} is shown over the excitation amplitude. The arithmetic mean rectified power output shows similar characteristics as the levels of deflection of the coordinate θ_{23}. The first five points show a rise in arithmetic mean rectified power output. At an excitation amplitude of 34 mm the power output shows two different levels. With a further increase in excitation amplitude the arithmetic mean rectified power output continues to increase.

6.3 Comparison of Different Pendulum Lengths

In this section the frequency responses for different pendulum lengths are compared to see the different dynamics of the energy harvester in a general overview figure. Figure 6.17 shows the frequency responses for the coordinates θ_{14} and θ_{23} for different pendulum lengths. To allow a clear differentiation between the different pendulum lengths the measurement points of the different frequency responses were connected. With a variation of the pendulum length the damping ratios vary for a pendulum length of $l = 0.75$ m damping ratios of $\xi_{14} = 0.0204$ and $\xi_{23} = 0.02$ are observed, for a pendulum length of $l = 0.6$ m damping ratios of $\xi_{14} = 0.0246$ and $\xi_{23} = 0.0201$, for a pendulum length of $l = 0.55$ m damping ratios of $\xi_{14} = 0.0235$ and $\xi_{23} = 0.0247$, for a pendulum length of $l = 0.5$ m damping ratios of $\xi_{14} = 0.037$ and $\xi_{23} = 0.037$ are observed, for a pendulum length of $l = 0.35$ m damping ratios of $\xi_{14} = 0.0373$ and $\xi_{23} = 0.0339$, and for a pendulum length of $l = 0.2$ m damping ratios of $\xi_{14} = 0.065$ and $\xi_{23} = 0.0699$ are observed. The energy harvester is excited with an excitation amplitude of $A = 32$ mm for all

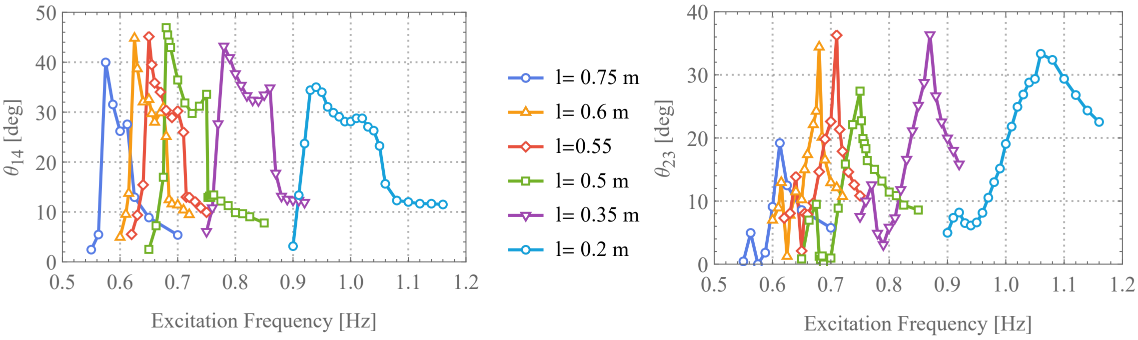

(a) Frequency responses of the coordinate θ_{14}

(b) Frequency responsse of the coordinate θ_{23}

Figure 6.17: Frequency responses over excitation frequency Ω for the pendulum energy harvester for different pendulum lengths in the low power take-off mode. The damping ratios variable depending on the length $l = 0.75$ m $\rightarrow \xi_{14} = 0.0204$ and $\xi_{23} = 0.02$, $l = 0.6$ m $\rightarrow \xi_{14} = 0.0246$ and $\xi_{23} = 0.0201$, $l = 0.55$ m $\rightarrow \xi_{14} = 0.0235$ and $\xi_{23} = 0.0247$, $l = 0.5$ m $\rightarrow \xi_{14} = 0.0325$ and $\xi_{23} = 0.0323$, $l = 0.35$ m $\rightarrow \xi_{14} = 0.0373$ and $\xi_{23} = 0.0339$, and $l = 0.2$ m $\rightarrow \xi_{14} = 0.065$ and $\xi_{23} = 0.0699$. The parameters of the energy harvester are: $m = 1.32$ kg, $\alpha_{offset} = 45°$, $A = 32$ mm, $R_P =$ NC, and $R_S = 10\ k\Omega$.

lengths of the pendulum rod. The frequency responses for the lengths $l = 0.5$ m and $l = 0.75$ m are repetitions of Figures 6.4 and 6.12.

Figure 6.17a shows the frequency responses for the coordinate θ_{14}. With a variation of the pendulum length the natural undamped frequency of the energy harvester changes, therefore as expected the different responses have their maximum deflection for different excitation amplitudes. However, it is interesting to note that the maxima do not increase constantly with a decrease in pendulum length. From a pendulum length 0.75 m to 0.5 m the maximum deflection of the coordinate θ_{14} increases by 7.0°, with a further decrease of the pendulum length from 0.5 m to 0.2 m, however, the maximum deflection drops by 11.9°. The maximum deflections are here not determined with sweep measurements and can therefore show slightly lower values. The measurements with sweeps are observed in Section 6.4.

The situation is different for the coordinate θ_{23} in Figure 6.17b. Here the deflection shows different maximum deflections over the shortening of the pendulum length. For a pendulum length of 0.75 m the maximum deflection has a value of 19.2°, for a pendulum length of 0.6 m the maximum deflection is 34.4°, for a pendulum length of 0.55 m the maximum deflection is 36.28°, for a pendulum length of 0.5 m the maximum deflection is 27.4°, for a pendulum length of 0.35 m the maximum deflection is 36.34°, and for a pendulum length of 0.2 m the deflection has a value of 33.3°.

6.4 Broadening of the Operational Range of the Omnidirectional Pendulum Energy Harvester

In this section the influence of excitation frequency up- and down-sweeps on the operational range of the energy harvester is examined. Figure 6.18 shows frequency responses for the coordinates θ_{14} and θ_{23} with a length of the pendulum of 0.55 m and an excitation amplitude of $A = 32$ mm. As mentioned in Section 3.3.1 the blue points were obtained by giving the system a constant excitation frequency input signal and observing the value of the deflection for the steady-state, henceforth as previously mentioned this is referred to as linear frequency response. The orange and red points were measured with a sweep input signal to the shaker table. For the orange points a down-sweep with the excitation frequencies of $\Omega = 0.66$ Hz to 0.63 Hz over a time of 200 s is used and for the red points a up-sweep starting with an excitation frequency of $\Omega = 0.69$ Hz to 0.82 Hz over a time of 200 s is used. The output signal is divided in six (down-sweep) and twenty (up-sweep) partitions where the arithmetic mean rectified deflection is calculated for each partition. The starting point of each sweep is marked with a black circle in the figures.

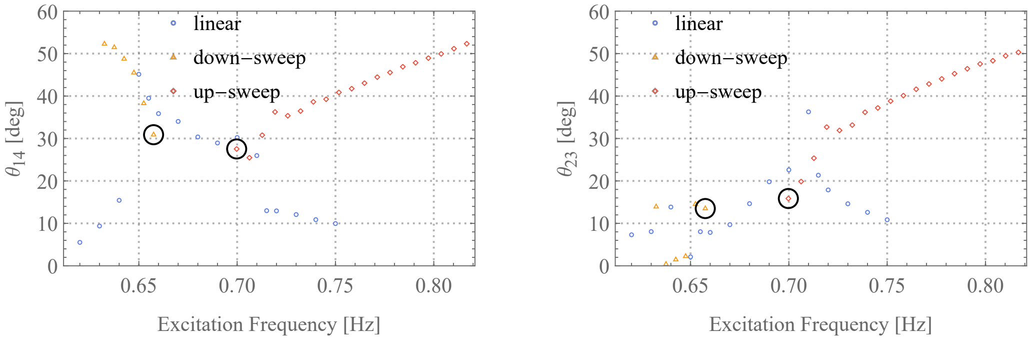

(a) Frequency response of the coordinate θ_{14}

(b) Frequency response of the coordinate θ_{23}

Figure 6.18: Frequency responses for the pendulum energy harvester in the low power take-off mode with up- and down-sweeps. The parameters of the pendulum energy harvester are: $l = 0.55$ m, $m = 1.32$ kg, $\alpha_{offset} = 45°$, $A = 32$ mm, $\xi_{14} = 0.0325$, $\xi_{23} = 0.0323$, $R_P = \text{NC}$, and $R_S = 10\ \text{k}\Omega$.

In Figure 6.18a the frequency response for the coordinate θ_{14} is shown. The linear part of the frequency response shows the common dynamics with the jump up to a local maximum followed by a local minimum, another local maximum, and a jump down back to a lower deflection value. The down-sweep (orange triangles) shows a lower value than the linear frequency response for the first circled point, this is because of the fact that the system is still in the transient response at that point. With a further decrease of the excitation frequency the deflection of the coordinate θ_{14} gradually decreases. Until the pendulum bob hits the cage at a value of the excitation frequency of $\Omega = 0.6375$ Hz, the value for the deflection should be larger but it is physically restricted. This physical restriction for an angle of $\theta_{14} = \theta_{23} = 52.3°$

is present at all pendulum lengths higher than $l = 0.4$ m. The up-sweep (red diamonds) shows lower deflections for the first two shown points, which is attributed to the transient dynamics of the system that are observed in this area. From there on the system shows a gradually increasing deflection until the physically achievable maximum is reached at an excitation frequency of $\Omega = 0.81675$ Hz. The upper and lower nonlinear jump regions broaden the operational range of the coordinate θ_{14} of the energy harvester compared to the linear operational range, see definition in Equations (3.7) and (3.6). The lower nonlinear jump region broadens the operational range by 29.17 % (0.0175 Hz) according to Equation (3.6). The upper nonlinear jump region broadens the range where the energy harvester shows high deflection values by 177.92 % (0.10675 Hz), according to Equation (3.7). The broadening of the operational range however is physically restricted by the pendulum cage and it can therefore only be assumed that a larger broadening is theoretically possible.

Figure 6.18b shows the frequency response for the coordinate θ_{23}. The down-sweep (orange triangles) has values that are close to zero and is therefore not relevant, the system is basically operating as a simple pendulum energy harvester in that region. The up-sweep (red diamonds) shows lower deflections than the linear frequency response for the first two measurements points which are attributed to the transient dynamics that are observed at the beginning of the up-sweep. From there on the deflection of the coordinate θ_{23} gradually increases. With an excitation frequency higher than $\Omega = 0.72$ Hz the trajectory of the spherical pendulums is similar to that of a conical pendulum. This shows that the operational range of the energy harvester can be drastically increased when starting the up-sweep in a region of the excitation frequency $\Omega = 0.65$ Hz to 0.71 Hz. The upper nonlinear jump region broadens the operational range of the harvester coordinate θ_{23} by 177.97 % (0.10675 Hz), according to Equation (3.7). Unfortunately, as mentioned before, pendulum lengths larger than 0.4 m are restricted by the cage and can therefore not show their full broadening potential. Therefore the pendulum length is reduced to a length of 0.35 m in the following experiments.

Figure 6.19 shows the frequency responses for the coordinates θ_{14} and θ_{23} with a pendulum length of $l = 0.35$ m with the same excitation amplitude as in Figure 6.18. This pendulum length is not physically restricted by the boundaries of the supporting cage since the pendulum bob operates above the horizontal reinforcement square tube. The frequency responses include up- and down-sweeps (red diamonds and orange triangles) to examine the operational range of the system and the frequency response that is measured with different steady-state measurement points is shown in blue colour. The starting points of the up- and down-sweeps at an excitation frequency of 0.84325 Hz and 0.7875 Hz are circled in black.

The first measurement point of the down-sweep for the coordinate θ_{14} in Figure 6.19a has a lower value than the linear frequency response. With a further decrease of the excitation frequency the deflection of the coordinate θ_{14} increases with a maximum deflection of 51.25°

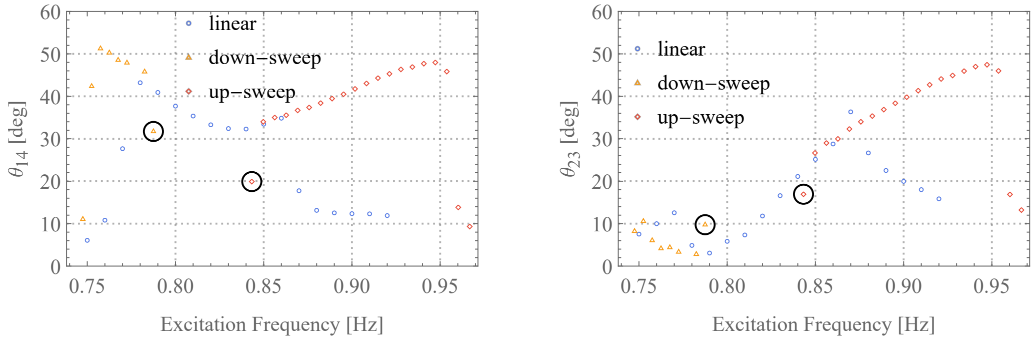

(a) Frequency response of the coordinate θ_{14} (b) Frequency response of the coordinate θ_{23}

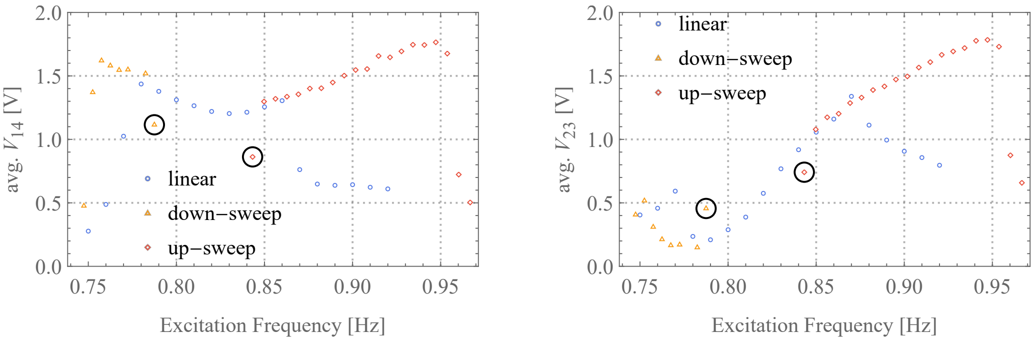

(c) Frequency response of the variable avg. V_{14} (d) Frequency response of the variable avg. V_{23}

Figure 6.19: Frequency responses and voltage output in the frequency domain for the pendulum energy harvester in the low power take-off mode with up- and down-sweeps. The parameters of the pendulum energy harvester are: $l = 0.35$ m, $m = 1.32$ kg, $\alpha_{offset} = 45°$, $A = 32$ mm, $\xi_{14} = 0.0373$, $\xi_{23} = 0.0339$, $R_P =$ NC, and $R_S = 10$ kΩ.

reached at an excitation frequency of 0.7575 Hz. From there on the deflection of the coordinate θ_{14} jumps down to a value close to the linear frequency response (blue circles) with an intermediate step. This intermediate step can be explained with the post-processing of the measurement data see Section 3.3.1. To obtain the down-sweep a value for the range over which the results are arithmetic averaged is picked, in this case a delta of 0.005 Hz is selected. This range is selected with care as a big value would decrease the accuracy and the exact value of the jump is harder to determine and when the frequency range delta gets too small different values cannot be arithmetically averaged anymore, which increases the error. Therefore, a reasonable middle course has to be found. The lower nonlinear jump region broadens the operational range of the coordinate θ_{14} by 0.0225 Hz which is equivalent to a value of 28.125 % according to Equation (3.6). The down-sweep of the coordinate θ_{23} in Figure 6.19b shows values that are close to zero and do not show any clear trend. This means that the omnidirectional pendulum energy harvester can be considered as a simple pendulum energy harvester for the lower nonlinear jumping region.

The starting point for the up-sweep is at an excitation frequency of 0.84325 Hz. For the coordinate θ_{14} in Figure 6.19a the deflection is lower than the linear frequency response deflection (blue circles) this is attributed to the transient dynamics in the arithmetically averaged bandwidth element. From there on the spherical pendulum shows dynamics that are similar to a conical pendulum with an increase in the excitation frequency until a maximum deflection for the coordinate θ_{14} of 47.97° and for the coordinate θ_{23} of 47.44° at an excitation frequency of 0.94725 Hz is reached. The following measurement points show a slightly lower value than the maximum deflection and the next measured value shows a jump down to values of the coordinates θ_{14} of 13.84° and $\theta_{23} = 16.88°$. With this jump down the circular trajectory of the pendulum bob that is observed from above changes to a linear motion that follows the excitation direction.

In Figure 6.19c the voltage output in the frequency domain with up- and down-sweeps is shown. The figure shows the arithmetic mean rectified voltage output avg. V_{14} the linear frequency response follows the one of the coordinate θ_{14} well. It shows a maximum voltage output of 1.43 V for a value of the excitation frequency of 0.78 Hz. With a further increase in the excitation frequency the arithmetic mean rectified voltage output decreases and reaches a local minimum of 1.20 V for a value of the excitation frequency of 0.83 Hz. The arithmetic mean rectified voltage output continues to increase afterwards with a further increase in the excitation frequency and reaches a local maximum of 1.32 V for a value of the excitation frequency of 0.86 Hz. With a further increase in the excitation frequency the linear frequency response shows a down jump to a value of the arithmetic mean rectified power output of 0.76 V. The upper nonlinear jump region in Figure 6.19c shows similar dynamics to the one in Figure 6.19a. The starting point has a lower voltage output than the linear response which is attributed to the transient dynamics that are prevailing in this area. With a further decrease of the excitation frequency the arithmetic mean rectified voltage output continues to increase and reaches a maximum of avg. $V_{14} = 1.61$ V for a value of the excitation frequency of 0.757 Hz. The arithmetic mean rectified voltage output continues to decrease with a further increase in the excitation frequency. The upper nonlinear jump region of the voltage output shows similar behaviour to the upper nonlinear jump region of the coordinate θ_{14} as well. Because of the transient dynamics in the area of the bandwidth element the starting point shows a lower arithmetic mean rectified voltage output than the linear frequency response. With a further increase in the excitation frequency the arithmetic mean rectified voltage output increases and reaches its maximum arithmetic mean rectified voltage output of 1.76 V at a value of the excitation frequency of 0.948 Hz. The arithmetic mean rectified voltage output jumps down to the arithmetic mean rectified voltage output value of 0.72 V with a further increase in excitation frequency.

The frequency response for the variable avg. V_{23} is shown in Figure 6.19d. The linear frequency response (blue circles) follows the linear frequency response of the coordinate θ_{23} well. The down-sweep shows similar characteristics. Because of the transient dynamics the first measurement point of the up-sweep has a lower value for the arithmetic mean rectified voltage output than the linear frequency response. With a further increase in the excitation frequency the arithmetic mean rectified voltage output increases and reaches its maximum of 1.78 V at a value of the excitation frequency of 0.948 Hz. The arithmetic mean rectified voltage output jumps down to a value of 0.88 V with a further increase in the excitation frequency.

The hardening and softening characteristics that can be seen in the frequency responses broaden the operational range of the omnidirectional pendulum energy harvester. The lower nonlinear jump region for the coordinate θ_{14} broadens the operating region, where the omnidirectional pendulum energy harvester shows high levels of deflections, by 28.125 % (0.0225 Hz) compared to the linear frequency response operational range see Equation (3.6). The upper nonlinear jump region of the coordinate θ_{14} broadens the operational range of the omnidirectional pendulum energy harvester by 109.0625 % (0.08725 Hz) compared to the linear frequency response operational range see Equation (3.7). Therefore, the coordinate θ_{14} is overall broadened by 137.1875 %. The broadening effect with the upper nonlinear jump region of the coordinate θ_{23} is for this work considered as the increase of the operational range after the global maximum of the linear frequency response is passed, therefore, the operational range is broadened by 109.0625 % (0.08725 Hz), according to Equation (3.7).

Figure 6.20 shows frequency responses for the coordinates θ_{14} and θ_{23} with the inclusion of an up-sweep (red diamonds) and down-sweep (orange triangles). For these two figures the power take-off was increased with the known procedure of changing the resistor values. The starting point for the down-sweep is at an excitation frequency of 0.7985 Hz. For the coordinate θ_{14} in Figure 6.20a the starting point shows a lower value than the value of the linear frequency response (blue circles), this is because the transient dynamics that are observed in this area. The following down-sweep measurement points have a slightly higher value than the linear frequency response (blue circles). For the coordinate θ_{23} the down-sweep shows a higher value than the linear frequency response for the first measurement point which is attributed to the

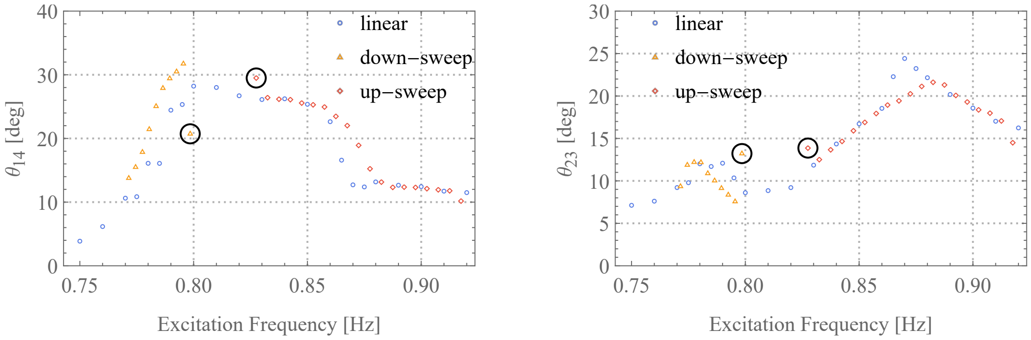

(a) Frequency response of the coordinate θ_{14}

(b) Frequency response of the coordinate θ_{23}

Figure 6.20: Frequency responses for the pendulum energy harvester in the high power take-off mode with up- and down-sweeps. The parameters of the pendulum energy harvester are: $l = 0.35$ m, $m = 1.32$ kg, $\alpha_{offset} = 45°$, $A = 32$ mm, $\xi_{14} = 0.0373$, $\xi_{23} = 0.0339$, $R_P = 10\ \Omega$, and $R_S = 0\ \Omega$.

transient dynamics of the pendulum energy harvester. The following measurement points show a lower initial deflection that gradually increases with a decrease of the excitation frequency.

The starting point of the up-sweep at an excitation frequency of 0.8225 Hz shows a higher deflection of the coordinate θ_{14} than the linear frequency response (blue circles) which is attributed to the transient dynamics that are predominant for this value of the excitation frequency. The following measurement points of the up-sweep show a good alignment with the steady-state frequency response. However, with the up-sweep a slight increase of the operational range is possible. The up-sweep of the coordinate θ_{23} in Figure 6.20b shows measurement points that are almost identical with two exceptions. The first one is the starting point which shows a higher deflection than the linear response because of the transient dynamics in the starting region of the sweep. Secondly, the local maximum of the linear frequency response (blue circles) cannot be seen with the up-sweep (red diamonds) which indicates that the frequency sweep changes the frequency too swiftly and the linear frequency response is simply not reached. Since this is a local phenomenon it hardly affects the overall results.

Since the frequency responses in Figure 6.20 now shows clear hardening or softening characteristics and in general for low deflections the excitation amplitude is increased to see whether these characteristics can be seen with a higher power take-off as well.

Figure 6.21 shows the frequency responses for the omnidirectional pendulum energy harvester with a high power take-off that is excited with an excitation amplitude of $A = 48$ mm. The blue circles indicate the linear frequency response, the orange triangles are measured with a down-sweep where the starting point is at an excitation frequency of $\Omega = 0.808$ Hz, and the red diamonds are attributed to the up-sweep with the starting point being at an excitation frequency of $\Omega = 0.8235$ Hz.

In Figure 6.21a the frequency response with sweeps for the coordinate θ_{14} is shown. The linear frequency response shows the well-known pattern that is described in greater detail in the figures. It starts with a low deflection of the coordinate θ_{14} that then jumps up to a maximum deflection with an increase in the excitation frequency. This is followed by a bowl-shaped trajectory that eventually jumps down back to a value of the deflection close to zero. The down-sweep which starts at an excitation frequency of $\Omega = 0.808$ Hz shows a lower deflection value for the first two shown measurement points, which is attributed to the transient dynamics of the system. From there on the deflection follows the linear frequency response well and increases the operational range slightly until the excitation frequency of $\Omega = 0.756$ Hz is exceeded. There the deflection decreases steeply and reaches a value close to 20° at the end. During the down-sweep the coordinate θ_{14} performs high deflections, however, the dynamics of the coordinate θ_{23} in Figure 6.21b show a deflection that is lower than 10°. Therefore, it is safe to assume that the spherical pendulum energy harvester can be considered as a simple pendulum energy harvester in the area of the down sweep where the coordinate θ_{14} has high levels of deflections.

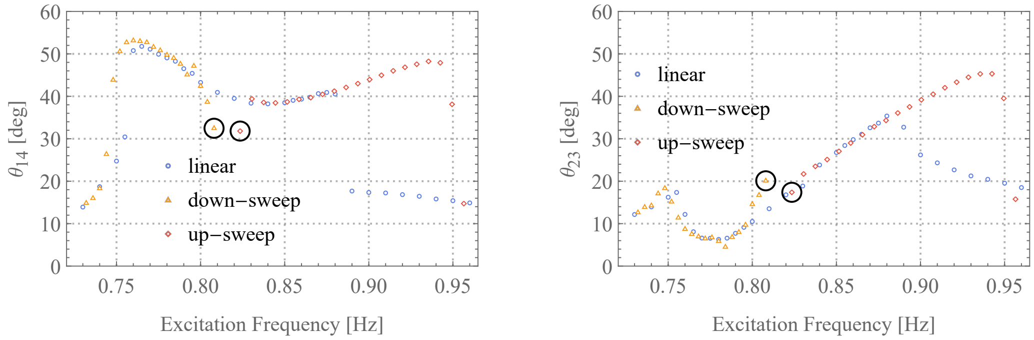

(a) Frequency response of the coordinate θ_{14}

(b) Frequency response of the coordinate θ_{23}

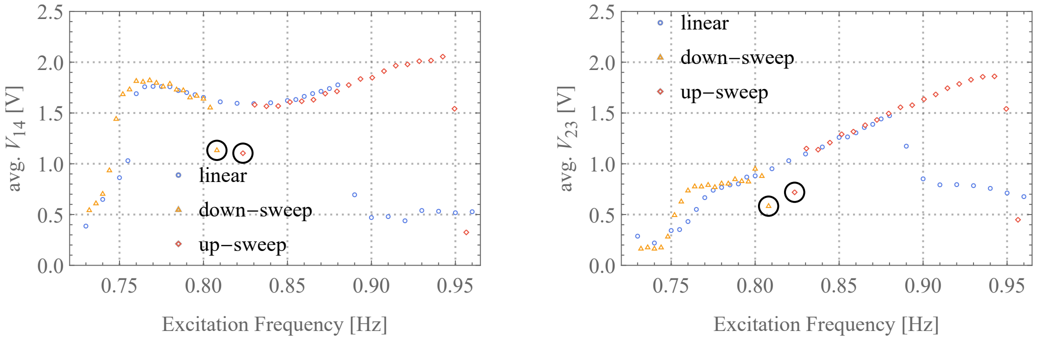

(c) Frequency response of the variable avg. V_{14}

(d) Frequency response of the variable avg. V_{23}

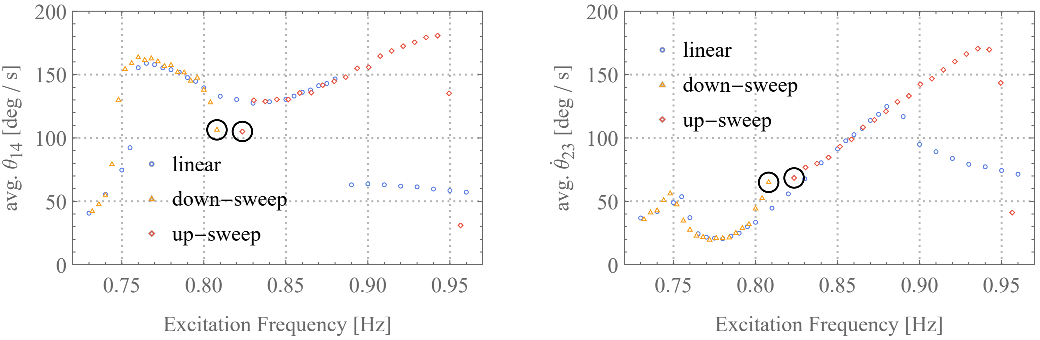

(e) Frequency response of $\dot{\theta}_{14}$

(f) Frequency response of $\dot{\theta}_{23}$

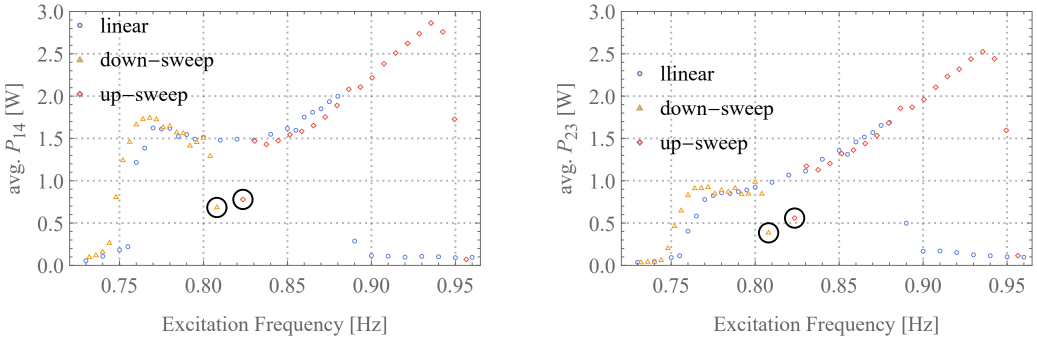

(g) Frequency response of the variable avg. P_{14}

(h) Frequency response of the variable avg. P_{23}

Figure 6.21: Frequency responses and voltage output, velocity, and power output in the frequency domain for the pendulum energy harvester in the high power take-off mode with up- and down-sweeps. The parameters of the pendulum energy harvester are: $l = 0.35$ m, $m = 1.32$ kg, $\alpha_{offset} = 45°$, $A = 48$ mm, $\xi_{14} = 0.0373$, $\xi_{23} = 0.0339$, $R_P = 10\ \Omega$, and $R_S = 0\ \Omega$.

The first measured point of the coordinate θ_{14} of the up-sweep shows a lower deflection than the linear frequency response which is because of the transient dynamics of the system. From there on the up-sweep follows the linear frequency response well. However, the jump down to a lower deflection value happens in the upper nonlinear jump region later than in the linear frequency response. This means the upper nonlinear jump region shows hardening properties which increase the operational range of the energy harvester drastically. After an excitation frequency of $\Omega = 0.943$ Hz is exceeded the deflection jumps down to a deflection value of 15° with an intermediate step. The dynamics of the coordinate θ_{23} in Figure 6.21b are similar to those of the coordinate θ_{14}. When looking at the omnidirectional pendulum energy harvester from the top the trajectory of the bob follows a circular pattern during the upper nonlinear jump region. This means that the dynamics upper nonlinear jump region are similar to those of a conical pendulum.

In Figure 6.21c the frequency response of the variable avg. V_{14} which is related to the coordinate θ_{14} is shown. The linear frequency response (blue circles) shows initially a strong increase of the arithmetic mean rectified voltage output and reaches a maximum of 1.73 V at a value of the excitation frequency of 0.77 Hz. With a further increase in the excitation frequency the mean rectified voltage output decreases slightly and reaches a local minimum of 1.59 V at a value of the excitation frequency of 0.83 Hz. The deflection of the arithmetic mean rectified voltage output increases and reaches a local maximum of 1.77 V for a value of the excitation frequency of 0.88 Hz as the excitation frequency increases. With a further increase in the excitation frequency the arithmetic mean rectified voltage output jumps down to a lower value of 0.697 V. The down-sweep (orange triangles) follows the down-sweep of the coordinate θ_{14} well. It overshoots the maximum arithmetic mean rectified voltage output of the linear frequency response slightly and shows its maximum arithmetic mean rectified voltage output value of 1.82 V at a value of the excitation frequency of 0.76 Hz. The up-sweep (red diamonds) shows a constant rise in arithmetic mean rectified voltage output with an increase of the excitation frequency until reaching its maximum value of the arithmetic mean rectified voltage output of 2.06 V at an excitation frequency of 0.94 Hz. With a further increase in the excitation frequency the arithmetic mean rectified voltage output V_{14} jumps down to a lower value. It is evident that the right local maximum shows a higher voltage output than the left local maximum. This is attributed to the fact that with an increase in the excitation frequency the oscillation frequency of the pendulum increases as well. The voltage output depends on the velocity and is therefore higher when the oscillation frequency of the pendulum is higher. This is the additional advantage of having the operational point in the upper nonlinear jump region.

The frequency response of the variable avg. V_{23} is shown in Figure 6.21d. It follows the frequency response of the coordinate θ_{23} well. The up-sweep (red diamonds) shows the same characteristics as the up-sweep of the coordinate θ_{23}. With an increase in the excitation frequency the arithmetic mean rectified voltage output continuously increases and reaches its maximum value for the arithmetic mean rectified voltage output of 1.86 V for a value of the excitation frequency of 0.94 Hz. The mean rectified voltage output jumps down to a lower value with a further increase in the excitation frequency.

The lower nonlinear jump region of the coordinate θ_{14} increases the operational range of the omnidirectional pendulum energy harvester slightly by 4.54 % (0.005 Hz), see Equation (3.6). The upper nonlinear jump region for the coordinate θ_{14} broadens the operational range of the omnidirectional energy harvester by 55.0 % (0.0605 Hz), according to Equation 3.7. This is an overall increase of the operational range of the coordinate θ_{14} by 59.55 %. For the coordinate θ_{23} the operational range is with the upper nonlinear jump region increased by 61.36 % (0.0675 Hz), according to Equation (3.7).

The arithmetica mean rectified velocity of the coordinates θ_{14} and θ_{23} is shown in Figures 6.21e and 6.21f to show the relationship between the voltage output and the velocity of the coordinates. In Figure 6.21e it is evident that the maximum velocity in the lower nonlinear jumping region is lower than the maximum velocity in the upper jump region. This is consistent with the mean rectified voltage output and shows the overall higher velocity on the right side of the total operational range.

In Figure 6.21g the frequency response of the the arithmetic mean rectified power output of the coordinate θ_{14} is shown. As mentioned in the methodology Section 3.3.1 the voltage output of the two generators is added and subsequently multiplied by the current to get the power output of the system. Overall this shows that the arithmetic mean rectified power output has the same characteristics as the other frequency responses. The arithmetic mean rectified power output of shaft 14 shows two overall maxima when including the excitation frequency sweeps. The first maximum is observed at an excitation frequency of 0.768 Hz where an arithmetic mean rectified power output of 1.74 W is observed. During the upper nonlinear jump region the second maxima with an arithmetic mean rectified power output of $P_{14} = 2.86$ W is observed for an excitation frequency of 0.9355 Hz. The higher arithmetic mean rectified power output can be explained with the higher velocity of the pendulum that is prevailing compared to the first maximum observed. The broadening of the operational range with the upper nonlinear jumping region and lower nonlinear jump region is in the frequency response of the arithmetic mean rectified power output can be seen as well.

The frequency response of the arithmetic mean rectified power output of the coordinate θ_{23} is shown in Figure 6.21h. The frequency response shows similar characteristics as the frequency responses for the deflection and arithmetic mean rectified voltage output. In the upper nonlinear jump region the maximum arithmetic mean rectified power output of 2.525 W is observed at an excitation frequency of 0.9355 Hz.

It is evident that the lower and upper nonlinear jumping regions drastically increase the operational range of the pendulum energy harvester. This is especially interesting for the upper nonlinear jump region since in this area both coordinates show a high deflection and therefore the power take-off is high. However, it is important that the stating excitation frequency is located between the two local maxima of the coordinate θ_{14} in order to archive this widening in operational range. The perfect operational point is therefore located in the upper nonlinear jump region. At this point the voltage and power output are the highest.

Chapter 7

Comparison of Numerical and Experimental Results

In this chapter, the numerical and experimental results are compared. To do this the generalised coordinates θ and ϕ are numerically calculated and then they are transformed to the coordinates θ_{n14} and θ_{n23} with the Equations (3.14) and (3.15) in the methodology in Section 3.6.

The frequency responses in the experimental section were created by arithmetically averaging the maximum deflections over a defined time period, see Section 3.3.1. For the experimentally determined linear part of the frequency response the maximum deflection values were arithmetically averaged over the last 20 s, see Figure 3.9. In order to allow a direct comparison between the experimental results and numerical results the numerical results need to be post-processed similarly to the experimental results. Therefore, the maximum deflections of the numerical coordinates θ_{n14} and θ_{n23} are arithmetically averaged over a range of $\tau = 800$ to 1200. This is performed for different excitation frequencies and the results are plotted in the frequency domain.

7.1 Omnidirectional Pendulum Energy Harvester with a Pendulum Length of 0.5 m

The section compares the experimental and numerical results of the pendulum energy harvester with and without a power take-off for a pendulum length of 0.5 m.

7.1.1 Dynamics of the Omnidirectional Pendulum Energy Harvester in the Low Power Take-Off Mode

Figure 7.1 shows the frequency responses for the experimentally and numerically calculated results for the coordinates θ_{14}, θ_{23}, θ_{n14}, and θ_{n23}. The experimentally determined frequency responses in Figures 7.1a and 7.1b are the same ones as Figures 6.4a and 6.4b with a slightly

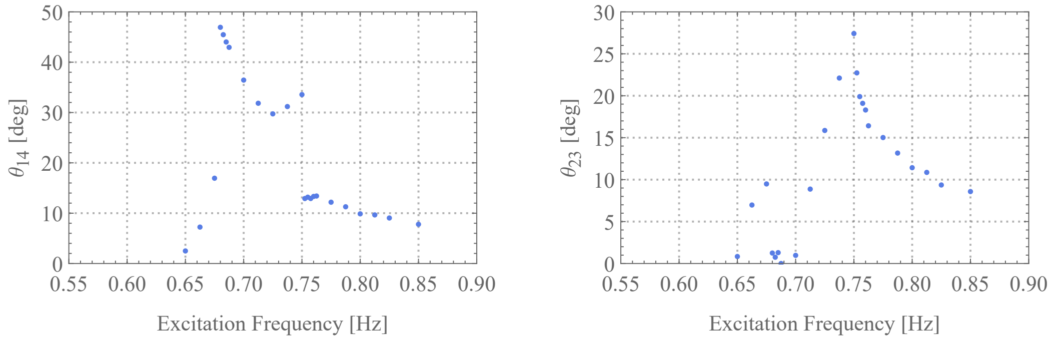

(a) Experimental frequency response of the coordinate θ_{14}

(b) Experimental frequency response of the coordinate θ_{23}

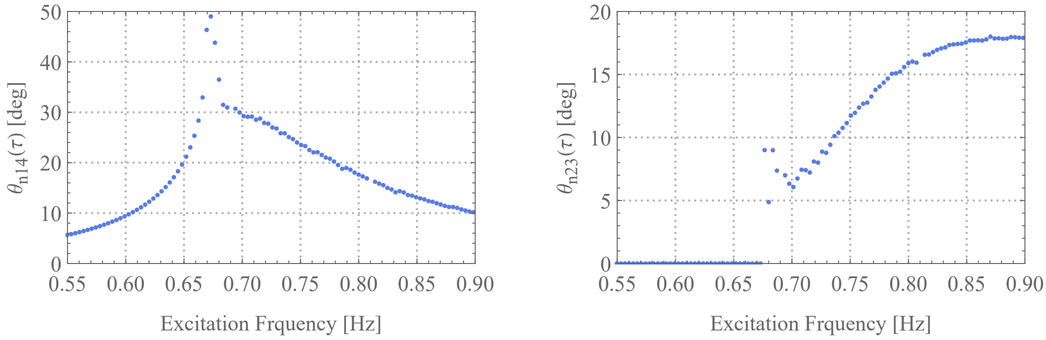

(c) Numerical frequency response of the coordinate θ_{n14}

(d) Numerical frequency response of the coordinate θ_{n23}

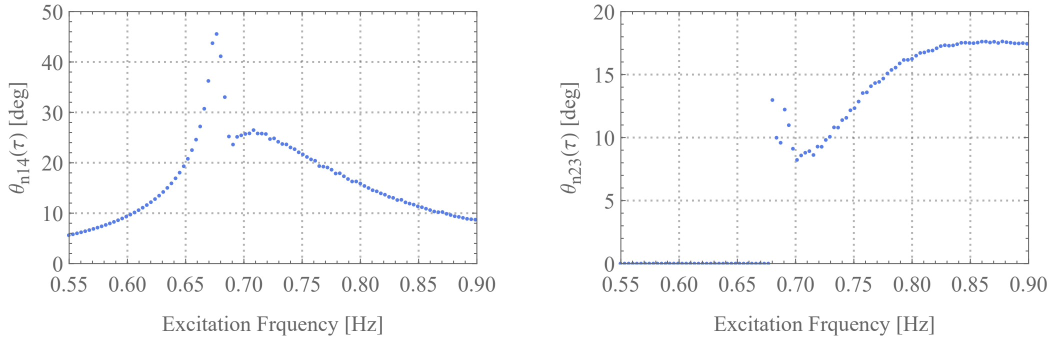

(e) Numerical frequency response of the coordinate θ_{n14} with slightly increased damping ratio $\alpha_\theta = \alpha_\phi = 0.071$

(f) Numerical frequency response of the coordinate θ_{n23} with slightly increased damping ratio $\alpha_\theta = \alpha_\phi = 0.071$

Figure 7.1: Experimentally and numerically calculated frequency responses for the pendulum energy harvester in the low power take-off mode. The parameters of the experimental evaluation of the energy harvester are: $l = 0.5$ m, $m = 1.32$ kg, $\alpha_{offset} = 45°$, $A = 32$ mm, $\xi_{14} = 0.0325$, $\xi_{23} = 0.0323$, $R_P =$ NC, and $R_S = 10$ kΩ. The values for the numerical analysis are: $l = 0.5$ m, $m = 1.32$ kg, $g = 9.81\ \frac{\mathrm{m}}{\mathrm{s}^2}$, $\alpha_\theta = \alpha_\phi = 0.0648$, $a_u = 0.064$, $a_v = a_w = 0$, and $P_\theta = P_\phi = 0$.

adapted excitation frequency range to make the numerical and experimental ranges equal in size and thus the figures can be directly compared. The repeated use of the experimental results increases the overall length of this work, however, increased clarity and readability for the reader justifies this. Thus, selected figures from Chapter 6 are reused in the following sections.

The experimentally determined coordinate θ_{14} in Figure 7.1a shows a maximum deflection of 46.92° for an excitation frequency of $\Omega = 0.68$ Hz. For more information on the experimental frequency response of the coordinate θ_{14} see Figure 6.4a. In Figure 7.1b the numerically calculated arithmetic mean frequency response for the coordinate θ_{n14} is shown. The spherical pendulum is excited in the u-direction with the damping ratio that is determined on the experimental rig. The maximum deflection of the coordinate θ_{n14} is reached at an excitation frequency of $\Omega = 0.673$ Hz an has a value of $\theta_{n14} = 49.0^\circ$. The numerically calculated maximum deflection shows a higher value than the experimental investigation. One possible explanation is that the excitation energy is transformed in three main components. The majority of the energy is transformed in kinetic energy that excites the pendulum bob. A small part of the energy is energy loss due to the damping properties of the harvester's mechanical parts and aerodynamic dissipation. The last part of the energy is transformed in high frequency vibrations in the mechanical parts of the energy harvester, for example the pendulum mass, pendulum rod or flat bars see Section 3.5. Since these high frequency vibrations are not taken into account in the numerical analysis, they must be incorporated by clever manipulation of the parameters, for which there are two methods. Note that these two approaches are purely theoretical methods to compensate for the energy loss because of high frequency vibration within the harvester. The first approach is to reduce the excitation amplitude and thus reducing the overall energy input in the system. Thus the part of the energy that is converted into high-frequency oscillations is not initially introduced to the energy harvester. This brings the maximum deflection of the coordinate θ_{n14} to the same level as the experimentally observed coordinate. After several iterations an excitation amplitude of $a_u = 0.061$ proves to be the adequate value. The second method is to increase the damping ratio slightly. After several iteration steps a damping ratio of $\alpha_\theta = \alpha_\phi = 0.071$ proves to be adequate. Unfortunately, these two purely theoretical approaches do not show the characteristic hardening effects of the experiment. This upper nonlinear jumping region is discussed in greater detail in the following in Section 7.3. The maximum deflection $\theta_{n14} = 45.56^\circ$ for this damping ratio is at an excitation frequency of $\Omega = 0.677$ Hz, see Figure 7.1e.

The purely theoretical adaption of the damping ratio decreases the maximum deflection of the coordinates slightly and therefore compensates for the higher frequency vibration within the mechanical parts of the energy harvester. Therefore, in this section theoretical frequency responses with for each case adapted damping ratios are additionally shown.

In Figure 7.1d the theoretical frequency response for the coordinate θ_{n23} is shown. Until the excitation frequency of $\Omega = 0.67$ Hz is not exceeded the coordinate shows no deflection, this means that in this area the omnidirectional pendulum energy harvester is showing the dynamics of a simple pendulum energy harvester. From there on the theoretical frequency response shows two local maxima with a deflection of $\theta_{n23} = 9.0°$. Afterwards, a local minimum is observed and then the deflection increases steadily. In Figure 7.1f, as with the coordinate θ_{n14}, the damping ratio is increased to a value of $\alpha_\theta = \alpha_\phi = 0.071$. For the higher damping ratios the coordinate θ_{n23} shows no deflection until the excitation frequency of $\Omega = 0.677$ Hz is exceeded. Then the deflection shows a local maximum at an excitation frequency of $\Omega = 0.68$ Hz with a deflection of $\theta_{n23} = 13.0$ Hz. From there on the numerical frequency response has a local minimum, and then the deflection of the coordinate θ_{n23} gradually increases with an increase in the excitation frequency.

Figure 7.2 shows θ_{n14} and θ_{n23} over the dimensionless time for different excitation frequencies. The excitation frequencies that are shown are the maximum deflections of the coordinate

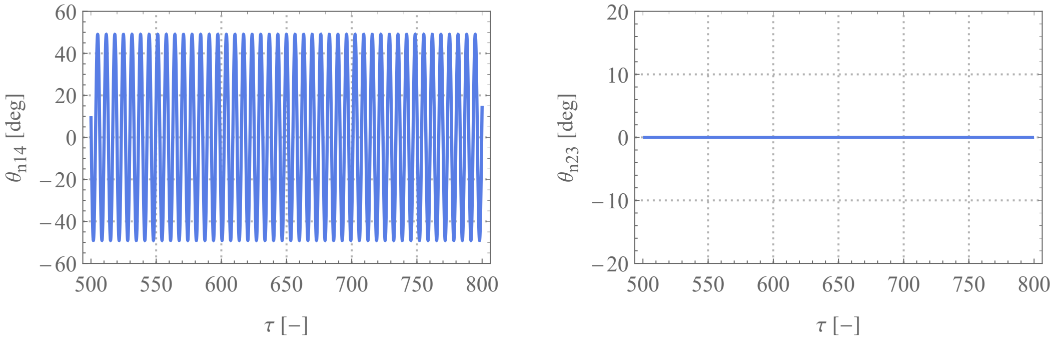

(a) θ_{n14} over τ for an excitation frequency of $\Omega = 0.673$ Hz

(b) θ_{n23} over τ for an excitation frequency of $\Omega = 0.673$ Hz

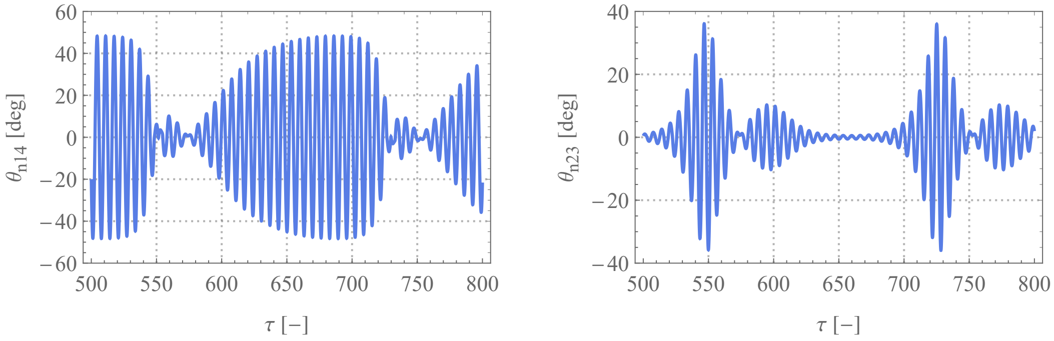

(c) θ_{n14} over τ for an excitation frequency of $\Omega = 0.683$ Hz

(d) θ_{n23} over τ for an excitation frequency of $\Omega = 0.683$ Hz

Figure 7.2: Numerically calculated deflection over time. The values for the numerical analysis are: $l = 0.5$ m, $m = 1.32$ kg, $g = 9.81\ \frac{\text{m}}{\text{s}^2}$, $\alpha_\theta = \alpha_\phi = 0.0648$, $a_u = 0.064$, $a_v = a_w = 0$, and $P_\theta = P_\phi = 0$.

θ_{n14} at a value of the excitation frequency of $\Omega = 0.673$ Hz and the following local minimum with a value of the excitation frequency of $\Omega = 0.683$ Hz. It can be seen that for a value of the excitation frequency of $\Omega = 0.673$ Hz the coordinate θ_{n14} is moving periodically while the coordinate θ_{n23} does not show any deflection, see Figures 7.2a and 7.2b. This is observed in the experimental results at the maximum deflection of the coordinates θ_{14} and θ_{23} as well see Figure 6.5.

For an excitation frequency of $\Omega = 0.683$ Hz, the system no longer shows periodic dynamics, see Figures 7.2c and 7.2d but instead a behaviour that suggests quasi-periodic dynamics are observed. This agrees with the experimental data, see for example Figures 6.5e and 6.5f.

Figure 7.3 shows frequency responses for the experimental and numerically determined coordinates θ_{14}, θ_{23}, θ_{n14}, and θ_{n23}. The numerically determined frequency responses are almost the same as in Figure 7.1, the difference being the direction of excitation. This allows one to compare if a variation in excitation direction has the potential to change the dynamics of the energy harvester. In Figure 7.3 a coupled excitation in the x- and y-directions is used to simulate the offset angle $\alpha_{offset} = 45^\circ$. To achieve this, both excitation amplitudes are multiplied by $\sin(45^\circ)$. The experimentally determined frequency responses in Figures 7.3a and 7.3b are identical to Figures 7.1a and 7.1b and have only been repeated for the sake of clarity and reader convenience.

In Figures 7.3c and 7.3d the frequency response for the numerically calculated coordinates θ_{n14} and θ_{n23} with the experimentally determined damping ratios of $\alpha_\theta = \alpha_\phi = 0.0648$ are shown. The theoretical frequency response for the coordinate θ_{n14} reaches its maximum deflection of $\theta_{n14} = 34.65^\circ$ at an excitation frequency of 0.673 Hz. Which is close to the experimentally observed maximum for the coordinate θ_{14}. From the maximum deflection onwards the value for the coordinate θ_{n14} drops rapidly. With a further increase in the excitation frequency the deflection of the coordinate θ_{n14} gradually decreases. The numerical frequency response for the coordinate θ_{n23} is shown in Figure 7.3d. With the maximum deflection of $\theta_{n23} = 36.86^\circ$ reached at an excitation frequency of 0.676 Hz. The frequency response is similar to the one of the coordinate θ_{n14} shown in Figure 7.3c. However, this commonality between the numerically calculated frequency responses shows that there are no similarities in comparison with the experimental frequency response. Nevertheless, the coupled excitation is investigated for the variation of the excitation amplitude in the following figures and a final conclusion on the usability of this approach is made at the end of this section.

Figures 7.3e and 7.3f show the numerically calculated frequency responses for the coordinates θ_{n14} and θ_{n23} with a slightly increased damping ratio of $\alpha_\theta = \alpha_\phi = 0.071$ to compensate for energy losses due to high frequency vibrations within the structure of the pendulum energy harvester. With the higher damping ratio the maximum deflection of the coordinate θ_{n14} has a lower value of 32.21° at a slightly higher excitation frequency of 0.677 Hz, see Figure 7.3e. The maximum deflection is slightly higher for the coordinate $\theta_{n23} = 38.29^\circ$ for slightly higher excitation frequency of 0.680 Hz.

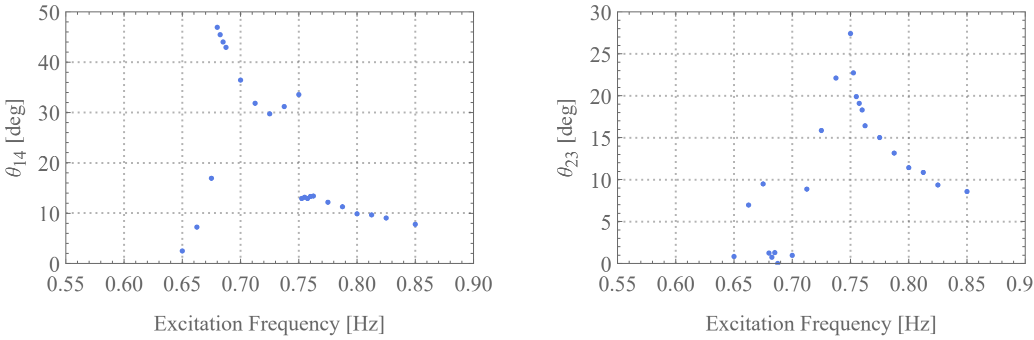

(a) Experimental frequency response of the coordinate θ_{14}

(b) Experimental frequency response of the coordinate θ_{23}

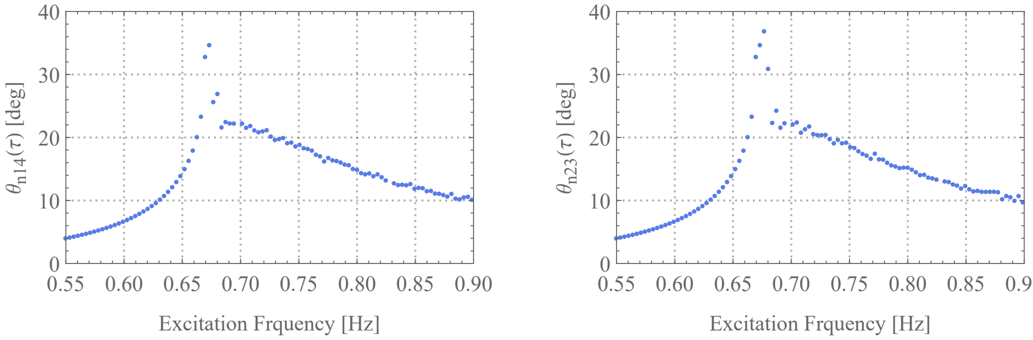

(c) Numerical frequency response of the coordinate θ_{n14}

(d) Numerical frequency response of the coordinate θ_{n23}

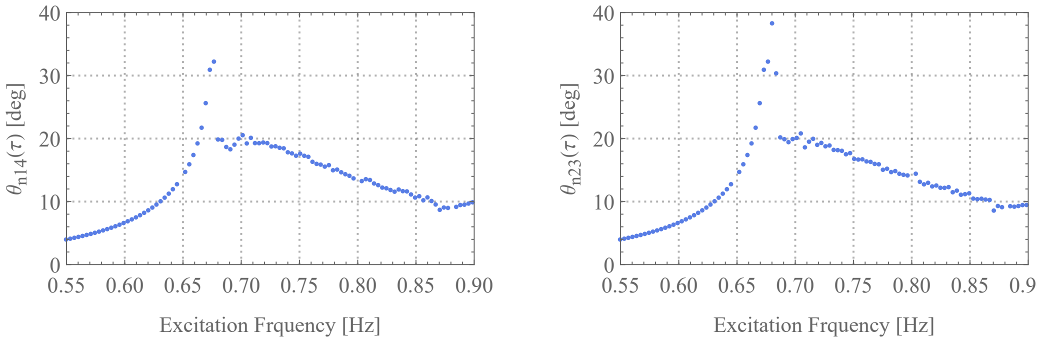

(e) Numerical frequency response of the coordinate θ_{n14} with slightly increased damping ratio $\alpha_\theta = \alpha_\phi = 0.071$

(f) Numerical frequency response of the coordinate θ_{n23} with slightly increased damping ratio $\alpha_\theta = \alpha_\phi = 0.071$

Figure 7.3: Experimentally and numerically calculated frequency responses for the pendulum energy harvester in the low power take-off mode. The parameters of the experimental evaluation of the energy harvester are: $l = 0.5$ m, $m = 1.32$ kg, $\alpha_{offset} = 45°$, $A = 32$ mm, $\xi_{14} = 0.0325$, $\xi_{23} = 0.0323$, $R_P =$ NC, and $R_S = 10$ kΩ. The values for the numerical analysis are: $l = 0.5$ m, $m = 1.32$ kg, $g = 9.81\ \frac{\text{m}}{\text{s}^2}$, $\alpha_\theta = \alpha_\phi = 0.0648$, $a_u = a_v = \frac{\sqrt{2}}{2}0.064$, $a_w = 0$, and $P_\theta = P_\phi = 0$.

Figure 7.4 shows deflections of the coordinates θ_{14}, θ_{23}, θ_{n14}, and θ_{n23} over the excitation amplitude in the x-direction with an excitation frequency of $\beta = 1.04615$ which equivalent to an experimental excitation frequency of 0.7375 Hz. The experimentally determined deflection

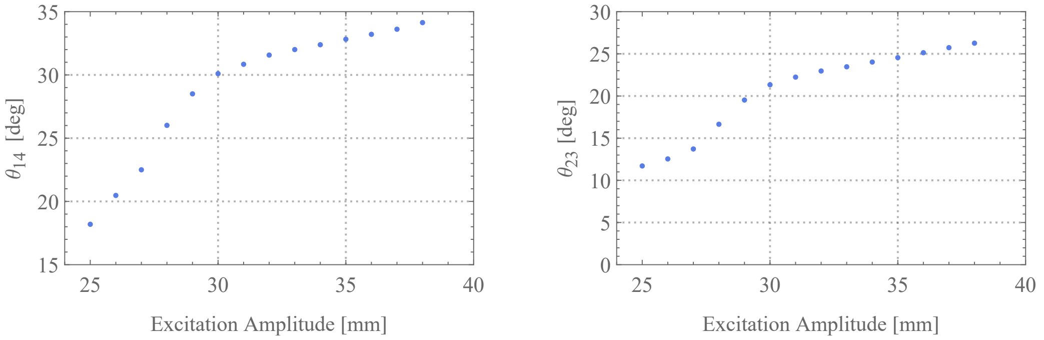

(a) Experimentally determined coordinate θ_{14} over the variation of the excitation amplitude

(b) Experimentally determined coordinate θ_{23} over the variation of the excitation amplitude

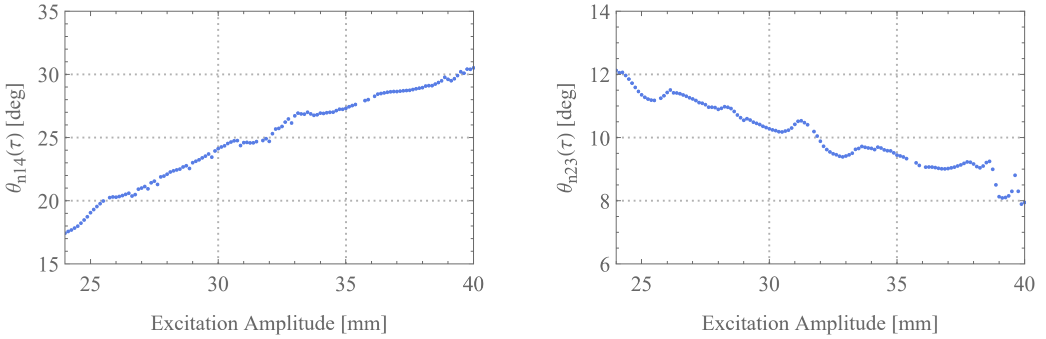

(c) Numerically determined coordinate θ_{n14} over the excitation amplitude

(d) Numerically determined coordinate θ_{n23} over the excitation amplitude

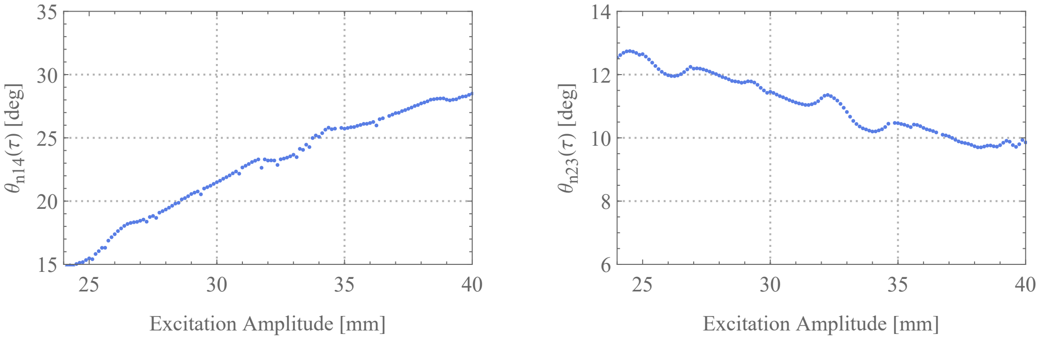

(e) Numerically determined coordinate θ_{n14} over the excitation amplitude with slightly increased damping ratio $\alpha_\theta = \alpha_\phi = 0.071$

(f) Numerically determined coordinate θ_{n23} over the excitation amplitude with slightly increased damping ratio $\alpha_\theta = \alpha_\phi = 0.071$

Figure 7.4: Experimentally and numerically calculated deflection over the excitation amplitude for the pendulum energy harvester in the low power take-off mode. The parameters of the experimental evaluation of the pendulum energy harvester are: $l = 0.5$ m, $m = 1.32$ kg, $\alpha_{offset} = 45°$, $\Omega = 0.7375$ Hz, $\xi_{14} = 0.0325$, $\xi_{23} = 0.0323$, $R_P = \text{NC}$, and $R_S = 10$ kΩ. The values for the numerical analysis are: $l = 0.5$ m, $m = 1.32$ kg, $g = 9.81\ \frac{\text{m}}{\text{s}^2}$, $\alpha_\theta = \alpha_\phi = 0.0648$, $\beta = 1.04615$, $a_v = 0$, $a_w = 0$, and $P_\theta = P_\phi = 0$.

over the excitation amplitude plots in Figures 7.4a and 7.4b are repetitions from Figure 6.6 which were repeated in this section to increase the clarity for the reader. As described previously the slope of the coordinates θ_{14} and θ_{23} increases steeply with an increase in the excitation amplitude until the excitation amplitude of 30 mm, from there on the slope decreases.

The numerically determined deflection of the coordinate θ_{n14} over the excitation amplitude is shown in Figure 7.4c. The deflection gradually increases with an increase in the excitation amplitude, however, the different slopes from the experimental results cannot be seen. Due to the absence of the steep slope in the area of the excitation amplitude from $A = 25$ to 30 mm the deflection for the coordinate θ_{n14} is generally lower than its experimentally determined value θ_{14}.

In Figure 7.4d the numerically determined deflection of the coordinate θ_{n23} over the excitation amplitude is shown. The deflection of the coordinate θ_{n23} decreases with an increase of the excitation amplitude. Over the shown range of the excitation amplitude the deflection decreases from 12° to 8°. Unfortunately, this does not agree with the experimental results.

As before, the damping ratios have been slightly increased to a value of $\alpha_\theta = \alpha_\phi = 0.071$ to compensate for the energy that is converted into higher frequency vibrations in the experimental rig. Figure 7.4e shows the deflection of the coordinate θ_{n14} over the excitation amplitude. Because of the higher damping ratios the overall deflection is lower than the one in Figure 7.4c. Over the shown range of excitation amplitudes the deflection gradually increases.

In Figure 7.4f the deflection of the coordinate θ_{n23} over the excitation amplitude with an increased damping ratio of $\alpha_\theta = \alpha_\phi = 0.071$ is shown. The deflection decreases with an increase of the excitation amplitude. Interestingly with a decrease of the damping ratio the overall deflection of the coordinate θ_{n23} increases slightly.

Figure 7.5 shows the deflection of the coordinates θ_{14}, θ_{23}, θ_{n14}, and θ_{n23} over the excitation amplitude. The numerically determined figures are determined with a coupled excitation in the x- and y-directions, this is implemented by multiplying both of the excitation amplitudes by $\sin(45^\circ)$. This is executed on the x-axis of the figure as well. This rescaling of the excitation amplitudes allows the numerical results and experimental results to be consistent and they can therefore be compared to the previous figures without any intermediate calculation steps. The experimentally determined deflection over the excitation amplitudes in Figures 7.5a and 7.5b are repetitions from Figure 6.6. They show a steep slope until the excitation amplitudes of $A = 30$ mm is reached. Afterwards the slope decreases and the deflection of the coordinates θ_{14} and θ_{23} increases in smaller steps with a further decrease in the excitation amplitudes.

In Figure 7.5c the deflection of the coordinate θ_{n14} over the excitation amplitudes is shown. The deflection gradually increases with an increase in the excitation amplitudes. However, the overall deflections are lower than the experimentally determined values in Figure 7.5a.

The coordinate θ_{n23} over the excitation amplitudes is shown in Figure 7.5d. With an increase of the excitation amplitudes the deflection of the coordinate θ_{n23} increases. The overall deflection of the coordinate θ_{n23} is lower than its experimentally determined equivalent θ_{23}.

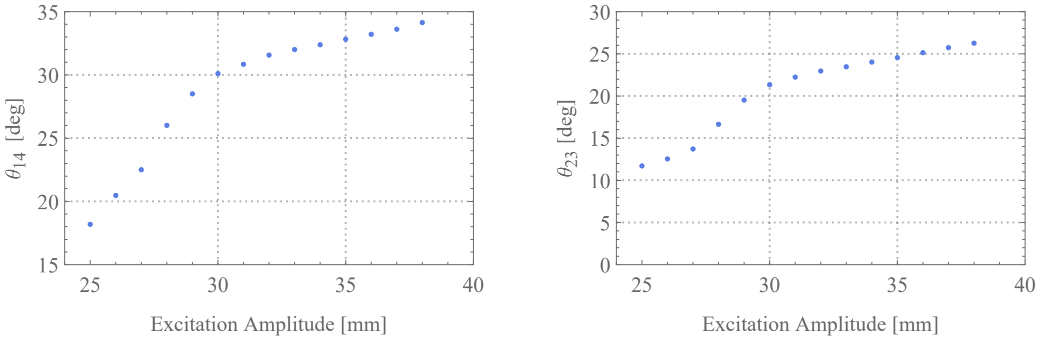

(a) Experimentally determined coordinate θ_{14} over the variation of the excitation amplitude

(b) Experimentally determined coordinate θ_{23} over the variation of the excitation amplitude

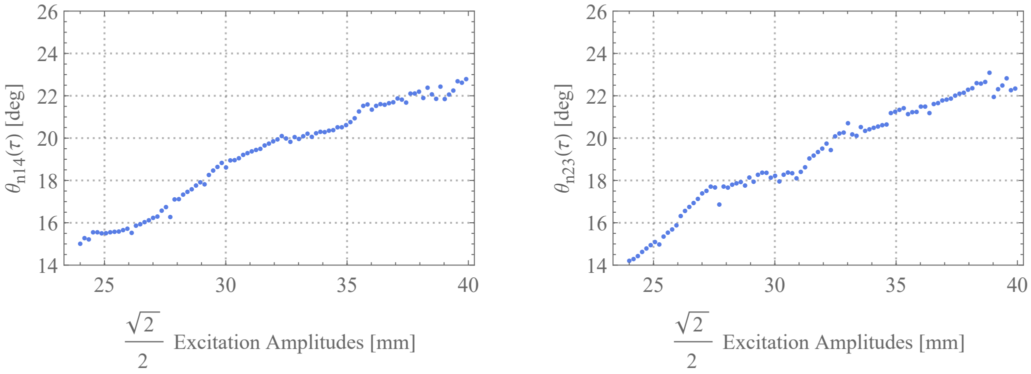

(c) Numerically determined coordinate θ_{n14} over the excitation amplitudes

(d) Numerically determined coordinate θ_{n23} over the excitation amplitudes

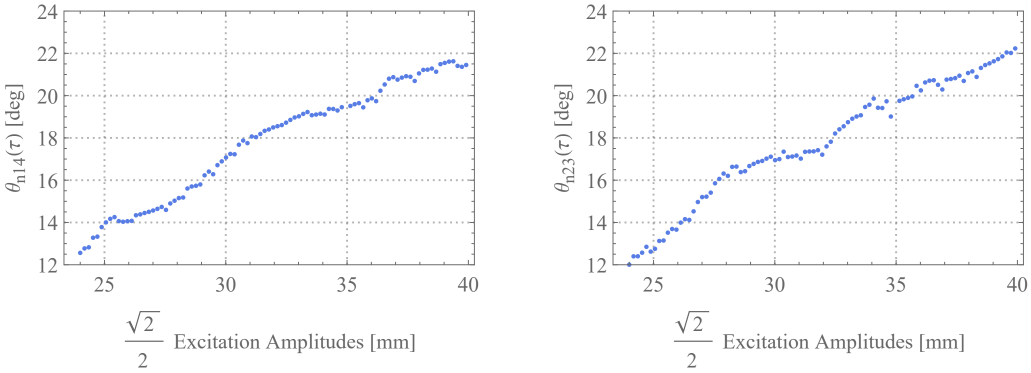

(e) Numerically determined coordinate θ_{n14} over the excitation amplitudes with slightly increased damping ratio $\alpha_\theta = \alpha_\phi = 0.071$

(f) Numerically determined coordinate θ_{n23} over the excitation amplitudes with slightly increased damping ratio $\alpha_\theta = \alpha_\phi = 0.071$

Figure 7.5: Experimentally and numerically calculated deflection over the excitation amplitude for the pendulum energy harvester in the low power take-off mode. The parameters of the experimental evaluation of the pendulum energy harvester are: $l = 0.5$ m, $m = 1.32$ kg, $\alpha_{offset} = 45°$, $\Omega = 0.7375$ Hz, $\xi_{14} = 0.0325$, $\xi_{23} = 0.0323$, $R_P =$ NC, and $R_S = 10$ kΩ. The values for the numerical analysis are: $l = 0.5$ m, $m = 1.32$ kg, $g = 9.81\ \frac{\text{m}}{\text{s}^2}$, $\alpha_\theta = \alpha_\phi = 0.0648$, $\beta = 1.04615$, $a_w = 0$, and $P_\theta = P_\phi = 0$.

For the last two figures the damping ratio is increased to a value of $\alpha_\theta = \alpha_\phi = 0.071$ to accommodate the energy transformation in higher frequency vibrations in the experimental rig see Section 3.5. Figure 7.5e shows the deflection of the coordinate θ_{n14} over the excitation amplitudes. The deflection increases with an increase in the excitation amplitudes and the overall deflection is lower which is attributed to the higher damping ratio.

In Figure 7.5f the deflection of the coordinate θ_{n23} over the excitation amplitudes is shown. With the increased damping ratio the deflection of the coordinate θ_{n23} in Figure 7.5f is lower than in Figure 7.5d.

The idea to use coupled excitations in Section 7.1.1 unfortunately does not show the expected results. They are therefore not used anymore in the following. However, it is noticed that an increase of the damping ratios brings the numerical analysis closer to the experimental results. Additionally, the increase of the damping ratios compensates for the higher frequency vibrations that are present in the experimental rig. Generally, it can be said that the dynamics of the coordinate θ_{n23} are harder to reproduce than the coordinate θ_{n14}.

7.1.2 Dynamics of the Omnidirectional Pendulum Energy Harvester in the High Power Take-Off Mode with Inclusion of the Arctangent Power Take-Off Term

The arctangent power take-off term is used to simulate the power take-off of the energy harvester in this section.

Figure 7.6 shows frequency responses for the experimental coordinates θ_{14} and θ_{23} and the numerical reconstruction of the experimental coordinates θ_{n14} and θ_{n23} with an inclusion of a power take-off torque $P_\theta = 0.0144$. This power take-off torque is selected after several iterations where the maximum deflection of θ_{n14} is reached by adapting the power take-off torque.

The frequency response for the experimentally determined coordinate θ_{14} is shown in Figure 7.6a. For the first two measurement points the coordinate θ_{14} shows a small deflection which then jumps up to a local maximum of 49.4° at a value of the excitation frequency of 0.675 Hz. With a further increase in the excitation frequency the deflection sees a local minimum with a deflection of 33.87° for a value of the excitation frequency of 0.725 Hz. Afterwards the deflection increases again and reaches a local maximum of 37.5° for a value of the excitation frequency of 0.7625 Hz. When the excitation frequency is increased further the deflection of the coordinate θ_{14} jumps down to a deflection value close to 15°.

Figure 7.6b shows the experimentally determined frequency response of the coordinate θ_{23}. The first two measurement points see an increase in deflection similar to those of the coordinate θ_{14}. With a further increase in the excitation frequency the coordinate θ_{23} shows a small deflection until the excitation frequency of $\Omega = 0.69$ Hz is exceeded. With a further

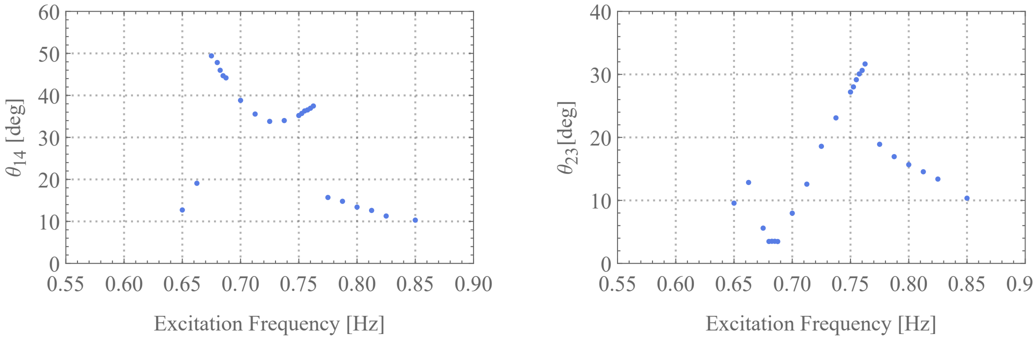

(a) Experimental frequency response of the coordinate θ_{14}

(b) Experimental frequency response of the coordinate θ_{23}

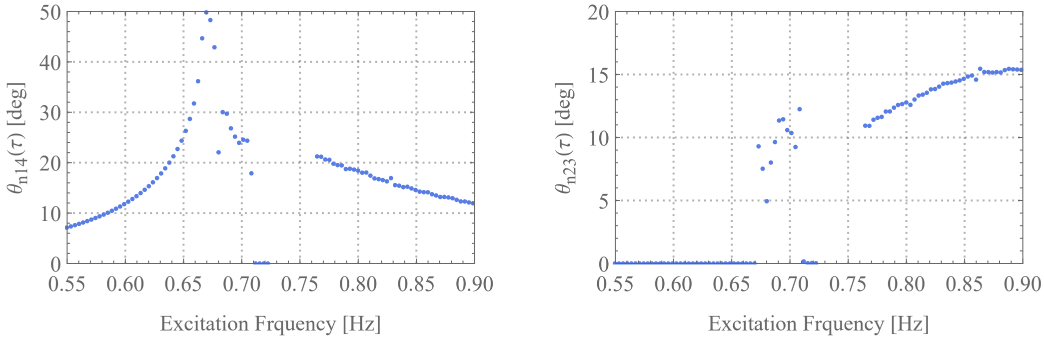

(c) Numerical frequency response of the coordinate θ_{n14} forced in $a_u = 0.088$ and $a_v = 0$

(d) Numerical frequency response of the coordinate θ_{n23} forced in $a_u = 0.088$ and $a_v = 0$

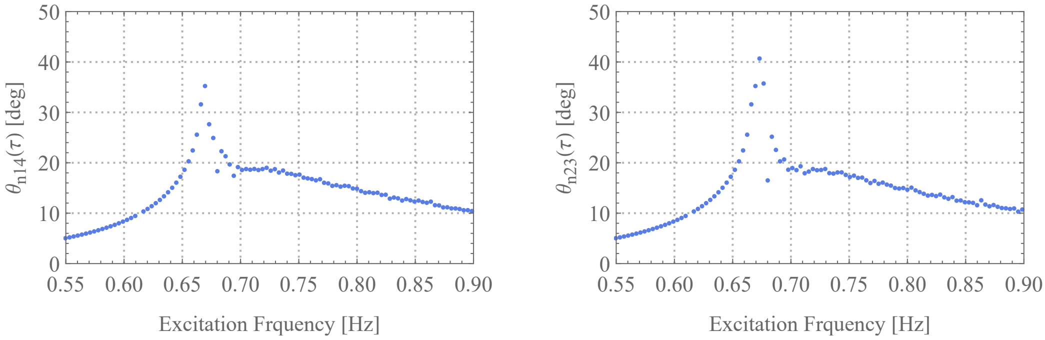

(e) Numerical frequency response of the coordinate θ_{n14} with coupled excitation $a_u = a_v = \frac{\sqrt{2}}{2}0.088$

(f) Numerical frequency response of the coordinate θ_{n23} with coupled excitation $a_u = a_v = \frac{\sqrt{2}}{2}0.088$

Figure 7.6: Experimentally and numerically calculated frequency responses for the pendulum energy harvester in the high power take-off mode. The parameters of the experimental evaluation of the pendulum energy harvester are: $l = 0.5$ m, $m = 1.32$ kg, $\alpha_{offset} = 45°$, $A = 44$ mm, $\xi_{14} = 0.0325$, $\xi_{23} = 0.0323$, $R_P = 10\ \Omega$, and $R_S = 0\ \Omega$. The values for the numerical analysis are: $l = 0.5$ m, $m = 1.32$ kg, $g = 9.81\ \frac{\mathrm{m}}{\mathrm{s}^2}$, $\alpha_\theta = \alpha_\phi = 0.0648$, $a_w = 0$, and $P_\theta = 0.0144$, $P_\phi = 0$.

increase in the excitation frequency the deflection rises gradually until reaching its maximum deflection of 31.4° for an excitation frequency of 0.7625 Hz. Then the deflection jumps down to a deflection value of around 20°.

The numerical analysis of the frequency response of the coordinate θ_{n14} is shown in Figure 7.6c. The deflection of the coordinate θ_{n14} increases with approximately exponential characteristics for a value of the excitation frequency from 0.55 Hz to 0.67 Hz. With the maximum deflection of 49.7° reached at an excitation frequency of 0.67 Hz. For an excitation frequency from 0.67 Hz to 0.71 Hz the deflection of the coordinate θ_{n14} decreases rapidly. This is followed by an area where the system cannot be solved numerically. With an excitation frequency higher than 0.76 Hz the coordinate θ_{n14} shows a gradual decrease with an increase of the excitation frequency.

In Figure 7.6d the numerically calculated frequency response for the coordinate θ_{23} is shown. Until the excitation frequency of 0.67 Hz is exceeded the coordinate does not show a deflection. This is followed by an area where the levels of deflections do not follow a clear trend. After an excitation frequency of 0.71 Hz is exceeded the system shows no deflection because of numerical issues. With an excitation frequency higher than 0.76 Hz the system shows a gradually increasing deflection until the end of the shown excitation frequency range.

The omnidirectional pendulum energy harvester is excited with a coupled excitation in the u- and v-directions with the amplitudes $a_u = a_v = \frac{\sqrt{2}}{2}0.088$. This simulates the excitation with an offset angle of $\alpha_{offset} = 45\ ^\circ$ and is here observed again for the sake of completeness. Figure 7.6e shows the theoretical frequency response for the coordinate θ_{n14}. The deflection of the coordinate θ_{n14} increases with approximately exponential characteristics for a value of the excitation frequency from $\Omega = 0.55$ Hz to 0.67 Hz. For an excitation frequency of 0.67 Hz the maximum deflection of the coordinate $\theta_{n14} = 35.1^\circ$ is reached. With a further increase in the excitation frequency the deflection of the coordinate θ_{n14} decreases rapidly. This is followed by an area where the deflection stays constant for an excitation frequency from $\Omega = 0.7$ Hz to 0.725 Hz. For a further increase in the excitation frequency the deflection of the coordinate θ_{n14} gradually decreases.

In Figure 7.6f the theoretical frequency response for the coordinate θ_{n23} that is excited in the u- and v-directions is shown. The deflection of the coordinate θ_{n23} increases with approximately exponential characteristics with an increase in the excitation frequency until a maximum deflection of the coordinate θ_{n23} of 40.7° for a value of the excitation frequency of 0.67 Hz is reached. With a further increase in the excitation frequency the deflection first decreases strongly. For a value of the excitation frequency from $\Omega = 0.698$ Hz to 0.73 Hz the deflection of the coordinate θ_{n23} does almost show no decrease. After the excitation frequency of 0.73 Hz is exceeded and the excitation frequency is further increased the deflection of the coordinate θ_{n23} decreases gradually.

7.2 Numerical Comparison of Different Pendulum Lengths

In this section, the frequency responses for different pendulum lengths are examined for the numerically calculated coordinates θ_{n14} and θ_{n23}. This is similar to the figures in Section 6.3 where the same figure is shown for the experimental results. The energy harvester is excited with an excitation amplitude of $A = 32$ mm. In the nondimensionalisation process the excitation amplitude is divided by the pendulum length the dimensionless excitation amplitudes a_u show different values for different pendulum lengths. The experimentally determined damping ratios for the different pendulum lengths were used for the numerical analyses.

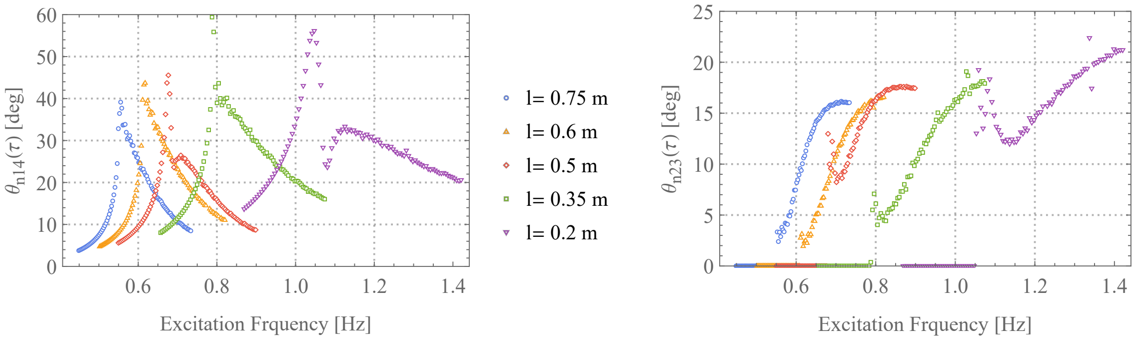

(a) Numerical frequency responses of the coordinate θ_{n14}

(b) Numerical frequency responses of the coordinate θ_{n23}

Figure 7.7: Numerical frequency responses over excitation frequency Ω for the pendulum energy harvester for different pendulum lengths. The values for the numerical analysis are: $m = 1.32$ kg, $g = 9.81\ \frac{\mathrm{m}}{\mathrm{s}^2}$, $a_v = a_w = 0$, $P_\theta = 0.$, and $P_\phi = 0$. The damping ratios, and nondimensional excitation amplitude are depending on the pendulum length and are therefore set to: $l = 0.75\ \mathrm{m} \rightarrow \alpha_\theta = \alpha_\phi = 0.0404$ and $a_u = 0.0426667$, $l = 0.6\ \mathrm{m} \rightarrow \alpha_\theta = \alpha_\phi = 0.0447$ and $a_u = 0.0533333$, $l = 0.5\ \mathrm{m} \rightarrow \alpha_\theta = \alpha_\phi = 0.0648$ and $a_u = 0.064$, $l = 0.35\ \mathrm{m} \rightarrow \alpha_\theta = \alpha_\phi = 0.0712$ and $a_u = 0.0914286$, and $l = 0.2\ \mathrm{m} \rightarrow \alpha_\theta = \alpha_\phi = 0.1349$ and $a_u = 0.16$.

The numerical frequency responses for the coordinate θ_{n14} is shown in Figure 7.7a. The frequency responses are placed over the shown range of the excitation frequency as is expected since the natural frequency of the spherical pendulum is dependent on the length in the pendulum rod. With a decrease of the pendulum length $l = 0.75$ m to 0.35 m the overall maximum deflection of the coordinate θ_{n14} increases. For a pendulum length of 0.2 m the maximum deflection of the coordinate θ_{n14} decreases compared to a pendulum length of 0.35 m.

In Figure 7.7b the theoretical frequency responses for the different pendulum lengths for the coordinate θ_{n23} are shown. Due to the different lengths of the pendulum and the resulting different natural frequencies, the theoretical frequency responses are distributed over the excitation frequency range. The maximum deflection of the coordinate θ_{n23} increases with a decrease of the pendulum length.

7.3 Numerical Replication of the Broadening Effect of the Omnidirectional Pendulum Energy Harvester

In the previous sections it became clear that the experimental results can unfortunately only be reproduced numerically to a limited extent when the same parameters as in the experimental evaluation are used. Especially the coordinate θ_{23} and the upper nonlinear jump region in Section 6.4 are difficult to reproduce numerically. The aim of this section is to reproduce these two effects with numerical analysis. To do this, the excitation amplitude has to be massively increased by a factor of 2 to 3.5 of the excitation amplitude values in the experimental evaluation. Unfortunately, because of safety reasons these high values of excitation amplitudes can only be investigated theoretically because although the excitation amplitudes are theoretically feasible for the shaker table, they are not for the dimensions and mass of the energy harvester.

It is important to examine how an increased excitation amplitude affects the dynamics of the pendulum energy harvester. This is accomplished, by comparing the experimentally determined frequency responses in Figures 6.20 and 6.21 where the pendulum energy harvester with a pendulum length of 0.35 m is excited with an excitation amplitude of 32 mm and 48 mm. It can be seen that with an increase in the excitation amplitude the operational range of the pendulum energy harvester increases drastically. The same is expected to be observed from the numerical analysis.

In Figure 7.8 experimental and numerical frequency responses are shown. The experimentally determined frequency responses in Figures 7.8a and 7.8b are a repetition of Figure 6.19 with a rescaled x-axis to allow a direct comparison between the experimental and numerical frequency responses. The spherical pendulum in the experimental frequency responses is excited with an excitation amplitude of $A = 32$ mm and is examined in the low power take-off mode. The dynamics of the frequency responses are described in greater detail in Section 6.4 see Figure 6.19.

Figures 7.8c and 7.8d show the numerically calculated frequency responses of the coordinates θ_{n14} and θ_{n23}. The spherical pendulum is excited with an excitation amplitude of $a_u = 0.314286$, in experimental excitation amplitude values this is a value of $A = 110$ mm. The excitation amplitude of the numerical analysis is therefore about 3.5 times higher than the experimental excitation amplitude in Figures 7.8a and 7.8b. The excitation amplitude must be selected to a high value because this is the first time that the hardening effect can clearly be seen this is discussed in greater detail with Figure 7.11 and is therefore not repeated here.

In Figure 7.8c the numerically determined frequency response of the coordinate θ_{n14} is shown. As already observed in the experimental evaluation with an increase in the excitation amplitude the operational range of the spherical pendulum increases. This is observed for the numerical analysis here as well. For a value of the excitation frequency from $\Omega = 0.5$ to 0.765 Hz the deflection of the coordinate θ_{n14} increases gradually and reaches its maximum

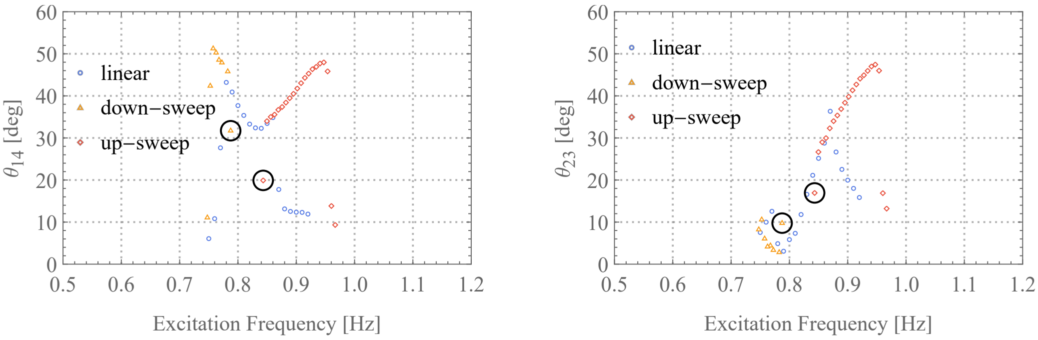

(a) Experimental frequency response of the coordinate θ_{14}

(b) Experimental frequency response of the coordinate θ_{23}

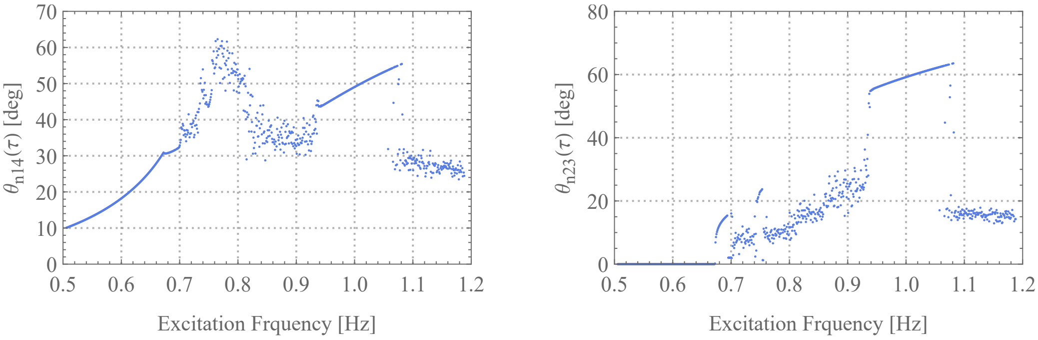

(c) Numerical frequency response of the coordinate θ_{n14}

(d) Numerical frequency response of the coordinate θ_{n23}

Figure 7.8: Experimental and numerical frequency responses for the pendulum energy harvester in the low power take-off mode. The values for the numerical analysis are: $l = 0.35$ m, $m = 1.32$ kg, $g = 9.81\ \frac{\text{m}}{\text{s}^2}$, $\alpha_\theta = \alpha_\phi = 0.0712$, $a_u = 0.314286$, $a_v = a_w = 0$, $P_\theta = 0$, and $P_\phi = 0$. The parameters of the experimental evaluation of the pendulum energy harvester are: $l = 0.35$ m, $m = 1.32$ kg, $\alpha_{offset} = 45°$, $A = 32$ mm, $\xi_{14} = 0.0373$, $\xi_{23} = 0.0339$, $R_P =$ NC, and $R_S = 10\,\text{k}\Omega$.

deflection of 62.2° at an excitation frequency of 0.765 Hz. With a further increase in the excitation frequency the deflection of the coordinate θ_{n14} decreases and reaches its minimum at an excitation frequency of 0.91 Hz. This is followed by a jump up to a higher deflection value. For a range of excitation frequencies from 0.91 Hz to 1.08 Hz the deflection of the coordinate θ_{n14} increases and reaches its maximum deflection of 55.1° at the end of the excitation frequency range. With a further increase in the excitation frequency the deflection of the coordinate θ_{n14} jumps down to a value of around 30° and decreases from there on gradually. The numerically determined frequency response of the coordinate θ_{n14} shows all the characteristics of the experimental frequency response of the coordinate θ_{14} in Figure 7.8a. The main difference is the overall higher deflection of the numerically determined coordinate θ_{n14} and the increased excitation frequency range that shows higher deflections which can both be fully attributed to the higher excitation amplitude. This is observed in the following figures as well.

In Figure 7.8d the theoretical frequency response of the coordinate θ_{n23} is shown. For a value of the excitation frequency from 0.5 Hz to 0.675 Hz the theoretical frequency response shows no deflection of the coordinate θ_{n23}. In the range of the excitation frequency from 0.675 Hz to 0.755 Hz the coordinate θ_{n23} sees levels of deflections similar to those at the beginning of the experimental frequency response in Figure 7.8b. With a further increase in the excitation frequency the deflection of the coordinate θ_{n23} increases until it jumps up to a higher deflection value of 53.9° at an excitation frequency value of 0.935 Hz. Until the excitation frequency of 1.08 Hz is exceeded the deflection of the coordinate θ_{n23} gradually increases and then jumps down to a deflection value of the coordinate θ_{n23} of around 18° with a further increase in the excitation frequency. The coordinate the numerically reproduction of the coordinate θ_{23} shows the same initial random appearing deflections and the hardening effect of the experimental results.

Figure 7.9 shows frequency responses for the numerical and experimental examined pendulum energy harvester in the high power take-off mode with a pendulum length of 0.35 m. The experimentally determined frequency responses in Figures 7.9a and 7.9b are repetitions of the experimental frequency responses shown in Figure 6.21. They show the experimental frequency responses for the pendulum energy harvester in the high power take-off mode that is excited with an excitation amplitude of $A = 48$ mm. The experimental frequency responses are examined in greater detail in Section 6.4 and is therefore not repeated here.

In Figures 7.9c and 7.9d the numerically determined frequency responses are shown. In the numerically determined frequency responses the omnidirectional pendulum energy harvester is excited with a value of the theoretical excitation amplitude of $a_u = 0.314286$ which transforms to an experimental excitation amplitude of $A = 110$ mm which is an increase in the excitation amplitude by around 2.3 times. The dimensionless power take-off torque is set to a medium value of $P_\theta = 0.0330964$.

The frequency response for the numerically determined coordinate θ_{n14} is shown in Figure 7.9c. For a range of excitation frequency from 0.5 Hz to 0.765 Hz the deflection of the coordinate θ_{n14} gradually increases. At an excitation frequency of 0.765 Hz the coordinate θ_{n14} reaches its global maximum of 62.0°. Until the excitation frequency of 0.89 Hz is reached the deflection of the coordinate θ_{n14} decreases. At a value of the excitation frequency of 0.94 Hz the deflection of the coordinate θ_{n14} jumps up to a value of 45.3°. With a further increase in the excitation frequency the deflection of the coordinate θ_{n14} increases and reaches its maximum of 54.6° at a value of the excitation frequency of 1.06 Hz. When this excitation frequency is further increased the deflection of the coordinate θ_{n14} jumps down to a value between 20° and 30°.

Figure 7.9d shows the theoretical frequency response for the coordinate θ_{n23}. For a value of the excitation frequency from 0.5 Hz to 0.68 Hz the coordinate θ_{n23} shows no deflection. Until the excitation frequency of 0.76 Hz is exceeded the system shows similar deflections to those in the experimental frequency response in Figure 7.9b. With a further increase in the excitation

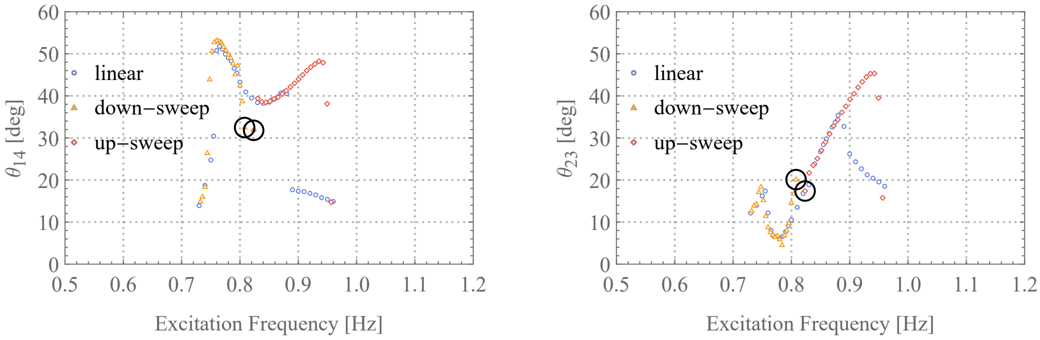

(a) Experimental frequency response of the coordinate θ_{14}

(b) Experimental frequency response of the coordinate θ_{23}

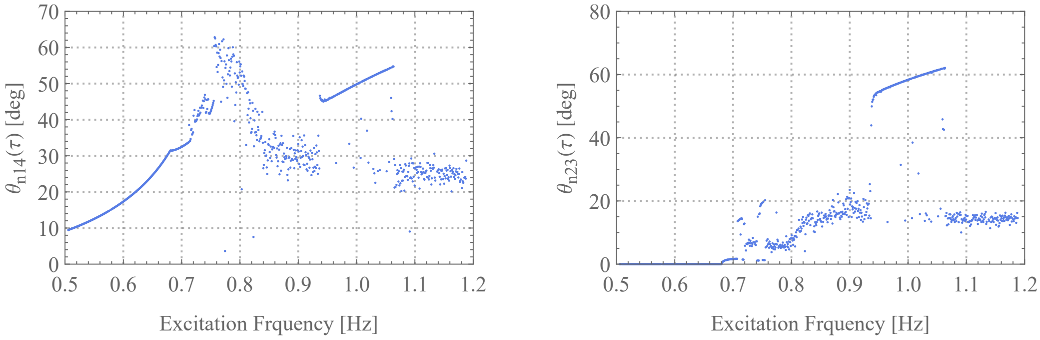

(c) Numerical frequency response of the coordinate θ_{n14}

(d) Numerical frequency response of the coordinate θ_{n23}

Figure 7.9: Experimental and numerical frequency responses for the pendulum energy harvester in the high power take-off mode. The values for the numerical analysis are: $l = 0.35$ m, $m = 1.32$ kg, $g = 9.81\ \frac{\mathrm{m}}{\mathrm{s}^2}$, $\alpha_\theta = \alpha_\phi = 0.0712$, $a_u = 0.314286$, $a_v = a_w = 0$, $P_\theta = 0.0330964$, and $P_\phi = 0$. The parameters of the experimental evaluation of the pendulum energy harvester are: $l = 0.35$ m, $m = 1.32$ kg, $\alpha_{offset} = 45°$, $A = 48$ mm, $\xi_{14} = 0.0373$, $\xi_{23} = 0.0339$, $R_P = 10\ \Omega$, and $R_S = 0\ \Omega$.

frequency the deflection of the coordinate θ_{n23} increases gradually. At a value of the excitation frequency of 0.936 Hz the deflection of the coordinate θ_{n23} jumps up to a value of 54.1°. From there on the deflection increases until reaching its maximum deflection of 62.0° at a value of the excitation frequency of 1.06 Hz. With a further increase in the excitation frequency the deflection of the coordinate θ_{n23} jumps down to a value close to 15°.

Both numerically determined frequency responses show the main characteristics of the experimental frequency responses.

In Figure 7.10 numerically determined frequency responses for the pendulum energy harvester in the low power take-off mode are shown. Since the dynamics of the system are highly dependent on the damping ratios different values for the damping ratios are examined here. The damping ratios are arbitrary selected to values 6.7 %, 15.2 %, and 18 % higher than the damping ratio in the low power take-off mode of the experimental evaluation with a pendulum

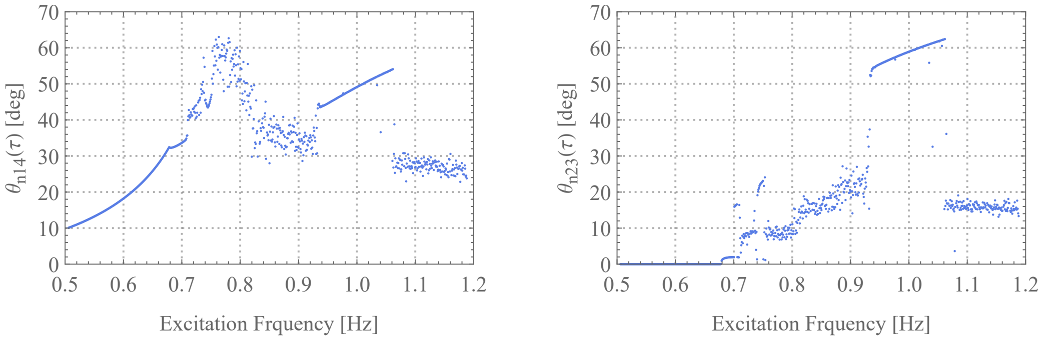

(a) Numerical frequency response of the coordinate θ_{n14} with $\alpha_\theta = \alpha_\phi = 0.076$

(b) Numerical frequency response of the coordinate θ_{n23} with $\alpha_\theta = \alpha_\phi = 0.076$

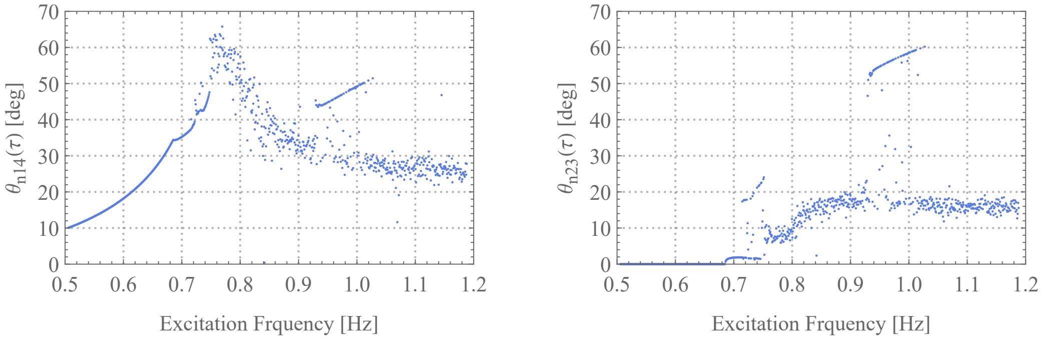

(c) Numerical frequency response of the coordinate θ_{n14} with $\alpha_\theta = \alpha_\phi = 0.082$

(d) Numerical frequency response of the coordinate θ_{n23} with $\alpha_\theta = \alpha_\phi = 0.082$

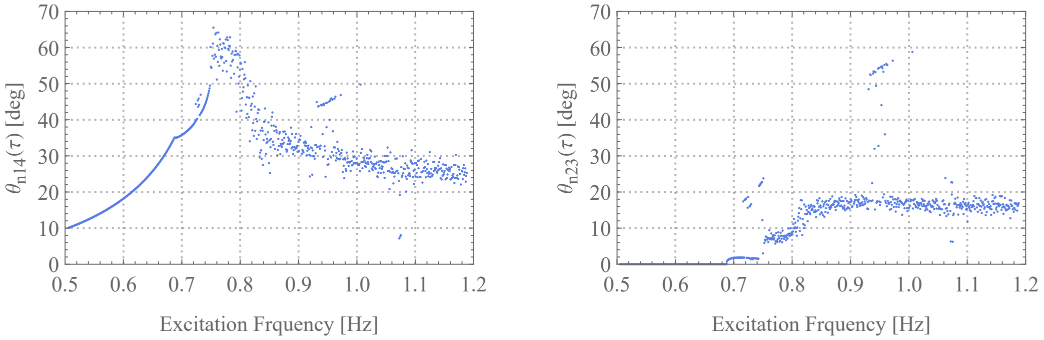

(e) Numerical frequency response of the coordinate θ_{n14} with $\alpha_\theta = \alpha_\phi = 0.084$

(f) Numerical frequency response of the coordinate θ_{n23} with $\alpha_\theta = \alpha_\phi = 0.084$

Figure 7.10: Numerical frequency responses for the pendulum energy harvester. The values for the numerical analysis are: $l = 0.35$ m, $m = 1.32$ kg, $g = 9.81\ \frac{\mathrm{m}}{\mathrm{s}^2}$, $a_u = 0.314286$, $a_v = a_w = 0$, $P_\theta = 0$, and $P_\phi = 0$.

length of 0.35 m. The excitation amplitude is selected to a value of $a_u = 0.314286$ which is a value of $A = 110$ mm in dimensionalised terms and is therefore only reachable theoretically.

The damping ratio is selected to a value of $\alpha_\theta = \alpha_\phi = 0.076$ in Figures 7.10a and 7.10b. In Figure 7.10a the thoretical frequency response for the coordinate θ_{n14} is shown. For a value of the excitation frequency from 0.5 Hz to 0.76 Hz the deflection of the coordinate θ_{n14} gradually increases and reaches its maximum deflection of 63.0° at a value of the excitation frequency of 0.76 Hz. With a further increase in the excitation frequency the deflection of the coordinate θ_{n14} decreases until the excitation frequency of 0.928 Hz is exceeded where the deflection jumps up to a higher deflection value of 43.5°. The deflection of the coordinate θ_{n14} gradually increases with a further increase in the excitation frequency and reaches its maximum deflection of 53.9° for a value of the excitation frequency of 1.06 Hz. With a further increase in the excitation frequency the deflection of the coordinate θ_{n14} jumps down to a value of around 30° and continues to slightly decrease for the rest of the shown frequency range.

Figure 7.10b shows the theoretical frequency response for the coordinate θ_{n14}. Until the excitation frequency of $\Omega = 0.68$ Hz is exceeded the coordinate θ_{n23} shows no deflection. For a range of excitation frequency from 0.68 Hz to 0.77 Hz coordinate θ_{n23} shows deflection values which are similar to the experimentally observed values. With a further increase in the excitation frequency the deflection of the coordinate θ_{n23} increases as well until jumping up to a higher deflection value of 54.1° at an excitation frequency of 0.935 Hz. Onward the deflection further increases and reaches its maximum of $\theta_{n23} = 62.7°$ for a value of the excitation frequency of 1.06 Hz. With a further increase in the excitation frequency the deflection jumps down to a value of the coordinate θ_{n23} of around 15°. And continues to decrease with a further increase in the excitation frequency.

In Figure 7.10c the theoretical frequency response for the coordinate θ_{n14} with an increased damping ratio of $\alpha_\theta = \alpha_\phi = 0.082$ is shown. The deflection of the coordinate θ_{n14} sees a gradual increase in deflection with an increase in the excitation frequency until reaching its maximum of 63.7° at an excitation frequency of 0.765 Hz. After the maximum is passed the deflection of the coordinate θ_{n14} decreases with an increase in the excitation frequency. At a value of the excitation frequency of 0.93 Hz the deflection jumps up to a higher value of $\theta_{n14} = 43.7°$ and gradually increases in value with an increase in the excitation frequency. The second local maximum with a value of 52.3° is reached for an excitation frequency of 1.04 Hz. With a further increase in the excitation frequency the deflection of the coordinate θ_{n14} jumps down to a value of 25° to 30°. For the rest of the shown frequency range the deflection of the coordinate θ_{n14} decreases.

The theoretical frequency response for the coordinate θ_{n23} with an increased damping ratio of $\alpha_\theta = \alpha_\phi = 0.082$ is shown in Figure 7.10d. For a range of excitation frequency from $\Omega =$ 0.5 Hz to 0.68 Hz the coordinate θ_{n23} shows no deflection. This is followed by an area where the diagram shows different deflection values comparable to the experimental results. For a value of the excitation frequency of 0.93 Hz the deflection of the coordinate θ_{n23} jumps up to a value of 51.1° and gradually increases from there on with an increase in the excitation frequency until reaching its maximum deflection of 60.8° at a value of the excitation frequency of 1.04 Hz. When this maximum deflection is exceeded the deflection jumps down to a deflection value of around 15° and stays constant for the rest of the shown excitation frequency.

In Figure 7.10e the theoretical frequency response for the coordinate θ_{n14} with an increased damping ratio of $\alpha_\theta = \alpha_\phi = 0.084$ is shown. The deflection of the coordinate θ_{n14} increases over a range of the excitation frequencies from 0.5 Hz to 0.768 Hz. The maximum deflection of the coordinate $\theta_{n14} = 64.06^\circ$ is reached at an excitation frequency of 0.768 Hz. With a further increase in the excitation frequency the deflection of the coordinate θ_{n14} decreases gradually. The hardening effect that can be seen in the two figures above almost vanishes with the selected damping ratio.

Figure 7.10f shows the theoretical frequency response for the coordinate θ_{n23} with a damping ratio of $\alpha_\theta = \alpha_\phi = 0.084$. Until the excitation frequency of $\Omega = 0.69$ Hz is exceeded the coordinate θ_{n23} shows no deflection. From there on the coordinate θ_{n23} shows deflection values similar to the experimental investigation until the excitation frequency of 0.756 Hz is exceeded. With a further increase in the excitation frequency the deflection of the coordinate θ_{n23} increases to a value of around 15° at an excitation frequency of 0.87 Hz. This value stays constant for the rest of the shown excitation frequency. For a range of excitation frequency from 0.93 Hz to 0.97 Hz a few points with a higher deflection can be seen similarly to the figures with a lower damping ratio above.

From the theoretical frequency responses in Figure 7.10 it can be concluded that with an increase of the damping ratios the hardening characteristics of the spherical pendulum energy harvester decrease. They even disappear completely when the damping ratios are increased further than a value of $\alpha_\theta = \alpha_\phi = 0.084$. Therefore it is evident that the damping ratio highly influences the hardening effect in the numerical analysis.

The theoretical dynamics of the omnidirectional pendulum energy harvester are not only dependent on the damping ratios but on the excitation amplitude as well. The influence of the different excitation amplitudes is examined in the following. In Figure 7.11 the theoretical frequency responses of the coordinate θ_{n14} and θ_{n23} are shown. In each row the excitation amplitude is increased to a higher value.

The theoretical frequency response for the coordinate θ_{n14} with an excitation amplitude of $a_u = 0.285714$ is shown in Figure 7.11a. This excitation amplitude is equivalent to a value of $A = 100$ mm and is therefore lower than the excitation amplitudes that are observed in Figure 7.8, 7.9, and 7.10 with having a value of 110 mm. For a range of excitation frequency from 0.5 Hz to 0.77 Hz the coordinate θ_{n14} increases gradually. The maximum deflection of the coordinate θ_{n14} of 66.06° is reached at an excitation frequency of 0.77 Hz. After the maximum is passed the deflection of the coordinate θ_{n14} decreases gradually. The hardening effect can be seen in between for a range of excitation frequencies from 0.938 Hz to 0.98 Hz and this results in an increase in the deflection of the coordinate θ_{n14}. With a further increase in the excitation frequency the deflection of the coordinate θ_{n14} jumps down to a lower deflection value and then decreases with a further increase in the excitation frequency.

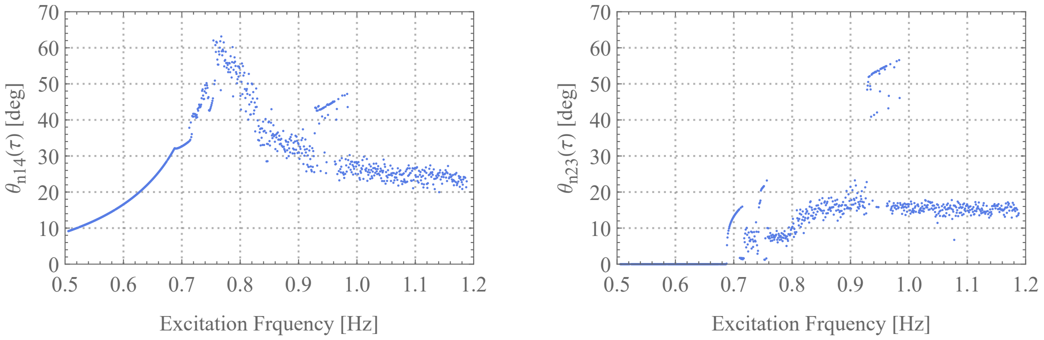

(a) Numerical frequency response of the coordinate θ_{n14} with $a_u = 0.285714$

(b) Numerical frequency response of the coordinate θ_{n23} with $a_u = 0.285714$

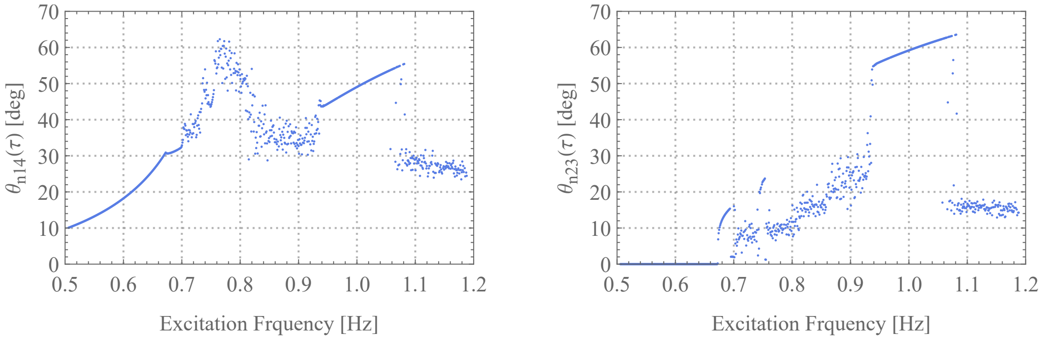

(c) Numerical frequency response of the coordinate θ_{n14} with $a_u = 0.314286$

(d) Numerical frequency response of the coordinate θ_{n23} with $a_u = 0.314286$

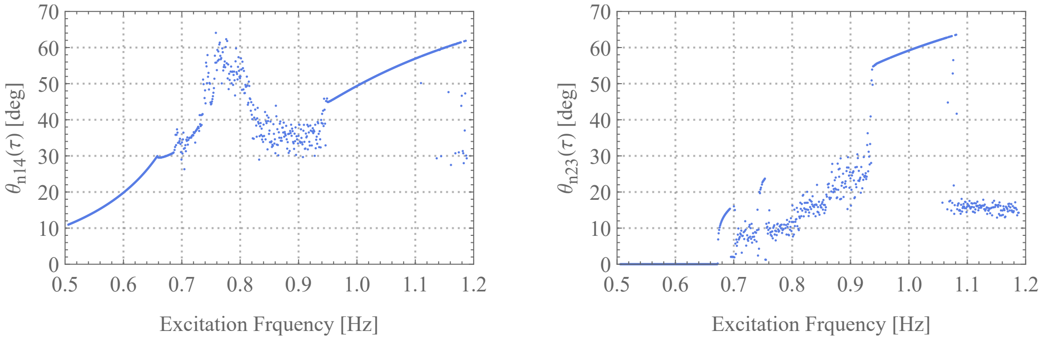

(e) Numerical frequency response of the coordinate θ_{n14} with $a_u = 0.342857$

(f) Numerical frequency response of the coordinate θ_{n23} with $a_u = 0.342857$

Figure 7.11: Numerical frequency responses for the pendulum energy harvester. The values for the numerical analysis are: $l = 0.35$ m, $m = 1.32$ kg, $g = 9.81\ \frac{\text{m}}{\text{s}^2}$, $\alpha_\theta = \alpha_\phi = 0.0712$, $a_v = a_w = 0$, $P_\theta = 0$, and $P_\phi = 0$.

In Figure 7.11b the theoretical frequency response for the coordinate θ_{n23} for a value of the excitation amplitude of $a_u = 0.285714$ is shown. The coordinate θ_{n23} shows no deflection until a value of the excitation frequency of 0.69 Hz is exceeded. For a range of excitation frequency from 0.69 Hz to 0.76 Hz the coordinate θ_{n23} shows similar dynamics to those of the experimentally determined coordinate θ_{23}. With a further increase in the excitation frequency the deflection of the coordinate θ_{n23} increases gradually until jumping up to a higher deflection value of 52.51° at a value for the excitation frequency of 0.94 Hz. With a further increase in the excitation frequency the deflection of the coordinate θ_{n23} increases and reaches its maximum deflection of 56.3° at a value of the excitation frequency of 0.98 Hz. Afterwards, the deflection jumps down to a value close to 15° which remains constant for the rest of the shown excitation frequency range.

In Figures 7.11c and 7.11d the excitation amplitude is increased to a value of $a_u = 0.314286$. These figures are repetitions of Figures 7.8c and 7.8d and detailed discussion can be found in the text related to these figures. The figures were included to directly allow a comparison for an increase in the excitation amplitude.

The theoretical frequency response for the coordinate θ_{n14} with an excitation amplitude $a_u = 0.342857$ of is shown in Figure 7.11e. For a range of excitation frequency from 0.5 Hz to 0.758 Hz the deflection gradually increases and the maximum deflection of the coordinate θ_{n14} of 64.07° is reached at the end of this range. With a further increase in the excitation frequency the deflection of the coordinate θ_{n14} decreases. The deflection starts to rise again after an excitation frequency of 0.9 Hz is exceeded. The deflection of the coordinate θ_{n14} reaches a local maximum of 62.0° at an excitation frequency of 1.185 Hz. With a further increase in the excitation frequency the deflection of the coordinate θ_{n14} jumps down to a lower value.

Figure 7.11f shows the theoretical frequency response for the coordinate θ_{n23} for the spherical pendulum that is excited with an excitation frequency of $a_u = 0.342857$. Until the excitation frequency of 0.73 Hz is exceeded the coordinate θ_{n23} shows no deflection. For a range of excitation frequency from 0.73 Hz to 0.756 Hz the coordinate θ_{n23} shows levels of deflections similar to the experimental investigation in this area. With a further increase in the excitation frequency the deflection of the coordinate θ_{n23} increases gradually. At a value of the excitation frequency of 0.938 Hz the deflection increases strongly for a short-range and then the slope flattens again and gradually increases with an increase in the excitation frequency. The maximum deflection of the coordinate θ_{n23} of 68.73° is reached at $\Omega = 1.19$ Hz. With a further increase in the excitation frequency the deflection of the coordinate θ_{n23} jumps down to a lower value and continues to decrease gradually.

From the theoretical frequency responses in Figure 7.11 it can be seen that a higher excitation amplitude increases the visibility of the hardening effect. With an excitation amplitude lower than $A = 100$ mm the hardening effect cannot be seen anymore for this configuration of parameters. Additionally, it can be seen that the hardening effect can be seen for a longer range of excitation frequencies when the excitation amplitude is higher. It becomes evident that the excitation amplitude of $A = 110$ mm is the first time that the hardening effect can clearly be seen. This is the reason for the excitation amplitude selected in Figures 7.8 and 7.9.

The last parameter that influences the dynamics of the pendulum energy harvester is the power take-off. This is examined here and therefore, in Figure 7.12 the theoretical frequency responses for the coordinates θ_{n14} and θ_{n23} for a variation of the power take-off torque are shown.

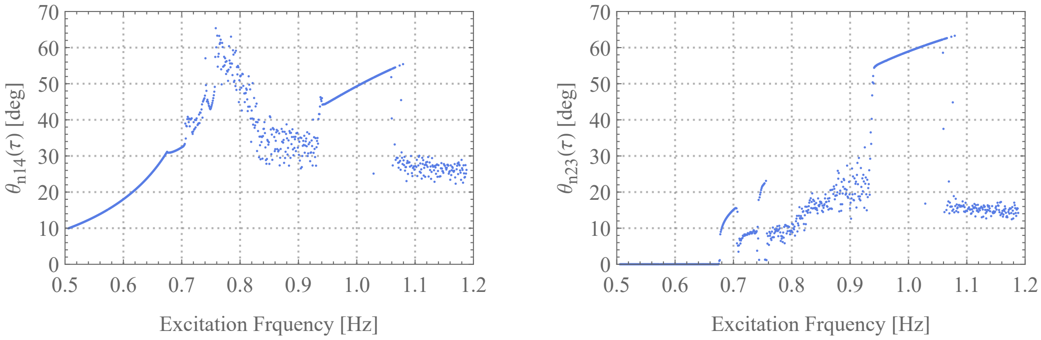

(a) Numerical frequency response of the coordinate θ_{n14} with $P_\theta = 0.0110321$

(b) Numerical frequency response of the coordinate θ_{n23} with $P_\theta = 0.0110321$

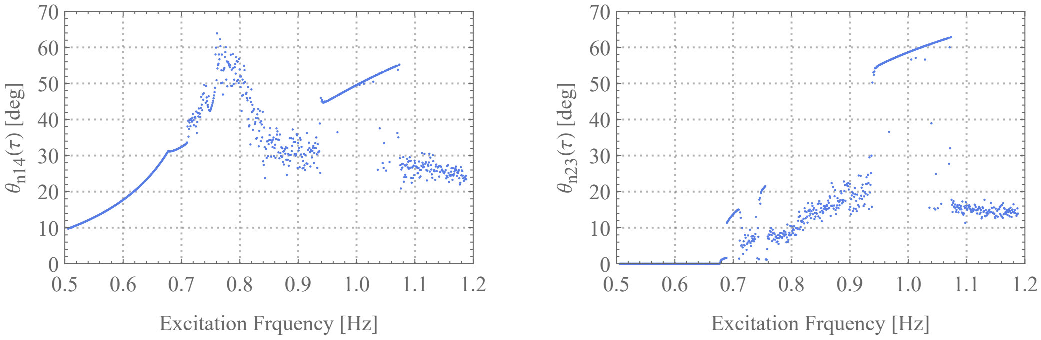

(c) Numerical frequency response of the coordinate θ_{n14} with $P_\theta = 0.0220642$

(d) Numerical frequency response of the coordinate θ_{n23} with $P_\theta = 0.0220642$

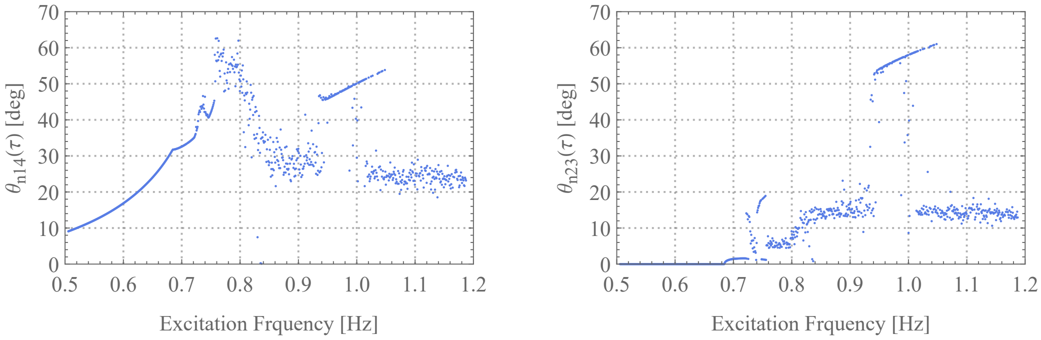

(e) Numerical frequency response of the coordinate θ_{n14} with $P_\theta = 0.0441285$

(f) Numerical frequency response of the coordinate θ_{n23} with $P_\theta = 0.0441285$

Figure 7.12: Numerical frequency responses for the pendulum energy harvester. The values for the numerical analysis are: $l = 0.35$ m, $m = 1.32$ kg, $g = 9.81\ \frac{\mathrm{m}}{\mathrm{s}^2}$, $\alpha_\theta = \alpha_\phi = 0.0712$, $a_u = 0.314286$, $a_v = a_w = 0$, and $P_\phi = 0$.

Figure 7.12a shows the theoretical frequency response for the coordinate θ_{n14} with a power take-off torque of $P_\theta = 0.0110321$. For a value of the excitation frequency from 0.5 Hz to 0.758 Hz the deflection of the coordinate θ_{n14} increases. The maximum deflection of 65.38° is reached at a value of the excitation frequency of 0.758 Hz. With a further increase in the excitation frequency the deflection of the coordinate θ_{n14} decreases and reaches a local minimum at around 0.9 Hz. Afterwards the deflection increases and reaches a local maximum of 55.07° at a value of the excitation frequency of 1.08 Hz. With a further increase in the excitation frequency the deflection of the coordinate θ_{n14} jumps down to a value close to 25°. For the rest of the shown excitation frequency the deflection of the coordinate θ_{n14} decreases gradually with an increase in the excitation frequency.

The theoretical frequency response for the coordinate θ_{n23} with a power take-off torque of $P_\theta = 0.0110321$ is shown in Figure 7.12b. The coordinate θ_{n23} shows no deflection until the excitation frequency of 0.676 Hz is exceeded. In the following range of excitation frequencies up to a value of 0.76 Hz the coordinate θ_{n23} shows different values of deflection that appear to follow no clear trend, this is similar to the in the experimentally determined frequency response observed results. The deflection of the coordinate θ_{n23} increases gradually until the excitation frequency of 0.92 Hz is exceeded where the slope of the decrease becomes very steep for a short while and then returns to a smaller slope subsequently. For a value of the excitation frequency of 1.075 Hz the theoretical frequency response shows a maximum deflection of the coordinate θ_{n23} of 63.09°. After the maximum is passed the deflection jumps down to a lower value of around 15°. With a further increase in the excitation frequency the deflection of the coordinate θ_{n23} decreases gradually.

In Figure 7.12c the numerical frequency response for the coordinate θ_{n14} with an increased value of the power take-off torque of $P_\theta = 0.0220642$ is shown. The deflection of the coordinate θ_{n14} gradually increases for a range of excitation frequencies from 0.5 Hz to 0.767 Hz. For a value of the excitation frequency of 0.767 Hz the maximum deflection of the coordinate θ_{n14} of 60.33° is reached. With a further increase in the excitation frequency the deflection of the coordinate θ_{n14} decreases and reaches a local minimum at a value of the excitation frequency of around 0.9 Hz. The deflection of the coordinate θ_{n14} jumps up to a value of 44.4° for a value of the excitation frequency of 0.94 Hz and gradually increases with an increase in the excitation frequency. Another local maximum of 55.3° is reached at a value of the excitation frequency of 1.08 Hz. With a further increase in the excitation frequency the deflection of the coordinate θ_{n14} jumps down to a deflection value of around 25° and decreases gradually with an increase in the excitation frequency.

Figure 7.12d shows the numerical frequency response for the coordinate θ_{n23} with an increased value of the power take-off torque of $P_\theta = 0.0220642$. Until the excitation frequency of 0.68 Hz is exceeded the coordinate θ_{n23} show no deflection. In the range of the excitation frequency from 0.68 Hz to 0.76 Hz the deflection of the coordinate θ_{n23} shows different deflection values that do not seem to follow any pattern, this is similar to the experimental examined results. With a further increase in the excitation frequency the deflection of the coordinate θ_{n23} increases as well until jumping up to a higher deflection of the coordinate θ_{n23} of 54.1° at $\Omega = 0.945$ Hz. The deflection continues to increase with an increase in the excitation frequency and reaches a local maximum of 62.83° at a value of the excitation frequency of 1.07 Hz. With a further increase in the excitation frequency the deflection of the coordinate θ_{n23} jumps down to a value of around 15° and decreases gradually.

The theoretical frequency response for the coordinate θ_{n14} with a power take-off torque of $P_\theta = 0.0441285$ is shown in Figure 7.12e. Until the excitation frequency of $\Omega = 0.77$ Hz is exceeded the deflection of the coordinate θ_{n14} increases gradually and reaches its maximum deflection of 65.1° at this point. With a further increase in the excitation frequency the deflection of the coordinate decreases and reaches a local minimum at an excitation frequency of around 0.9 Hz. At a value of the excitation frequency of 0.94 Hz the deflection of the coordinate θ_{n14} jumps up to a deflection value of 45.4° and increases onwards with an increase in the excitation frequency. Another local maximum of $\theta_{n14} = 54.1°$ is reached at an excitation frequency of $\Omega = 1.05$ Hz. With a further increase in the excitation frequency the deflection of the coordinate θ_{n14} jumps down to a value of around 25° and decreases gradually onwards with a further increase in the excitation frequency.

In Figure 7.12f the numerical frequency response for the coordinate θ_{n23} with a power take-off torque of $P_\theta = 0.0441285$ is shown. The coordinate θ_{n23} shows no deflection until a value for the excitation frequency of 0.68 Hz is exceeded. For a range of excitation frequency from 0.68 Hz to 0.76 Hz the coordinate θ_{n23} shows defections that do not follow any particular pattern similar to those in the experimental investigation. The deflection continues to rise with an increase in the excitation frequency until reaching an excitation frequency of 0.936 Hz where the deflection of the coordinate θ_{n23} jumps up to a value of 53.2°. With a further increase in the excitation frequency the deflection of the coordinate continues to increase until seeing a maximum deflection of 61.1° at a value of the excitation frequency of 1.05 Hz. The high deflection jumps down to a deflection of around 15° and continues to decrease with a further increase in the excitation frequency.

From the theoretical frequency response in Figure 7.12 it can be concluded that the increase in the power take-off torque mainly shortens the hardening branch of the theoretical frequency response and therefore reduces the operational range of the pendulum energy harvester slightly. With a power take-off torque higher than $P_\theta = 0.057367$ the hardening effect completely disappears and therefore drastically less energy can be drawn from the system in this area.

It is evident that the theoretical frequency responses are highly dependent on the excitation frequency, damping ratios and the power take-off torque. With an adapted selection of these parameters the general characteristics of the experimental frequency responses can be reproduced with the numerical computation. The coordinate θ_{n14} shows a theoretical frequency response with two local maxima and a local minimum in-between similar to those in the experiments. This includes the hardening characteristics that are observed in the experiments as well. This applies to both coordinates. Additionally, it can be seen that similar to the experimental examination at the beginning of the frequency responses the spherical pendulum shows the dynamics of a simple pendulum, where only shaft 14 shows a deflection. This is followed by a transformation to dynamics that represent the trajectory of a conical pendulum during the operation on the hardening branch. The selection of the high excitation amplitude is therefore responsible for the high levels of deflections of coordinate θ_{n23} on the hardening branch. It can be concluded the numerical investigation with a higher excitation amplitude shows all the characteristics of the experimentally determined frequency responses.

Chapter 8

Towards an Application of the Omnidirectional Pendulum Energy Harvester

The energy harvester discussed in this thesis is a pre-prototype, therefore it is crucial to define the next steps toward applications for the energy harvester.

8.1 Possible Areas of Application

The omnidirectional pendulum energy harvester can be used in various areas of application. According to the application the physical size of the energy harvester changes. In the following discussion two different applications are proposed at the small and large ends of the size spectrum. In Figure 8.1 an earring pendulum energy harvester is shown. The idea behind this concept is to power a hearing aid by utilising the movement of the person who is wearing the earring. The combination of a medical device and a mode fashionable accessory has the potential to motivate people to tackle their hearing problems earlier and remove the stigma of hearing aids being devices for pensioners. Additionally, the device can be used to monitor the fitness levels of the user by calculating the number of steps. This can have an overall positive effect on the health of the user.

An application at the other end of the size spectrum is a wave energy harvester, see Figure 8.2. A large-scale device can be used to convert energy from sea waves. This can be used purely as an energy harvesting device or it is possible to use the energy harvester as an additional power supply for a self-sustained monitoring buoy. This can be used to substitute phases in which photovoltaic cells do not produce enough electricity. A monitoring buoy can collect civil data like weather data, water quality, tidal measurements, and wave measurements.

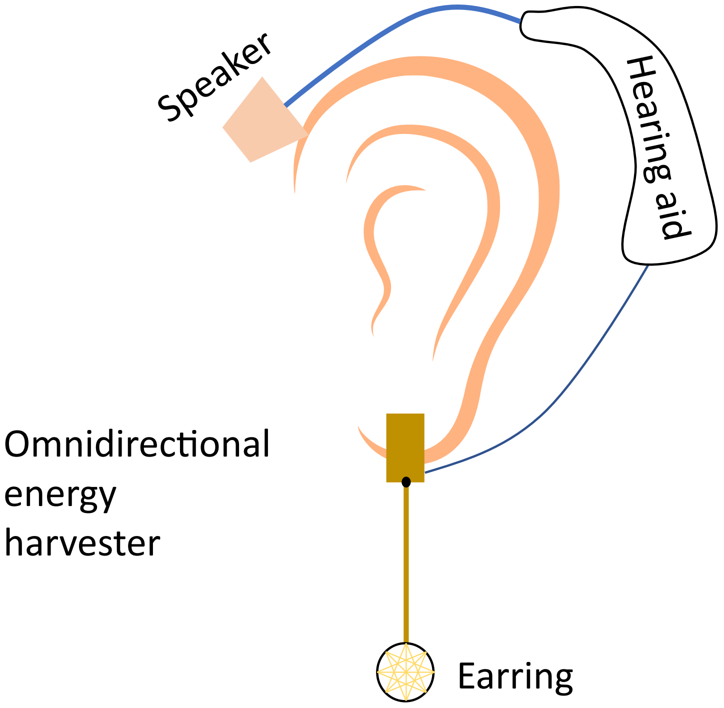

Figure 8.1: Application of the omnidirectional pendulum energy harvester as a self-sustained hearing aid with earring

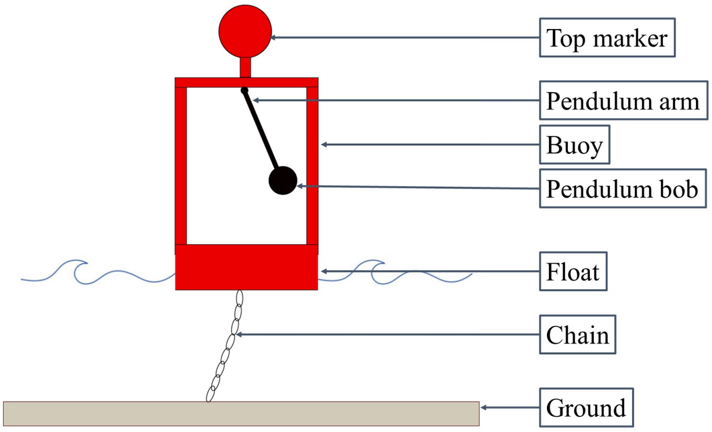

Figure 8.2: Application of the omnidirectional pendulum energy harvester as a wave energy harvester

8.2 Different Control Strategies of the Power Take-Off for the Energy Harvester

The electrical load of the energy harvester discussed in this work is implemented with the most economic option possible which is a resistor that can be replaced accordingly to apply different electrical loads see Figure 3.5 in the methodology section. This however means that the power take-off is constantly applied to the energy harvester. Even though this is sufficient for the observed experiments it has two main downsides.

Firstly, the power take-off is applied constantly over the whole operational area even at the start of the excitation where the dynamics of the energy harvester are showing transient dynamics. Therefore, an optimal operational point may be reached later than otherwise possible. Secondly, in low deflections of the energy harvester the power take-off is applied as well and in some cases this results in a complete stop of the oscillation of the pendulum bob. This decreases the efficiency of the energy harvester as well. Additionally, the operational range of the energy harvester is within a narrow frequency range. It would be advantageous to be able to move the frequency response along the frequency axis to the optimum point, to accommodate for different excitation frequencies. To increase the efficiency of the energy harvester a control is necessary. Different scholars have observed the optimisation and control of various energy harvesters and these are reviewed in the theory Section 2.4 of this thesis. Different theoretical approaches for an optimised power take-off control strategy for the omnidirectional energy harvester are discussed in the following three sections.

8.2.1 Switching Control with Three Conditions

From the theory Section 2.4 on the electrical power take-off a few general conclusions for an optimised electrical power take-off for the omnidirectional energy harvester can be drawn. It is important to be able to control the speed or the power take-off of the generators. This allows the operation of the energy harvester to be based on the highest possible deflections and velocity.

For an optimised power take-off of the omnidirectional pendulum energy harvester three general conditions are defined that always need to be fulfilled. Firstly, the coordinates θ_{14} and θ_{23} should always have a higher deflection than a definable lower switching off limit. This is because for low deflection values the load due to the requested power output can completely cancel out the oscillations of the pendulum. Therefore, it is advantageous only to convert energy when the maximum deflection angle is higher than a definable lower switch off limit. In this first case an arbitrary value of 20° is selected as the lower switch off limit. This value is from here on referred to as the lower switch off limit. The lower switch off limit prevents the movement of one or both shafts to be damped too strongly, which would cause the oscillation to stop. Therefore the power take-off should be switched off completely for the shaft whose deflection is lower than 20°. It should be assessed whether it is sensible that for different deflection angles different levels of power take-off torques should applied see Section 8.2.2. The second condition is that during the transient response the power take-off is switched off. This can be applied easily with a timer but a threshold for deflections of the shaft is possible as well. The third condition is a safety feature that prevents against the destruction of the energy harvester. The maximum possible deflection value is dependent on the length of the pendulum. For a pendulum length of 0.5 m the maximum deflection value gets higher than 52.3°. This is from here on referred to as the safety limit. The conditions for the control strategy are shown

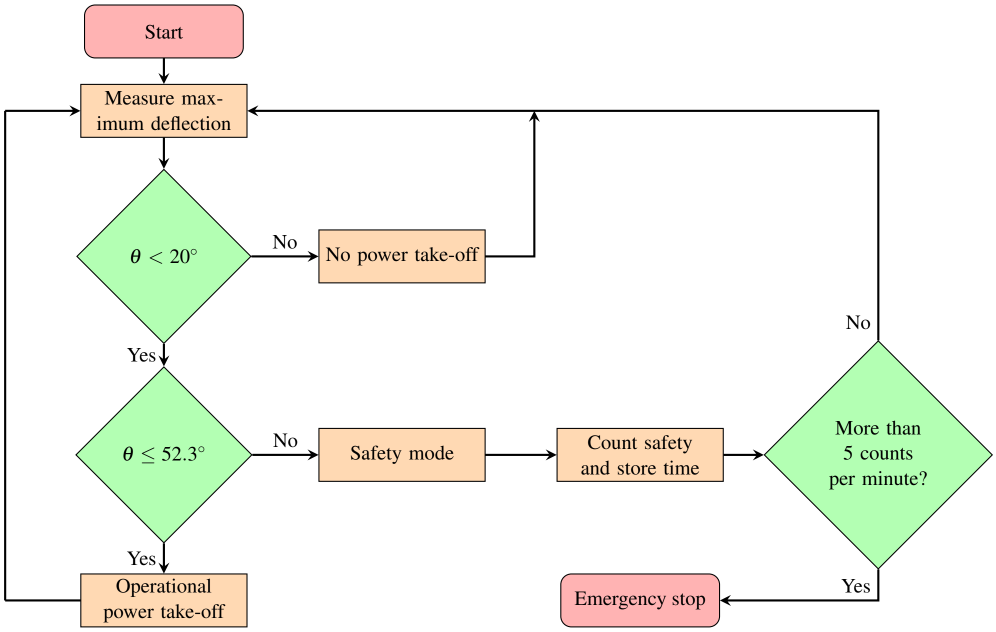

Figure 8.3: Conditions for an optimised power take-off flow chart with three conditions

in the flow chart see Figure 8.3.

The differential Equations (4.36) and (4.37) are extended by two terms $a(\tau)$ and $b(\tau)$ see Equations (8.1) and (8.2). With these terms the numerical integration within the NDSolve tool in *Wolfram Mathematica*® can directly be influenced. The terms $a(\tau)$ and $b(\tau)$ are from now on referred to using terminology from *Mathematica*®, as discrete variables. These variables are used for the controlled power take-off as described in the flow chart in Figure 8.3. Where the discrete variable $a(\tau)$ controls the level of the power take-off and the variable $b(\tau)$ simulates an emergency brake to bring the energy harvester into safety mode. This is done by increasing the damping ratios by a factor of 10 and doubling the power take-off torque. When the deflection of the coordinate θ gets higher than 52.3° the safety break applies, this is simulated in the damping term of the differential equations. The ordinary differential equations with the discrete variables are shown in Equations (8.1) and (8.2).

$$\begin{aligned}&\ddot{\theta}(\tau)+b(\tau)\alpha_\theta\dot{\theta}(\tau)-\sin(\theta(\tau))\cos(\theta(\tau))\dot{\phi}(\tau)^2+\sin(\theta(\tau))\\&\quad=-a_u\beta_u^2\cos(\theta(\tau))\sin(\phi(\tau))\cos(\beta_u\tau)+a_v\beta_v^2\cos(\theta(\tau))\cos(\phi(\tau))\cos(\beta_v\tau)\\&\quad+a_w\beta_w^2\sin(\theta(\tau))\cos(\beta_w\tau)-a(\tau)\frac{2P_\theta}{\pi}\tan^{-1}\left(\frac{\dot{\theta}(\tau)}{\varepsilon_r}\right).\end{aligned} \tag{8.1}$$

$$
\begin{aligned}
\ddot{\phi}(\tau) + b(\tau)\frac{\alpha_\phi}{\sin^2(\theta(\tau))}\dot{\phi}(\tau) + \frac{2\dot{\theta}(\tau)\cos(\theta(\tau))\dot{\phi}(\tau)}{\sin(\theta(\tau))} \\
= -a_u\beta_u^2\frac{\cos(\phi(\tau))}{\sin(\theta(\tau))}\cos(\beta_u\tau) - a_v\beta_v^2\frac{\sin(\phi(\tau))}{\sin(\theta(\tau))}\cos(\beta_v\tau) \\
- a(\tau)\frac{2P_\phi}{\pi\sin^2(\theta(\tau))}\tan^{-1}\left(\frac{\dot{\phi}(\tau)}{\varepsilon_\mathrm{r}}\right).
\end{aligned}
\tag{8.2}
$$

In Figure 8.4 the *Mathematica*® code for an NDSolve function following the flow chart in Figure 8.3 is shown. The first line shows the input of Equations (8.1) and (8.2). In the second

```
NDSolve[{equation1, equation2,
  θ[0] == IC, ϕ[0] == IC, θ'[0] == IC, ϕ'[0] == IC,
  a[0] == 1, b[0] == 1,
  WhenEvent[θ'[t] == 0 && RealAbs[θ[t]] < 0.35,
   {a[t] → 0, b[t] → 1}],
  WhenEvent[θ'[t] == 0 && 0.91 ≥ RealAbs[θ[t]] ≥ 0.35,
   {a[t] → 1, b[t] → 1}],
  WhenEvent[θ'[t] == 0 && RealAbs[θ[t]] > 0.91,
   {a[t] → 2, b[t] → 10}]},
 {θ, ϕ, a, b}, {t, 0, tend}, DiscreteVariables → {a, b}]
```

Figure 8.4: Numerical integration strategy of the controlled power take-off with NDSolve

and third line the initial conditions are selected reasonably as defined at the beginning of Section 5. The next following six lines are WhenEvent commands. These commands allow for the switching off and on of the power take-off in accordance with the pre-defined thresholds. In the first WhenEvent the power take-off is switched off when the deflection of the coordinate θ falls below a definable limit in this case 20° (or 0.35 rad). The second WhenEvent describes the activation of the operational power take-off. The last WhenEvent simulates the safety mode where the power take-off and the damping ratios are increased drastically to break down the pendulum bob and bring it to a halt to prevent destruction of the energy harvester. This has no influence on the energy harvesting capabilities but is used purely as a safety feature. The last line of *Mathematica*® code defines the different variables (θ, ϕ, a, and b), the independent variable (dimensionless time τ in this case abbreviated as t), and the discrete variables (a and b).

In Equation (8.3) the power take-off function of the coordinate θ is shown. It is used to visualise the power take-off over the dimensionless time in Figure 8.5.

$$
PTO_{\theta arc}(\tau) = -a(\tau)\frac{2P_\theta}{\pi}\tan^{-1}\left(\frac{\dot{\theta}(\tau)}{\varepsilon_\mathrm{r}}\right). \tag{8.3}
$$

Figure 8.5 shows time responses of the acceleration of the coordinate θ and the power take-off function from Equation (8.3) over the dimensionless time τ. The arithmetic mean rectified power output is calculated as described in Section 5.4 and is shown in the figures. The system

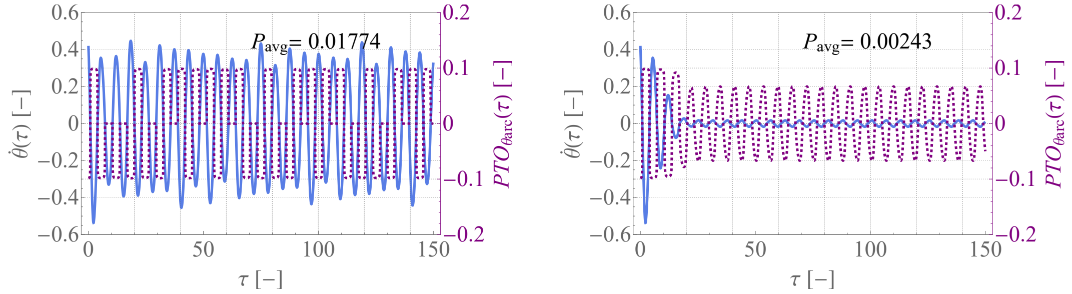

(a) With optimised power take-off $\beta = 1.0$

(b) Without optimised power take-off $\beta = 1.0$

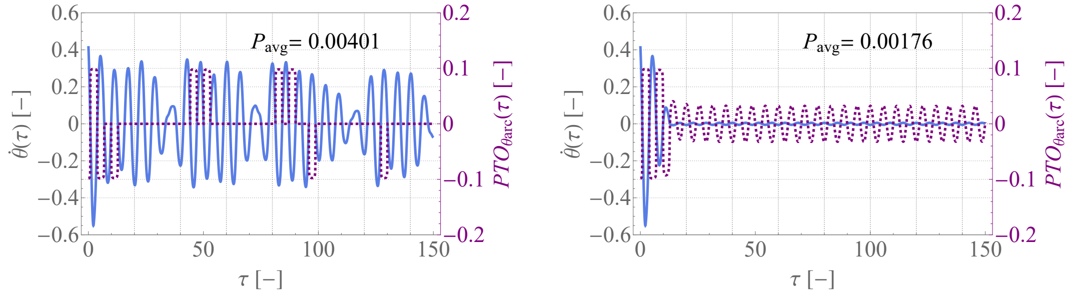

(c) With optimised power take-off $\beta = 1.1$

(d) Without optimised power take-off $\beta = 1.1$

Figure 8.5: Power take-off and velocity of the coordinate θ over τ the parameters set to: $l = 0.5$ m, $m = 1.32$ kg, $g = 9.81\ \frac{\text{m}}{\text{s}^2}$, $\alpha_\theta = \alpha_\phi = 0.0648$, $a_u = a_v = a_w = 0.064$, $\beta_u = \beta_v = 1.0$, $\beta_w = 2.0$, $P_\theta = 0.1$, $P_\phi = 0$, lower switch off limit = 20°, and safety limit = 52.3°.

is excited with relative low excitation amplitudes to prevent the safety break operating. This allows a concentration on the optimisation of the power take-off rather than the operational safety of the energy harvester. In the first row of figures the energy harvester is excited with an excitation frequency of $\beta = 1.0$ and in the second row with an excitation frequency of $\beta = 1.1$. In the left column the energy harvesters' power take-off is optimised and in the right column a constant power take-off torque is applied similar to the numerical Section 5.3 in this work.

In Figure 8.5a the energy harvester is excited with an excitation frequency of $\beta = 1.0$ and the power take-off is controlled. It can be seen that with the optimised power take-off the oscillation of the energy harvester is sustained over the whole time period shown. It can also be seen that the power take-off is switched off when the deflection of the coordinate θ is lower than 20°. The arithmetic mean rectified power output shown over the dimensionless time period is 0.01744.

Figure 8.5b shows the energy harvester that is excited with an excitation frequency of $\beta = 1.0$ and a constant power take-off. The velocity of the coordinate θ is constantly reduced with the power take-off torque and with a τ higher than 20 the velocity is below a level where energy can be sufficiently converted from the energy harvester. The arithmetic mean rectified power output over the shown dimensionless time period is 0.00243.

In Figure 8.5c the energy harvester is excited with an excitation frequency of $\beta = 1.1$. The switching off of the power take-off when the lower limit of 20° is reached sustains the swing of the pendulum arm longer compared to the constant power output in Figure 8.5d. This is clear for the arithmetic mean rectified power output of both systems as well. With the optimised power take-off an arithmetic mean rectified power output of 0.00401 is reached and without the optimised power output an arithmetic mean rectified power output of 0.00176 is achieved.

In the cases shown the direct comparison between the different levels of power output is not significant since in the constant power take-off mode the velocity of the coordinate θ does not show sufficient deflections with a time higher than $\tau = 20$ for $\beta = 1.0$ or $\tau = 15$ for $\beta = 1.1$. Since the power output is a multiplication of the velocity of the coordinate θ and the power take-off torque the arithmetic mean rectified power output becomes close to zero with $\tau > 20$ for $\beta = 1.0$ or $\tau > 15$ for $\beta = 1.1$. Nevertheless, the arithmetic mean rectified power output indicates that the switching control within NDSolve can optimise the power output and sustain the oscillations of the pendulum for longer.

8.2.2 Switching Control with Four Conditions

In this section an additional switching condition is added to the three condition switching control shown in Section 8.2.1. The goal is to further optimise the power take-off algorithm. In Figure 8.6 the flow chart for the four condition switching control is shown. With a deflection angle of the coordinate θ below 10° the power take-off is set to zero. This prevents the load due to the required power take-off to reducing the oscillations of the pendulum in such a way that they are completely stopped. For deflection values of θ from 10° to 20° the power take-off is set to a value of half of the operational power take-off. This is done to get a power output from the energy harvester without it being too high and cancelling out the oscillation. When the deflection of the coordinate θ is between a value of 20° and 52.3° the energy harvester operates with the pre-defined operational power take-off offering a medium load. With an increase in the deflection higher than 52.3° the energy harvester goes into a safety mode to prevent the destruction of the experimental rig. In the safety mode the power take-off is selected to a high value and additionally the damping ratio is increased drastically which simulates an applied braking force. Every time the safety mode is reached a counter stores the amount of the safety modes over the last minutes. If this value is higher than 5 counts per minute it is assumed that the excitation force is currently too high and therefore an emergency stopping procedure is initiated.

In Figure 8.7 the velocity of θ and the power take-off over time is shown for the optimised power take-off control with four conditions and different excitation frequencies. Figure 8.7a

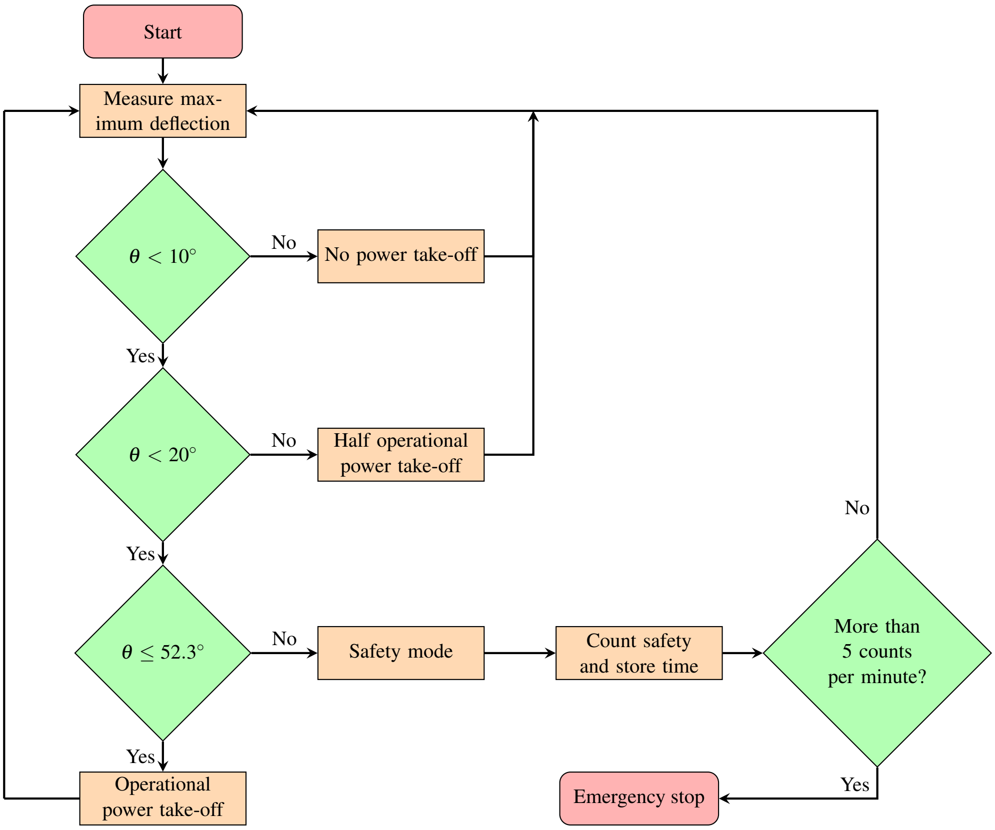

Figure 8.6: Conditions for an optimised power take-off flow chart with three conditions

shows the optimised power take-off with an excitation frequency of $\beta = 1.0$. The switching of power take-off to half its value is observed and over the shown time period the oscillations of $\dot{\theta}(\tau)$ are sustained. Over the shown range the arithmetic mean rectified power output has a value of $P_{avg} = 0.01545$. In Figure 8.7b the energy harvester is forced under the same conditions but the power take-off is applied with a constant power take-off torque. The oscillation of the coordinate $\dot{\theta}(\tau)$ decays fast and with a value for τ higher than 20 almost no significant oscillations of $\dot{\theta}(\tau)$ are observed. Therefore, the arithmetic mean rectified power output is significantly lower with a value of $P_{avg} = 0.00243$.

With an increase in excitation frequency to a value of $\beta = 1.1$ the dynamics of the system change for the optimised power take-off, see Figure 8.7c. The optimised power take-off forces the dynamics of the system in such a way that the velocity values are lower overall and this results in an arithmetic mean rectified power output of $P_{avg} = 0.00232$. In Figure 8.7d the system under the same forcing conditions is shown with a constantly applied power take-off. The oscillations decay fast and the arithmetic mean rectified power output has a value of $P_{avg} = 0.00176$.

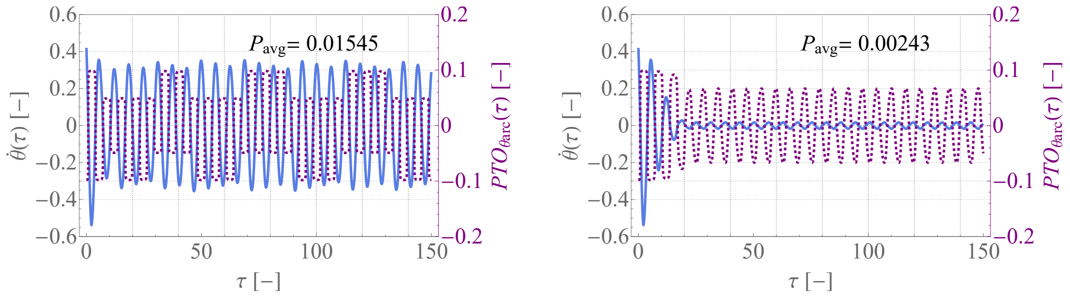

(a) With optimised power take-off with $\beta = 1.0$

(b) Without optimised power take-off with $\beta = 1.0$

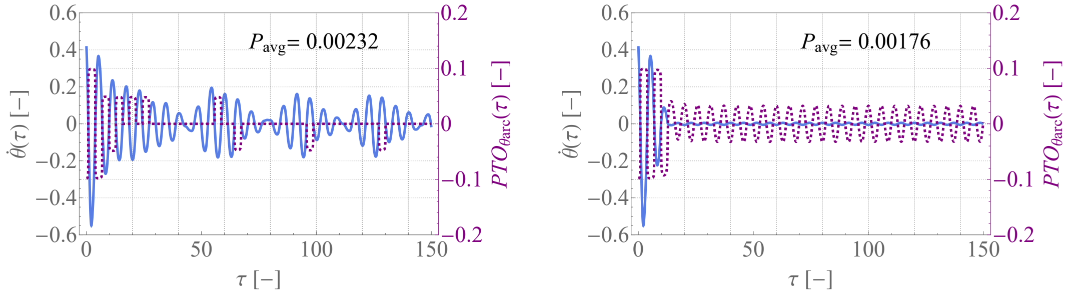

(c) With optimised power take-off with $\beta = 1.1$

(d) Without optimised power take-off with $\beta = 1.1$

Figure 8.7: Power take-off and velocity of the coordinate θ over τ the parameters set to: $l = 0.5$ m, $m = 1.32$ kg, $g = 9.81\ \frac{\text{m}}{\text{s}^2}$, $\alpha_\theta = \alpha_\phi = 0.0648$, $a_u = a_v = a_w = 0.064$, $P_\theta = 0.1$, $P_\phi = 0$, lower switch off limit = 10°, operational power take-off limit = 20°, and safety limit = 52.3°.

It is observed that the introduced additional half power take-off switching limit does not increase the power output of the energy harvester for the forcing conditions shown. Therefore, the switching limits need to be examined in the following.

8.2.3 Comparison of the Different Limits for the Power Take-Off

When comparing Figures 8.5 and 8.7 it is evident that the arithmetic mean rectified power output is reduced with the additionally introduced condition. The limits for the switching on and off of the power take-off torque so far were selected arbitrarily to see the general functionality of the controlled power take-off. Therefore, the switching limits are investigated further in the following section. Figure 8.8 shows the flow chart for the investigation of the lower limit. The upper limit that activates the safety mode is set to 90° to be able to investigate the full potential of the energy harvester[1].

---

[1] This is only theoretically possible because in the experiment the cage restricts high deflections.

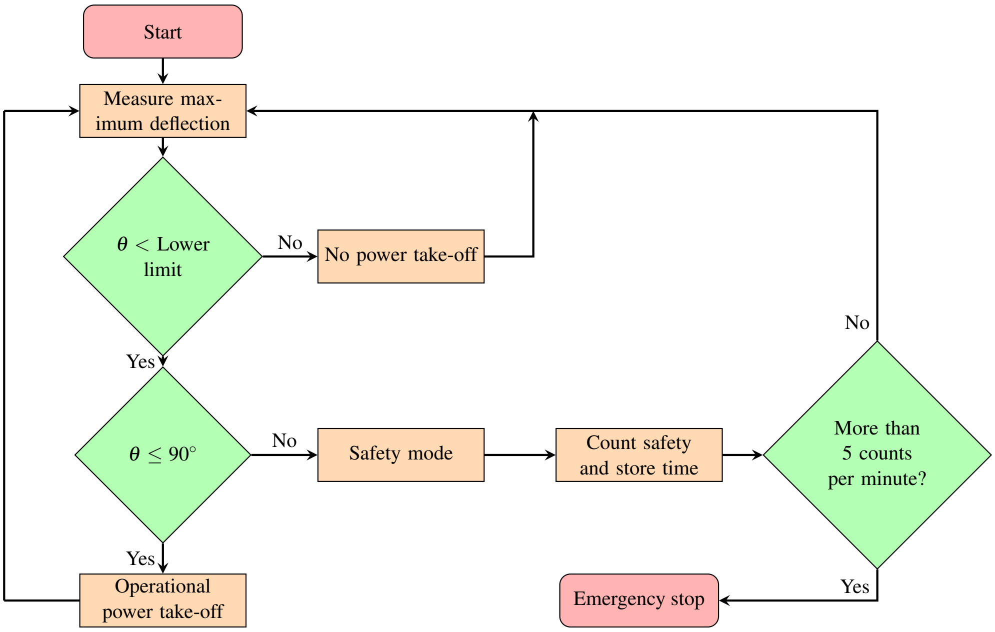

Figure 8.8: Determination of the lower limit for the power take-off

In the following the numerical integration is repeatedly iterated with the lower limit parameter being incremented. The mean rectified power output over the lower switch off limit for different levels of the power take-off torque is shown in Figure 8.9. In Figure 8.9a the power take-off torque is set to a value of 0.1. The rectified mean rectified power output increases gradually and reaches a maximum value of 0.0587 at a lower value of the threshold of 1.05 rad (60.16°). With a further increase of the lower switch on limit of the power take-off the arithmetic mean rectified power output jumps down to zero. The power take-off torque is increased to a value of 0.2 in Figure 8.9b. The arithmetic mean rectified power output increases gradually with an increase in the lower switch off limit. During the gradual rise plateaus are observed where the power output does not change for a range of lower switching off limits. The maximum mean rectified power output of 0.109 is reached at a lower power take-off limit of 1.11 rad (63.60°). With a further increase in the switching off value a power output is not possible anymore. Figure 8.9c shows the mean rectified power output over the lower switching off value for a power take-off torque of 0.3. For a low switching off value no power can be converted from the energy harvester. Afterwards, the power output increases with an increase in the lower switching off limit and reaches its maximum arithmetic mean rectified power output of 0.1517 at a lower switching off value of 1.15 rad (65.90°). With a further increase in the lower switching off limit the power output of the energy harvester drops to zero. In Figure 8.9d the power take-off torque is increased to a value of 0.4. Until a lower switching off limit of 0.316 is exceeded the energy harvester shows almost no power output. With a further increase in the lower switching off limit the arithmetic mean rectified power output increases gradu-

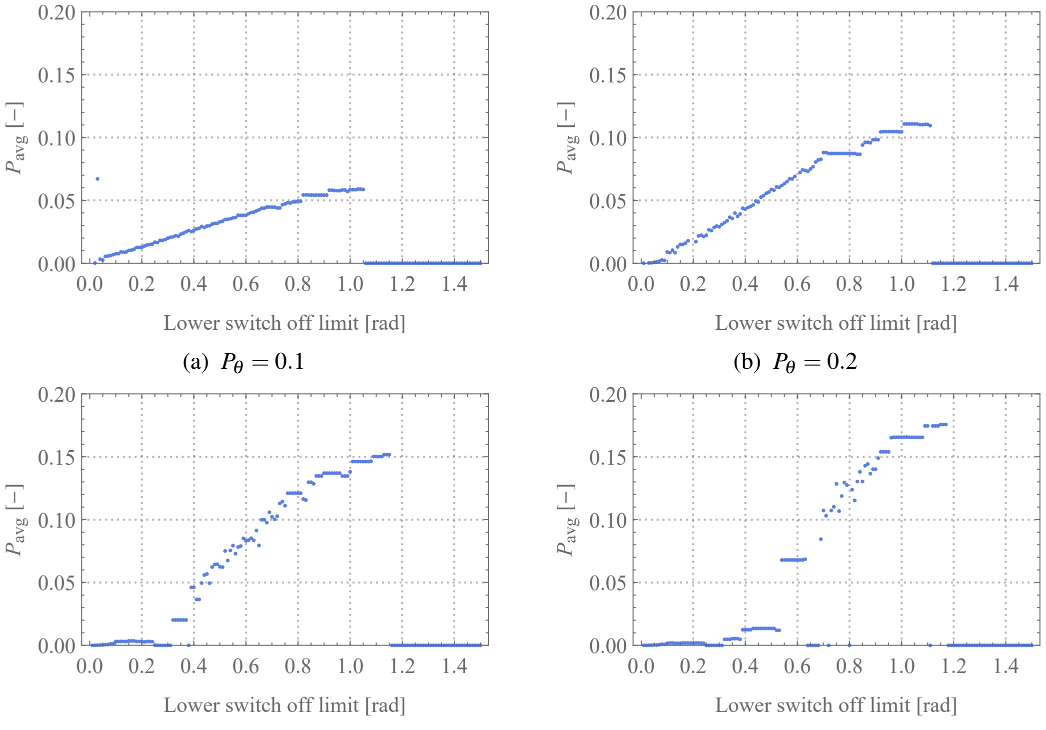

(a) $P_\theta = 0.1$ (b) $P_\theta = 0.2$ (c) $P_\theta = 0.3$ (d) $P_\theta = 0.4$

Figure 8.9: Arithmetic mean rectified power output of the energy harvester P_{avg} over the lower power take-off switching off level. With the variables set to: $l = 0.5$ m, $m = 1.32$ kg, $g = 9.81\ \frac{\text{m}}{\text{s}^2}$, $\alpha_\theta = \alpha_\phi = 0.0648$, $a_u = a_v = a_w = 0.064$, $\beta = 1.0$, and $P_\phi = 0$, and safety limit = 90°

ally. Throughout the increase different plateaus can be seen. The maximum power output of 0.1756 is reached for a lower switch off limit of 1.17 rad (64.0°). It is evident that a relatively high selected lower switching off limit of around 60° to 64° shows the highest power output of the energy harvester. Therefore, it is reasonable only to switch on the power take-off for high deflections.

8.2.4 Comparison of the Radiusing Parameter ε_r for a Switching Control with Three Conditions

In this calculation the optimised power take-off as shown in the flow chart in Figure 8.8 is used for a comparison of the radiusing parameter ε_r over the power take-off. The power take-off function in a real application can physically never be a pure square wave function and therefore it is important to investigate the effect of the radiusing parameter on the power take-off. In Figure 8.10 the arithmetic mean rectified power output is shown over the radiusing parameter ε_r for different power take-off torques. Figure 8.10a shows the development of the arithmetic mean rectified power output over the radiusing parameter ε_r for a power take-off torque of 0.1. For a low radiusing parameter the highest arithmetic mean rectified power output of 0.0591 is

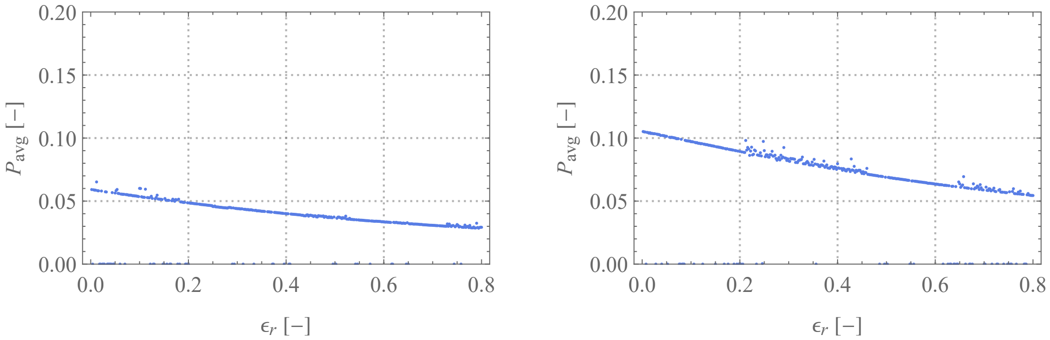

(a) $P_\theta = 0.1$ (b) $P_\theta = 0.2$

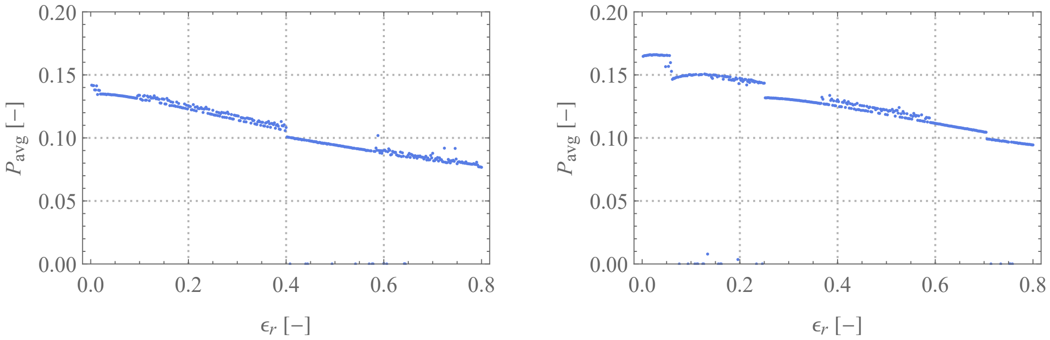

(c) $P_\theta = 0.3$ (d) $P_\theta = 0.4$

Figure 8.10: Arithmetic mean rectified power output of the energy harvester P_{avg} over the radiusing parameter ε_r. With the variables set to: $l = 0.5$ m, $m = 1.32$ kg, $g = 9.81$ $\frac{\mathrm{m}}{\mathrm{s}^2}$, $\alpha_\theta = \alpha_\phi = 0.0648$, $a_u = a_v = a_w = 0.064$, $\beta = 1.0$, $P_\phi = 0$, lower switch off limit = 1 rad (57.3°), and safety limit = 90°.

reached. With a further increase in the radiusing parameter the observed arithmetic mean rectified power output decreases gradually. The power take-off torque is increased to a value of 0.2 in Figure 8.10b. For the lowest observed radiusing parameter of 0.002 the highest arithmetic mean rectified power output of 0.1052 is observed. With an increase in the radiusing parameter the arithmetic mean rectified power output gradually decreases. In Figure 8.10c the power take-off torque is increased to a value of 0.3. The highest arithmetic mean rectified power output of 0.1418 is reached at a radiusing parameter equal to 0.002. With a further increase in the radiusing parameter the arithmetic mean rectified power output of the energy harvester gradually decreases. In Figure 8.10d the power take-off torque is increased to a value of 0.4. The maximum value of the arithmetic averaged power output 0.1660 is reached for a radiusing parameter of 0.03. With a further increase in the radiusing parameter the arithmetic mean rectified power output gradually decreases. It is evident that with an increase in the power take-off torque the decrease in arithmetic mean rectified power output diverges from an initial straight line. Generally, it is observed that with an increase in the radiusing parameter the converted power of the energy harvester decreases.

In Figure 8.11 the arithmetic mean rectified power output is shown over the radiusing parameter for a variation of the lower switching off limit, as defined in Figure 8.8. The lower switching off limit is set to a value of 30° in Figure 8.11a. The highest arithmetic mean rectified power output of 0.0625 is reached for a radiusing parameter of 0.004. With a further increase in the radiusing parameter the arithmetic mean rectified power output gradually decreases until slightly increasing again with a value for the radiusing parameter higher than 0.623. The lower switching off limit is increased to a value of 40° in Figure 8.11b. The highest arithmetic mean rectified power output of 0.0888 is reached for a radiusing parameter of 0.008. With a further increase in the radiusing parameter the arithmetic mean rectified power output decreases continuously. In Figure 8.11c the lower switching off limit is increased by 10° to a value of 50°. For a radiusing parameter of 0.006 the maximum arithmetic mean rectified power output of 0.0974 is reached. With a further increase in the radiusing parameter the arithmetic mean rectified power output decreases. The lower switching off limit is further increased to a value of 60° in Figure 8.11d. The maximum arithmetic mean rectified power output of 0.113 is reached for a radiusing parameter of 0.006. With a further increase in the radiusing parameter the arithmetic mean rectified power output gradually decreases until jumping down to zero for

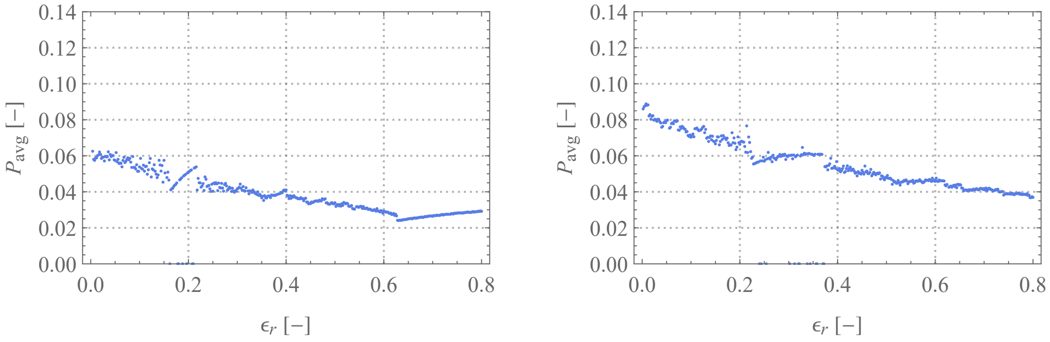

(a) Lower switching off limit 0.524 rad (30°)

(b) Lower switching off limit 0.698 rad (40°)

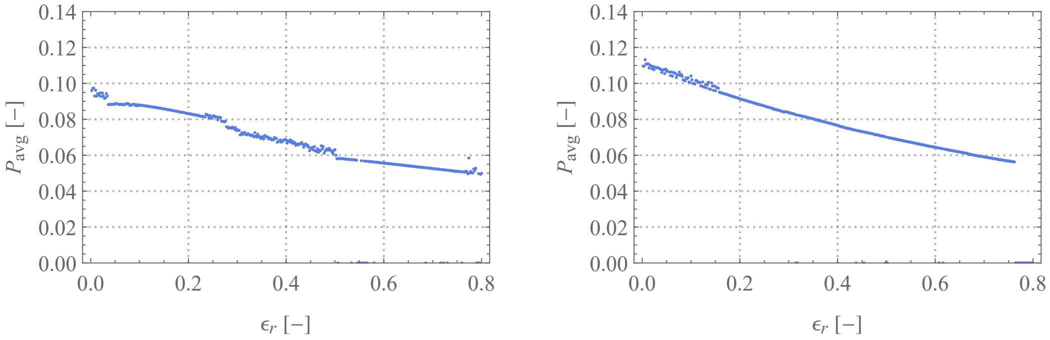

(c) Lower switching off limit 0.873 rad (50°)

(d) Lower switching off limit 1.0472 rad (60°)

Figure 8.11: Arithmetic mean rectified power output of the energy harvester P_{avg} over the radiusing parameter ε_r. With the variables set to: $l = 0.5$ m, $m = 1.32$ kg, $g = 9.81$ $\frac{\text{m}}{\text{s}^2}$, $\alpha_\theta = \alpha_\phi = 0.0648$, $a_u = a_v = a_w = 0.064$, $\beta = 1.0$, $P_\theta = 0.2$, $P_\phi = 0$, and safety limit = 90°.

a radiusing parameter higher than 0.762.

From Figures 8.10 and 8.11 it can be concluded that the lower the power take-off torque is the more the arithmetic mean rectified power output forms a line with little to no outliers. Additionally, it is observed that a lower switching off limit increases the complexity of the relationship between the arithmetic mean rectified power output over the radiusing parameter. It is therefore important to examine the radiusing of the power take-off function at the final stage when all the other excitation and design parameters are known or defined to fine-tune the power take-off.

In the following Figures 8.12 and 8.13 the safety limit is set back to the experimental value of 52.3°.

Figure 8.12 shows the arithmetic mean rectified power output over the radiusing parameter ε_r with the lower switch off limit set to 30°. The power take-off torque is varied for the different figures. In Figure 8.12a the power take-off torque is set to a value of 0.1. The maximum arithmetic mean rectified power output of 0.035 is reached for a radiusing parameter of 0.014. The power output decreases and reaches a local minimum of 0.0237 for a radiusing parameter

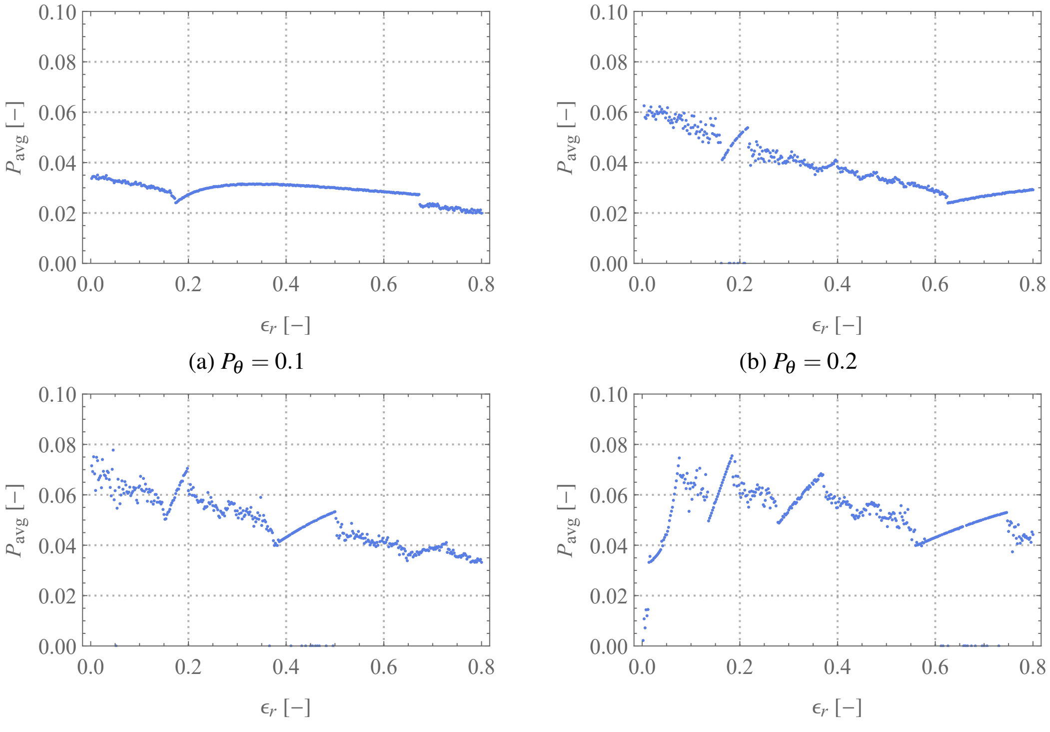

(a) $P_\theta = 0.1$

(b) $P_\theta = 0.2$

(c) $P_\theta = 0.3$

(d) $P_\theta = 0.4$

Figure 8.12: Arithmetic mean rectified power output of the energy harvester P_{avg} over the radiusing parameter ε_r. With the variables set to: $l = 0.5$ m, $m = 1.32$ kg, $g = 9.81\ \frac{\text{m}}{\text{s}^2}$, $\alpha_\theta = \alpha_\phi = 0.0648$, $a_u = a_v = a_w = 0.064$, $\beta = 1.0$, $P_\phi = 0$, lower switch off limit = 30°, and safety limit = 52.3°.

of 0.174. After the local minimum is passed the power output increases shortly and continues to decrease afterwards with a further increase in the radiusing parameter. In Figure 8.12b the power take-off torque is increased to a value of 0.2. With an increase in the power take-off torque the individual points become more disordered compared to a power take-off torque of 0.1. The maximum observed power output of 0.0625 is reached for a radiusing parameter of 0.004. With a further increase in the radiusing parameter the power take-off torque gradually decreases. During this decrease two exceptions are observed where the power output increase. These range from a radiusing parameter from 0.164 to 0.217 and from 0.626 to 0.804. In Figure 8.12c the power take-off torque is increased to a value of 0.3. The maximum power output is 0.0777 and it is reached at a radiusing parameter of 0.046. The power output decreases generally with an increase in the radiusing parameter. As before areas can be seen in which the power output increases e.g. for a radiusing parameter from 0.155 to 0.199 and 0.381 to 0.503. The power take-off torque is increased to a value of 0.4 in Figure 8.12d. The maximum power output of 0.0755 is reached for a radiusing parameter of 0.184.

In Figure 8.13 the arithmetic mean rectified power output is shown over the radiusing parameter for different lower switching off limits. The lower switching off limit is set to a value of 35° in Figure 8.13a. The maximum power output of 0.0625 is reached for a radiusing parameter of 0.004. The power output generally decreases with a further increase in the radiusing parameter. An exemption of this decrease are small areas in which the power output slightly increases for a small range of the radiusing parameter. The areas are from a radiusing parameter from 0.161 to 0.2418 and 0.628 to 0.8. In the next step the lower switching off limit is increased to a value of 40° see Figure 8.13b. The maximum power output of 0.0888 is observed for a radiusing parameter of 0.008. With a further increase in the radiusing parameter the power output of the energy harvester decreases. In Figure 8.13c the lower switching off limit is increased to a value of 45°. The maximum power output of 0.0889 is reached for a radiusing parameter of 0.042. With a further increase in the radiusing parameter the power output gradually decreases. In Figure 8.13d the lower switching off limit is set to a value of 50°. With this high switching off limit the single observed points start to form an ordered pattern. The maximum power output of 0.0696 is reached for a radiusing parameter of 0.24. But an almost similar high power output is reached over the complete area of the radiusing parameter from 0.033 to 0.328. With a further increase in the radiusing parameter the power output of the energy harvester decreases gradually.

When comparing the figures without a safety limit (Figures 8.10 and 8.11) to the ones with a safety limit (Figures 8.12 and 8.13) it can be seen that the safety mode is switched on often and therefore the power output curve of the energy harvester becomes generally more irregular. Generally, from a design point of view it can be said that it is advantageous to keep the movement of the pendulum arm as unrestricted as possible.

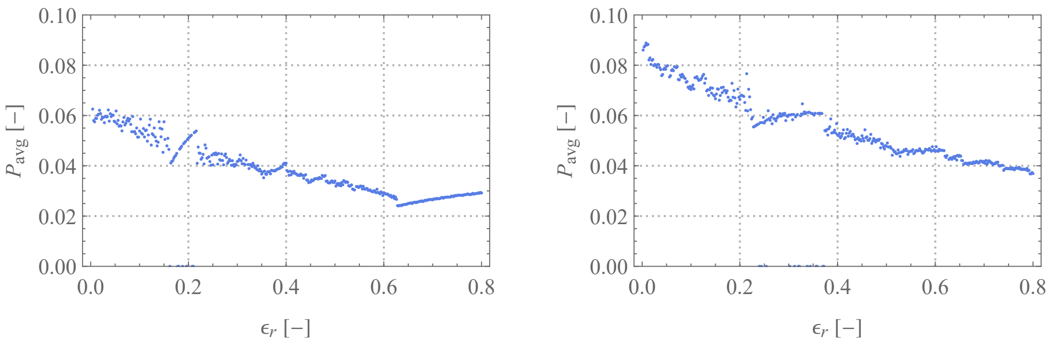

(a) Lower switching off limit 0.611 rad (35°)

(b) Lower switching off limit 0.698 rad (40°)

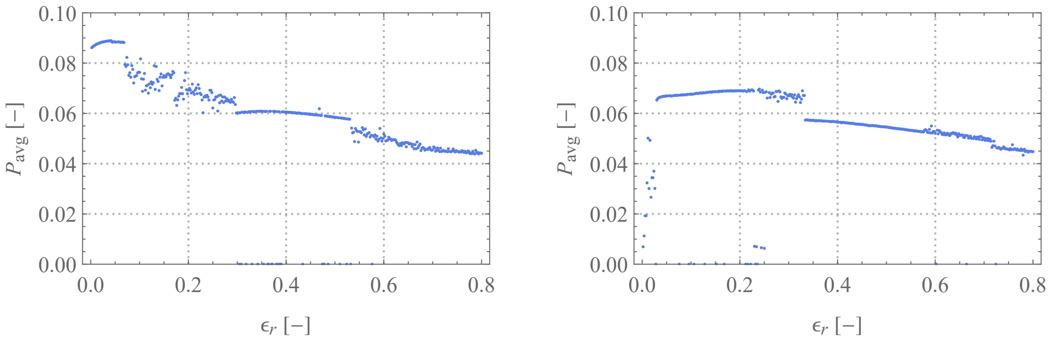

(c) Lower switching off limit 0.785 rad (45°)

(d) Lower switching off limit 0.873 rad (50°)

Figure 8.13: Arithmetic mean rectified power output of the energy harvester P_{avg} over the radiusing parameter ε_r. With the variables set to: $l = 0.5$ m, $m = 1.32$ kg, $g = 9.81\ \frac{\text{m}}{\text{s}^2}$, $\alpha_\theta = \alpha_\phi = 0.0648$, $a_u = a_v = a_w = 0.064$, $\beta = 1.0$, $P_\theta = 0.2$, $P_\phi = 0$, and safety limit = 52.3°

8.2.5 Comparison of the Different Control Strategies

Previously different control strategies for the power take-off were investigated. It is shown that the oscillations of the pendulum can be sustained for longer with a controlled power take-off torque. This in return has a positive effect on the power of the energy harvester that can be converted see Section 8.2.1. Additionally, a second lower switching off limit with half of the power take-off torque was investigated but it unfortunately did not increase the power output of the energy harvester, see Section 8.2.2. Therefore in the following Section 8.2.3 the amount of the energy that can be converted depending on the lower switch off limit is investigated. Generally, it can be seen that the arithmetic mean rectified power output increases until a definable limit after which it jumps down to zero. For the investigated cases the maximum arithmetic mean rectified power output is reached for a lower switching off limit from 60° to 64°. Note that this is examined with a high limit for the safety mode of 90°. It is therefore concluded that it is advantageous to build an experimental rig that is restricted by the supporting structure as little as possible. This is shown in the future work Section 10.6. In Section 8.2.4 the arithmetic mean rectified power output over the radiusing parameter is shown. It is evident that generally with an increase of the radiusing parameter the power output of the energy harvester decreases.

Unfortunately, the control within is restricted by the possibilities within the numerical solver, therefore other control strategies could not be implemented. But even a simplified control shows advantages over a constantly applied power take-off torque.

Chapter 9

Conclusions

The literature discusses a wide variety of simple pendulum energy harvesters. But with the introduction of an extra degree of freedom the number of energy harvesters discussed to date decreases drastically. The main advantage of an additional degree of freedom is that the possible areas of application of the energy harvester are increased. The aim of this work was to investigate an effective omnidirectional pendulum energy harvester that can harvest energy in three orthogonal axes and, in principle, from rotations about those axes. Therefore, this thesis proposed a newly designed omnidirectional pendulum energy harvester defined by two generalised coordinates. The dynamics of the omnidirectional pendulum energy harvester were numerically evaluated at the beginning of the work. For this a mathematical model that incorporates forcing terms in all orthogonal directions, damping terms, and an active power take-off term was introduced. The results were plotted in the time domain, bifurcation diagrams, in Poincaré sections, and in figures that showed the power output of the energy harvester over various parameters. In the following work the dynamics, voltage, and power output of the experimental rig were compared for different pendulum lengths and power take-off modes. The experimental results were mainly plotted in the frequency domain to get the operational range of the energy harvester. The thesis includes a comparison of the numerically and experimentally obtained results. The final chapter introduced various concepts that could be developed for an application-based energy harvester, with the main focus being on the numerical optimisation of the power take-off.

The developed mathematical model, which consists of two ordinary differential equations with two generalised coordinates with an active power take-off term, was solved through a numerical integration procedure in Chapter 5. The polar coordinates of the three-dimensional system θ and ϕ were selected. The omnidirectional pendulum energy harvester was forced under different excitation conditions in up to three orthogonal directions. This showed the energy harvesters' capability for converting energy, independent of the direction of excitation. The active power take-off term uses an arctangent function to simulate a square wave function, with the edges being slightly rounded. This increased the numerical stability drastically compared to using a power take-off with a sign function. The numerical section mainly showed bifurcation diagrams and Poincaré sections but figures in the time domain and trajectory plots of the pendulum bob in 2D and 3D were shown as well. From the numerical evaluation a few general observations can be made. Generally it can be said that the numerical analysis showed the softening characteristics of a pendulum well. This was observed in the frequency domain where the highest deflection of the coordinate θ was observed at an excitation frequency value lower than the natural frequency. In the bifurcation diagrams it was observed that the dynamics of the system can show quasi-periodic or chaotic appearing dynamics. It was evident that the system showed more periodic dynamics when the system was excited with an excitation frequency of ten per cent lower than the natural frequency compared to it being excited directly at the natural frequency or at a higher excitation frequency. Additionally, it was clear that the dynamics of the omnidirectional pendulum energy harvester were more periodic when an excitation in the vertical direction was included. When the excitation amplitude was used as a control parameter for the bifurcation diagrams it became evident that the dynamics of the energy harvester were nonlinear as well. Ranges of excitation amplitudes were observed where the energy harvester's dynamics were periodic, but quasi-periodicity and areas that suggest chaotic dynamics were observed as well. In this work the difference between different constant power take-off torques was also compared. The difference between an omnidirectional pendulum energy harvester that was loaded with a low and a high power take-off was, for the most part, that the system became more periodic when the power take-off torque was increased. The arithmetic mean rectified power output was highly dependent on the excitation amplitude, the excitation frequency, and the power take-off torque. Therefore caution was required when selecting an optimal operational point. An analysis of a simple pendulum energy harvester using the perturbation method of multiple scales concluded the analytical section of this thesis.

The experimental analysis of the omnidirectional energy harvester was shown in Chapter 6. The energy harvester consists of two shafts that were deflected through coordinates θ_{14} and θ_{23}, defining the overall deflection of the pendulum. For the most part frequency responses of the system were observed. The linear frequency responses for the coordinate θ_{14} showed two local maxima at the upper jump point and the lower jump point. Between them a local minimum was observed. The coordinate θ_{23} showed various levels of deflections, without a clear trend for low excitation frequencies, and then displayed a frequency response similar to the one for a linear system for the remaining frequency range. In the region of the first local maximum of the coordinate θ_{14} the coordinate θ_{23} showed almost no deflections. The dynamics of the energy harvester were therefore similar to those of a simple pendulum harvester in that region. The second local maximum of the coordinate θ_{14} was observed at the same excitation frequency as the maximum of the coordinate θ_{23}. At this excitation frequency the trajectory of the pendulum bob was of almost perfect circular shape and can therefore be considered to be operating as a conical pendulum. Additionally, the arithmetic mean rectified voltage and power output of the generators was measured. Section 6.4 examines the possible broadening of the omnidirectional pendulum energy harvester and was therefore the most significant section in the experimental analysis. This was achieved by the inclusion of excitation frequency with up- and down-sweeps. The lower nonlinear jumping region increased the operational range of the energy harvester of the coordinate θ_{14} slightly. An up-sweep of the excitation frequency increased the operational range of the energy harvester for both coordinates drastically. Because both shafts showed high levels of deflections during the upper nonlinear jump region an optimal operational point of the energy harvester was therefore located there. The trajectory of the pendulum bob was of almost perfect circular shape and can therefore be considered to be operating as a conical pendulum at the optimal operational point. An additional advantage of this position was that oscillations of the pendulum were at a higher frequency compared to the lower nonlinear jumping region. With the higher resulting velocity the generators produced a higher maximum voltage output. Therefore the overall efficiency of the energy harvester was highest at the optimal operational point. To reach this optimal operational point an excitation frequency (between the two maxima of the linear frequency response of the coordinate θ_{14}) has to be selected from where the up-sweep was performed. It is important to mention that the upper nonlinear jump region was an unstable hardening branch. Meaning a sweep that increased the excitation frequency too high results in a jumping down of the deflection. The deflections of the omnidirectional energy harvester were compared through a variation of the excitation amplitude as well. It was evident that the deflection did not increase linearly with an increase in the excitation amplitude. For the observed excitation amplitudes the deflection increased steeply at the beginning and then the slope flattens with a further increase in the excitation amplitude. For optimal energy harvesting it was therefore important to excite the energy harvester with an excitation amplitude at a value where the steep slope was already passed, to take full advantage of this steep rise in deflection. In the frequency responses of the experimental analysis similar characteristics were observed, and with an increase in the excitation amplitude the operational range of the energy harvester increased.

In Chapter 7 the experimental results were compared to the numerical analysis. The numerical coordinates θ and ϕ were transformed into the numerical-experimental coordinates θ_{n14} and θ_{n23}. At the beginning of the comparison the damping ratios in the numerical analysis were the same as those observed in the experimental analysis. In this case the coordinate θ_{n14} showed the maximum at the same position as the experimental results. The absolute deflection value of the coordinate however was slightly higher in the numerical analysis than in the experimental analysis. Unfortunately, the second local maximum and the upper nonlinear jump region, which were observed in the experimental results, were not visible in the numerical analysis. The coordinate θ_{n23} unfortunately did not show any similarities with the experimental results. In the next part of the work the damping ratio in the numerical analysis was adapted slightly to accommodate for the energy loss because of higher frequency vibrations that were observed in the experimental rig. This decreased the overall deflection of the coordinates and brings them closer to the experimental results. This is followed by a theoretical investigation of the damping ratio, excitation amplitude and power take-off torque. For these investigations the excitation amplitude was several times greater than that used in the experimental investigation. With this higher value of the theoretical excitation amplitude two main characteristics were observed. Firstly, the overall area where the omnidirectional pendulum energy harvester showed a higher deflection value widens, as observed in the experimental results as well. Secondly, an upper nonlinear jump region was observed for the coordinates θ_{n14} and θ_{n23}. This hardening effect broadened the operational range of the energy harvester drastically. This was in accordance with the experimentally observed results, where the frequency sweeps were incorporated into the measurements.

The following necessary steps from a pre-prototype, to an application of the omnidirectional energy harvester, was explained in Chapter 8. In the beginning possible areas of application for different dimensions were highlighted. Additionally, a controlled power take-off was introduced in the numerical analysis and investigated for a variety of various power take-off parameters.

The omnidirectional pendulum energy harvester proposed in this thesis showed that energy conversion was possible for a physical construction in which the two generalised coordinates respond. Therefore, energy harvesting was possible, independent of the direction of excitation. In the experimental and numerical parts of the thesis different dynamics of the energy harvester were observed that were highly dependent on the excitation frequency and excitation amplitude. The numerical analysis was able to reproduce the position and level of the first local maximum of the coordinate θ_{14}. Additionally, the upper nonlinear jumping region was reproduced numerically for both coordinates with an increased excitation amplitude.

Chapter 10

Future Work

The omnidirectional pendulum energy harvester studied in this research is a pre-prototype that was developed and produced with a strong focus on the harvester as an economic experiment. Different changes to the design of the energy harvester, a new design, an optimised power take-off, and a downscaling procedure are proposed in the following final discussion. These should be investigated as they might allow for a further improvement of the efficiency of the energy harvester.

10.1 Possible Improvements to the Pre-Prototype

In the pre-prototype of this work high frequency vibrations within the rotational mechanism and the pendulum rod are observed. This is described in greater detail in Section 3.5. These higher frequency vibrations can directly affect the efficiency of the energy harvester. It is therefore of crucial importance to adapt the design of the different moving parts of the energy harvester with specific focus on the reduction of vibrations. A special focus should be laid on the examination of the fatigue under excitation conditions where the dynamics of the system show quasi-periodic or chaotic dynamics. This should always be compared to the general goal of construction, to keep the mass moment of inertia and mass of the moving parts of the pendulum energy harvester as low as possible.

10.2 Proposal for Different Prototype Design

This pre-prototype demonstrated the general dynamics of a feasible system well, but it is important to implement the experiences gained and draw improvement recommendations for any following research. The proposed energy harvester in this thesis harvests energy from both of the shafts. Therefore energy harvesting is possible independent of the direction of excitation. In the following, a different design is proposed that also has the potential to harvest energy independent of the direction of excitation. It may be of interest for future researchers to examine that design with a focus on its efficiency. In Figure 10.1 a diagram for such a design is shown. The coordinates for this model are identical to those of the mathematical model in this work. The difference between that and the omnidirectional pendulum energy harvester that is proposed in this work is that the complete power take-off is realised in the direction of the coordinate θ, and the coordinate ϕ only rotates to accommodate different directions of excitation. This way the energy harvester can accommodate different excitation directions. It remains to be investigated whether a bearing in the position of the coordinate ϕ would be sufficient for adjusting the rotation, or if a stepper motor and a more complicated control of the coordinate ϕ is necessary. Both of these variations generally require a more complex design than the one proposed in this work, and would therefore be more costly as well. This is in contrast with the fact that the power take-off is only applied to one shaft, therefore the construction is generally more reliable and an interaction between two different shafts in the power take-off is not needed.

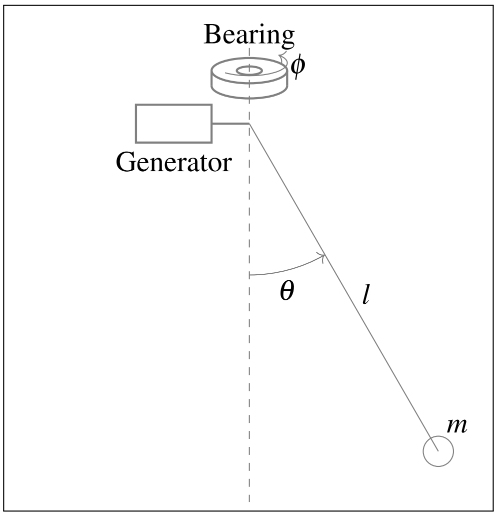

Figure 10.1: Diagram for the proposal of a different prototype

The change in the design of the energy harvester comes with different advantages and disadvantages. Generally, the construction of the alternative energy harvester would be more costly. But in return the risk that the different shafts have a coupling effect to each other is reduced. Another advantage is that the numerical results do not need to be transformed in order to compare them to the experimental results. Additionally, the new proposal for the design would have fewer moving parts and therefore the overall mass and the mass moment of inertia of the energy harvester are lower. Therefore, the energy harvester has the potential to be more effective. There are, however, a few disadvantages and uncertainties that need to be examined. It is questionable if the rotation in the direction of the coordinate ϕ would work without any kind of control. And if a control mechanism is needed can it still be considered as an omnidirectional pendulum energy harvester, or does it turn into a simple pendulum energy harvester with active direction control? It has to be investigated if the upper nonlinear jump region, which is observed in Section 6.4, would still occur with such a changed design.

10.3 Proposal for a Pendulum Energy Harvester with an Adaptive and Controllable Pendulum Length

Li et. al. propose a simple pendulum that can adapt to different excitation frequencies by changing its rod length [56]. The most important advantage of incorporating an adaptive pendulum arm in the omnidirectional energy harvester is the possibility of operating the energy harvester over a broader range of excitation frequencies. Therefore, the area for application of the energy harvester becomes larger.

There is another interesting concept that can be performed. Assuming an omnidirectional pendulum energy harvester with an adaptive pendulum rod is excited with a constant excitation frequency. However, the energy harvester is supposed to operate at its optimal operational point on the upper nonlinear jumping region as described in Section 6.4. To reach this operational point it is theoretically possible to slowly reduce the pendulum length, which increases the natural frequency of the energy harvester, and this could have a similar effect to the frequency up-sweeps observed in the experimental section. In Figure 10.2 the frequency response with the up and down-sweep from the experimental section is shown as a qualitative figure. This is a repetition of Figure 6.21a where the single measurement points are joined and the frequency sweeps only show the points that increase the operational area, to increase clarity. Additionally, the calculated natural undamped frequency for a pendulum length of 0.35 m and 0.3 m is shown. It is clear that with a decrease in pendulum length the natural frequency of the energy harvester increases. Therefore a controlled decrease in the pendulum length over time is, in theory, potentially similar to an excitation frequency sweep. An experimental evaluation of an omnidirectional energy harvester with adaptive pendulum length has not been published, as yet.

Certainly, an adaptive pendulum arm system also has various disadvantages that need to be considered. Generally it can be assumed that such a system would be more fragile and therefore more susceptible to damage. Additionally, the construction of an adaptive pendulum arm system is more complex and therefore expensive. Nevertheless, the feasibility and potential of such a concept is an interesting topic for future research.

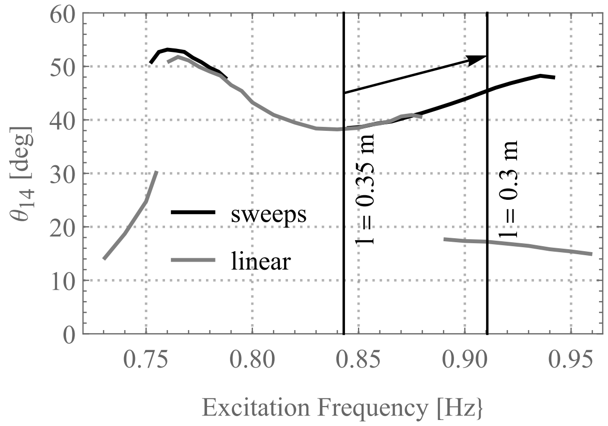

Figure 10.2: Qualitative frequency response with the natural frequencies for a pendulum length of 0.35 m and 0.3 m marked

10.4 Downscaling of the Omnidirectional Pendulum Energy Harvester

The omnidirectional pendulum energy harvester has the potential to operate in different environments, from the field of wave energy harvesting to powering small devices that need a supply voltage e.g. pacemakers or hearing aids are possibilities, see Chapter 8. Since the natural frequency, and therefore the ideal operational region of the energy harvester, is defined by the pendulum length it is of interest to observe smaller energy harvester designs. It is likely that the scaling factor will not be linear and therefore this scaling of energy harvesters has the potential to further optimise the design. A theoretical study in terms of dynamic scaling of a space tether was accomplished by Cartmell and Ziegler [159]. This article would be a useful basis for the theoretical background.

10.5 Does the Sweep Rate Affect the Broadening of the Energy Harvester?

It is generally known that the frequency sweep rate affects the jump down points in nonlinear systems. The higher the sweep rate the lower the amount of time available for the collection of the data becomes, and this has the potential to influence the jumping down points. In an ideal world the sweep rate would be infinitesimally slow [160]. In Section 6.4 the sweep rate was kept reasonably low. However it is interesting to investigate how the operational range of the energy harvester increases when the sweep rate goes towards zero. A proposal for a measurement procedure is shown in Figure 10.3. The frequency up-sweep is performed with a high sweep rate after the marked point is reached the sweep rate is reduced. With this low

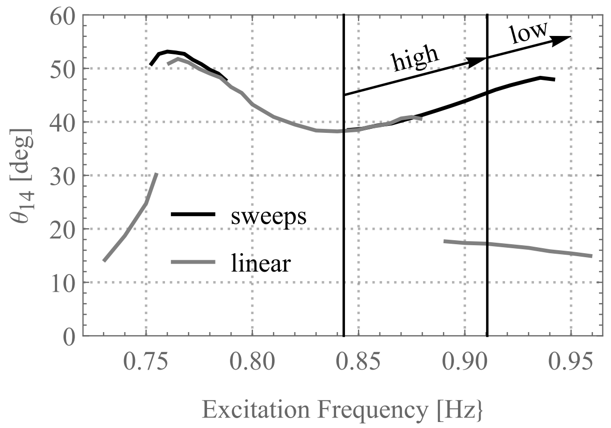

Figure 10.3: Qualitative frequency response with a proposed measuring process for the up-sweep by inclusion of a fast and slow frequency sweep rate

sweep rate the exact jump down point can be determined within a relatively reasonable time frame.

10.6 Almost Unrestricted Movement of the Pendulum

In the experimental Section 6 it is stated several times that the pendulum bob can hit the cage when the excitation amplitude is set to a high value. This has the potential to cause destruction to the rig. Additionally, in Chapter 8 it was proposed that with higher deflections more power can be converted in the energy harvester. Therefore, in Figure 10.4 a design is suggested that allows an almost unrestricted movement of the pendulum bob. The spherical cage offers sufficient clearance for the pendulum bob for all possible deflection angles. The only slight restriction to the pendulum is around connection between the cage and the power take-off sub-

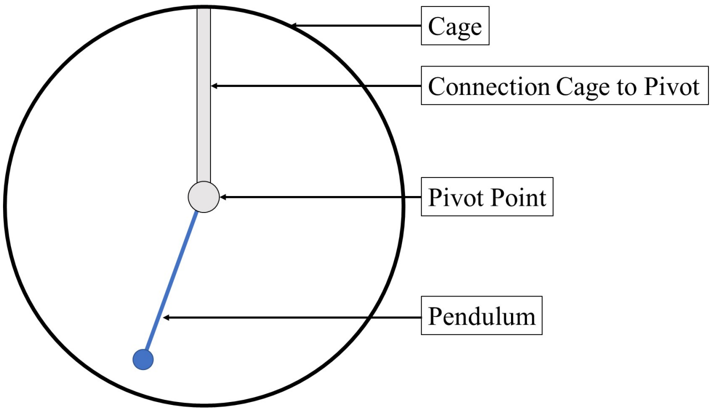

Figure 10.4: Almost unrestricted movement of the pendulum energy harvester without supporting structure which prevents rolling movement

system (pivot point). This mechanical connection point needs to be optimised with regards to vibrations that act on it to ensure reliable operation.

10.7 Optimisation of the Energy Harvester with Power Electronics

The thesis presented has a strong focus on the mechanical aspect of the energy harvester. However, it previous research showed the potential of optimising the power output of energy harvesters with power electronics. A selection of these articles are listed in the theoretical Section 2.4. It may be of interest for future researchers to form a multidisciplinary team to examine the power electronics with a focus on the optimisation of the power take-off of the energy harvester by using power electronics.

Appendix A

Approximate Analytical Solution using the Perturbation Method of Multiple Scales for a Spherical Pendulum

This analysis in this section summarises an attempt to use the perturbation method of multiple scales to find an approximate analytical solution to the dynamics of the spherical pendulum harvester. This analysis was initiated through discussions with the first supervisor, and reproduced his informal notes provided as a starting point for this analysis. In this analysis, the dimensionless differential equation for the coordinate θ (4.34) is recalled and a parameter ω^2 is introduced in front of the $\sin(\theta(\tau))$ term. The value for ω^2 is equal to 1 and this is done to make the equation mathematically more consistent with conventional forms of the 2^{nd} order differential equations, and as required for a perturbation analysis.

$$\omega^2 = \frac{\omega_n^2}{\omega_0^2} = 1. \tag{A.1}$$

$$\begin{aligned} &\ddot{\theta}(\tau) + \alpha_\theta \dot{\theta}(\tau) + \omega^2 \sin(\theta(\tau)) - \sin(\theta(\tau))\cos(\theta(\tau))\dot{\phi}(\tau)^2 \\ &\quad + a_u\beta_u^2 \cos(\theta(\tau))\sin(\phi(\tau))\cos(\beta_u\tau) - a_v\beta_v^2 \cos(\theta(\tau))\cos(\phi(\tau))\cos(\beta_v\tau) \\ &\quad - a_w\beta_w^2 \sin(\theta(\tau))\cos(\beta_w\tau) = -\frac{2P_\theta}{\pi}\tan^{-1}\left(\frac{\dot{\theta}(\tau)}{\varepsilon_{\mathrm{r}}}\right). \end{aligned} \tag{A.2}$$

To apply the perturbation method of multiple scales for these particular ordinary differential equations, a dummy restoring force term for the equation ϕ is required. The dimensionless differential equation for the coordinate ϕ (4.36) is extended by the introduction of the term $\bar{\psi}^2\phi(\tau)$. This term is intended to be physically small $\psi < 1$, with it being a numerical fraction of the restoring force term of the coordinate θ, but its presence ensures that the governing equation is in the required form and can be solved using an asymptotic technique such as multiple scales.

$$\begin{aligned}\ddot{\phi}(\tau)+\frac{\alpha_{\phi}}{\sin^2(\theta(\tau))}\dot{\phi}(\tau)+\frac{2\dot{\theta}(\tau)\cos(\theta(\tau))\dot{\phi}(\tau)}{\sin(\theta(\tau))}\boxed{+\bar{\psi}^2\phi(\tau)}\\ +a_u\beta_u^2\frac{\cos(\phi(\tau))}{\sin(\theta(\tau))}\cos(\beta_u\tau)+a_v\beta_v^2\frac{\sin(\phi(\tau))}{\sin(\theta(\tau))}\cos(\beta_v\tau)=0.\end{aligned} \tag{A.3}$$

Subsequently, the various trigonometric terms can be expanded using the appropriate Maclaurin expansions.

$$\sin\theta(\tau)=\theta(\tau)-\frac{\theta(\tau)^3}{6}+\frac{\theta(\tau)^5}{120}-... \tag{A.4}$$

$$\cos\theta(\tau)=1-\frac{\theta(\tau)^2}{2}+\frac{\theta(\tau)^4}{24}-... \tag{A.5}$$

$$\cos\theta(\tau)\sin\theta(\tau)=\theta(\tau)-\frac{2\theta(\tau)^3}{3}+\frac{2\theta(\tau)^5}{15}-... \tag{A.6}$$

$$\sin\phi(\tau)=\phi(\tau)-\frac{\phi(\tau)^3}{6}+\frac{\phi(\tau)^5}{120}-... \tag{A.7}$$

$$\cos\phi(\tau)=1-\frac{\phi(\tau)^2}{2}+\frac{\phi(\tau)^4}{24}-... \tag{A.8}$$

$$\cos\theta(\tau)\sin\phi(\tau)=\phi(\tau)-\frac{\phi(\tau)^3}{6}-\frac{\phi(\tau)\theta(\tau)^2}{2}+... \tag{A.9}$$

$$\cos\theta(\tau)\cos\phi(\tau)=1-\frac{\phi(\tau)^2}{2}-\frac{\theta(\tau)^2}{2}+\frac{\phi(\tau)^2\theta(\tau)^2}{4}+\frac{\theta(\tau)^4}{24}+\frac{\phi(\tau)^4}{24}+... \tag{A.10}$$

The following Equations (A.11) to (A.14) have a $\sin\theta(\tau)$ or $\sin^2\theta(\tau)$ term in their denominators.

$$\frac{\cos\theta(\tau)}{\sin\theta(\tau)}=\frac{1}{\theta(\tau)}-\frac{\theta(\tau)}{3}-\frac{\theta(\tau)^3}{45}+... \tag{A.11}$$

$$\frac{\cos\phi(\tau)}{\sin\theta(\tau)}=\frac{1}{\theta(\tau)}-\frac{\phi(\tau)^2}{2\theta(\tau)}+\frac{\phi(\tau)^4}{24\theta(\tau)}+\frac{\theta(\tau)}{6}-\frac{\theta(\tau)\phi(\tau)^2}{12}+\frac{7}{360}\theta(\tau)^3+... \tag{A.12}$$

$$\frac{\sin\phi(\tau)}{\sin\theta(\tau)}=\frac{\phi(\tau)}{\theta(\tau)}-\frac{\phi(\tau)^3}{6\theta(\tau)}+\frac{\theta(\tau)\phi(\tau)}{6}+... \tag{A.13}$$

$$\frac{1}{\sin^2\theta(\tau)}=\frac{1}{\theta(\tau)^2}+\frac{1}{3}+\frac{\theta(\tau)^2}{15}+... \tag{A.14}$$

Equation (A.15) shows the Arctangent function for the power take-off. The Arctangent term is also expanded using the Maclaurin expansion. The numerical validation of the Arctangent power take-off can be found in Section 5.2. Note that the parameter ε_r defines the radius of the power take-off and is not equivalent to the small perturbation parameter ε. The parameter ε_r is set to 1 and the power take-off function is therefore in the form of an Arctangent function.

More on the radiusing parameter with regards to the method of multiple scales can be found in Section 5.5.

The Maclaurin expansion of the power take-off term is given here.

$$\tan^{-1}\left(\frac{\dot{\theta}(\tau)}{\varepsilon_r}\right) = \frac{\dot{\theta}(\tau)}{\varepsilon_r} - \frac{\dot{\theta}(\tau)^3}{3\varepsilon_r^3} + \dots \tag{A.15}$$

Equations (A.4) to (A.15) are now introduced in the differential Equations (A.2) and (A.3). Terms that are higher order than $O(3)$ are not considered.

$$\begin{aligned}
&\ddot{\theta}(\tau) + \alpha_\theta \dot{\theta}(\tau) + \omega^2 \left(\theta(\tau) - \frac{\theta(\tau)^3}{6}\right) - \Big(\theta(\tau)\Big)\dot{\phi}(\tau)^2 \\
&\quad + a_u \beta_u^2 \cos(\beta_u \tau) \left(\phi(\tau) - \frac{\phi(\tau)^3}{6} - \frac{\phi(\tau)\theta(\tau)^2}{2}\right) \\
&\quad - a_v \beta_v^2 \cos(\beta_v \tau) \left(1 - \frac{\phi(\tau)^2}{2} - \frac{\theta(\tau)^2}{2}\right) \\
&\quad - a_w \beta_w^2 \cos(\beta_w \tau) \left(\theta(\tau) - \frac{\theta(\tau)^3}{6}\right) = -\frac{2P_\theta}{\pi}\left(\frac{\dot{\theta}(\tau)}{\varepsilon_r} - \frac{\dot{\theta}(\tau)^3}{3\varepsilon_r^3}\right).
\end{aligned} \tag{A.16}$$

$$\begin{aligned}
&\ddot{\phi}(\tau) + \alpha_\phi \dot{\phi}(\tau) \left(\frac{1}{\theta(\tau)^2} + \frac{1}{3} + \frac{\theta(\tau)^2}{15}\right) + 2\dot{\theta}(\tau)\dot{\phi}(\tau)\left(\frac{1}{\theta(\tau)} - \frac{\theta(\tau)}{3} - \frac{\theta(\tau)^3}{45}\right) \\
&\quad + \bar{\Psi}^2 \phi(\tau) \\
&\quad + a_u \beta_u^2 \cos(\beta_u \tau) \left(\frac{1}{\theta(\tau)} - \frac{\phi(\tau)^2}{2\theta(\tau)} + \frac{\phi(\tau)^4}{24\theta(\tau)} + \frac{\theta(\tau)}{6} - \frac{\theta(\tau)\phi(\tau)^2}{12} + \frac{7}{360}\theta(\tau)^3\right) \\
&\quad + a_v \beta_v^2 \cos(\beta_v \tau) \left(\frac{\phi(\tau)}{\theta(\tau)} - \frac{\phi(\tau)^2}{6\theta(\tau)} + \frac{\theta(\tau)\phi(\tau)}{6}\right) = 0.
\end{aligned} \tag{A.17}$$

Equation (A.16) and (A.17) can be re-cast, according to a reasonably physically plausible ordering scheme. Generally the trigonometric Maclaurin expansions were used up to the third order to ensure that the nonlinearities of the terms were adequately represented in the analysis. The small parameter ε $(\varepsilon < 1)$ is introduced in the following. Firstly, looking at the differential Equation (A.16), the general requirement to order the ordinary differential equation is that the lowest order equation in the perturbation hierarchy is linear and therefore analytically solvable. The structure of Equation (A.16) suggests that a standard generating equation of the form, $\ddot{\theta}_0 + \theta_0 = 0$ can be obtained. This gives the normal linear solution in complementary function form, $\theta_0 = Ae^{(i\omega T_0)} + \bar{A}e^{(-i\omega T_0)}$ where $\bar{A}$ is the complex conjugate of A and A is a cmoplex amplitude. The damping, excitation and loading term can then subsequently be in the terms to $O(\varepsilon^1)$ and $O(\varepsilon^2)$. The nonlinear stiffness term (restoring force term) is controlled by $-\frac{\theta(\tau)^3}{6}$ so it could reasonably be scaled to $O(\varepsilon^1)$.

The cubic term $-\theta(\tau)\dot{\phi}(\tau)^2$ is, large when compared to the other cubic terms. The only way this term can be removed from the $O(\varepsilon^0)$ perturbation equation is to restrict $\dot{\phi}(\tau)$ to reasonably low values. As long as $\dot{\phi}(\tau)$ is reasonably small $\dot{\phi}(\tau)^2$ will be very small. This shows that the analysis is not restricted to very small $\dot{\phi}(\tau)$. This means that that Equation (A.16) can be structured to contain $-\varepsilon\dot{\phi}(\tau)^2\theta(\tau)$ and Equation (A.17) to contain $\frac{\varepsilon\alpha_\phi}{3}\dot{\phi}(\tau)$. Additionally, the term $\frac{1}{\theta(\tau)^2}$ was by intention scaled to $\frac{\varepsilon}{\theta(\tau)^2}$ to ensure that it appears in the first order perturbation hierarchy. This approach ensures that the lowest order perturbation equation is equal to zero, and is more in line with the approach of a lightly damped pendulum. From this the following relations (A.18) and (A.19) can be observed.

$$\begin{aligned}
&\alpha_\theta = \varepsilon\bar{\alpha}_\theta, && \frac{1}{6} = \varepsilon\bar{\gamma}, && a_u = \varepsilon\bar{a}_u,\\
&a_v = \varepsilon\bar{a}_v, && a_w = \varepsilon\bar{a}_w, && P_\theta = \varepsilon\bar{P}_\theta,\\
&\frac{1}{15} = \varepsilon\bar{\nu}, && 2 = \varepsilon\bar{\rho}, && \frac{1}{3} = \varepsilon\bar{\sigma}(= 2\varepsilon\bar{\gamma}).
\end{aligned} \tag{A.18}$$

$$\begin{aligned}
&\dot{\phi}(\tau)^2\theta(\tau) \to \varepsilon^2\bar{\delta}\dot{\phi}(\tau)^2\theta(\tau), && \frac{\phi(\tau)\theta(\tau)^2}{2} \to \varepsilon\bar{\eta}\phi(\tau)\theta(\tau)^2,\\
&\frac{\phi(\tau)^2}{2} \to \varepsilon\bar{\eta}\phi(\tau)^2, && \frac{\theta(\tau)^2}{2} \to \varepsilon\bar{\eta}\theta(\tau)^2,\\
&\frac{1}{\theta(\tau)^2} \to \frac{\varepsilon}{\theta(\tau)^2}, && \frac{\phi(\tau)^2}{2\theta(\tau)} \to \varepsilon\bar{\eta}\frac{\phi(\tau)^2}{\theta(\tau)}.
\end{aligned} \tag{A.19}$$

After introducing the Maclaurin expansions (A.4) to (A.15) and the relations (A.18), (A.19) in Equations (A.2), (A.3) the Equations (A.20) and (A.21) are obtained.

$$\begin{aligned}
&\ddot{\theta}(\tau) + \varepsilon\bar{\alpha}_\theta\dot{\theta}(\tau) + \omega^2\theta(\tau) - \varepsilon\bar{\gamma}\omega^2\theta(\tau)^3 - \varepsilon^2\bar{\delta}\theta(\tau)\dot{\phi}(\tau)^2\\
&\quad + \varepsilon a_u\beta_u^2\cos(\beta_u\tau)\left(\phi(\tau) - \varepsilon\bar{\gamma}\phi(\tau)^3 - \varepsilon\bar{\eta}\phi(\tau)\theta(\tau)^2\right)\\
&\quad - \varepsilon a_v\beta_v^2\cos(\beta_v\tau)\left(1 - \varepsilon\bar{\eta}\phi(\tau)^2 - \varepsilon\bar{\eta}\theta(\tau)^2\right)\\
&\quad - \varepsilon a_w\beta_w^2\cos(\beta_w\tau)\left(\theta(\tau) - \varepsilon\bar{\gamma}\theta(\tau)^3\right) = -\frac{\varepsilon 2P_\theta}{\pi}\left(\frac{\dot{\theta}(\tau)}{\varepsilon_r} - \frac{(\bar{\sigma}\varepsilon)\,\dot{\theta}(\tau)^3}{\varepsilon_r^2}\right).
\end{aligned} \tag{A.20}$$

$$
\begin{aligned}
&\ddot{\phi}(\tau)+\bar{\alpha}_{\phi}\dot{\phi}(\tau)\left(\frac{\varepsilon}{\theta(\tau)^2}+\varepsilon\bar{\sigma}+\varepsilon^2\bar{\nu}\theta(\tau)^2\right)+\varepsilon\bar{\rho}\dot{\phi}(\tau)\dot{\theta}(\tau)\left(\frac{1}{\theta(\tau)}-\varepsilon\bar{\sigma}\theta(\tau)\right)\\
&\quad+\bar{\psi}^2\phi(\tau)+\varepsilon a_u\beta_u^2\cos(\beta_u\tau)\left(\frac{1}{\theta(\tau)}-\frac{\varepsilon\bar{\eta}\phi(\tau)^2}{\theta(\tau)}+\varepsilon\bar{\gamma}\theta(\tau)\right)\\
&\quad+\frac{\varepsilon a_v\beta_v^2\cos(\beta_v\tau)\,\phi(\tau)}{\theta(\tau)}=0.
\end{aligned}
\tag{A.21}
$$

Introducing the independent variables according to the well-known asymptotic analysis procedure of perturbation in the literature [153], [154], [155] and [156].

$$
T_n=\varepsilon^n\tau, \qquad \text{for} \qquad n=0,1,2,... \tag{A.22}
$$

This is followed by treatment the derivatives with respect to timescaling.

$$
\begin{aligned}
\frac{d}{d\tau}=&\frac{dT_0}{d\tau}\frac{\partial}{\partial T_0}+\frac{dT_1}{d\tau}\frac{\partial}{\partial T_1}+...=\frac{\partial}{\partial T_0}+\varepsilon\frac{\partial}{\partial T_1}+...=D_0+\varepsilon D_1+...\\
\frac{d^2}{d\tau^2}=&\frac{\partial^2}{\partial T_0^2}+2\varepsilon\frac{\partial^2}{\partial T_0\partial T_1}+\varepsilon^2\left(2\frac{\partial^2}{\partial T_0\partial T_2}+\frac{\partial^2}{\partial T_1^2}\right)+...\\
=&D_0^2+2\varepsilon D_0D_1+\varepsilon^2(D_1^2+2D_0D_2)+...
\end{aligned}
\tag{A.23}
$$

It can be assumed that the coordinates θ and ϕ can be represented by the truncated power series.

$$
\theta(\tau)=\theta_0(T_0,T_1,T_2)+\varepsilon\theta_1(T_0,T_1,T_2)+... \tag{A.24}
$$

$$
\phi(\tau)=\phi_0(T_0,T_1,T_2)+\varepsilon\phi_1(T_0,T_1,T_2)+... \tag{A.25}
$$

With Equations (A.22) to (A.25), the perturbation hierarchy for the coordinate θ is obtained with the help of code written in Mathematica® to do the requisite analysis.

$$
D_0^2\theta_0+\omega^2\theta_0=0. \tag{A.26}
$$

$$
\begin{aligned}
D_0^2\theta_1+\omega^2\theta_1=&-2\left(D_0D_1\theta_0\right)-\bar{\alpha}_{\theta}\left(D_0\theta_0\right)+\bar{\gamma}\omega^2\theta_0^3\\
&-\bar{a}_u\beta_u^2\cos(\beta_u\tau)\,\phi_0+\bar{a}_v\beta_v^2\cos(\beta_v\tau)\\
&+\bar{a}_w\beta_w^2\cos(\beta_w\tau)\,\theta_0-\frac{(2\bar{P}_{\theta})\,(D_0\theta_0)}{\pi\varepsilon_r}.
\end{aligned}
\tag{A.27}
$$

$$\begin{aligned} D_0^2\theta_2+\omega^2\theta_2 = & -D_1^2\theta_0-2\left(D_0D_2\theta_0\right)-2\left(D_0D_1\theta_1\right) \\ & +\bar{\delta}\left(D_0\phi_0\right)^2\theta_0+3\bar{\gamma}\omega^2\theta_0^2\theta_1-\bar{\alpha}_\theta\left(D_1\theta_0\right)-\bar{\alpha}_\theta\left(D_0\theta_1\right) \\ & +\bar{\eta}\bar{a}_u\beta_u^2\cos\left(\beta_u\tau\right)\theta_0^2\phi_0+\bar{\gamma}\bar{a}_u\beta_u^2\cos\left(\beta_u\tau\right)\phi_0^3 \\ & -\bar{a}_u\beta_u^2\cos\left(\beta_u\tau\right)\phi_1-\bar{\eta}\bar{a}_v\beta_v^2\cos\left(\beta_v\tau\right)\theta_0^2 \\ & -\bar{\eta}\bar{a}_v\beta_v^2\cos\left(\beta_v\tau\right)\phi_0^2-\bar{\gamma}\bar{a}_w\beta_w^2\cos\left(\beta_w\tau\right)\theta_0^3 \\ & +\bar{a}_w\beta_w^2\cos\left(\beta_w\tau\right)\theta_1+\frac{\left(2\bar{\sigma}\bar{P}_\theta\right)\left(D_0\theta_0\right)^3}{\pi\varepsilon_r^3} \\ & -\frac{\left(2\bar{P}_\theta\right)\left(D_1\theta_0\right)}{\pi\varepsilon_r}-\frac{\left(2\bar{P}_\theta\right)\left(D_0\theta_1\right)}{\pi\varepsilon_r}. \end{aligned} \tag{A.28}$$

And subsequently, with Equations (A.22) to (A.25) the perturbation hierarchy for the coordinate ϕ is also obtained. Recalling the assumed power series solution for the coordinate θ in Equation (A.24), this expression is introduced in the denominator of Equation (A.21) and therefore the denominators are of the form $\theta_0(T_0,T_1,T_2)+\varepsilon\theta_1(T_0,T_1,T_2)+...$ or $(\theta_0(T_0,T_1,T_2)+\varepsilon\theta_1(T_0,T_1,T_2)+...)^2$. However, these denominators cannot be ordered with respect to ε and this prevents the future analysis, therefore the denominators need to be truncated to $\theta_0(T_0,T_1,T_2)$ and $\theta_0(T_0,T_1,T_2)^2$. Physically this means that the terms in the denominator are linearised, which is a gross approximation, but is required to make some future progress.

$$D_0^2\phi_0+\bar{\psi}^2\phi_0=0. \tag{A.29}$$

$$\begin{aligned} D_0^2\phi_1+\bar{\psi}^2\phi_1 = & -2\left(D_0D_1\phi_0\right)-\frac{\bar{\rho}\left(\left(D_0\theta_0\right)\left(D_0\phi_0\right)\right)}{\theta_0} \\ & -\bar{\sigma}\bar{\alpha}_\phi\left(D_0\phi_0\right)-\frac{\bar{\alpha}_\phi\left(D_0\phi_0\right)}{\theta_0^2}-\frac{\bar{a}_u\beta_u^2\cos\left(\beta_u\tau\right)}{\theta_0} \\ & -\frac{\bar{a}_v\beta_v^2\cos\left(\beta_v\tau\right)\phi_0}{\theta_0}. \end{aligned} \tag{A.30}$$

$$\begin{aligned} D_0^2\phi_2+\bar{\psi}^2\phi_2 = & -D_1^2\phi_0-2\left(D_0D_2\phi_0\right)-2\left(D_0D_1\phi_1\right)-\frac{\bar{\rho}\left(\left(D_1\theta_0\right)\left(D_0\phi_0\right)\right)}{\theta_0} \\ & -\frac{\bar{\rho}\left(\left(D_0\theta_1\right)\left(D_0\phi_0\right)\right)}{\theta_0}-\frac{\bar{\rho}\left(\left(D_0\theta_0\right)\left(D_1\phi_0\right)\right)}{\theta_0}-\frac{\bar{\rho}\left(\left(D_0\theta_0\right)\left(D_0\phi_1\right)\right)}{\theta_0} \\ & +\bar{\rho}\bar{\sigma}\left(D_0\theta_0\right)\left(D_0\phi_0\right)\theta_0-\bar{\gamma}\bar{a}_u\beta_u^2\cos\left(\beta_u\tau\right)\theta_0 \\ & +\frac{\bar{\eta}\bar{a}_u\beta_u^2\left(\cos\left(\beta_u\tau\right)\phi_0^2\right)}{\theta_0}-\frac{\bar{a}_v\beta_v^2\left(\cos\left(\beta_v\tau\right)\phi_1\right)}{\theta_0}-\bar{\sigma}\bar{\alpha}_\phi\left(D_1\phi_0\right) \\ & -\bar{\sigma}\bar{\alpha}_\phi\left(D_0\phi_1\right)-\frac{\bar{\alpha}_\phi\left(D_1\phi_0\right)}{\theta_0^2}-\frac{\bar{\alpha}_\phi\left(D_0\phi_1\right)}{\theta_0^2}-\bar{\alpha}_\phi\bar{\nu}\left(D_0\phi_0\right)\theta_0^2. \end{aligned} \tag{A.31}$$

The generating solution is obtained by solving the lowest order Equation (A.26) for the coordinate θ.

$$\theta_0=A(T_1,T_2)e^{i\omega T_0}+\bar{A}(T_1,T_2)e^{-i\omega T_0}. \tag{A.32}$$

Solving the lowest order Equation (A.29) in the perturbation hierarchy for the coordinate ϕ gives the generating solution for the coordinate ϕ.

$$\phi_0 = B(T_1,T_2)e^{i\bar{\psi}T_0} + \bar{B}(T_1,T_2)e^{-i\bar{\psi}T_0}. \tag{A.33}$$

Additionally, the derivatives of the zeroth order perturbation solutions with respect to timescale T_0 area as follows.

$$D_0\theta_0 = i\omega A(T_1,T_2)e^{i\omega T_0} - i\omega\bar{A}(T_1,T_2)e^{-i\omega T_0}. \tag{A.34}$$

$$D_0\phi_0 = i\bar{\psi}B(T_1,T_2)e^{i\bar{\psi}T_0} - i\bar{\psi}\bar{B}(T_1,T_2)e^{-i\bar{\psi}T_0}. \tag{A.35}$$

The excitation terms are converted from the trigonometric form to exponential form.

$$\cos(\beta T_0) = \frac{1}{2}e^{i\beta T_0} + \frac{1}{2}e^{-i\beta T_0} \quad \text{where} \quad \tau \approx T_0. \tag{A.36}$$

Introducing the solutions of θ_0 (A.32) and ϕ_0 (A.33) into the first-order perturbation hierarchy term for the coordinate θ (A.27) gives Equation (A.37). Note that the arguments (T_1,T_2) after the complex amplitude functions $A,\bar{A},B$ and $\bar{B}$ are removed from here on to increase clarity.

$$\begin{aligned}
D_0^2\theta_1 + \omega^2\theta_1 = & -2i\omega D_1Ae^{i\omega T_0} + 2i\omega D_1\bar{A}e^{-i\omega T_0} \\
& - \bar{\alpha}_\theta i\omega Ae^{i\omega T_0} + \bar{\alpha}_\theta i\omega\bar{A}e^{-i\omega T_0} \\
& + \bar{\gamma}\omega^2A^3e^{3i\omega T_0} + 3\bar{\gamma}\omega^2A^2\bar{A}e^{i\omega T_0} + 3\bar{\gamma}\omega^2\bar{A}^2Ae^{-i\omega T_0} + \bar{\gamma}\omega^2\bar{A}^3e^{-3i\omega T_0} \\
& - \frac{1}{2}\bar{a}_u\beta_u^2Be^{i\bar{\psi}T_0 - i\beta_uT_0} - \frac{1}{2}\bar{a}_u\beta_u^2Be^{i\bar{\psi}T_0 + i\beta_uT_0} \\
& - \frac{1}{2}\bar{a}_u\beta_u^2\bar{B}e^{-i\bar{\psi}T_0 - i\beta_uT_0} - \frac{1}{2}\bar{a}_u\beta_u^2\bar{B}e^{-i\bar{\psi}T_0 + i\beta_uT_0} \\
& + \frac{1}{2}\bar{a}_v\beta_v^2e^{i\beta_vT_0} + \frac{1}{2}\bar{a}_v\beta_v^2e^{-i\beta_vT_0} \\
& + \frac{1}{2}\bar{a}_w\beta_w^2\bar{A}e^{-i\omega T_0 + i\beta_wT_0} + \frac{1}{2}\bar{a}_w\beta_w^2Ae^{i\omega T_0 - i\beta_wT_0} \\
& + \frac{1}{2}\bar{a}_w\beta_w^2Ae^{i\omega T_0 + i\beta_wT_0} + \frac{1}{2}\bar{a}_w\beta_w^2\bar{A}e^{-i\omega T_0 - i\beta_wT_0} \\
& - \frac{2\bar{P}_\theta i\omega A}{\pi\varepsilon_r}e^{i\omega T_0} + \frac{2\bar{P}_\theta i\omega\bar{A}}{\pi\varepsilon_r}e^{-i\omega T_0}.
\end{aligned} \tag{A.37}$$

The secular terms in Equation (A.37) are those that include the expression $e^{i\omega T_0}$. These need to be set equal to zero to prevent an unbounded growth of the solution to θ, over time. Removal of the secular terms leads to

$$-2i\omega D_1A - \bar{\alpha}_\theta i\omega A + 3\bar{\gamma}\omega^2A^2\bar{A} - \frac{2\bar{P}_\theta i\omega A}{\pi\varepsilon_r} = 0. \tag{A.38}$$

The system will be excited close to the natural frequency for β_u and β_v which means that these values can be set to ω. The excitation frequency β_w applies the the principle of parametric resonance therefore β_w is set to 2ω. Note that this approach does not here allow any detuning. Recalling that $\bar{\psi}$ is physically small ($\bar{\psi} < 1$) therefore it can be assumed that the expression $e^{i\bar{\psi}T_0 + i\beta_u T_0}$ can be approximated by $e^{i\beta_u T_0}$. This approximation is applied to the other excitation terms as well. After implementing this approximation four additional secular generating terms are obtained.

$$\begin{aligned}&-2i\omega D_1 A - \bar{\alpha}_\theta i\omega A + 3\bar{\gamma}\omega^2 A^2 \bar{A} - \frac{1}{2}\bar{a}_u \omega^2 B - \frac{1}{2}\bar{a}_u \omega^2 \bar{B} + \frac{1}{2}\bar{a}_v \omega^2 + 2\bar{a}_w \omega^2 \bar{A} \\ &- \frac{2\bar{P}_\theta i\omega A}{\pi \varepsilon_r} = 0.\end{aligned} \tag{A.39}$$

Removing the secular terms from Equation (A.37) gives.

$$\begin{aligned}D_0^2\theta_1 + \omega^2\theta_1 = &+ \bar{\gamma}\omega A^3 e^{3i\omega T_0} + \bar{\gamma}\omega \bar{A}^3 e^{-3i\omega T_0} \\ &+ 2\bar{a}_w \omega^2 A e^{3i\omega T_0} + 2\bar{a}_w \omega^2 \bar{A} e^{-3i\omega T_0}.\end{aligned} \tag{A.40}$$

Equation (A.40) is solved analytically using code written in Mathematica® and the particular integral part of this solution is shown in Equation (A.41).

$$\begin{aligned}\theta_1 = \frac{1}{48\omega^2} e^{-5i\omega T_0} \Bigg[&\Bigg(A^3 e^{4i\omega T_0} \Big(8e^{\frac{3}{2}e^{-i\omega T_0}\left(-1+e^{2i\omega T_0}\right)\omega} - 8e^{\left(\frac{3}{2}e^{-i\omega T_0}\left(-1+e^{2i\omega T_0}\right)\omega + 2i\omega T_0\right)} \\ &- 6e^{2i\omega T_0}\omega - 3e^{4i\omega T_0}\omega + 3e^{6i\omega T_0}\omega \Big) + \Big(8e^{\frac{3}{2}\omega\left(e^{-i\omega T_0} - e^{i\omega T_0} + 4iT_0\right)} \\ &- 8e^{\left(\frac{1}{2}\omega\left(3e^{-i\omega T_0} - 3e^{i\omega T_0} + 8iT_0\right)\right)} + 3\omega - 3e^{2i\omega T_0}\omega - 6e^{4i\omega T_0}\omega \Big) \bar{A}^3 \Bigg) \bar{\gamma} \\ &- 2\omega \Bigg(A e^{4i\omega T_0} \Big(-8e^{\frac{3}{2}e^{-i\omega T_0}\left(-1+e^{2i\omega T_0}\right)\omega} + 8e^{\left(\frac{3}{2}e^{-i\omega T_0}\left(-1+e^{2i\omega T_0}\right)\omega + 2i\omega T_0\right)} \\ &+ 6e^{2i\omega T_0}\omega + 3e^{4i\omega T_0}\omega - 3e^{6i\omega T_0}\omega \Big) + \Big(-8e^{\frac{3}{2}\omega\left(e^{-i\omega T_0} - e^{i\omega T_0} + 4iT_0\right)} \\ &+ 8e^{\left(\frac{1}{2}\omega\left(3e^{-i\omega T_0} - 3e^{i\omega T_0} + 8iT_0\right)\right)} - 3\omega + 3e^{2i\omega T_0}\omega + 6e^{4i\omega T_0}\omega \Big) \bar{A} \Bigg) \bar{a}_w \Bigg].\end{aligned} \tag{A.41}$$

Introducing Equations (A.32) and (A.33) into Equation (A.30) gives Equation (A.42).

$$\begin{aligned} D_0^2\phi_1+\bar{\psi}^2\phi_1 = &-2D_1 i\bar{\psi}Be^{i\bar{\psi}T_0}+2D_1 i\bar{\psi}\bar{B}e^{-i\bar{\psi}T_0} \\ &-\bar{\rho}\frac{\left(i\omega Ae^{i\omega T_0}-i\omega\bar{A}e^{-i\omega T_0}\right)\left(i\bar{\psi}Be^{i\bar{\psi}T_0}-i\bar{\psi}\bar{B}e^{-i\bar{\psi}T_0}\right)}{Ae^{i\omega T_0}+\bar{A}e^{-i\omega T_0}} \\ &-\bar{\sigma}\bar{\alpha}_\phi i\bar{\psi}Be^{i\bar{\psi}T_0}+\bar{\sigma}\bar{\alpha}_\phi i\bar{\psi}\bar{B}e^{-i\bar{\psi}T_0} \\ &-\frac{\bar{\alpha}_\phi i\bar{\psi}Be^{i\bar{\psi}T_0}-\bar{\alpha}_\phi i\bar{\psi}\bar{B}e^{-i\bar{\psi}T_0}}{A^2e^{2i\omega T_0}+2A\bar{A}+\bar{A}^2e^{-2i\omega T_0}} \\ &-\frac{\frac{1}{2}\bar{a}_u\beta_u^2e^{i\beta_uT_0}+\frac{1}{2}\bar{a}_u\beta_u^2e^{-i\beta_uT_0}}{Ae^{i\omega T_0}+\bar{A}e^{-i\omega T_0}} \\ &-\frac{\left(\frac{1}{2}\bar{a}_v\beta_v^2e^{i\beta_vT_0}+\frac{1}{2}\bar{a}_v\beta_v^2e^{-i\beta_vT_0}\right)\left(Be^{i\bar{\psi}T_0}+\bar{B}e^{-i\bar{\psi}T_0}\right)}{Ae^{i\omega T_0}+\bar{A}e^{-i\omega T_0}}. \end{aligned} \tag{A.42}$$

After introducing $\beta_u=\beta_v=\omega$, Equation (A.42) becomes as follows.

$$\begin{aligned} D_0^2\phi_1+\bar{\psi}^2\phi_1 = &-2D_1 i\bar{\psi}Be^{i\bar{\psi}T_0}+2D_1 i\bar{\psi}\bar{B}e^{-i\bar{\psi}T_0} \\ &-\bar{\rho}\frac{\left(i\omega Ae^{i\omega T_0}-i\omega\bar{A}e^{-i\omega T_0}\right)\left(i\bar{\psi}Be^{i\bar{\psi}T_0}-i\bar{\psi}\bar{B}e^{-i\bar{\psi}T_0}\right)}{Ae^{i\omega T_0}+\bar{A}e^{-i\omega T_0}} \\ &-\bar{\sigma}\bar{\alpha}_\phi i\bar{\psi}Be^{i\bar{\psi}T_0}+\bar{\sigma}\bar{\alpha}_\phi i\bar{\psi}\bar{B}e^{-i\bar{\psi}T_0} \\ &-\frac{\bar{\alpha}_\phi i\bar{\psi}Be^{i\bar{\psi}T_0}-\bar{\alpha}_\phi i\bar{\psi}\bar{B}e^{-i\bar{\psi}T_0}}{A^2e^{2i\omega T_0}+2A\bar{A}+\bar{A}^2e^{-2i\omega T_0}} \\ &-\frac{\frac{1}{2}\bar{a}_u\omega^2e^{i\omega T_0}+\frac{1}{2}\bar{a}_u\omega^2e^{-i\omega T_0}}{Ae^{i\omega T_0}+\bar{A}e^{-i\omega T_0}} \\ &-\frac{\left(\frac{1}{2}\bar{a}_v\omega^2e^{i\omega T_0}+\frac{1}{2}\bar{a}_v\omega^2e^{-i\omega T_0}\right)\left(Be^{i\bar{\psi}T_0}+\bar{B}e^{-i\bar{\psi}T_0}\right)}{Ae^{i\omega T_0}+\bar{A}e^{-i\omega T_0}}. \end{aligned} \tag{A.43}$$

The secular terms in Equation (A.43) are defined by the presence of $e^{i\bar{\psi}T_0}$. This gives the following secular terms for the coordinate ϕ.

$$\begin{aligned} &-2D_1 i\bar{\psi}B-\bar{\rho}\frac{\left(i\omega Ae^{i\omega T_0}-i\omega\bar{A}e^{-i\omega T_0}\right)}{Ae^{i\omega T_0}+\bar{A}e^{-i\omega T_0}}\left(i\bar{\psi}B\right)-\bar{\sigma}\bar{\alpha}_\phi i\bar{\psi}B \\ &-\frac{\bar{\alpha}_\phi i\bar{\psi}B}{A^2e^{2i\omega T_0}+2A\bar{A}+\bar{A}^2e^{-2i\omega T_0}}-\frac{\left(\frac{1}{2}\bar{a}_v\omega^2e^{i\omega T_0}+\frac{1}{2}\bar{a}_v\omega^2e^{-i\omega T_0}\right)}{Ae^{i\omega T_0}+\bar{A}e^{-i\omega T_0}}B=0. \end{aligned} \tag{A.44}$$

To solve the secular term Equations (A.39) and (A.44) the following polar notation is introduced for the complex amplitudes A and B. The polar notation is characterised by use of the subscript p.

$$A=\frac{a_p}{2}e^{i\alpha_p},\qquad \bar{A}=\frac{a_p}{2}e^{-i\alpha_p},\qquad a_p=a_p(T_1),\qquad \alpha_p=\alpha_p(T_1). \tag{A.45}$$

$$B=\frac{b_p}{2}e^{i\beta_p},\qquad \bar{B}=\frac{b_p}{2}e^{-i\beta_p},\qquad b_p=b_p(T_1),\qquad \beta_p=\beta_p(T_1). \tag{A.46}$$

The derivative of A with respect to T_1 is.

$$D_1A = \frac{a_p'}{2}e^{i\alpha_p} + \frac{a_p}{2}i\alpha_p'e^{i\alpha_p}. \tag{A.47}$$

The derivative of B with respect to T_1 is.

$$D_1B = \frac{b_p'}{2}e^{i\beta_p} + \frac{b_p}{2}i\beta_p'e^{i\beta_p}. \tag{A.48}$$

The terms in Equation (A.39) are rearranged.

$$D_1A = -\frac{1}{2}\bar{\alpha}_\theta A - \frac{3}{2}\bar{\gamma}\omega i A^2\bar{A} + \frac{1}{4}\bar{a}_u\omega i B + \frac{1}{4}\bar{a}_u\omega i\bar{B} - \frac{1}{4}\bar{a}_v\omega i - \bar{a}_w\omega i\bar{A} - \frac{\bar{P}_\theta A}{\pi\varepsilon_r}. \tag{A.49}$$

Introducing the polar notation from Equations (A.45) to (A.48) into the secular terms equation for the coordinate θ and separating the real and imaginary parts leads to.

$$\begin{aligned} a_p' =& \frac{1}{4}\omega\sin(\alpha_p-\beta_p)\,b_p\bar{a}_u + \frac{1}{4}\omega\sin(\alpha_p+\beta_p)\,b_p\bar{a}_u - \frac{1}{2}\omega\sin(\alpha_p)\,\bar{a}_v \\ &- \omega\sin(2\alpha_p)\,a_p\bar{a}_w - \frac{2a_p\bar{P}_\theta}{\pi\varepsilon_r} - \frac{1}{2}a_p\bar{\alpha}_\theta. \end{aligned} \tag{A.50}$$

$$\begin{aligned} a_p\alpha_p' =& -\frac{3}{8}\omega\bar{\gamma}a_p^3 + \frac{1}{4}\omega\cos(\alpha_p-\beta_p)\,b_p\bar{a}_u + \frac{1}{4}\omega\cos(\alpha_p+\beta_p)\,b_p\bar{a}_u \\ &- \frac{1}{2}\omega\cos(\alpha_p)\,\bar{a}_v - \omega\cos(2\alpha_p)\,a_p\bar{a}_w. \end{aligned} \tag{A.51}$$

Rearranging the terms in Equation (A.44) gives:

$$\begin{aligned} D_1B =& -\frac{1}{2}\bar{\rho}\frac{\left(i\omega Ae^{i\omega T_0} - i\omega\bar{A}e^{-i\omega T_0}\right)}{Ae^{i\omega T_0}+\bar{A}e^{-i\omega T_0}}B - \frac{1}{2}\bar{\sigma}\bar{\alpha}_\phi B \\ &- \frac{1}{2}\frac{\bar{\alpha}_\phi B}{A^2e^{2i\omega T_0}+2A\bar{A}+\bar{A}^2e^{-2i\omega T_0}} + \frac{1}{2}\frac{\left(\frac{1}{2}\bar{a}_v\omega^2e^{i\omega T_0}+\frac{1}{2}\bar{a}_v\omega^2e^{-i\omega T_0}\right)}{Ae^{i\omega T_0}+\bar{A}e^{-i\omega T_0}}\left(\frac{i}{\bar{\psi}}B\right). \end{aligned} \tag{A.52}$$

Introducing the polar coordinates from Equations (A.48) and (A.49) into Equation (A.52) and separating the real and imaginary parts gives:

$$b_p' = -\frac{1}{2}\bar{\sigma}b_p\bar{\alpha}_\phi - \frac{\sec^2(\omega T_0+\alpha_p)\,b_p\bar{\alpha}_\phi}{2a_p^2} + \frac{1}{2}\omega\bar{\rho}b_p\tan(\omega T_0+\alpha_p). \tag{A.53}$$

$$b_p\beta_p' = \frac{\omega^2\cos(\omega T_0)\cos(\omega T_0+\alpha_p)\,b_p\bar{a}_v}{(1+\cos(2(\omega T_0+\alpha_p)))\,\bar{\psi}a_p}. \tag{A.54}$$

The Equations (A.50), (A.51), (A.53) and (A.54) can be solved by using numerical integration. In order to do this the faster time scale T_0 is replaced with εT_1 to ensure that the equations are numerically consistently structured. It is observed that the equations can only be solved numerically if the system is solely excited vertically. Therefore a_u and a_v are set equal to zero. Unfortunately, a switching on of the power take-off causes a numerical error and an examination is therefore not possible.

The results for amplitude and phase for the coordinate θ are shown in Figures A.1a and A.1b. As expected they show a transient response that decays over time and settle to a fixed value. In Figures A.1c and A.1d the amplitude and phase for the coordinate ϕ are shown. Looking at the amplitude b_p it can be seen that the value is normally equal to zero but arbitrarily jumps to a large positive or negative value. The value for β_p shows a constant value of 1. The simplification of the denominators for the perturbation hierarchy of the coordinate ϕ introduces complicated higher order dependencies. Since this work has a strong focus on the experimental and numerical analysis the perturbation method has been abandoned but further research could address the problems to find a more trackable representation of these differential equations for the full spherical system.

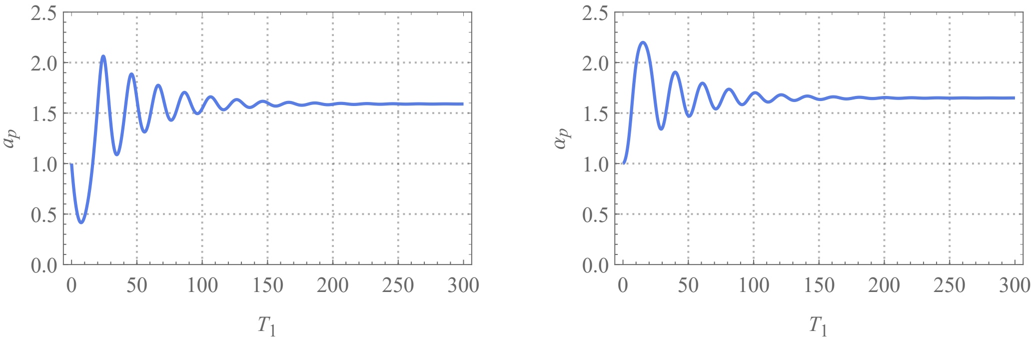

(a) Amplitude for the coordinate θ

(b) Phase for the coordinate θ

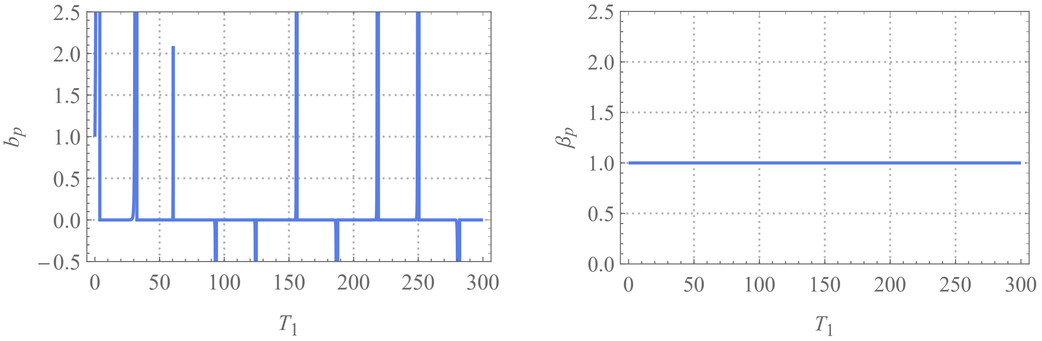

(c) Amplitude for the coordinate ϕ

(d) Phase for the coordinate ϕ

Figure A.1: Numerical analysis of the secular terms. With the variables set to: $\omega = 1, \bar{\psi} = 0.05, \bar{\alpha}_\theta = 0.05, \bar{\alpha}_\phi = 0.05, \bar{a}_u = 0, \bar{a}_v = 0, \bar{a}_w = 0.16, \bar{P}_\theta = 0, \bar{\gamma} = \frac{1}{6}, \bar{\sigma} = \frac{1}{3}, \bar{\rho} = 2, \varepsilon_r = 1, \varepsilon = 0.1, \text{ICs} = 1$

Appendix B

Larger Version of Image

[This page is intentionally left blank.]

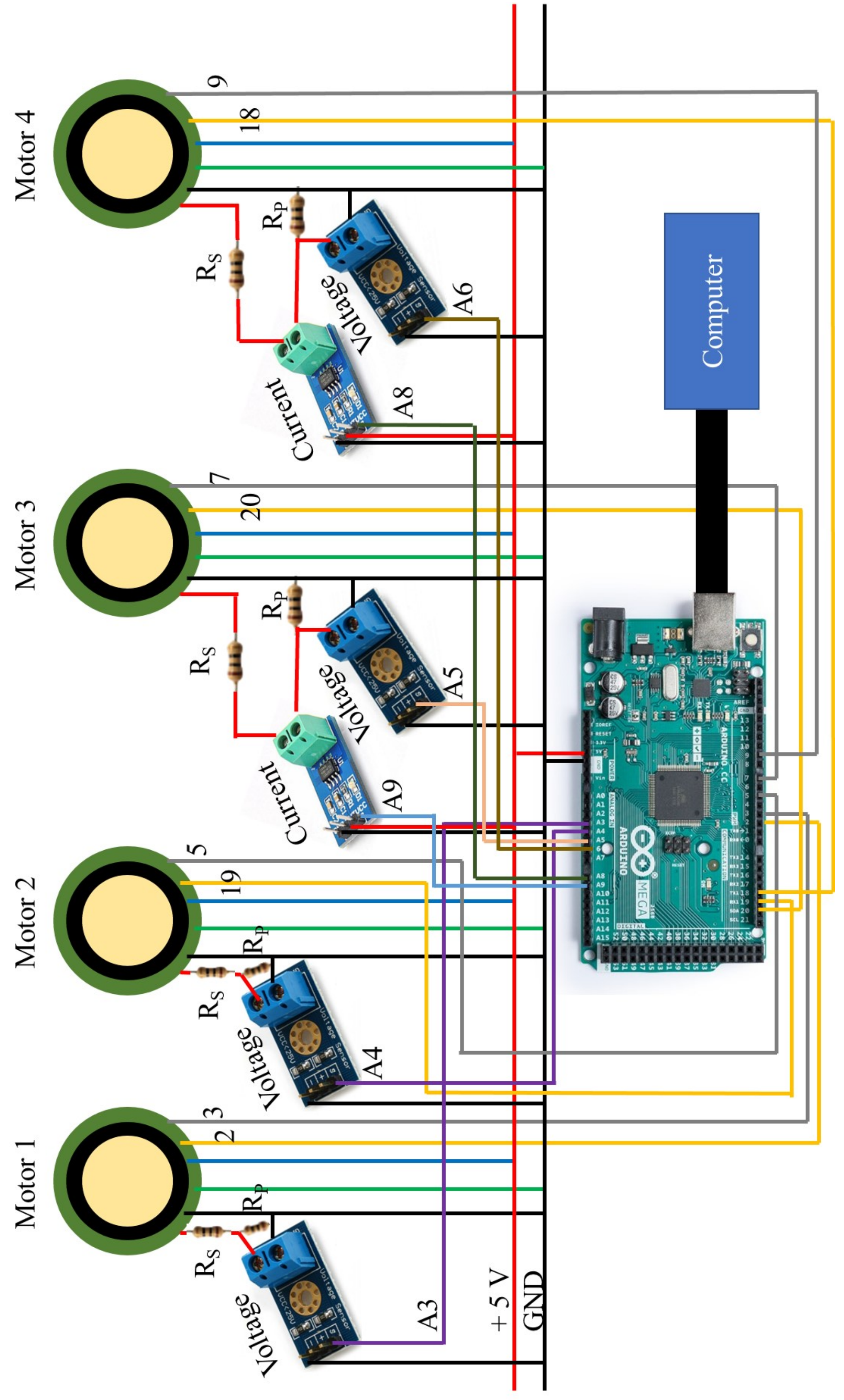

Figure B.1: Connection schematic of the experimental equipment

Bibliography

[1] SOMMERMANN, P. & CARTMELL, M. P. The dynamics of an omnidirectional pendulum harvester. In: (May 2021), pp. 1–12. DOI: 10.1007/s11071-021-06479-z. URL: https://doi.org/10.1007/s11071-021-06479-z (cit. on pp. III, 22, 57, 60, 69, 106, 116, 123).

[2] SOMMERMANN, P. & CARTMELL, M. P. A comparison of the numerically and experimentally determined dynamics of an omnidirectional pendulum energy harvester. In: (2022), pp. -. DOI: -. URL: - (cit. on p. III).

[3] SOMMERMANN, P. Videos of the omnidirectional pendulum energy harvester under different forcing conditions. https://www.youtube.com/watch?v=Y4BfxcNZJuE&list=PL-xLlI0wqZMuid9J9Oo5Z2LpTwyZcp24J. [online accessed 15-Mai-2022]. 2022 (cit. on pp. 3, 128).

[4] EVANS, H. B. Handbook of Ancient Water Technology. In: 95.1 (2001), p. 86. ISSN: 00098418. DOI: 10.2307/4352633. URL: https://www.worldcat.org/title/handbook-of-ancient-water-technology/oclc/1001220706 (cit. on p. 4).

[5] DRACHMANN, A. Heron's Windmill. 1961 (cit. on p. 4).

[6] ANURAKPANDIT, T., TOWNSEND, N. C. & WILSON, P. A. The numerical and experimental investigations of a gimballed pendulum energy harvester. In: 120 (Apr. 2020), p. 103384. ISSN: 00207462. DOI: 10.1016/j.ijnonlinmec.2019.103384 (cit. on pp. 4, 10, 11, 21).

[7] PARADISO, J. A. & STARNER, T. Energy scavenging for mobile and wireless electronics. In: 4.1 (Jan. 2005), pp. 18–27. ISSN: 15361268. DOI: 10.1109/MPRV.2005.9 (cit. on p. 4).

[8] SELVAN, K. V. & MOHAMED ALI, M. S. Micro-scale energy harvesting devices: Review of methodological performances in the last decade. In: 54 (Feb. 2016), pp. 1035–1047. ISSN: 18790690. DOI: 10.1016/j.rser.2015.10.046 (cit. on p. 4).

[9] VULLERS, R. J. et al. Micropower energy harvesting. In: 53.7 (July 2009), pp. 684–693. ISSN: 00381101. DOI: 10.1016/j.sse.2008.12.011 (cit. on p. 4).

[10] BRIAND, D., YEATMAN, E. & ROUNDY, S. Micro Energy Harvesting. 2015, pp. 1–468. ISBN: 9783527672943. DOI: `10.1002/9783527672943` (cit. on p. 4).

[11] PRIYA, S. & INMAN, D. J. Energy harvesting technologies. Springer US, 2009, pp. 1–517. ISBN: 9780387764634. DOI: `10.1007/978-0-387-76464-1` (cit. on p. 4).

[12] JIA, D. & LIU, J. Human power-based energy harvesting strategies for mobile electronic devices. In: 3.1 (Mar. 2009), pp. 27–46. ISSN: 16737393. DOI: `10.1007/s11708-009-0002-4`. URL: `http://www.infineon.com` (cit. on p. 4).

[13] KNIGHT, C., DAVIDSON, J. & BEHRENS, S. Energy options for wireless sensor nodes. In: 8.12 (Dec. 2008), pp. 8037–8066. ISSN: 14248220. DOI: `10.3390/s8128037`. URL: `http://www.mdpi.com/1424-8220/8/12/8037` (cit. on p. 4).

[14] BLOKHINA, E. et al. Nonlinearity in Energy Harvesting Systems. Springer International Publishing, 2016. DOI: `10.1007/978-3-319-20355-3` (cit. on pp. 4–8).

[15] MITCHESON, P. D. et al. Energy harvesting from human and machine motion for wireless electronic devices. In: 96.9 (2008), pp. 1457–1486. ISSN: 00189219. DOI: `10.1109/JPROC.2008.927494` (cit. on p. 5).

[16] ROUNDY, S., WRIGHT, P. K. & RABAEY, J. A study of low level vibrations as a power source for wireless sensor nodes. In: 26.11 (July 2003), pp. 1131–1144. ISSN: 01403664. DOI: `10.1016/S0140-3664(02)00248-7` (cit. on p. 5).

[17] GATTI, G. et al. Harvesting energy from the vibration of a passing train using a single-degree-of-freedom oscillator. In: 66-67 (Jan. 2016), pp. 785–792. ISSN: 10961216. DOI: `10.1016/j.ymssp.2015.06.026` (cit. on p. 5).

[18] ASHRAF, K. et al. A wideband, frequency up-converting bounded vibration energy harvester for a low-frequency environment. In: 22.2 (Feb. 2013), p. 025018. ISSN: 09641726. DOI: `10.1088/0964-1726/22/2/025018`. URL: `https://iopscience.iop.org/article/10.1088/0964-1726/22/2/025018%20https://iopscience.iop.org/article/10.1088/0964-1726/22/2/025018/meta` (cit. on p. 5).

[19] BARTON, D. A., BURROW, S. G. & CLARE, L. R. Energy harvesting from vibrations with a nonlinear oscillator. In: 132.2 (2010), pp. 0210091–0210097. ISSN: 10489002. DOI: `10.1115/1.4000809`. URL: `http://asmedigitalcollection.asme.org/vibrationacoustics/article-pdf/132/2/021009/5831025/021009_1.pdf` (cit. on p. 5).

[20] TANG, L. & YANG, Y. A nonlinear piezoelectric energy harvester with magnetic oscillator. In: 101.9 (Aug. 2012), p. 094102. ISSN: 00036951. DOI: `10.1063/1.4748794`. URL: `http://aip.scitation.org/doi/10.1063/1.4748794` (cit. on p. 5).

[21] GRAVES, J., KUANG, Y. & ZHU, M. Scalable pendulum energy harvester for unmanned surface vehicles. In: 315 (Nov. 2020), p. 112356. ISSN: 09244247. DOI: `10.1016/j.sna.2020.112356` (cit. on pp. 5, 10).

[22] LIANG, C., WU, Y. & ZUO, L. Broadband pendulum energy harvester. In: 25.9 (Aug. 2016), p. 095042. ISSN: 1361665X. DOI: `10.1088/0964-1726/25/9/095042`. URL: `https://iopscience.iop.org/article/10.1088/0964-1726/25/9/095042%20https://iopscience.iop.org/article/10.1088/0964-1726/25/9/095042/meta` (cit. on pp. 5, 10).

[23] ELVIN, N. & ERTURK, A. Introduction and methods of mechanical energy harvesting. Vol. 9781461457. Springer New York, Sept. 2013, pp. 3–14. ISBN: 9781461457053. DOI: `10.1007/978-1-4614-5705-3\_1` (cit. on p. 5).

[24] DUDKA, A. Study, optimization and silicon implementation of a smart high-voltage conditioning circuit for electrostatic vibration energy harvesting system. In: (Feb. 2014). URL: `https://tel.archives-ouvertes.fr/tel-01056404` (cit. on p. 6).

[25] LI, W. J. et al. Infrared signal transmission by a laser-micromachined vibration-induced power generator. In: *Midwest Symposium on Circuits and Systems*. Vol. 1. 2000, pp. 236–239. DOI: `10.1109/mwscas.2000.951628` (cit. on p. 6).

[26] LI, Z., BRINDAK, Z. & ZUO, L. Modeling of an electromagnetic vibration energy harvester with motion magnification. In: *ASME 2011 International Mechanical Engineering Congress and Exposition, IMECE 2011*. Vol. 7. PARTS A AND B. 2011, pp. 285–293. ISBN: 9780791854938. DOI: `10.1115/imece2011-65613`. URL: `http://asmedigitalcollection.asme.org/IMECE/proceedings-pdf/IMECE2011/54938/285/2779663/285_1.pdf` (cit. on p. 6).

[27] WANG, P. et al. A micro electromagnetic low level vibration energy harvester based on MEMS technology. In: 15.6 (June 2009), pp. 941–951. ISSN: 09467076. DOI: `10.1007/s00542-009-0827-0` (cit. on p. 6).

[28] TAO, K. et al. A novel two-degree-of-freedom MEMS electromagnetic vibration energy harvester. In: 26.3 (Feb. 2016), p. 035020. ISSN: 13616439. DOI: `10.1088/0960-1317/26/3/035020`. URL: `https://iopscience.iop.org/article/10.1088/0960-1317/26/3/035020%20https://iopscience.iop.org/article/10.1088/0960-1317/26/3/035020/meta` (cit. on p. 6).

[29] MENINGER, S. et al. Vibration-to-electric energy conversion. In: 9.1 (Feb. 2001), pp. 64–76. ISSN: 10638210. DOI: `10.1109/92.920820` (cit. on p. 6).

[30] NARUSE, Y. et al. Electrostatic micro power generation from low-frequency vibration such as human motion. In: 19.9 (Aug. 2009), p. 5. ISSN: 09601317. DOI: `10.1088/0960-1317/19/9/094002`. URL: `https://iopscience.iop.org/article/10.1088/0960-1317/19/9/094002%20https://iopscience.iop.org/article/10.1088/0960-1317/19/9/094002/meta` (cit. on p. 6).

[31] WU, C. et al. Triboelectric Nanogenerator: A Foundation of the Energy for the New Era. In: 9.1 (Jan. 2019), p. 1802906. ISSN: 16146840. DOI: `10.1002/aenm.201802906`. URL: `http://doi.wiley.com/10.1002/aenm.201802906` (cit. on p. 6).

[32] ROUNDY, S. & WRIGHT, P. K. A piezoelectric vibration based generator for wireless electronics. In: 13.5 (Oct. 2004), pp. 1131–1142. ISSN: 09641726. DOI: `10.1088/0964-1726/13/5/018`. URL: `https://iopscience.iop.org/article/10.1088/0964-1726/13/5/018%20https://iopscience.iop.org/article/10.1088/0964-1726/13/5/018/meta` (cit. on p. 6).

[33] FRISWELL, M. I. et al. Non-linear piezoelectric vibration energy harvesting from a vertical cantilever beam with tip mass. In: 23.13 (Sept. 2012), pp. 1505–1521. ISSN: 1045389X. DOI: `10.1177/1045389X12455722`. URL: `http://journals.sagepub.com/doi/10.1177/1045389X12455722` (cit. on p. 6).

[34] LIU, J. Q. et al. A MEMS-based piezoelectric power generator array for vibration energy harvesting. In: 39.5 (May 2008), pp. 802–806. ISSN: 00262692. DOI: `10.1016/j.mejo.2007.12.017` (cit. on p. 6).

[35] KAMTHAN, P. AUTO Software for Continuation and Bifurcation Problems in Ordinary Differential Equations. online accessed 17.12.2022. URL: `http://indy.cs.concordia.ca/auto/` (cit. on p. 7).

[36] HANSEN, N. et al. COCO: The Experimental Procedure. In: (Mar. 2016). DOI: `10.48550/arxiv.1603.08776`. URL: `https://arxiv.org/abs/1603.08776` (cit. on p. 7).

[37] MUTHUSWAMY, B. & BANERJEE, S. Introduction to Nonlinear Circuits and Networks. 2019, p. 360. ISBN: 9783319673240. DOI: `10.1007/978-3-319-67325-7` (cit. on p. 8).

[38] HARAOUBIA, B. Nonlinear electronics 1: Nonlinear dipoles, harmonic oscillators and switching circuits. 2018, pp. 1–360. ISBN: 9781785483004. DOI: `10.1016/C2017-0-01442-8` (cit. on p. 8).

[39] DUFFING, G. Erzwungene Schwingungen bei veränderlicher Eigenfrequenz und ihre technische Bedeutung [Forced Oscillations in the Presence of Variable Eigenfrequencies]. 1918, pp. 1–134 (cit. on pp. 8, 13).

[40] WANG, X., WU, H. & YANG, B. Nonlinear multi-modal energy harvester and vibration absorber using magnetic softening spring. In: 476 (June 2020), p. 115332. ISSN: 10958568. DOI: `10.1016/j.jsv.2020.115332` (cit. on p. 9).

[41] SUHAIMI, K., RAMLAN, R. & PUTRA, A. A Combined Softening and Hardening Mechanism for Low Frequency Human Motion Energy Harvesting Application. In: 2014 (2014). ISSN: 1687627X. DOI: `10.1155/2014/217032`. URL: `http://dx.doi.org/10.1155/2014/217032` (cit. on p. 9).

[42] REZAEI, M., TALEBITOOTI, R. & FRISWELL, M. I. Efficient acoustic energy harvesting by deploying magnetic restoring force. In: 28.10 (Sept. 2019), p. 105037. ISSN: 1361665X. DOI: `10.1088/1361-665X/ab3a6a`. URL: `https://iopscience.iop.org/article/10.1088/1361-665X/ab3a6a%20https://iopscience.iop.org/article/10.1088/1361-665X/ab3a6a/meta` (cit. on p. 9).

[43] YUAN, T. C., YANG, J. & CHEN, L. Q. Nonlinear dynamics of a circular piezoelectric plate for vibratory energy harvesting. In: 59 (June 2018), pp. 651–656. ISSN: 10075704. DOI: `10.1016/j.cnsns.2017.12.010` (cit. on p. 9).

[44] DAI, X. An vibration energy harvester with broadband and frequency-doubling characteristics based on rotary pendulums. In: 241 (Apr. 2016), pp. 161–168. ISSN: 09244247. DOI: `10.1016/j.sna.2016.02.004` (cit. on pp. 9, 10).

[45] BOROWIEC, M. et al. Dynamic response of a pendulum-driven energy harvester in the presence of noise. In: 476.1 (2013). ISSN: 17426596. DOI: `10.1088/1742-6596/476/1/012038` (cit. on p. 10).

[46] MARSZAL, M. et al. Energy harvesting from pendulum oscillations. In: 94.March (2017), pp. 251–256. ISSN: 00207462. DOI: `10.1016/j.ijnonlinmec.2017.03.022` (cit. on p. 10).

[47] GRAVES, J. & ZHU, M. Design and experimental validation of a pendulum energy harvester with string-driven single clutch mechanical motion rectifier. In: (Dec. 2021), p. 113237. ISSN: 09244247. DOI: `10.1016/j.sna.2021.113237`. URL: `https://linkinghub.elsevier.com/retrieve/pii/S0924424721007007` (cit. on p. 10).

[48] WU, Y. et al. A piezoelectric spring pendulum oscillator used for multi-directional and ultra-low frequency vibration energy harvesting. In: 231 (Dec. 2018), pp. 600–614. ISSN: 03062619. DOI: `10.1016/j.apenergy.2018.09.082` (cit. on p. 10).

[49] JIANG, W. et al. Improving energy harvesting by internal resonance in a spring-pendulum system. In: 36.3 (2020), pp. 618–623. ISSN: 16143116. DOI: `10.1007/s10409-020-00945-4`. URL: `https://doi.org/10.1007/s10409-020-00945-4` (cit. on p. 10).

[50] PUNYAKAEW, S. & PARNICHKUN, M. Vibration energy harvesting for low frequency using auto-tuning parametric rolling pendulum under exogenous multi-frequency excitations. In: 10.6 (Nov. 2020), pp. 448–455. ISSN: 20950349. DOI: `10.1016/j.taml.2020.01.059` (cit. on p. 10).

[51] MALAJI, P. V. & ALI, S. F. Analysis of energy harvesting from multiple pendulums with and without mechanical coupling. In: 224.14-15 (2015), pp. 2823–2838. ISSN: 19516401. DOI: `10.1140/epjst/e2015-02591-7` (cit. on p. 10).

[52] MALAJI, P. V. & ALI, S. F. Broadband energy harvesting with mechanically coupled harvesters. In: 255 (Mar. 2017), pp. 1–9. ISSN: 09244247. DOI: `10.1016/j.sna.2016.12.003` (cit. on p. 10).

[53] GRAVES, J., KUANG, Y. & ZHU, M. Counterweight-Pendulum Energy Harvester with Reduced Resonance Frequency for Unmanned Surface Vehicles. In: 321 (Jan. 2021), p. 112577. ISSN: 09244247. DOI: `10.1016/j.sna.2021.112577` (cit. on p. 10).

[54] PAN, J. et al. Harvesting weak vibration energy by integrating piezoelectric inverted beam and pendulum. In: 227 (July 2021), p. 120374. ISSN: 03605442. DOI: `10.1016/j.energy.2021.120374` (cit. on p. 10).

[55] CARTMELL, M. P. & LAWSON, J. Performance enhancement of an autoparametric vibration absorber by means of computer control. In: 177.2 (Oct. 1994), pp. 173–195. ISSN: 0022460X. DOI: `10.1006/jsvi.1994.1426` (cit. on p. 10).

[56] LI, X. et al. The pendulum adaptive frequency oscillator. In: 179 (Nov. 2022), p. 109361. ISSN: 08883270. DOI: `10.1016/j.ymssp.2022.109361` (cit. on pp. 10, 30, 211).

[57] MCROBB, M. Development and Enhancement of Various Mechanical Oscillators for Application in Vibrational Energy Harvesting. PhD thesis. 2014 (cit. on pp. 10, 21, 59, 66, 88).

[58] JAHANGIRI, V. & SUN, C. Integrated bi-directional vibration control and energy harvesting of monopile offshore wind turbines. In: 178 (Apr. 2019), pp. 260–269. ISSN: 00298018. DOI: `10.1016/j.oceaneng.2019.02.015` (cit. on p. 11).

[59] WANG, T., LOU, H. & ZHU, S. Prototyping and Electromagnetic Analysis of a Biaxial-Pendulum Wave Energy Harvester. In: *OCEANS 2021: San Diego Porto*. IEEE, Sept. 2022, pp. 1–5. ISBN: 978-0-692-93559-0. DOI: `10.23919/oceans44145.2021.9706060`. URL: `https://ieeexplore.ieee.org/document/9706060/` (cit. on pp. 11, 21).

[60] KACHAPI, S. & GANJI, D. Dynamics and Vibrations. Vol. 202. Solid Mechanics and Its Applications. Springer Netherlands, 2013. ISBN: 9789400767744. DOI: `10.1007/978-94-007-6775-1` (cit. on pp. 11, 12).

[61] ELLIOTT, S. J., TEHRANI, M. G. & LANGLEY, R. S. Nonlinear damping and quasi-linear modelling. In: 373.2051 (Sept. 2015). ISSN: 1364503X. DOI: `10.1098/rsta.2014.0402`. URL: `http://dx.doi.org/10.1098/rsta.2014.0402` (cit. on p. 12).

[62] DAQAQ, M. F. On intentional introduction of stiffness nonlinearities for energy harvesting under white Gaussian excitations. In: *Nonlinear Dynamics* 69 (3 Aug. 2012), pp. 1063–1079. ISSN: 0924090X. DOI: `10.1007/S11071-012-0327-0/FIGURES/16`. URL: `https://link.springer.com/article/10.1007/s11071-012-0327-0` (cit. on p. 12).

[63] MANN, B. P., STANTON, S. C. & BERNARD, B. P. Intentional nonlinearity in energy harvesting systems. In: *Understanding Complex Systems* (2019), pp. 84–95. ISSN: 18600840. DOI: `10.1007/978-3-030-10892-2_10/FIGURES/5`. URL: `https://link.springer.com/chapter/10.1007/978-3-030-10892-2_10` (cit. on p. 12).

[64] BRENNAN, M. J. et al. On the jump-up and jump-down frequencies of the Duffing oscillator. In: 318.4-5 (Dec. 2008), pp. 1250–1261. ISSN: 10958568. DOI: `10.1016/j.jsv.2008.04.032` (cit. on p. 13).

[65] HILBORN, R. C. Chaos and Nonlinear Dynamics. Oxford University Press, Jan. 2010. ISBN: 9780198507239. DOI: `10.1093/acprof:oso/9780198507239.001.0001` (cit. on pp. 14, 15, 17).

[66] GIBBS, J. W. Elementary principles in statistical mechanics developed with especial reference to the rational foundation of thermodynamics. C. Scribner, Nov. 1902. DOI: `10.5962/bhl.title.32624`. URL: `http://www.biodiversitylibrary.org/bibliography/32624` (cit. on p. 14).

[67] ARGYRIS, J. et al. An exploration of dynamical systems and chaos: Completely revised and enlarged second edition. Springer Berlin Heidelberg, Jan. 2015, pp. 1–865. ISBN: 9783662460429. DOI: `10.1007/978-3-662-46042-9` (cit. on pp. 16, 17).

[68] GAN, W. S. Techniques in the application of chaos theory in signal and image processing. In: *Control and Dynamic Systems*. Vol. 77. Academic Press Inc., Jan. 1996, pp. 339–387. DOI: `10.1016/S0090-5267(96)80034-X` (cit. on p. 17).

[69] ASTON, P. J. Bifurcations of the horizontally forced spherical pendulum. In: 170.3-4 (1999), pp. 343–353. ISSN: 00457825. DOI: `10.1016/S0045-7825(98)00202-3` (cit. on pp. 17, 21, 26, 27).

[70] PIKOVSKY, A. & POLITI, A. Lyapunov Exponents: A Tool to Explore Complex Dynamics. Vol. 70. 3. 2017, pp. 62–63. ISBN: 9781107030428 (cit. on p. 19).

[71] BARREIRA, L. Lyapunov exponents. 2017, pp. 1–273. ISBN: 9783319712611. DOI: `10.1007/978-3-319-71261-1`. URL: `9781107030428` (cit. on p. 19).

[72] VALLEJO, J. C. & SANJUAN, M. A. F. Predictability of Chaotic Dynamics. 2017, pp. 129–136. ISBN: 978-3-319-51892-3 (cit. on p. 19).

[73] MATTHEWS, M. R., GAULD, C. F. & STINNER, A. The pendulum: Scientific, historical, philosophical and educational perspectives. Springer Netherlands, 2005, pp. 1–542. ISBN: 140203525X. DOI: `10.1007/1-4020-3526-8` (cit. on p. 19).

[74] SOMMERIA, J. Foucault and the rotation of the Earth. Vol. 18. 9-10. Elsevier Masson s.r.l., Nov. 2017, pp. 520–525. DOI: `10.1016/j.crhy.2017.11.003` (cit. on p. 19).

[75] CONDURACHE, D. & MARTINUSI, V. Foucault Pendulum-like problems: A tensorial approach. In: 43.8 (Oct. 2008), pp. 743–760. ISSN: 00207462. DOI: `10.1016/j.ijnonlinmec.2008.03.009` (cit. on p. 19).

[76] BERGMANN, J. von & BERGMANN, H. von. Foucault pendulum through basic geometry. In: 75.10 (Oct. 2007), pp. 888–892. ISSN: 0002-9505. DOI: `10.1119/1.2757623`. URL: `http://aapt.scitation.org/doi/10.1119/1.2757623` (cit. on p. 19).

[77] ACZEL, A. D. & ROMER, R. H. PENDULUM-Léon Foucault and the Triumph of Science. In: 72.2 (Feb. 2004), pp. 286–287. ISSN: 0002-9505. DOI: `10.1119/1.1637901` (cit. on p. 19).

[78] CONLIN, M. F. The Popular and Scientific Reception of the Foucault Pendulum in the United States. In: 90.2 (1999), pp. 181–204. ISSN: 0021-1753. DOI: `10.1086/384321`. URL: `https://www.jstor.org/stable/237048?seq=1` (cit. on p. 19).

[79] SENKAL, D., EFIMOVSKAYA, A. & SHKEL, A. M. Dual Foucault Pendulum gyroscope. In: *2015 Transducers - 2015 18th International Conference on Solid-State Sensors, Actuators and Microsystems, TRANSDUCERS 2015*. Institute of Electrical and Electronics Engineers Inc., Aug. 2015, pp. 1219–1222. ISBN: 9781479989553. DOI: `10.1109/TRANSDUCERS.2015.7181149` (cit. on p. 19).

[80] PRIKHODKO, I. P. et al. Foucault pendulum on a chip: Angle measuring silicon MEMS gyroscope. In: *Proceedings of the IEEE International Conference on Micro Electro Mechanical Systems (MEMS)*. 2011, pp. 161–164. ISBN: 9781424496327. DOI: `10.1109/MEMSYS.2011.5734386` (cit. on p. 19).

[81] CARTMELL, M. P. et al. On the modelling and testing of a laboratory-scale Foucault pendulum as a precursor for the design of a high-performance measurement instrument. In: 476.2238 (June 2020), p. 20190680. ISSN: 1364-5021. DOI: `10.1098/rspa.2019.0680` (cit. on p. 19).

[82] TRUEBA, J. L., BALTANÁS, J. P. & SANJUÁN, M. A. A generalized perturbed pendulum. In: 15.5 (Mar. 2003), pp. 911–924. ISSN: 09600779. DOI: `10.1016/S0960-0779(02)00210-2` (cit. on p. 19).

[83] OLEJNIK, P. & AWREJCEWICZ, J. Coupled oscillators in identification of nonlinear damping of a real parametric pendulum. In: 98 (Jan. 2018), pp. 91–107. ISSN: 10961216. DOI: 10.1016/j.ymssp.2017.04.037 (cit. on p. 19).

[84] KECIK, K. & WARMINSKI, J. Dynamics of an autoparametric pendulum-like system with a nonlinear semiactive suspension. In: 2011 (2011). ISSN: 1024123X. DOI: 10.1155/2011/451047 (cit. on p. 19).

[85] WARMINSKI, J. & KECIK, K. Autoparametric vibrations of a nonlinear system with a pendulum and magnetorheological damping. In: 181 (2012), pp. 1–61. ISSN: 09250042. DOI: 10.1007/978-94-007-2473-0_1 (cit. on p. 19).

[86] RAFAT, M. Z., WHEATLAND, M. S. & BEDDING, T. R. Dynamics of a double pendulum with distributed mass. In: 77.3 (Mar. 2009), pp. 216–223. ISSN: 0002-9505. DOI: 10.1119/1.3052072. eprint: 0812.0393. URL: http://aapt.scitation.org/doi/10.1119/1.3052072 (cit. on p. 19).

[87] LEVIEN, R. B. & TAN, S. M. Double pendulum: An experiment in chaos. In: 61.11 (Nov. 1993), pp. 1038–1044. ISSN: 0002-9505. DOI: 10.1119/1.17335. URL: http://aapt.scitation.org/doi/10.1119/1.17335 (cit. on p. 19).

[88] STACHOWIAK, T. & OKADA, T. A numerical analysis of chaos in the double pendulum. In: 29.2 (July 2006), pp. 417–422. ISSN: 09600779. DOI: 10.1016/j.chaos.2005.08.032 (cit. on p. 19).

[89] SHINBROT, T. et al. Chaos in a double pendulum. In: 60.6 (June 1992), pp. 491–499. ISSN: 0002-9505. DOI: 10.1119/1.16860. URL: http://aapt.scitation.org/doi/10.1119/1.16860 (cit. on p. 19).

[90] MARCELO TUSSET, A. et al. Chaos control and sensitivity analysis of a double pendulum arm excited by an RLC circuit based nonlinear shaker. In: 22.17 (Oct. 2016), pp. 3621–3637. ISSN: 17412986. DOI: 10.1177/1077546314564782. URL: http://journals.sagepub.com/doi/10.1177/1077546314564782 (cit. on p. 19).

[91] KANA, D. D. & FOX, D. J. Distinguishing the transition to chaos in a spherical pendulum. In: 5.1 (1995), pp. 298–310. ISSN: 10541500. DOI: 10.1063/1.166077 (cit. on pp. 20, 26).

[92] PALACIOS, A., GROSS, L. M. & ROCKWOOD, A. P. Dynamics and Chaos: The Spherical Pendulum. In: 15.4 (Oct. 1996), pp. 263–270. ISSN: 0167-7055. DOI: 10.1111/1467-8659.1540263. URL: https://onlinelibrary.wiley.com/doi/10.1111/1467-8659.1540263 (cit. on p. 20).

[93] CARTWRIGHT, J. H. & TRITTON, D. J. Chaotic dynamics and reversal statistics of the forced spherical pendulum: Comparing the Miles equations with experiment. In: 25.1 (2010), pp. 1–16. ISSN: 14689367. DOI: `10.1080/14689360902751574` (cit. on pp. 20, 21, 27).

[94] MILES, J. W. Stability of forced oscillations of a spherical pendulum. In: 20.1 (1962), pp. 21–32. ISSN: 0033-569X. DOI: `10.1090/qam/133521` (cit. on pp. 20, 21, 25, 26).

[95] MILES, J. Resonant motion of a spherical pendulum. In: 11.3 (1984), pp. 309–323. ISSN: 01672789. DOI: `10.1016/0167-2789(84)90013-7` (cit. on pp. 20, 26).

[96] MILES, J. W. & ZOU, Q. P. Parametric excitation of a detuned spherical pendulum. In: 164.2 (1993), pp. 237–250. ISSN: 10958568. DOI: `10.1006/jsvi.1993.1211` (cit. on p. 20).

[97] OLSSON, M. G. The precessing spherical pendulum. In: 46.11 (Nov. 1978), pp. 1118–1119. ISSN: 0002-9505. DOI: `10.1119/1.11151` (cit. on pp. 20, 26).

[98] OLSSON, M. G. Spherical pendulum revisited. In: 49.6 (1981), pp. 531–534. ISSN: 0002-9505. DOI: `10.1119/1.12666` (cit. on pp. 20, 21, 59, 117).

[99] TRITTON, D. J. Ordered and chaotic motion of a forced spherical pendulum. In: 7.3 (1986), pp. 162–169. ISSN: 01430807. DOI: `10.1088/0143-0807/7/3/003` (cit. on pp. 20, 26).

[100] IRONS, F. E. Concerning the nonlinear behaviour of the forced spherical pendulum including the dowsing pendulum. In: 11.2 (1990), pp. 107–115. ISSN: 01430807. DOI: `10.1088/0143-0807/11/2/009` (cit. on p. 20).

[101] BRYANT, P. J. & MILES, J. W. On a periodically forced, weakly damped pendulum. Part 1: Applied torque. In: 32.October 1989 (1990), pp. 1–22 (cit. on p. 20).

[102] BRYANT, P. J. & MILES, J. W. On a periodically forced, weakly damped pendulum. Part 2: Horizontal forcing. In: 32.October 1989 (1990), pp. 23–41 (cit. on p. 20).

[103] BRYANT, P. J. & MILES, J. W. On a periodically forced, weakly damped pendulum. Part 3: Vertical forcing. In: 32.October 1989 (1990), pp. 1–22 (cit. on p. 20).

[104] DE JONG, M. L. Chaos and the simple pendulum. In: 30.2 (1992), pp. 115–121. ISSN: 0031-921X. DOI: `10.1119/1.2343491` (cit. on p. 20).

[105] BRYANT, P. J. Breakdown to chaotic motion of a forced, damped, spherical pendulum. In: 64.1-3 (1993), pp. 324–339. ISSN: 01672789. DOI: `10.1016/0167-2789(93)90263-Z` (cit. on pp. 20, 26).

[106] TRITTON, D. J. & GROVES, M. Lyapunov exponents for the Miles' spherical pendulum equations. In: 126.1-2 (1999), pp. 83–98. ISSN: 01672789. DOI: `10.1016/S0167-2789(98)00263-2` (cit. on pp. 20, 26, 27).

[107] MARKEYEV, A. P. The dynamics of a spherical pendulum with a vibrating suspension. In: 63.2 (1999), pp. 205–211. ISSN: 00218928. DOI: `10.1016/S0021-8928(99)00028-3`. URL: `www.elsevier.com/locate/jappmat` (cit. on p. 21).

[108] LEUNG, A. Y. & KUANG, J. L. On the chaotic dynamics of a spherical pendulum with a harmonically vibrating suspension. In: 43.3 (Feb. 2006), pp. 213–238. ISSN: 0924090X. DOI: `10.1007/s11071-006-7426-8` (cit. on p. 21).

[109] SHVETS, A. Y. Deterministic chaos of a spherical pendulum under limited excitation. In: 59.4 (2007), pp. 602–614. DOI: `10.1007/s11253-007-0039-7` (cit. on p. 21).

[110] NÁPRSTEK, J. & FISCHER, C. Types and stability of quasi-periodic response of a spherical pendulum. In: 124 (2013), pp. 74–87. ISSN: 00457949. DOI: `10.1016/j.compstruc.2012.11.003`. URL: `http://dx.doi.org/10.1016/j.compstruc.2012.11.003` (cit. on pp. 21, 27).

[111] POSPÍŠIL, S., FISCHER, C. & NÁPRSTEK, J. Experimental analysis of the influence of damping on the resonance behavior of a spherical pendulum. In: 78.1 (2014), pp. 371–390. DOI: `10.1007/s11071-014-1446-6` (cit. on pp. 21, 27, 59).

[112] LITAK, G. et al. Dynamic response of the spherical pendulum subjected to horizontal Lissajous excitation. In: (Nov. 2020), pp. 1–18. ISSN: 1573269X. DOI: `10.1007/s11071-020-06023-5`. URL: `https://doi.org/10.1007/s11071-020-06023-5` (cit. on pp. 21, 27).

[113] LOU, H., WANG, T. & ZHU, S. Design, modeling and experiments of a novel biaxial-pendulum vibration energy harvester. In: *Energy* 254 (Sept. 2022), p. 124431. ISSN: 03605442. DOI: `10.1016/j.energy.2022.124431` (cit. on p. 21).

[114] IKEDA, T., HARATA, Y. & TAKEEDA, A. Nonlinear responses of spherical pendulum vibration absorbers in towerlike 2DOF structures. In: 88.4 (2017), pp. 2915–2932. ISSN: 1573269X. DOI: `10.1007/s11071-017-3421-5` (cit. on pp. 21, 29, 58, 59).

[115] MILES, J. Internal resonance of a detuned spherical pendulum. In: 36.4 (July 1985), pp. 609–615. ISSN: 00442275. DOI: `10.1007/BF00945300` (cit. on p. 26).

[116] TÊTU, A. Power Take-Off Systems for WECs. In: *Handbook of Ocean Wave Energy*. Springer, Cham, 2017, pp. 203–220. DOI: `10.1007/978-3-319-39889-1\_8` (cit. on pp. 29, 30).

[117] OZKOP, E. & ALTAS, I. H. Control, power and electrical components in wave energy conversion systems: A review of the technologies. In: 67 (2017), pp. 106–115. ISSN: 18790690. DOI: `10.1016/j.rser.2016.09.012`. URL: `http://dx.doi.org/10.1016/j.rser.2016.09.012` (cit. on p. 30).

[118] ZHOU, Z. et al. Permanent magnet generator control and electrical system configuration for Wave Dragon MW wave energy take-off system. In: *IEEE International Symposium on Industrial Electronics*. 2008, pp. 1580–1585. ISBN: 1424416655. DOI: `10.1109/ISIE.2008.4677255` (cit. on p. 30).

[119] KAZMIERKOWSKI, M. P. & JASIŃSKI, M. Power electronics for renewable sea wave energy. In: (2010), pp. 4–9. ISSN: 18420133. DOI: `10.1109/OPTIM.2010.5510476` (cit. on p. 30).

[120] O'SULLIVAN, D. et al. Development of an electrical power take off system for a sea-test scaled offshore wave energy device. In: 36.4 (Apr. 2011), pp. 1236–1244. ISSN: 09601481. DOI: `10.1016/j.renene.2010.10.007` (cit. on p. 30).

[121] KOVALTCHOUK, T. et al. Model Predictive Control of a Direct Wave Energy Converter Constrained by the Electrical Chain using an Energetic Approach. In: 10.1 (2015), pp. 1–10. ISSN: 2309-1983. URL: `https://hal.archives-ouvertes.fr/hal-01195536` (cit. on p. 30).

[122] DICKEN, J. et al. Power-extraction circuits for piezoelectric energy harvesters in miniature and low-power applications. In: *IEEE Transactions on Power Electronics* 27 (11 2012), pp. 4514–4529. ISSN: 08858993. DOI: `10.1109/TPEL.2012.2192291` (cit. on p. 30).

[123] HONG, Y. et al. Review on electrical control strategies for wave energy converting systems. In: 31 (Mar. 2014), pp. 329–342. ISSN: 13640321. DOI: `10.1016/j.rser.2013.11.053` (cit. on p. 31).

[124] MARIA-ARENAS, A. et al. Control strategies applied to wave energy converters: State of the art. In: 12.16 (2019). ISSN: 19961073. DOI: `10.3390/en12163115` (cit. on p. 31).

[125] GIORGI, G. & RINGWOOD, J. V. Implementation of latching control in a numerical wave tank with regular waves. In: 2.2 (May 2016), pp. 211–226. ISSN: 21986452. DOI: `10.1007/s40722-016-0052-8` (cit. on p. 31).

[126] RINGWOOD, J. & BUTLER, S. Optimisation of a wave energy converter. In: 37.10 (2004), pp. 155–160. ISSN: 14746670. DOI: `10.1016/S1474-6670(17)31738-X` (cit. on p. 31).

[127] ASHBY, D. Electrical engineering 101: Everything you should have learned in school but probably Didn't. Elsevier Science, Jan. 2011, pp. 1–291. ISBN: 9780123860019. DOI: `10.1016/B978-0-12-386001-9.00010-6` (cit. on pp. 32, 33).

[128] Bildstein, M., Mann, K. & Richter, B. Regenerative braking system. In: *Fundamentals of Automotive and Engine Technology*. Springer Vieweg, Wiesbaden, 2014, pp. 240–243. DOI: `10.1007/978-3-658-03972-1\_22`. URL: `https://link.springer.com/chapter/10.1007/978-3-658-03972-1_22` (cit. on p. 33).

[129] Adib, A. & Dhaouadi, R. Performance analysis of regenerative braking in permanent magnet synchronous motor drives. In: 3.1 (2018), pp. 460–466. ISSN: 24156698. DOI: `10.25046/aj030156` (cit. on p. 33).

[130] Dubey, M. K. & Bobba, P. B. Variable switch regenerative braking technique for PM BLDC motor driven electric two-wheeler. In: *E3S Web of Conferences*. Vol. 87. 2019. DOI: `10.1051/e3sconf/20198701029`. URL: `https://doi.org/10.1051/e3sconf/201` (cit. on p. 33).

[131] Mitcheson, P. D. et al. Tuning the resonant frequency and damping of an electromagnetic energy harvester using power electronics. In: *IEEE Transactions on Circuits and Systems II: Express Briefs* 58 (12 2011), pp. 792–796. ISSN: 15583791. DOI: `10.1109/TCSII.2011.2173966` (cit. on p. 33).

[132] Wolfram Research, Inc. Documentation NDSolve. `https://reference.wolfram.com/language/ref/NDSolve.html`. [online accessed 30-August-2021]. 2019 (cit. on p. 34).

[133] Wolfram Research, Inc. Advanced Numerical Differential Equation Solving in the Wolfram Language. `https://reference.wolfram.com/language/tutorial/NDSolveOverview.html`. [online accessed 30-August-2021] (cit. on p. 34).

[134] Wolfram Research, Inc. "ExplicitRungeKutta" Method for NDSolve. `https://reference.wolfram.com/language/tutorial/NDSolveExplicitRungeKutta.html`. [online accessed 30-August-2021] (cit. on p. 34).

[135] Wolfram Research, Inc. How to | Check the Results of NDSolve. `https://reference.wolfram.com/language/howto/CheckTheResultsOfNDSolve.html`. [online accessed 30-August-2021] (cit. on p. 34).

[136] Cochelin, B. Numerical computation of nonlinear normal modes using HBM and ANM. In: *CISM International Centre for Mechanical Sciences, Courses and Lectures* 555 (2014), pp. 251–292. ISSN: 23093706. DOI: `10.1007/978-3-7091-1791-0_6/COVER`. URL: `https://link.springer.com/chapter/10.1007/978-3-7091-1791-0_6` (cit. on p. 35).

[137] Karkar, S., Cochelin, B. & Vergez, C. A comparative study of the harmonic balance method and the orthogonal collocation method on stiff nonlinear systems. In: *Journal of Sound and Vibration* 333 (12 June 2014), pp. 2554–2567. ISSN: 0022-460X. DOI: `10.1016/J.JSV.2014.01.019` (cit. on p. 35).

[138] SOMMERMANN, P. Numerical and Experimental Code. `https://github.com/PhilSom/PhD`. [online accessed 14-February-2022]. 2022 (cit. on pp. 35, 41, 59).

[139] BARTNIK, N. Moved Encoded Motor driver from separete repo. [online accessed 29-September-2021]. URL: `https://github.com/NikodemBartnik/Small-Projects/tree/main/Encoded%5C%20Motor%5C%20Driver` (cit. on p. 41).

[140] DEJAN. How Rotary Encoder Works and How To Use It with Arduino. `https://howtomechatronics.com/tutorials/arduino/rotary-encoder-works-use-arduino/`. [online accessed 29-September-2021] (cit. on p. 41).

[141] DRONEBOT WORKSHOP. How Rotary Encoder Works and How To Use It with Arduino. `https://dronebotworkshop.com/rotary-encoders-arduino/`. [online accessed 29-September-2021] (cit. on p. 41).

[142] WORKSHOP, D. How Rotary Encoder Works and How To Use It with Arduino. `https://dronebotworkshop.com/dc-volt-current/`. [online accessed 29-September-2021] (cit. on p. 41).

[143] APPLE INC. Getting Raw Accelerometer Events. `https://developer.apple.com/documentation/coremotion/getting_raw_accelerometer_events`. [online accessed 22-November-2021] (cit. on p. 42).

[144] BOSCH SENSORTEC GMBH. Accelerometers. [online accessed 22-November-2021]. URL: `https://www.bosch-sensortec.com/products/motion-sensors/accelerometers/` (cit. on p. 42).

[145] RWTH AACHEN UNIVERSITY. Phyphox. `https://phyphox.org/`. [online accessed 22-November-2021] (cit. on p. 42).

[146] BOLDEA, I. Electric Generators Handbook - Two Volume Set. CRC Press, Oct. 2018. DOI: `10.1201/9781315214191` (cit. on p. 46).

[147] PYRHÖNEN, J., JOKINEN, T. & HRABOVCOVÁ, V. Design of Rotating Electrical Machines. John Wiley & Sons Ltd, Oct. 2013. ISBN: 9781118701591. DOI: `10.1002/9781118701591`. URL: `http://doi.wiley.com/10.1002/9781118701591` (cit. on p. 46).

[148] BECKLEY, P. Industrial magnetic measurements. In: 215 (June 2000), pp. 664–668. ISSN: 03048853. DOI: `10.1016/S0304-8853(00)00253-5` (cit. on p. 47).

[149] PARLE, J., MADRIGAL, M. & ACHA, E. Trends in Power Quality Monitoring. In: 21 (10 Aug. 2002), pp. 3–21. ISSN: 0272-1724. DOI: `10.1109/39.954584` (cit. on p. 47).

[150] TAN, P. C., MORRISON, R. E. & HOLMES, D. G. Voltage form factor control and reactive power compensation in a 25-kV electrified railway system using a shunt active filter based on voltage detection. In: 39 (2 Mar. 2003), pp. 575–581. ISSN: 00939994. DOI: `10.1109/TIA.2003.809455` (cit. on p. 47).

[151] RWTH Aachen University. Phyphox Sensor Database. `https://phyphox.org/sensordb/`. [online accessed 22-November-2021] (cit. on p. 49).

[152] Watt, D. & Cartmell, M. P. An externally loaded parametric oscillator. In: 170.3 (1994), pp. 339–364. ISSN: 10958568. DOI: `10.1006/jsvi.1994.1067` (cit. on p. 66).

[153] Nayfeh, A. H. Perturbation Methods. Wiley, Aug. 1973. ISBN: 0-471-63059-4. URL: `https://onlinelibrary.wiley.com/doi/book/10.1002/9783527617609` (cit. on pp. 119, XLVI).

[154] Nayfeh, A. H. & Mook, D. T. Nonlinear Oscillations. Wiley, May 1979. ISBN: 0-471-03555-6. URL: `https://onlinelibrary.wiley.com/doi/book/10.1002/9783527617586` (cit. on pp. 119, XLVI).

[155] Nayfeh, A. H. Introduction to Perturbation Techniques. Vol. 3. 1981, p. 533. ISBN: 0-471-08033-0 (cit. on pp. 119, XLVI).

[156] Cartmell, M. P. Introduction to Linear, Parametric and Nonlinear Vibrations. Champman and Hall, 1990. ISBN: 0412307308 (cit. on pp. 119, 125, 126, XLVI).

[157] Khanin, R., Cartmell, M. P. & Gilbert, A. A Computerized implementation of the multiple scales perturbation method using Mathematica. In: 76 (5 July 2000), pp. 565–575. ISSN: 00457949. DOI: `10.1016/S0045-7949(99)00184-4` (cit. on p. 119).

[158] Xu, X. & Wiercigroch, M. Approximate analytical solutions for oscillatory and rotational motion of a parametric pendulum. In: 47.1-3 (2007), pp. 311–320. ISSN: 0924090X. DOI: `10.1007/s11071-006-9074-4` (cit. on pp. 125, 126).

[159] Cartmell, M. P. & Ziegler, S. W. Terrestrial scale model testing of a motorised propulsion tether. In: *36th AIAA/ASME/SAE/ASEE Joint Propulsion Conference and Exhibit*. American Institute of Aeronautics and Astronautics Inc., 2000, p. 3612. DOI: `10.2514/6.2000-3612`. URL: `https://arc.aiaa.org/doi/abs/10.2514/6.2000-3612` (cit. on p. 212).

[160] Malatkar, P. et al. Pitfalls an engineer needs to be aware of during vibration testing. In: vol. 2006. 2006, pp. 1887–1892. ISBN: 1424401526. DOI: `10.1109/ECTC.2006.1645918` (cit. on p. 212).